The phenomenology of sub-THz radar sea clutter

Aleksanteri Benjamin Vattulainen

A thesis submitted for the degree of PhD
at the
University of St Andrews

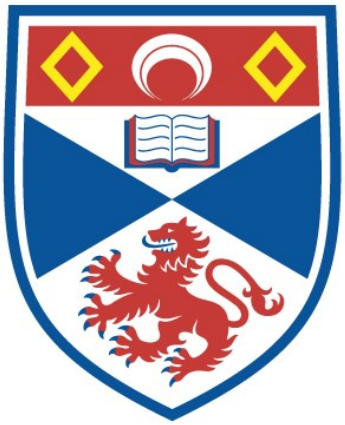

2025

It is possible to commit no mistakes and still lose. That is not a weakness, that is life.
J. L. Picard

Candidate's declaration

I, Aleksanteri Benjamin Vattulainen, do hereby certify that this thesis, submitted for the degree of PhD, which is approximately 72,000 words in length, has been written by me, and that it is the record of work carried out by me, or principally by myself in collaboration with others as acknowledged, and that it has not been submitted in any previous application for any degree. I confirm that any appendices included in my thesis contain only material permitted by the 'Assessment of Postgraduate Research Students' policy.

I was admitted as a research student at the University of St Andrews in September 2020.

I received funding from an organisation or institution and have acknowledged the funder(s) in the full text of my thesis.

Date 29.8.24 Signature of candidate

Supervisor's declaration

I hereby certify that the candidate has fulfilled the conditions of the Resolution and Regulations appropriate for the degree of PhD in the University of St Andrews and that the candidate is qualified to submit this thesis in application for that degree. I confirm that any appendices included in the thesis contain only material permitted by the 'Assessment of Postgraduate Research Students' policy.

Date 29.8.24 Signature of supervisor

Permission for publication

In submitting this thesis to the University of St Andrews we understand that we are giving permission for it to be made available for use in accordance with the regulations of the University Library for the time being in force, subject to any copyright vested in the work not being affected thereby. We also understand, unless exempt by an award of an embargo as requested below, that the title and the abstract will be published, and that a copy of the work may be made and supplied to any bona fide library or research worker, that this thesis will be electronically accessible for personal or research use and that the library has the right to migrate this thesis into new electronic forms as required to ensure continued access to the thesis.

I, Aleksanteri Benjamin Vattulainen, confirm that my thesis does not contain any third-party material that requires copyright clearance.

The following is an agreed request by candidate and supervisor regarding the publication of this thesis:

Printed copy

No embargo on print copy.

Electronic copy

No embargo on electronic copy.

Date 29.8.24 Signature of candidate

Date 29.8.24 Signature of supervisor

Underpinning Research Data or Digital Outputs

Candidate's declaration

I, Aleksanteri Benjamin Vattulainen, understand that by declaring that I have original research data or digital outputs, I should make every effort in meeting the University's and research funders' requirements on the deposit and sharing of research data or research digital outputs.

Date 29.8.24 Signature of candidate

Permission for publication of underpinning research data or digital outputs

We understand that for any original research data or digital outputs which are deposited, we are giving permission for them to be made available for use in accordance with the requirements of the University and research funders, for the time being in force.

We also understand that the title and the description will be published, and that the underpinning research data or digital outputs will be electronically accessible for use in accordance with the license specified at the point of deposit, unless exempt by award of an embargo as requested below.

The following is an agreed request by candidate and supervisor regarding the publication of underpinning research data or digital outputs:

No embargo on underpinning research data or digital outputs.

Date 29.8.24 Signature of candidate

Date 29.8.24 Signature of supervisor

Acknowledgements

I would not have been able to complete this Ph.D. without the support of a great number of people around me, despite an apparently hereditary stubbornness. It has been a period of immense personal growth, bringing with it both the joys of accomplishment and the pains of change. Growing people need patience, and I've been fortunate to be afforded so much.

First and foremost, I wish to thank my supervisors, Duncan and Samiur, for their consistent support, timely words, and invaluable wisdom. My success is entirely tied to your collective efforts. I also acknowledge the impact of the 'lifers' of the Millimetre-wave & EPR Group: Graham, Dav, Rob, and Hassane. All the advice, help, and laughs won't be forgotten. Your contributions made all the difference, as undergrad tutors, during a summer project, my Master's project, and finally in the lab during my Ph.D. And to my Ph.D. student colleagues – Matt, Daniel, Yujie, Mark, and Will – your camaraderie at conferences, in the lab, and at coffee times was always welcome.

I wish to extend my gratitude to the collaborators on the broader STREAM project at the University of Birmingham – Marina, Anum, Dillon, Liam (now at QinetiQ), Mike, Ed, Sam, and Andy – you all played an important role in the successes of my work. I fondly remember our shared field work experiences, where for me the opportunity to get out of the lab and do some peculiar radar stuff in interesting places was one of the draws of this project. A particular highlight was the late night hot-tub soak in the Lake District with Dillon, Liam, Sam and Ed (who declined to get wet). I'd also like to specifically thank Andy for his formative advice on sea clutter processing methods, and willingness to discuss anything at length and with good humour. I also acknowledge our collaborators Shane, Ryan, Simon, and Doug at the Sea Mammal Research Unit in St Andrews – our trial at the seal tank was particularly memorable. I also wish to thank the staff of the School of Physics and Astronomy for the welcoming atmosphere, excellent tuition, and essential supporting work behind the scenes, during both my undergrad and Ph.D. studies.

And lastly, this moment of reflection reveals to me the true wealth of my life – my friends and family – and just how rich I am from their charity. This fortune is practically uncountable in both number and value, but you are all cherished.

Funding

This Ph.D. was funded through a Doctoral Training Grant and additionally supported by the UK Engineering and Physical Sciences Research Council (EPSRC) under grant number EP/S032851/1.

Research Data/Digital Outputs access statement

Research data and digital outputs underpinning this thesis are available at: https://doi.org/10.17630/453af9ae-05e2-45f0-b27d-e82efa1dc142.

Abstract

This thesis presents the design and development of a new 201 GHz / 207 GHz frequency modulated continuous wave (FMCW) Doppler radar, 'Theseus', for environmental sensing and the measurement of targets, and shows the results of measurements made by this radar of low grazing angle sea clutter. The development of the radar and the measurement of sub-THz sea clutter was motivated by the future sensing needs of marine autonomy.

The design process for the Theseus radar is described, where each radar subsystem is characterised separately, along with the characterisation of the instrument as a whole. The range calibration matches modelled results well, the average difference being −1.66 dB at 201 GHz and −1.61 dB at 207 GHz. The noise floor is measured to be ∼−74 dBm between 30 to 120 m. An improvement to the instrument noise floor due to a reduction in transmitter phase noise is demonstrated.

Sea clutter measurements made at a wave tank are then analysed: first qualitatively alongside coincident video; and then quantitatively with both the distribution of amplitude values and the mean σ^0 being examined. The key results are: vertical-vertical polarisation (VV) returns initially increase and then plateau with wave height; between $\gamma = 5°$ and $\gamma = 8°$, backscatter intensity increases by >15 dB in both polarisations; horizontal-horizontal polarisation (HH) returns are greater than VV returns by ∼10 dB; and where in general, the mean σ^0 between $\gamma = 5°$ and $\gamma = 8°$ is −20 to 0 dB, and similar to published results at W-band. The amplitude distributions tend to become longer-tailed with the same trends as increasing backscatter, and in general are much longer-tailed than results at lower frequencies.

Contents

List of Figures

List of Tables

Abbreviations

ADC analogue to digital converter. 35, 37, 103, 106, 107, 112–114, 146, 162–164, 169, 174–176, 183, 264, 267

AIS automatic identification system. 2

ASV autonomous surface vessel. 2–5, 98, 262

AUT antenna under test. 128–131, 135, 139

BPF band-pass filter. xx, 109, 111, 141–143, 152

CAD computer aided design. xix, 119, 120, 122

CCDF complementary cumulative distribution function. xxvii–xxix, xxxii, 9, 188, 212, 214–217, 219, 221, 222, 224–229, 231–237, 239–243, 245–247, 250, 254, 255, 257, 259, 260, 269–271

CDF cumulative distribution function. 216

CNR clutter to noise ratio. xix, 101, 102, 104, 105, 111, 114, 165, 175, 264, 266, 272

CPI coherent processing interval. 34, 164

CRF chirp repetition frequency. 34, 35, 100, 103, 106–108, 114, 165, 264, 265

CRI chirp repetition interval. 34, 103, 106, 107, 165

CST CST Studio Suite®. xix, xx, xxx, 115, 116, 119, 126, 128, 129, 133, 136–139

CW continuous wave. 99

DAR differential absorption radar. 99, 100

DDS direct digital synthesis. xix, xx, xxiii, 36, 106, 109, 110, 113, 114, 121, 123, 125, 140, 141, 143, 144, 167, 168, 178, 264

DRG digital ramp generator. 106, 264

DRO dielectric resonator oscillator. xxi, 109, 110, 113, 139, 143, 144, 177, 264, 265, 272

DSB double sideband. 153, 163

DSLR digital single lens reflex. xxiv, xxv, 181–183, 267

EIO extended interaction oscillator. 98

EM electromagnetic. 19, 20, 47, 52, 54, 62

ENOB estimated number of bits. 175

EPSRC Engineering and Physical Sciences Research Council. vi, 2

FFD far field distance. 129, 130, 169

FFT Fast Fourier Transform. 16, 23, 34, 35, 103, 106, 107, 112, 163, 164, 173–175, 264

FMCW frequency modulated continuous wave. vii, xvi, xvii, xxiii, 3, 4, 10–14, 16, 23, 35, 36, 38, 98, 99, 108, 114, 143, 163, 263

FT Fourier transform. 34

FWHM full width half maximum. 25, 50

GIT Georgia Institute of Technology. 67, 74, 76

GNSS global navigation satellite system. 2

GOLA Gaussian optics lens antenna. xix, xx, xxiii, xxxi, 96, 115, 117, 119, 120, 122, 126–129, 131–135, 137–140, 166, 172, 265

H horizontal polarisation. 26, 56

HDPE high density polyethylene. xix, 118, 119, 121, 134

HH horizontal-horizontal polarisation. vii, xvii, xviii, xxv, xxvi, xxviii, xxix, xxxi, 27, 56, 58–60, 62–64, 66, 67, 69, 74–76, 78–80, 86–90, 92–95, 104, 115, 131, 165, 187, 189, 190, 192, 193, 195, 196, 199–204, 206–209, 211, 213, 219, 226, 228–233, 235, 236, 238–261, 268–272

HP Hewlett-Packard Ltd.. 139, 140, 144–146, 160

HPF high-pass filter. 151

HV horizontal-vertical polarisation. 27, 56, 58, 104, 165

IC integrated circuit. 113

IEEE Institute of Electrical and Electronics Engineers. 21

IF intermediate frequency. xx–xxiii, xxxi, 9, 13–16, 20, 35, 37–39, 103, 108, 112, 114, 121, 129–131, 143–147, 149, 151–154, 156, 162–164, 166, 168, 169, 173–175, 177, 178, 188, 198, 202, 207, 224, 264, 267, 272

InISAR interferometric inverse synthetic aperture radar. 99

ISAR inverse synthetic aperture radar. 98, 99

ITU International Telecommunications Union. 20, 21, 169

JONSWAP Joint North Sea Wave Observation Project. xvii, 49, 50

LFM linear frequency modulation. 14, 109, 110

LGA low grazing angle. 5, 62, 73, 74, 76, 79–81, 87, 89, 93, 94, 101, 202, 248, 262

LN log-normal. 69, 70

LNA low noise amplifier. 4, 99, 112, 131, 145, 151, 175, 178, 266, 272

LO local oscillator. xxi, xxii, xxx, 37, 38, 40, 109, 112, 126, 143, 144, 149–154, 156, 265

LPF low-pass filter. 109, 112, 131, 146, 147, 151, 154

MAE mean absolute error. xxiv, 170–172

MC Mini-Circuits. xx, 143–146, 151, 183

MGA medium grazing angle. 76, 78, 79, 82

MMIC millimetre-wave monolithic integrated circuit. 98

NESZ noise equivalent sigma zero. xxix, 29, 89, 247, 249

NRCS normalised radar cross section. xviii, xix, xxvii, xxix, xxx, xxxii, 9, 28, 29, 33, 56, 62, 64, 74–76, 78, 80–83, 86–94, 100, 103–105, 146, 164, 165, 188, 191, 199, 209, 212, 218–223, 246–261, 263, 266, 269–271

NRL Naval Research Laboratory. xxx, 61, 69, 86, 91, 93, 95, 209

OIP3 third-order output intercept point. xxi, 146–148

OML Inc. Oleson Microwave Laboratories Incorporated. 128

PA power amplifier. xxii, 110, 111, 127, 142, 157–160, 162, 175, 266, 272

PDF probability density function. 70–72

PLL phase-locked loop. 177

PM Pierson-Moskowitz. 47, 49, 51

PPI plan position indicator. xviii, 82, 85, 86, 88, 134, 198

PRF pulse repetition frequency. 100

PSD power spectral density. 38, 39

R&S Rohde & Schwarz. 146, 161, 175, 272

RCS radar cross section. 7, 20, 27, 28, 75, 85, 86, 91, 92, 98, 100, 104, 146, 164, 165, 167–171, 266

RF radio frequency. xxii, 96, 105, 142, 151–155, 160, 169, 175, 178, 265, 267, 272

RMS root mean square. 62

RRE radar range equation. 19–21, 28, 102

RSS rough surface scattering. xxv, 90, 92, 93, 190, 193, 197, 198, 206, 210, 214, 261, 268

RTI range-time-intensity. xvii, xviii, xxv–xxvii, 56, 57, 59, 75, 85, 86, 146, 188–190, 192–197, 200–205, 207, 208, 211, 215, 226, 247, 254, 255, 268

SAR synthetic aperture radar. xviii, 76, 78, 79, 82–84, 99

SFCW stepped frequency continuous wave. 99

SGH standard gain horn. xx, 126, 129, 130, 135

SHM sub-harmonic mixer. xxii, 111, 112, 126, 127, 131, 149–154, 156, 174, 265, 267, 272

SLL side lobe level. 25

SMRU Sea Mammal Research Unit. 6

SNR signal to noise ratio. xix, 4, 11–13, 82, 97, 100, 101, 104, 105, 114, 165

SS sea state. xviii, 45, 47, 59, 60, 65, 87, 92

SSB single sideband. 163

STALO stable local oscillator. 109, 110

STFT short-time Fourier transform. 35

STREAM Sub-THz Radar Environmental sensing for future Autonomous Marine platforms. 2, 4, 5, 7, 8, 20, 62, 73, 89, 91, 97, 100, 179

SWH significant wave height. xxv, xxvi, xxviii, xxix, xxxi, 45–47, 69, 74, 82, 183–187, 189–192, 195, 196, 198–211, 213, 236, 237, 252, 253, 268

TK Thomas Keating Ltd.. xxiii, 160, 161

TTL transistor-transistor logic. 160

V vertical polarisation. 26, 56

VDI Virginia Diodes Inc.. xxiii, 110, 111, 127, 157, 158, 160–162, 167

VH vertical-horizontal polarisation. 27, 56, 58, 80, 104, 165

VNA vector network analyser. 99, 128, 139

VV vertical-vertical polarisation. vii, xvii, xviii, xxv, xxvi, xxviii, xxix, xxxi, 27, 56–60, 62–67, 69, 74, 78–80, 82, 84, 87–90, 92–95, 104, 115, 131, 165, 187, 189, 190, 192, 194–197, 199, 201–209, 211, 213, 219, 226, 227, 229–231, 233–235, 237–261, 268–272

WMO World Meteorological Organisation. 46, 67

Nomenclature

A clutter patch area. 29

$A_{\mathbf{b}}$ beamwidth limited clutter patch area. 30, 31

$A_{\mathbf{r}}$ range-gate limited clutter patch area. 30, 31, 101, 102

$A_{\mathbf{e}}$ antenna effective area. 117

$B_{\mathbf{w}}$ window function noise bandwidth factor. 23, 39, 103

B_2 doubled-sided bandwidth. 37

$B_{\mathbf{N}}$ noise bandwidth. 21–23, 102–104, 153, 154, 176

$B_{\mathbf{S}}$ signal bandwidth. 11, 16, 106, 164

D antenna directivity. 26, 102, 117

F noise factor. xxxi, 23, 24, 102, 104, 155, 156, 165, 264, 266

$F_{\mathbf{t}}$ total noise factor. 24, 155

$F_{\mathbf{i}}$ noise factor of component i. 155

$F_{\mathbf{p}}$ one-way propagation factor. 60

G gain [dB]. xxxi, 156

$G_{\mathbf{A}}$ antenna gain. 26, 102, 171

$G_{\mathbf{IF}}$ gain of the IF chain. 169

$G_{\mathbf{lin},j}$ linear gain of component j. 155

$G_{\mathbf{lin}}$ gain (on a linear scale). xxxi, 22–24, 102, 155, 156

$G_{\mathbf{rec}}$ receiver gain. 20, 101, 102, 130, 169, 171, 174

$G_{\mathbf{r}}$ receive antenna gain. 19, 20, 29, 101, 130

$G_{\mathbf{t}}$ transmit antenna gain. 19, 20, 29, 101, 130

$G_{\mathbf{w}}$ IF windowing gain. 163, 164

H histogram. 216

$H_{\mathbf{p}}$ histogram of probability values (normalised by number of counts). 216

$H_{1/3}$ significant wave height. xxviii, xxix, 45, 47, 50, 51, 68, 69, 186, 206, 208, 210, 226, 229–235, 238, 240–247, 249, 252, 253, 257, 258, 260, 261, 269–271

$L_{\mathbf{A}}$ antenna loss. 26, 102–104

$L_{\mathbf{at}}$ atmospheric loss. 19–21, 101–104

$L_{\mathbf{c}}$ mixer conversion loss. 154, 155, 169

M reflected phase noise modulation. 39, 40

N_{ϵ} output noise power in the absence of additive noise. 22

$N_{\mathbf{add}}$ additive noise power. 22, 23

$N_{\mathbf{c}}$ number of chirps. 34, 189

$N_{\mathbf{in}}$ input noise power. 21, 22

$N_{\mathbf{out}}$ output noise power. 23, 101, 102

$N_{\mathbf{FFT}}$ number of FFT samples. 106, 107, 264

$N_{\mathbf{r}}$ receiver noise power. 101, 102, 104

$N_{\mathbf{s,H}}$ number of samples in a histogram. 216

P_{ϕ} reflected phase noise power spectrum. 39

$P_{\mathbf{C}}$ noise power of cold noise source. 153, 154

$P_{\mathbf{H}}$ noise power of hot noise source. 153, 154

$P_{\mathbf{IF}}$ power from downconversion mixer IF port. 20, 130, 169

$P_{\mathbf{N}}$ noise power. 153

$P_{\mathbf{c}}$ clutter power. 101, 102

$P_{\mathbf{i}}$ incident power density. 27

$P_{\mathbf{r}}$ receive power. 19, 20, 29, 33, 169

$P_{\mathbf{s}}$ scattered power density. 27, 28

$P_{\mathbf{t}}$ transmit power. 19, 20, 29, 101, 102, 104, 130, 165, 264, 266

Q non-coherent sum of intensity. 71, 72

R slant range. xvi, 11, 15, 17–19, 27, 29–31, 33, 38–40, 101, 102, 104, 130, 164, 214

RH relative humidity. 21, 169, 170

$R_{\mathbf{ff}}$ far field range. 24, 130

$R_{\mathbf{g}}$ ground range. xvi, 17–19

$R_{\mathbf{l}}$ lens radius of curvature. 118

$R_{\mathbf{max,I}}$ maximum instrumented range. 37, 103, 106, 107

$R_{\mathbf{max,u}}$ maximum unambiguous range. 16

S signal power. 104

SS sea state. 60, 63, 69

T temperature. xvi, 20, 22, 170

$T_{\mathbf{0}}$ noise temperature reference. 21–23, 102–104

$T_{\mathbf{C}}$ noise temperature of cold noise source. 154

$T_{\mathbf{H}}$ noise temperature of hot noise source. 154

$T_{\mathbf{N}}$ noise temperature. 22, 23, 153

$T_{\mathbf{R}}$ noise temperature of receiver. 154

$T_{\mathbf{s}}$ sampling period. 37, 39

Δ ADC quantisation. 163, 164

$\Delta\theta$ angular resolution. 25

ΔR slant range resolution. 16, 18, 19, 30, 31, 102–104, 106

$\Delta R_{\mathbf{g}}$ ground range resolution. 18, 19, 30, 31

$\Delta\delta$ uncertainty in radar depression angle. xxvii, 221, 222

$\Delta f_{\mathbf{D}}$ Doppler resolution. 34

$\Delta f_{\mathbf{IF}}$ IF frequency resolution. 16, 23, 39, 103, 107

Δh uncertainty in radar height. xxvii, 221, 222

Γ gamma function. 51, 70–72

Ω_A antenna beam solid angle. 26, 102, 117

Ξ ADC amplitude conversion factor. 163

α normalised threshold. 216, 218, 249, 257

$\bar{H}$ average wave height. 67, 68

β reflectivity grazing angle model fitting constant. 62

$\beta_{\mathbf{C}}$ radar system constant for clutter. xix, 102, 104, 105, 164, 165, 266

$\beta_{\mathbf{S}}$ system constant for targets. 104

δ depression angle. xxv–xxviii, 17, 186, 195, 199–203, 207, 208, 211, 213, 215, 222, 225, 226, 230, 238, 244, 247, 255, 256, 268

γ grazing angle. vii, xvi, xviii, xxvii–xxx, 17–19, 29–32, 55, 59, 62, 63, 67–69, 90, 92, 101, 186, 214, 215, 224–235, 238, 240–254, 256–261, 270, 271

$\gamma_{\mathbf{c}}$ critical grazing angle. 30, 31, 62

$\lambda_{\mathbf{r}}$ radar wavelength. 19, 20, 24, 26, 29, 54, 55, 62, 67, 68, 85, 91, 101–104, 117, 130

$\lambda_{\mathbf{w}}$ water wave wavelength. 41, 55

$\langle q \rangle$ mean intensity. 70–72, 216, 218

$\mathbb{P}_{\mathbf{K,m}}$ multi-look K distribution. 72

$\mathbb{P}_{\mathbf{K}}$ single-look K distribution. 71

$\mathbb{P}_{\mathbf{fa}}$ probability of false alarm. 86, 212, 216

$\mathbb{P}_{\mathbf{s,m}}$ probability density function for multi-look speckle scattering. 72

$\mathbb{P}_{\mathbf{s}}$ probability density function for speckle scattering. 70, 71

$\mathbb{P}_{\mathbf{t}}$ probability density function for texture scattering. 70, 71

$\mathcal{C}$ clutter to noise ratio. 101, 102, 164

$\mathcal{K}$ Modified Bessel function of the second kind. 71, 72

$\mathcal{L}$ phase noise power spectrum. xxi, 38–40, 144

$\mathcal{N}$ noise figure. xxxi, 23, 156

$\mathcal{N}_{\mathbf{mix}}$ mixer noise figure. 154, 155

$\mathcal{N}_{\mathbf{r}}$ receiver noise figure. 154, 174

$\mathcal{S}$ signal to noise ratio. 104

$\mathcal{Y}$ Y-factor. 153, 154

ν K distribution shape parameter. 70–72, 86, 87, 95

ω_0 beam waist radius. 117

ϕ_1 one-way −3 dB azimuthal beamwidth. xxiv, 26, 102, 117, 181

ϕ_2 two-way −3 dB azimuthal beamwidth. 26, 30, 31, 102–104

$\phi_{\mathbf{b}}$ azimuth boresight angle. xvi, 17

ψ wave direction. xxv, xxvi, xxix, 60, 64, 195, 199–201, 203–205, 208, 211, 226, 229, 230, 238, 245, 249–251, 255, 256, 269, 270

$\rho_{\mathbf{w}}$ water vapour density. xvi, 21, 22, 169, 170

σ radar cross section. 19, 20, 27–29, 85, 91, 104

σ^0 normalised radar cross section. vii, xviii, 28, 29, 33, 54, 58, 60–62, 64–69, 74, 78, 79, 90, 92, 101, 102, 164, 258, 266

$\sigma_{\mathbf{h}}$ RMS wave height. 62

τ time delay. xvi, 11, 14, 15

CPI coherent processing interval. 34

CRF chirp repetition frequency. 34, 106, 107

CRI chirp repetition interval. xvi, 11, 12, 14, 16, 103, 106, 107, 189

$\mathbf{DR_{ADC}}$ ADC dynamic range. 175

ENOB estimated number of bits. 175

PRI pulse repetition interval. xvi, 11, 12

θ_1 one-way −3 dB elevation beamwidth. xxiv, 26, 102, 117, 181

θ_2 two-way −3 dB elevation beamwidth. 26, 30, 31

$\theta_{\mathbf{bw,1}}$ one-way beamwidth. 25

$\theta_{\mathbf{b}}$ elevation boresight angle. xvi, 17

$\theta_{\mathbf{ET}}$ edge taper angle. 118

$\tilde{H}$ histogram normalised by number of counts and mean intensity. 216

$\vec{r}$ lens profile radial position vector. 118

ξ wind direction. 60, 64

ζ water surface displacement. 45, 186

b K distribution scale parameter. 70–72

c speed of light. 11, 15, 16, 34, 37, 39, 106, 164

$d_{\mathbf{a}}$ antenna diameter. 24, 25

$d_{\mathbf{l}}$ lens diameter. 118

$f_{\mathbf{D}}$ Doppler frequency. 34

f_0 centre frequency. xxiv, 11, 14, 15, 34, 90, 92, 99, 106, 109, 181, 257, 258

$f_{\mathbf{CG}}$ chirp generator output frequency. 109, 110, 142

$f_{\mathbf{CLK}}$ clock frequency. 106, 113

$f_{\mathbf{DDS}}$ DDS output frequency. 109, 110, 112

$f_{\mathbf{DRG}}$ digital ramp generator update frequency. 106

$f_{\mathbf{IF,max}}$ maximum IF frequency. 37, 107

$f_{\mathbf{IF}}$ downconversion mixer IF frequency. xvi, 14, 15, 38–40, 164, 174, 267

$f_{\mathbf{LO}}$ LO output frequency. 110

$f_{\mathbf{RF}}$ RF output frequency. 109, 111

$f_{\mathbf{mix}}$ upconversion mixer output frequency. 109, 110

$f_{\mathbf{r}}$ radar frequency. 55, 67–69

$f_{\mathbf{s}}$ sampling rate. 37, 106, 107, 113, 264

h radar height. xvi, 17, 19, 101, 222

$h_{\mathbf{PN,lin}}$ linear phase noise multiplication gain. 40

$h_{\mathbf{PN}}$ phase noise multiplication gain. 40, 176, 178

$k_{\mathbf{B}}$ Boltzmann's constant $1.380649 \cdot 10^{-23}\,\mathrm{J\,K^{-1}}$. 21–23, 102, 104, 153, 154

l aperture side length. 26

$l_{\mathbf{f}}$ lens focal length. 118

$n_{\mathbf{S}}$ ADC samples per chirp. 163, 164

$n_{\mathbf{a}}$ air refractive index. 118

$n_{\mathbf{l}}$ lens refractive index. 118

p pressure. xvi, 20, 22, 170

q intensity. 70, 71, 216

$q_{\mathbf{t}}$ intensity threshold. 218

s chirp slope. 11, 13–15, 36, 37, 164

$s_{\mathbf{IF}}$ IF signal. 14

$s_{\mathbf{r}}$ received signal. 14

$s_{\mathbf{t}}$ transmitted signal. 14, 34

t time. 14, 34, 38, 39, 189

$t_{\mathbf{c}}$ chirp time. xvi, 11–13, 16, 39, 40, 103, 106, 107, 164, 264

$t_{\mathbf{p}}$ pulse width. xvi, 11, 12

$v_{\mathbf{r}}$ radial velocity component. 34

$v_{\mathbf{max}}$ maximum unambiguous Doppler velocity. 34, 103, 106, 108

$v_{\mathbf{w}}$ wind velocity. 45, 47, 60, 63, 68, 69

$z_{\mathbf{l}}$ lens profile. 118

1

Motivation

SINCE the inception of radar in the 1930s, one of its key applications has been the surveillance of the marine environment. Early radar pioneers observed reflections from the water's surface and found that these were often the limiting factor in detecting their target. The characterisation of these returns, known as sea clutter or sea backscatter, has been an active area of research ever since because of the key role radar sensing plays at sea [1, p. 18].

The importance of the marine environment cannot be overstated. It covers the majority of the surface of the Earth and contains vast quantities of resources. As a result, it greatly influences our climate and is a great reservoir of biodiversity, as well as being enormously important to the economy and a strategic, geopolitical focus. Military forces were the original driver for radar usage at sea, given the major tactical advantage to being able to detect enemy ships and aircraft at long range. Navies remain at the forefront of radar development for this reason, as cutting-edge capability is critical for national security. Once the technology became widely available however, marine radar sensing was also adopted universally as an invaluable aid to navigation [2, pp. 4–7]. In economic terms, the contribution of the marine sector was estimated 'very conservatively' to be USD 1.5 trillion in 2010, equivalent to ~2.5% of global gross value added, by the OECD [3, p. 13], where additionally shipping accounted for 90% of all international trade volume [3, p. 26]. The marine radar market size was itself determined to be USD 1.44 billion in 2023, with a projected growth to USD 2.45 billion by 2032 [4]. Ferries are also an essential mode of transport for many across the world, and the development and maintenance of marine infrastructure, especially for offshore energy, is of continuing and growing importance [3, p. 65] [5]. Aquaculture, surveying, and general research are also areas of growing importance. All of these uses rely on radar technology, where increasing sensing capabilities will have major impacts on society.

This thesis centres around the characterisation of sea clutter to enable the design of high resolution sensors for autonomous marine vessels, also known as autonomous surface vessels (ASVs). As part of the fourth industrial revolution [6, pp. 18, 21], autonomy at sea is expected to be of benefit for several reasons. Firstly, by removing people from the often inherently hazardous working conditions found at sea, the general safety of the sector would be improved. Additionally, the constraints placed on crewed vessels in terms of space, energy, and design due to the need to support people on board could also be relaxed when crews are reduced, wholly or in part. This means that life-support systems and living space could be removed or reconfigured for cargo or for better hydro- and aerodynamic performance, with either change increasing operating efficiency. It would also combat crew shortages, reduce the need for resupply, and provide new or increased capabilities on missions which could benefit from a distributed group of ASVs performing many small tasks in parallel instead of one large ship making sequential progress [7] [8].

Of interest to this thesis, and to the broader Engineering and Physical Sciences Research Council (EPSRC) funded Sub-THz Radar Environmental sensing for future Autonomous Marine platforms (STREAM) project it is part of, are specifically small- to medium-sized vessels, which have different sensing needs to larger ships. In contrast, they are often more agile and tend to operate in more crowded and complex environments close to shore whilst also being more vulnerable to the movement of the waves. Given they are generally more responsive than large ships, they can potentially make better use of sensing information from their immediate surroundings to change heading and behaviour. At present, some examples of ASVs in this size class include Autonaut [9], Saildrone [10], Sailbuoy [11], and the C-Worker 5 [12], designed and deployed for missions including surveying, research, and surveillance. The navigational sensors they are equipped with include global navigation satellite system (GNSS) and automatic identification system (AIS) transceivers, electro-optical systems, and radar – depending on the size of platform. The capability of these sensors currently limits ASVs by the need to manage lower performance under certain environmental conditions, or to mitigate risks associated with the low positional fidelity of the sensors. This means these ASVs must either operate at daytime or clear weather, in remote areas not requiring ship-to-ship interactions of complex manoeuvres, or be very low tonnage to prevent damage if a collision should occur.

Radar sensing in the mm-wave to sub-THz range offers an alternative which may be able to solve these issues. Conventional marine radar systems have long been in use at S-, C-, or X-band [13, p. 2] (radar frequency bands are defined in Subsection 2.1.5), and can provide extremely long range sensing (in the tens of kilometres), can

operate in darkness, and see through rain and fog. These sensors are not designed for close-range sensing however, in fact often having significant minimum ranges (due to pulsed operation) and coarse range resolutions which make situational awareness of the immediate surroundings impossible. As a typical example, a Furuno DRS6A X-Class navigational radar operates at X-band with a 1.4° one-way horizontal beamwidth from a 1.795 m antenna, and has a minimum range of ~116 m [14]. Sensing at mm-wave to sub-THz frequencies, realised with frequency modulated continuous wave (FMCW) architectures, could overcome these limitations whilst still preserving the robust sensing of conventional marine radar systems, albeit at a shorter range. The increased capability of ASVs, enabled by improved sensing, would then generally allow for navigation in congested and complex areas including harbours and coastal waters, as well as increasing the roles available to these vessels to include, for example, harbour tugs, minesweepers, and the servicing and maintenance of marine infrastructure. Lidar and electro-optical sensing are also alternatives which are being explored for use in this area as they both provide resolution increases compared to conventional marine radar. Electro-optical systems use mature hardware and can leverage a wide array of image processing techniques, however as passive systems they are daytime limited. Lidar is an active sensor and so does not encounter this issue, as well as offering better ranging precision than electro-optical and generally excellent angular resolution. Both types of sensor are however limited by fog or sea-spray, which leaves radar with a clear advantage.

Radar sensing operating above Ka-band has the following benefits compared to lower frequencies:

1. It is easier to achieve a finer range resolution given the greater available bandwidth.
2. Since antenna size scales inversely with frequency, the antenna size is reduced for an equivalent angular resolution, meaning sensors can be more compact or have greater angular resolution.
3. Doppler resolution is increased, providing better detail of the motion of slow moving marine targets.
4. The sensor is more sensitive to surface textures, providing additional information not available at lower frequencies.

Marine autonomy has strong parallels to the sensing needs of self-driving cars, which need reliable and detailed sensor coverage of the local environment to make navigational decisions. In this domain, FMCW E-band sensing at 77 GHz has become a standard [15]. Sub-THz sensing is also of interest for terrestrial autonomy [16] due to the

benefits listed above [17]. For these sensors, FMCW architectures are favourable given their lower power overheads compared to pulsed designs and since they are feasibly implemented with entirely solid-state components. This feature eventually improves system integration and manufacturing scalability to a great degree when produced by microelectronics manufacturing techniques. Further details on the benefits of FMCW sensing are provided in Section 2.1.1.

When comparing the two environments – static terrain for autonomous cars, versus a dynamic sea surface for ASVs – the marine case is expected to be more challenging. This makes the additional information which can be gathered at sub-THz comparatively more important for marine autonomy. It is also hoped that recent and continuing advances in computation along with the additional data provided by these sensors will further emerging methods of target detection and classification based on machine learning and artificial intelligence [18] [19]. For these reasons, radars operating above ~100 GHz are of interest, and this thesis explores the use of the sub-THz region for sensing in the marine environment as part of the STREAM project.

Exploiting this frequency region is however not without drawbacks. Maximum range is generally limited by the following factors:

1. lower transmit powers,
2. higher receiver noise figures,
3. greater atmospheric absorption (see Fig. 2.5),
4. greater free space path loss (see Eq. 2.16),
5. and worsening backscatter from atmospheric obscurants with increasing frequency.

These signal to noise ratio (SNR) challenges are alleviated for the applications of the STREAM project, since vessels in the intended size class may only need situational awareness up to a range of ~200 m. Such sensors would not however be generally useful for larger ships given their lower manoeuvrability. Additionally, sub-THz radar has previously been very difficult to achieve technologically due to the lack of affordable and efficient signal components, where low transmit powers and high noise figures compound issues with SNR, and there are generally fewer options available for components which are all of relatively higher cost. Recent trends are however making key signal components such as power amplifiers, mixers, and low noise amplifiers (LNAs) more available into D-band and above, largely driven by the push in communications technology associated with 6G [20]. For this reason, the sub-THz region is seeing growing interest for sensing applications as practicable implementations are becoming a reality.

To design marine radars at higher frequencies and to test algorithms for the detection of targets, empirical measurements of both sea clutter and marine targets are required to formulate models and understand the phenomenology of the environment at the relevant frequencies. These data are required for numerous functions which are further outlined in Subsection 2.3.1. More specifically, it is the low grazing angle (LGA) observation case which is of interest, since sensors on smaller platforms cannot be placed very high above the water's surface. Given that most marine radars operate at X-band or below, the vast majority of empirical sea clutter data are consequently at these frequencies (the largest collection being Nathanson's tables [21, pp. 275–278]), with very few above Ka-band in the open literature (Chapter 3 contains a review of the available literature on sea clutter in W-band and above). Similarly, measurements of marine targets are even more scarce. This then presents the first obstacle in the development of sub-THz sensors for ASVs.

The primary goal of the STREAM project was to begin to answer the question of the suitability of sub-THz sensing for marine autonomy, by the collection and analysis of new data of the marine environment. The project considered the following frequencies during the campaign: 24, 77/79, 94, 150, 207, and 300 GHz. Frequencies from 24 to 94 GHz, which are not in the sub-THz region, are of interest to the project since 24 GHz provides a link to established measurements and 77/79 GHz and 94 GHz radars are relatively well technologically established but not yet significantly explored for use at sea. The work specifically constituting this thesis concerns the development and testing of the radar used for measurements at 207 GHz, and the collection and analysis of sea clutter data at that frequency.

Research objectives

The broader aim of the STREAM project was to answer the question:

How well suited is sub-THz sensing to the application of marine autonomy?

Where in summary, the goals of the project were:

- To collect sea clutter data in different conditions at a range of sub-THz frequencies, and to analyse these in terms of amplitude and Doppler statistics.
- To collect data of marine targets, including flotsam and jetsam, boats, sea mammals, and people in the water, and analyse these to determine marine target signatures.
- To develop detection and classification algorithms based on the data gathered throughout the project.

Specifically, the research question of this thesis was:

What are the amplitude statistics of sub-THz radar sea clutter?

Where the research objectives were:

1. The development and testing of a radar at 207 GHz for data collection.
2. The collection of sea clutter data at 207 GHz.
3. The analysis of the collected data to determine the amplitude statistics of sea clutter for different environmental and observation conditions.

Phases of work

A time line of the primary phases of work which occurred during this Ph.D. and contributed towards the writing of this thesis are summarised here, presented in approximately chronological order within each section:

1. ***Review***
    - Literature review of radar principles, radar sea clutter, and sea clutter above Ka-band, as covered in Chapters 2 and 3.
    - Literature review of G-/Y-band radars, as covered in Chapter 4.
2. ***Radar design and development***
    - 207 GHz radar development, covered in Chapters 4 and 5.
    - 207 GHz radar upgrades, covered in Chapters 4 and 5.
3. ***Field trials and data collection***
    - Field trial at the Bruce Embankment, St Andrews, December 2020.
    - Field trial at Sea Mammal Research Unit (SMRU), St Andrews, September 2021.
    - Field trial at Coniston Water, Lake District, August 2020.
    - Field trial at FloWave, University of Edinburgh, July 2023, the results of which are covered in Chapter 6 and 7.
4. ***Data analysis***
    - Qualitative analysis of sea clutter radar data and video footage, as covered in Chapter 6.
    - Development of sea clutter amplitude analysis methods, covered in Chapter 7.

5. ***Publications and outreach***

   - Contributed to the writing of a conference paper on K-band and W-band sea clutter amplitude statistics (January 2022), which I then presented at IEEE Radar Conference 2022, March 2022 [22].
   - Lead author on a conference paper written on radar development (March 2022), for SPIE Radar Sensor Technology XXVI, March 2022 [23].
   - Contributed to the writing of a conference paper on the millimetre wave radar signatures of sea lions (July 2022), for IET International Conference on Radar Systems, October 2022 [24].
   - Presentation given at SoMaR Radar Workshop 2023, National Oceanographic Centre, June 2023.
   - Contributed to the writing of a conference paper on the Doppler characteristics of sea clutter at K-band and W-band (August 2023), for IEEE International Radar Conference, November 2023 [25].
   - Lead author on a conference paper on 207 GHz sea clutter amplitude statistics (September 2023), for IEEE International Radar Conference, November 2023 [26].
   - Contributed to the writing of a paper on maritime target classification using machine learning, for IET Radar, Sonar, and Navigation, October 2023 [27].
   - Contributed to the writing of a special issue paper on the radar signatures of sea lions at K-band and W-band, for IET Radar, Sonar, and Navigation, October 2023 [28].
   - Lead author on a journal article written on the design and testing of the 207 GHz radar, for IEEE Transactions on Radar Systems, March 2024, [29].
   - Contributed to the writing of a conference paper on target sub-THz radar cross section (RCS) results from the FloWave trial, for IEEE European Radar Conference, September 2024, [30].

Publications with contributions by the author, associated with the STREAM project

[22] S. Rahman, A. Vattulainen, and D. A. Robertson, "Amplitude Characteristics of Littoral Sea Clutter Data at K-band and W-band," in *2022 IEEE Radar Conf.*, New York City, NY, USA: IEEE, Mar. 2022, pp. 1–6. DOI: 10.1109/RadarConf2248738.2022.9764262.

[23] A. B. Vattulainen, S. Rahman, and D. A. Robertson, "G-band FMCW Doppler

radar for sea clutter and target characterization," in *Radar Sens. Technol. XXVI*, A. M. Raynal and K. I. Ranney, Eds., vol. 12108, Orlando, Florida, USA: SPIE, May 2022. DOI: 10.1117/12.2618497.

[24] S. Rahman, A. B. Vattulainen, D. A. Robertson, *et al.*, "Millimetre wave radar signatures of sea lions," in *Int. Conf. Radar Syst. (RADAR 2022)*, Edinburgh: Institution of Engineering and Technology, 2022, pp. 14–19. DOI: 10.1049/icp.2022.2284.

[25] S. Rahman, A. B. Vattulainen, and D. A. Robertson, "Doppler Characteristics of Sea Clutter at K-band and W-band: Results from the St Andrews and Coniston Water Trials," in *2023 IEEE Int. Radar Conf.*, Sydney, Australia: IEEE, Nov. 2023, pp. 1–6. DOI: 10.1109/RADAR54928.2023.10371023.

[26] A. B. Vattulainen, S. Rahman, A. G. Stove, *et al.*, "Amplitude Distribution of Low Grazing Angle G-band Littoral Sea Clutter," in *2023 IEEE Int. Radar Conf.*, Sydney, Australia: IEEE, Nov. 2023, pp. 1–6. DOI: 10.1109/RADAR54928.2023.10371097.

[27] S. Rahman, A. B. Vattulainen, and D. A. Robertson, "Machine learning-based approach for maritime target classification and anomaly detection using millimetre wave radar Doppler signatures," *IET Radar, Sonar Navig.*, vol. 18, no. 2, pp. 344–360, Dec. 2023. DOI: 10.1049/rsn2.12518.

[28] S. Rahman, A. B. Vattulainen, D. A. Robertson, *et al.*, "Radar signatures of sea lions at K-band and W-band," *IET Radar, Sonar Navig.*, vol. 18, no. 1, pp. 147–157, Jan. 2024. DOI: 10.1049/rsn2.12498.

[29] A. B. Vattulainen, S. Rahman, and D. A. Robertson, "G-Band FMCW Doppler Radar for Close-Range Environmental Sensing," *IEEE Trans. Radar Syst.*, vol. 2, pp. 355–371, 2024. DOI: 10.1109/TRS.2024.3378123.

[30] A. Stove, A. Vattulainen, D. Kumar, *et al.*, "Radar Cross Sections of Flotsam at Sub-THz Frequencies," in *2024 21st Eur. Radar Conf.*, IEEE, Sep. 2024, pp. 91–94. DOI: 10.23919/EuRAD61604.2024.10734965.

Thesis outline

The chapters of this thesis are summarised as follows:

Chapter 1: Motivation The context and motivating background to this thesis and the broader STREAM project, outlining the research objectives, and the main phases of work which were undertaken.

Chapter 2: Introduction The background radar theory relevant to the later chapters in this thesis is covered in Section 2.1. This is followed by Section 2.2 which covers the aspects of the sea which are needed to understand sea clutter, where the following section, Section 2.3, details the literature of radar sea clutter up to Ka-band.

Chapter 3: Sea Clutter Amplitude Statistics Above Ka-Band A review of the published literature on radar sea clutter amplitude data (mostly) above Ka-band, predominantly consisting of W-band results. Trends are identified across publications, and compared to the lower frequency results discussed in Section 2.3.

Chapter 4: G-band Doppler Radar Design This chapter first discusses the motivations for developing a radar operating at G-band, followed by a review of published G-band radar designs. The forward modelling of a new 207 GHz radar is then performed, based on design requirements. This helps to define the presented system architecture, and informs the design of the antennas which is presented next. Finally, the mechanical design aspects of the radar are discussed.

Chapter 5: G-band Doppler Radar Characterisation The first section of this chapter covers the characterisation of each subsystem in the design: the antennas, chirp generator, intermediate frequency (IF) chain, receive chain, and transmit chain. This is then followed by a description of the radar range processing which is applied to the raw data. The final section presents the results of the full system characterisation, including the range calibration, the measurement of the radar noise floor, and the results of upgrades made to the chirp generator to reduce transmitter phase noise.

Chapter 6: 207 GHz Sea Clutter Data Collection and Qualitative Analysis This chapter first describes the field trial conducted at the FloWave wave tank facility at the University of Edinburgh, including the motivations for undertaking a trial at this facility, details of the apparatus used, and an explanation of the data collection methods. The second half of this chapter then discusses the qualitative features of the radar data which were collected along with simultaneous video footage of the waves in the tank. This discusses the scattering types which were observed, and how these were affected by the measurement parameters.

Chapter 7: 207 GHz Sea Clutter Amplitude Statistics This chapter continues the analysis of the data from the FloWave trial in a quantitative manner. The amplitude statistics processing methods are first outlined, these being the calculation of the mean normalised radar cross section (NRCS) and the complementary cumulative distribution function (CCDF) curves, which show the mean reflectivity and the distribution of backscatter intensity samples respectively. The methods for quantifying their errors are also shown. The chapter then continues with the results of the CCDF and NRCS analysis threads, both of which evaluated the effects of the trial measurement parameters. The chapter then ends with a discussion which compares the results from 207 GHz with those discussed in Section 2.3 and Chapter 3.

Chapter 8: Conclusion A summary of the conclusions from each chapter and the avenues for future research which are identified as a result of this thesis.

2

Introduction

THIS chapter begins the literature review of this thesis. Later chapters detail the development and characterisation of a new FMCW radar, and cover the measurements and analysis of sea clutter amplitude statistics made with the instrument. Section 2.1 of this chapter explains the essential FMCW radar theory for developing the radar, and then the concepts needed to make and understand surface clutter measurements. Section 2.2 presents the definitions, nomenclature, and concepts required to characterise the sea, and the context in which sea clutter measurements are made. Finally, Section 2.3 reviews the established sea clutter literature, and summarises the key trends of the amplitude statistics up to and including Ka-band.

2.1 Theory of FMCW radar and surface clutter measurements

This section presents the relevant theory for making radar measurements of surface clutter (namely of the sea) and targets. It begins by discussing the principles of FMCW radar measurement and the benefits of this modality versus pulsed radar, and then continues by covering general aspects of radar theory including the range resolution, observation geometry, the radar range equation, radar frequency bands, noise, and antenna properties. Two subsections then explain the measurement of reflectivity from targets and clutter. The section then ends with a description of Doppler measurement and an overview of elements of radar hardware theory.

2.1.1 FMCW radar measurement principles

Radar derives its name from the acronym 'RAdio Detection And Ranging', where most radars (apart from purely continuous wave sensors) are capable of measuring the

range to a scatterer. Radars do this by first measuring a round-trip time-of-flight τ to a scatterer in the environment, and then calculating the range by using the speed of light in the transmission medium, according to Eq. 2.1:

$$R = \frac{c\tau}{2} \tag{2.1}$$

where R is more properly known as the *slant range*, this being the range directly along the line-of-sight between the radar and the scatterer. This measurement can be achieved using short bursts of radiation, known as pulsed radar, where simply the time between signal transmission and echo reception is used to determine range as per Eq. 2.1. An alternative to this approach is FMCW operation, where a time dependent frequency modulation is applied to a continuous signal, thus encoding the time of transmission. This is typically a linear ramp known as a 'chirp' (either up or down in frequency). Some general sources for FMCW theory used to write this subsection include [31, Chapter 2] and [32, Chapter 11]. Examples of pulsed radar and FMCW waveforms are illustrated in Fig. 2.1. This figure shows the key timing parameters of these radar waveforms:

- **Pulsed**
  - t_{p}, the pulse width [s]
  - PRI, the pulse repetition interval [s]
- **FMCW**
  - t_{c}, the chirp time [s]
  - CRI, the chirp repetition interval [s].

Both of these waveforms are also defined by their carrier frequency, f_0. The FMCW waveform is additionally defined by the signal bandwidth of the frequency sweep B_{S}, and a sweep rate of slope, s, derived in Eq. 2.2:

$$s = \frac{B_{\mathrm{S}}}{t_{\mathrm{c}}} \tag{2.2}$$

As discussed in Chapter 1, the radar modality used in this research is FMCW. In addition to the reasons discussed there, a summary of the benefits of FMCW over pulsed operation is provided:

1. The SNR depends on signal duration but the range resolution depends on bandwidth, where in FMCW, the available longer integration time makes low transmit

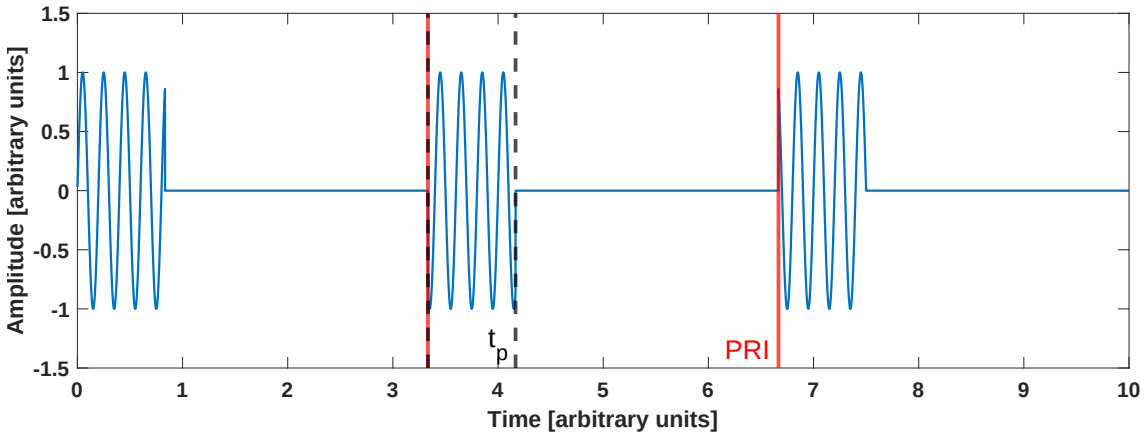

(a)

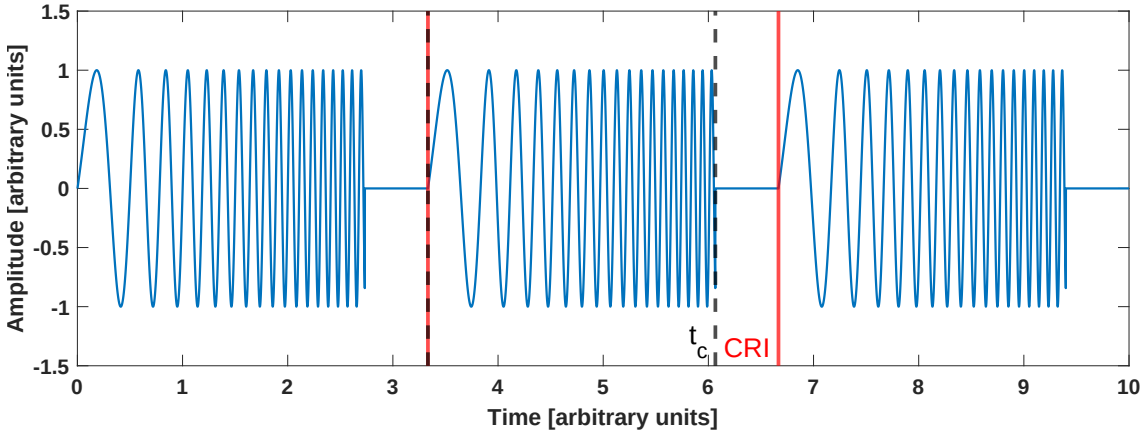

(b)

Figure 2.1: Plots of signal amplitude versus time of a pulsed waveform (a) and an FMCW waveform (b). Waveforms are shown with arbitrary units. For the pulsed waveform, the pulse width t_p and pulse repetition interval PRI are shown, with the corresponding parameters in the FMCW waveform being the chirp time t_c and chirp repetition interval CRI.

signal powers feasible. Modern pulsed radars often also use frequency modulation to decouple SNR and range resolution, however due to shorter transmission times the peak powers must be significantly higher.

2. The low transmission power requirements of FMCW are compatible with solid state signal generation. This is beneficial, as in comparison to vacuum tubes, solid state components are smaller, lighter, have a longer lifetime and lower input power needs. Lower transmission and input power operation is inherently safer, has very little cooling overhead, and is less likely to cause interference with other equipment. Additionally, high carrier frequency radars such as those operating at millimetre wave or sub-THz frequencies are easier to implement with solid state components and thus as FMCW systems.

3. Close range operation is easier with FMCW radar. Due to point 1., in pulsed radar the transmitted pulse is necessarily of a very high peak power and thus the receiver must be protected by a switch for the duration of the pulse (at a minimum) to prevent radiation from the transmitter damaging the receiver, meaning that the minimum range is restricted to, at the very least, a range resolution cell away from the instrument. FMCW radar is not subject to this restriction, thus the minimum range for such systems approaches zero.

Conversely, some of the drawbacks of FMCW operation which need to be taken into consideration or mitigated are:

1. Moving scatterers introduce range ambiguity (also known as scatterer range migration). This is caused by the Doppler effect, where radial velocity changes the received frequency from which the range information is derived.
2. Transmitted signals in FMCW radars must still be sufficiently isolated from the receiver to prevent receiver saturation or damage, where this is more challenging when transmission is continuous. Commonly this is achieved using separate antennas for transmission and reception (but which increase system size), or with a circulator for a single antenna FMCW radar (which can be expensive and limit achievable noise figure due to finite transmit-receive leakage).
3. In linearly chirped FMCW radar, the frequency modulation must be highly linear to prevent degradation of range resolution, where this can be difficult to achieve with hardware. Typical modulation schemes assume a linear frequency ramp with a constant rate s, where any deviations from the ramp rate will translate to a phase error in the IF and introduce range uncertainty. These effects can however be mitigated with various correction schemes.
4. Transmitter phase noise in an FMCW radar must be kept low to prevent degrading the system noise floor and thus compromising SNR. This occurs by two effects: the first being a spreading of a scatterer's point response whereby a bright target can obscure an adjacent target with lower SNR; the second being an interference effect where phase noise can cause a lobed pattern to appear around a point scatterer or a general increase in noise floor level from a distributed target. Phase noise in FMCW radar is discussed further in Subsection 2.1.12.
5. The round-trip time delay to scatterers at maximum range must be much less than the FMCW waveform sweep time t_c, shown in Fig. 2.1b. Since the SNR of an FMCW signal depends on the proportion of overlap between the transmitted and received frequency sweeps, a longer delay time reduces SNR.

6. The detected IF is a product of s and τ, and thus in long range and high bandwidth systems the IF may require high speed sampling hardware, which can be expensive or otherwise lacking in resolution.

2.1.1.1 FMCW ranging

As alluded to above, ranging in FMCW radars is achieved by relating the changing frequency of the signal to the time-of-flight. This proceeds as follows:

- Signals scattered from the environment are received by the radar as an echo of the transmitted signal with a time delay τ as per Eq. 2.1, and as shown in Fig. 2.2.
- The received signal is mixed with a copy of the transmitted signal (known as homodyne operation, see Subsection 2.1.11) and low-pass filtered, producing a 'beat' frequency corresponding to the difference between the two frequencies. This is known as the intermediate frequency (IF), and is denoted f_{IF}.
- The IF is then measured, where this corresponds to the time delay according to Eq. 2.6, and as shown in Fig. 2.2.

This process can be expressed mathematically, beginning with the signal model for the transmitted linear frequency modulation (LFM) chirped waveform shown in Eq. 2.3:

$$s_{\text{t}}(t) = \exp\left(j2\pi\left[f_0 t + \frac{1}{2}st^2\right]\right) \tag{2.3}$$

where the amplitude of the signal is arbitrarily assumed to be unity, and the centre or carrier frequency is defined as f_0. The received signal is the same as that shown in Eq. 2.3, but with an added time delay of τ (ignoring any amplitude changes or additive noise), as shown in Eq. 2.4:

$$s_{\text{r}}(t) = \exp\left(j2\pi\left[f_0\{t-\tau\} + \frac{1}{2}s\{t-\tau\}^2\right]\right) \tag{2.4}$$

Mixing these signal together yields the IF signal shown in Eq. 2.5:

$$\begin{aligned} s_{\text{IF}}(t) &= s_{\text{t}}(t)s_{\text{r}}{}^*(t) \\ &= \exp\left(j2\pi\left[f_0 t + \frac{1}{2}st^2\right] - j2\pi\left[f_0\{t-\tau\} + \frac{1}{2}s\{t-\tau\}^2\right]\right) \\ &= \exp\left(j2\pi\left[f_0\tau + st\tau - \frac{1}{2}s\tau^2\right]\right) \\ &\approx \exp\left(j2\pi[f_0\tau + st\tau]\right) \quad \text{for } \tau < t < \text{CRI} \end{aligned} \tag{2.5}$$

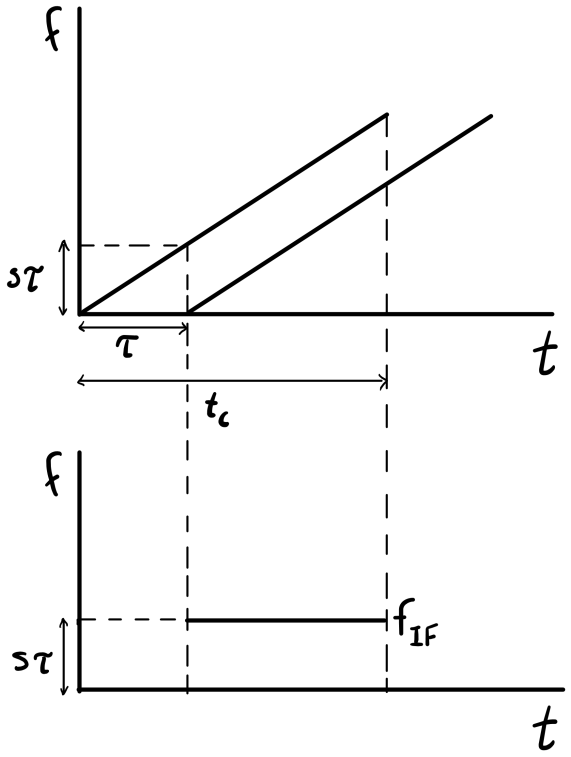

Figure 2.2: Two frequency-time plots of the signals in a radar receiver: the first showing a copy of the transmitted waveform and the received, time-delayed echo; the second showing the receiver mixer output, with beat frequency f_{IF}, and how this relates to the time delay τ.

where the beat or IF frequency, f_{IF}, is identified as being proportional to to the round-trip time delay in the final term of the final line $s\tau = f_{\mathrm{IF}}$, the τ^2 term having been dropped as this is much smaller than the linear terms. The higher frequency term proportional to f_0 is removed by low-pass filtering prior to sampling [33]. This relationship is shown in Eq. 2.6.

$$f_{\mathrm{IF}} = s\tau \tag{2.6}$$

To relate this to a range value, Eq. 2.1 is rearranged and substituted into Eq. 2.6 to give Eq. 2.7:

$$R = \frac{f_{\mathrm{IF}}c}{2s} \tag{2.7}$$

A graphical interpretation of this process is also shown in Fig. 2.2.

2.1.2 Range resolution and maximum unambiguous range

Considering the ranging capability of radar, an important property is the *range resolution*, i.e. the minimum separation between two scatterers at which a radar can distinguish these as distinct returns, rather than just a single extended signal. In FMCW radar, since IF frequencies are mapped to ranges, the range resolution (also known as range bin width or the range resolution cell) is a length determined by the frequency resolution, Δf_{IF}, of the Fast Fourier Transform (FFT) applied to the IF signal. As frequency and time are reciprocal parameters, this resolution is set by the reciprocal of the signal observation period, which in this case is the chirp sweep time t_{c}. This is shown in Eq. 2.8.

$$\Delta f_{\mathrm{IF}} = \frac{1}{t_{\mathrm{c}}} \tag{2.8}$$

Given Eq. 2.7 relating the IF frequency to range as shown above, the range resolution can be expressed as:

$$\Delta R = \frac{\Delta f_{\mathrm{IF}} c t_{\mathrm{c}}}{2B_{\mathrm{S}}} \tag{2.9}$$

which combined with Eq. 2.8 gives the well-known form of the range resolution for FMCW radar in Eq. 2.10:

$$\Delta R = \frac{c}{2B_{\mathrm{S}}} \tag{2.10}$$

Another important specification to consider is the maximum unambiguous range of the radar. Considering the transmitted signals are repeated with a period defined as the CRI, time delays exceeding the CRI will result in ambiguous range values. Thus the maximum unambiguous range is given by Eq. 2.11, where scatterers at a range greater than this will appear as aliases at shorter ranges.

$$R_{\mathrm{max,u}} = \frac{c \cdot \mathrm{CRI}}{2} \tag{2.11}$$

2.1.3 Radar observation geometry

This subsection and those that follow cover topics which are more general to all radar modalities (unless otherwise stated). As well as the previously referenced textbooks, the following sources were consulted for these sections [21], [34], [35], and [36].

Radar measurements of surface clutter or targets on a surface are dependent on the observation geometry. A diagram illustrating the key geometric parameters of radar

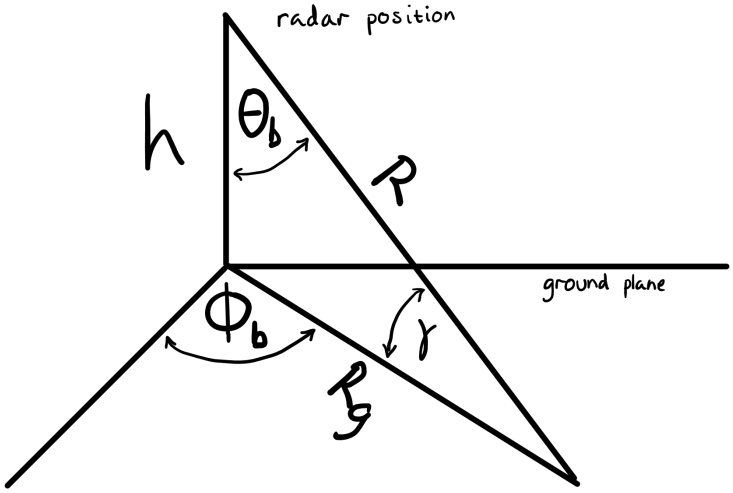

Figure 2.3: A diagram showing a radar observation of the ground plane from a height h, elevation boresight angle of θ_b, and azimuth boresight angle of ϕ_b. This results in a slant range along boresight of R, a grazing angle of γ between the ground plane and boresight path, and a ground range of R_g.

observation is shown in Fig. 2.3, where the parameters are defined as:

- h, the radar height above the ground plane [m],
- θ_b, the radar boresight elevation angle [°],
- ϕ_b, the radar boresight azimuth angle [°],
- R, the slant range [m],
- R_g, the ground range [m],
- γ, the boresight grazing angle [°].

It should be noted that the elevation angle can also be defined with 0° at horizontal, in which case it is known as the depression angle δ. It can also be seen that $\gamma = 90° - \theta_b$ (with the flat Earth approximation), and so in reality the elevation pointing of the radar boresight can be defined by specifying any of these parameters. The relationship between slant range (what the radar directly measures, since this is the line of sight) and the ground range (the slant range projected on to the ground plane) is given by Eq. 2.12:

$$R_g = R\cos(\gamma) \tag{2.12}$$

which can be used to transform from the spherical coordinate system of the radar frame of reference into a Cartesian coordinate system in the ground plane frame of reference.

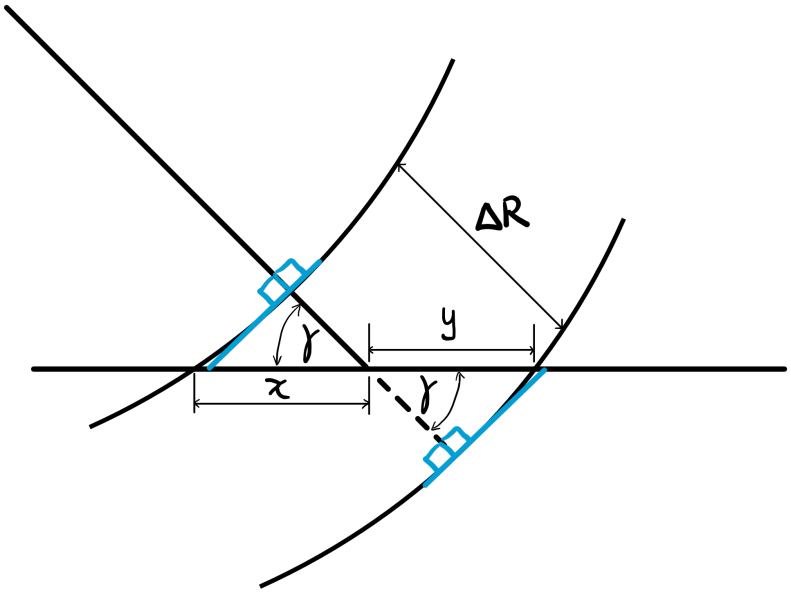

Figure 2.4: Diagram for the derivation of the ground range resolution.

Perhaps unintuitively, the ground range resolution cannot simply be derived as a similar projection i.e. $\Delta R_g \neq \Delta R \cos(\gamma)$. The correct expression is derived using Fig. 2.4. This shows two spherical range shells separated in range by the range resolution. The ground plane intersects the boresight ray at a slant range approximately halfway between the two shells, implying that the lengths x and y are effectively equal. The length x is then calculated using Eq. 2.13:

$$\begin{aligned} \cos(\gamma) &= \frac{\Delta R}{2}\frac{1}{x} \\ x &= \frac{\Delta R}{2\cos(\gamma)} \end{aligned} \tag{2.13}$$

where the ground range resolution is then $x + y$ and so $\Delta R_g = 2x$, giving the final expression in Eq. 2.14:

$$\Delta R_g = \Delta R \sec(\gamma) \tag{2.14}$$

The error incurred by approximating the spherical range shells as having constant curvature is minimal if considering the far field condition (see Subsection 2.1.7), where the shells approximate plane waves. To understand the relationship of slant range and ground range, and their resolutions, it is useful to consider the behaviour of the Equations 2.12 and 2.14 with grazing angle:

- **When** $\gamma \to 0°$
  - $R_g \to R$; this is expected since when looking at the horizon, the ground

range must be equal to the slant range,

- $\Delta R_g \rightarrow \Delta R$; since consequently when looking at the horizon the ground range resolution must be equal to the range resolution.

- **When** $\gamma \rightarrow 90°$
  - $R_g \rightarrow 0$; as when looking at either nadir or zenith, the ground range projection must be zero,
  - $\Delta R_g \rightarrow \infty$; meaning that when observing at nadir or zenith the ground range resolution will encompass a whole plane (for the plane wave approximation). In reality, the range resolution and ground range resolution cells trace a series of boresight centred annuli on the surface (for a symmetric beam pattern).

The relationship between grazing angle, radar height, and the resulting slant range is given by Eq. 2.15.

$$R = \frac{h}{\sin(\gamma)} \tag{2.15}$$

Since the received power is a function of the slant range (as discussed in Subsection 2.1.4), this implies the grazing angle and height change the received power for a typical terrestrial measurement where the position of the radar is fixed, since the range to target is varied by these parameters. Measurements which are taken with a completely fixed observation geometry are termed *staring mode*, whereas measurements which vary azimuth angle are known as *scanning mode*.

As well as affecting the slant range for a radar at fixed height, electromagnetic (EM) scattering from surfaces is a function of incidence angle and thus also of grazing angle, as explained in Subsection 2.1.8.

2.1.4 The radar range equation

Radar detection is predicated on receiving enough signal power to overcome sources of noise in the instrument. The received power of a signal is given by the radar range equation (RRE), which is a key indicator of performance. This is expressed in Eq. 2.16:

$$P_r = \frac{P_t G_t G_r {\lambda_r}^2 \sigma}{(4\pi)^3 R^4 L_{at}} \tag{2.16}$$

where the variables are defined:

- P_r, the received power [W],

- P_t, the transmitted power [W],
- G_r, the receive antenna gain [unitless],
- G_t, the transmit antenna gain [unitless],
- λ_r, the radar signal wavelength [m],
- σ, the point target RCS [m^2],
- L_{at}, the atmospheric path loss [unitless].

The RRE describes the power at the output of the receive antenna, which is then passed to the receiver. This is a function of the radar properties, target reflectivity, and range, where this equation is key for the design and calibration of a radar system [34, Chapter 2].

When considering a complete radar system, the output power of interest is that at the end of the receiver rather than simply at the terminals of the antenna. This quantity is denoted P_{IF}, the power at the end of the IF chain of the receiver (see Section 2.1 for further details). This is equal to the received power shown in Eq. 2.16 multiplied by the receiver gain as shown in Eq. 2.17.

$$P_{IF} = G_{rec} P_r \tag{2.17}$$

2.1.5 Radar frequency bands and atmospheric loss

The interaction of EM radiation with media is fundamentally dependent on frequency, and so this plays a key role in radar design and operation. It is useful to classify sections of the electromagnetic spectrum into frequency bands which can serve as an indication of what phenomena or design considerations are important in that regime. The radar bands of interest to this thesis are shown in Table 2.1. Specifically of interest here and to the broader STREAM project is the 'sub-THz' region, this being a relatively new term which is generally defined as frequencies in the range 100 to 300 GHz, such as by [37], [38], [39], [40], and [41].

EM radiation is variably absorbed by the atmosphere due to the molecular resonances of its constituent gases, affecting radar received power. The level of absorption is a function of temperature, atmospheric pressure, absolute humidity or water vapour density, frequency, and range. Absorption curves for different conditions are shown in Fig. 2.5 for attenuation at a range of 100 m, calculated using the 'gaspl' function in MATLAB®, which is based on the 2013 International Telecommunications Union (ITU) model for atmospheric attenuation due to atmospheric gases [42]. Apart from the differing humidity levels, these are all calculated at the US Standard Atmosphere (1976) parameters of pressure $p = 101325$ Pa (sea level) and temperature $T = 15°C$.

Frequency range [GHz]	Letter designation	Scheme
1 to 2	L	IEEE
2 to 4	S	IEEE
4 to 8	C	IEEE
8 to 12	X	IEEE
12 to 18	Ku	IEEE
18 to 26.5	K	IEEE
26.5 to 40	Ka	IEEE
40 to 75	V	IEEE
60 to 90	E	waveguide
75 to 110	W	IEEE
90 to 140	F	waveguide
110 to 170	D	waveguide
140 to 220	G	waveguide
170 to 260	Y	waveguide

Table 2.1: The radar frequency bands which are relevant to this thesis.

The US Standard Atmosphere water vapour density is $\rho_w = 7.5\ \mathrm{g\,m^{-3}}$ (relative humidity $RH = 58.5\%$), as defined by the ITU [43]. Water vapour density values were calculated from relative humidity using Eq. D2 in Speirs [44, p. 279]. Additional curves for different humidity levels are shown to illustrate the impact of water vapour on the level of atmospheric loss.

The atmospheric attenuation (as a function of range) features in the RRE in Eq. 2.16 as L_{at}, but can often be mostly ignored for radars operating at short ranges (~<500 m) and frequencies in W-band and below when not near to an absorption peak. The absorption becomes more significant at higher sub-THz frequencies such as G-band and should be accounted for, particularly in humid air, for the range values of interest to this project of ~100 to ~200 m.

2.1.6 Radar noise

The following discussion on radar receiver noise is based on the chapter on *Radio Telescope Receivers* by Tiuri and Räisänen in [45, pp. 7–1, 7–74].

The receiver is modelled as a 'two-port' device i.e. a device with only an input and an output. The problem is posed in terms of the *additive noise* measured at the output versus the input noise, where the noise is assumed to be ideal thermal noise. The input noise is defined as that from a black-body radiator at a reference temperature, taken to be 290 K [45, Eq. (7-44)]. The input noise is then defined as Eq. 2.18:

$$N_{in} = k_B T_0 B_N \tag{2.18}$$

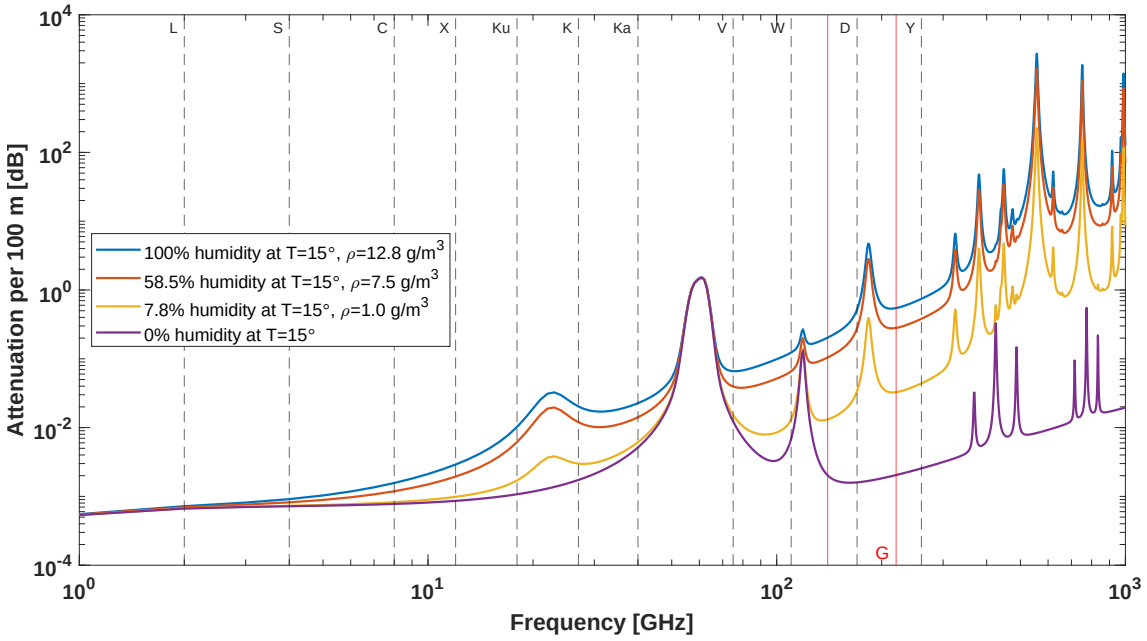

Figure 2.5: One-way atmospheric propagation loss over a range of 100 m. These curves are plotted as a function of frequency and for different levels of humidity at constant values of temperature $T = 15°\text{C}$ and pressure $p = 101325$ Pa which are used for the US Standard Atmosphere (1976), having a water vapour density $\rho_w = 7.5\ \text{g m}^{-3}$ (red curve).

where the variables are defined:

- N_{in}, the input noise power [W],
- k_B, Boltzmann's constant $1.380649 \cdot 10^{-23}\ \text{J K}^{-1}$,
- T_0, the reference temperature of 290 K,
- B_N, the noise bandwidth [Hz].

The gain (on a linear scale) of the two-port device is defined as the ratio of the input noise and N_ϵ, the output noise *in the absence of any additive noise*. This is shown in Eq. 2.19:

$$G_{lin} = \frac{N_\epsilon}{N_{in}} \tag{2.19}$$

where the gain on a linear scale is a unitless ratio, and N_ϵ has units of W [45, Eq. (7-45)].

The *additive noise power* is the additional noise power at the output of the two-port device due to sources of noise within it, and is defined as N_{add}. This can be thought of as equivalent to a situation where the two-port device generates no noise but instead the input noise is at a temperature T_N, and experiences the gain of the device, as shown in Eq. 2.20 [45, Eq. (7-46)].

$$N_{\text{add}} = G_{\text{lin}} k_{\text{B}} T_{\text{N}} B_{\text{N}} \tag{2.20}$$

The noise factor F is then defined in Eq. 2.21 [45, Eq. (7-48)].

$$F \coloneqq \frac{N_{\text{out}} + N_{\text{add}}}{N_{\text{out}}} = 1 + \frac{N_{\text{add}}}{N_{\text{out}}} \tag{2.21}$$

Combining Equations 2.18, 2.19, 2.20, and 2.21, the noise temperature of the device T_{N} can be expressed in terms of the noise factor and the reference temperature as shown in Eq. 2.22 [45, Eq. (7-50)].

$$T_{\text{N}} = (F - 1) T_0 \tag{2.22}$$

The final output noise power, N_{out}, of the device can then be written in terms of the noise factor and the reference temperature as shown in Eq. 2.23 [45, Eq. (7-68)]. It should be noted that many texts omit the -1 term associated with the noise factor, which is an acceptable approximation for devices where F is large but is not strictly correct. The form shown in Eq. 2.23 is the definitive formula.

$$N_{\text{out}} = G_{\text{lin}} k_{\text{B}} (F - 1) T_0 B_{\text{N}} \tag{2.23}$$

The noise factor is often expressed as the noise figure, which is simply the equivalent in decibel units as shown in Eq. 2.24.

$$\mathcal{N} = 10 \log_{10}(F) \tag{2.24}$$

It should be noted that in general, the linear gain, noise factor, and noise figure are functions of frequency and thus the noise power is also a function of frequency.

In FMCW radar, the relevant B_{N} is generally the range FFT frequency resolution as shown in Eq. 2.8 multiplied by the noise bandwidth factor of the windowing used:

$$B_{\text{N}} = B_{\text{w}} \Delta f_{\text{IF}} \tag{2.25}$$

such that the noise power is expressed as per FFT bin.

Typically, the noise figure of each receiver component is measured individually and calculated by way of Eq. 2.21. The total noise figure of the receiver is then calculated from the noise factor, where this total is calculated using the Friis formula for noise Eq. 2.26 [45, Eq. (7-58)], which cascades the different gain and noise factors of each component. This equation shows that the greatest contribution to the total noise factor typically comes from the first component in the chain.

$$F_{\mathrm{t}} = F_1 + \sum_{i=2}^{Q} \left(\frac{F_i - 1}{\prod_{j=1}^{i-1} G_{\mathrm{lin},j}} \right) \tag{2.26}$$

With the variables in Eq. 2.26 defined as:

- F_{t} is the total noise factor [unitless],
- Q is the total number of receiver components,
- i and j are iterators.

2.1.7 Antenna properties

Antennas are used to couple radiation between the radar and the environment in both transmission and reception. This is achieved by performing two functions:

1. impedance matching, and
2. phase transformation.

The first function requires that the impedance of the antenna is matched to that of the transmission line, e.g., waveguide, such that the energy to be transmitted is not reflected at the interface. The performance of an antenna in this regard is determined by an S parameter measurement. In general these are given as S_{nm} where n is the stimulus port and m is the measurement port, and the S value represents the ratio between the power measured at the measurement port to that measured at the stimulus port. For ideal impedance matching, the transmission through the device (defined as S_{21}) would be 1. It is, however, inconvenient to measure the power emitted at the free-space port of an antenna and so the return loss (S_{11}) is used instead for these devices, where this is ideally as low as possible.

The second function determines the direction of the transmitted power by spatially varying the phase of the waves passing through the antenna, achieved using a variety of different designs [46]. The intensity of radiation can be mapped through elevation and azimuth angles to produce cuts in the principal planes of the antenna beam pattern, as shown in Fig. 2.6. These are often measured in the far field, defined as a distance from the antenna in Eq. 2.27:

$$R_{\mathrm{ff}} = \frac{2{d_{\mathrm{a}}}^2}{\lambda_{\mathrm{r}}} \tag{2.27}$$

where the variables are defined:

- R_{ff}, the far field distance [m],

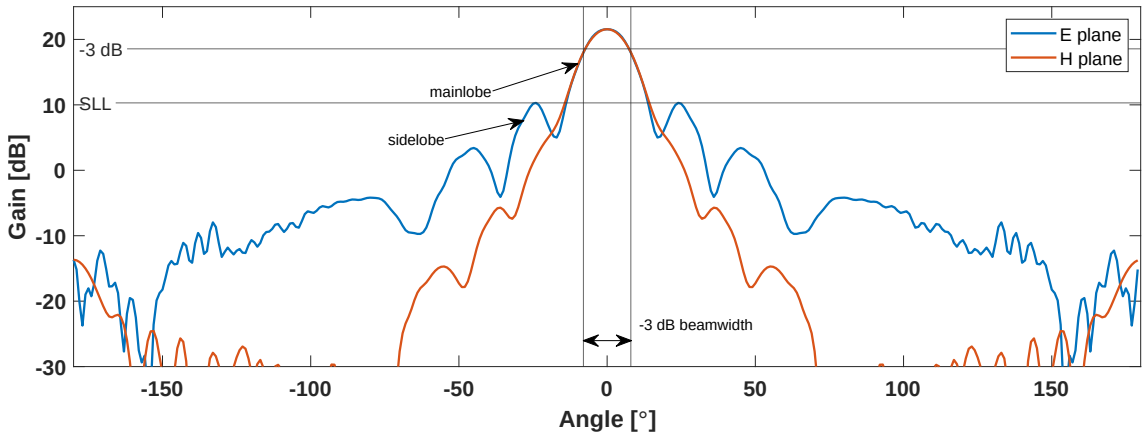

Figure 2.6: Example data of cuts of a far field antenna beam pattern in the principal planes of E and H.

- d_a, the antenna diameter [m].

Far field measurements have the helpful property that the measured antenna pattern as a function of angle is approximately invariant beyond this range since the emitted radiation approaches a plane wave. In reality, at any distance less than infinity the radiation will deviate from a plane wave, where the deviation is parameterised in the equation as an allowable phase error which results in the factor of 2 in Eq. 2.27 [46, p. 810].

Figure 2.6 shows beam pattern curves from the principal electromagnetic planes of E and H, where in the E-plane the E-vector of the radiation from the antenna is aligned with the measurement plane, and likewise in the H-plane the measurement plane is aligned with the H-vector. Also labelled in the figure are two of the main features seen in antenna patterns; the main lobe and side lobes. The width of the main lobe determines the angular resolution of the antenna, the minimum angular separation required to resolve two objects, defined in Eq. 2.28:

$$\Delta\theta \approx \theta_{\mathrm{bw},1} \tag{2.28}$$

where $\Delta\theta$ is the angular resolution and $\theta_{\mathrm{bw},1}$ is the one-way main lobe width, specified as the full width half maximum (FWHM) of the main lobe in a one-way antenna pattern, also known as the −3 dB beamwidth [46, p. 28]. Side lobes are an artefact of the confinement of the main lobe power [46, p. 517] and the level of the highest side lobe relative to the main lobe peak is known as the side lobe level (SLL). The SLL should be minimised to prevent receiving spurious signals from outside the main beam, which introduce ambiguity in the source of the received signal and can make results more difficult to interpret.

The beamwidth is generally specified by the measurements in the principal electromagnetic planes of E and H, where the resulting values are θ_1 and ϕ_1 respectively, where the subscript 1 denotes that these are one-way measurements. For radar measurements it is also useful to define the two-way beamwidths of θ_2 and ϕ_2, corresponding to the E and H beamwidths of the two-way antenna pattern, since often the same antenna or an identical pair of antennas are used for both transmit and receive. The two-way antenna pattern is the self-convolution of the one-way pattern, giving the relations between these quantities as $\theta_2 = \theta_1/\sqrt{2}$ and $\phi_2 = \phi_1/\sqrt{2}$.

The directivity, D, of an antenna is defined as the measure of the angular confinement of the main beam relative to an isotropic radiator, expressed in Eq. 2.29.

$$D = \frac{4\pi}{\Omega_A} \quad \text{where } \Omega_A \approx \theta_1\phi_1 \tag{2.29}$$

The angular confinement of the beam is expressed as the beam solid angle Ω_A which is approximated by multiplying the one-way beamwidths in each plane (see [46, pp. 25, 26] for a more rigorous derivation). An equivalent definition of directivity is as the ratio between the solid angle of the beam and the solid angle of a sphere.

A greater degree of angular confinement (e.g. for a horn, reflector, or lens antenna) is produced for a larger antenna dimension in the corresponding plane, such as in the equation for the directivity of a square aperture under uniform illumination shown in Eq. 2.30:

$$D = 4\pi \frac{l^2}{\lambda_r{}^2} \tag{2.30}$$

where l is the aperture side length in m [46, p. 571]. Since confinement of energy to the main beam results in more radiation being transmitted in a particular direction, this is related to a gain value for signals passing through the antenna. The antenna gain is expressed in Eq. 2.31:

$$G_A = \frac{D}{L_A} \tag{2.31}$$

where G_A is the antenna gain, and L_A is the antenna loss.

The differences between the two cuts in Fig. 2.6 arise from the rotational asymmetry of the antenna and from the input feed to the antenna. The radar developed in this project has antennas fed by rectangular waveguide, which imposes a linear polarisation on the signal passing through it. The polarisation is defined with respect to the orientation of the E vector to the horizon – vertical polarisation (V) has an E vector aligned vertically, and in horizontal polarisation (H) it is aligned horizontally.

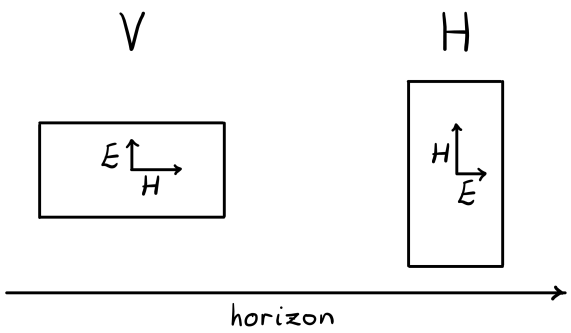

Figure 2.7: A diagram showing the orientation of the E and H fields within a rectangular waveguide, and the resulting polarisation (V or H) with respect to the horizon.

This is shown in Fig. 2.7.

For radar, signal polarisation is specified in terms of both transmission and reception, i.e. for a signal which is transmitted in V and received in V this is vertical-vertical polarisation (VV), with the further combinations for linear polarisation being horizontal-horizontal polarisation (HH), horizontal-vertical polarisation (HV), and vertical-horizontal polarisation (VH), where the former two are termed co-polar and the latter two cross-polar.

2.1.8 Radar cross section and clutter

The reflectivity of a scatterer which is unresolved in both range or angle (i.e. one which is contained within one resolution cell) is defined as the RCS, σ. RCS is a measure of the proportion of scattered power from an object relative to the power incident on the object [21, p. 147]. The incident power on the object is a power density P_i multiplied by the cross section of the target, σ, with units of area m^2. The scattered power density P_s will then be the incident power divided by the scattering solid angle, which for uniform scattering is 4π sr).[1] Measured at a range R, the power will then be divided over the area of a sphere $4\pi R^2$, deriving the scattered power density as Eq. 2.32.

$$P_\mathrm{s} = \frac{\sigma P_\mathrm{i}}{4\pi R^2} \tag{2.32}$$

Taking $R \to \infty$ to derive the far field limit, the σ is given by Eq. 2.33 [34, p. 219]:

$$\sigma = \lim_{R\to\infty} 4\pi R^2 \frac{P_\mathrm{s}}{P_\mathrm{i}} \tag{2.33}$$

For non-uniform scattering, the scattered power has an angular dependence. In practice, this dependency is absorbed into σ, which is allowed to scale as a function

[1] Where sr is the steradian, the unit of solid angle.

of angle. Since the reaction of the object to the incident radiation is also a function of radar wavelength, polarisation, object material, surface roughness, and size, P_s is further a function of all of these variables, where this dependence is similarly passed on to σ.

RCS is then a property of scatterers observed by a radar. Signals from scatterers are often classified in binary terms either as a *target* or as *clutter*, where the former are signals from the intended object of observation and the latter are generally signals from everything else. It should be stated however, that what constitutes as either of these and whether this terminology is useful is dependent on context, as it introduces the *intent* of the radar operator into the definition. Generally, radar textbooks tend to label returns from the environment as being clutter [34, p. 165], [35, p. 189], [47, p. 470], [48, p. 1], where it is an ever-present problem to separate targets from the clutter background. Clutter does however carry significant information about the environment, and since the classification scheme is binary, a detailed characterisation of clutter also simultaneously aids in the classification of a target within it. Further to this, there are specific instances where environmental scattering would be the intended measurement, e.g. for Earth observation, so the common usage of clutter = unwanted background returns would be a misnomer here. In the context of this thesis, environmental returns of the sea are of primary interest, however due to the existing nomenclature these data will continue to be referred to as sea *clutter* here. As should also be clear from the above, clutter is distinct from noise since clutter is simply signal from scatterers whereas, in the case of thermal noise, this originates from an entirely different physical process.

2.1.9 NRCS and beam footprint

The RRE shown in Eq. 2.16 is formulated in terms of the RCS of a point scatterer, meaning it is entirely contained within a radar resolution cell. Whilst this condition holds, the RCS is invariant with the size of the resolution cell. Rather than a single scatterer, a real resolution cell contains a continuum of scattering centres from an object or surface, where the coherent sum produces the observed σ whilst they remain contained within the resolution cell.

In the case where the resolution cell is smaller than the collection of scattering centres, the number of scatterers then scales with the cell size, since a greater number of scattering centres are covered by the cell. This is the behaviour seen with area scattering, where it then becomes useful to parameterise the RCS instead in terms of an RCS per unit area. This is known as the normalised radar cross section (NRCS), denoted as σ^0. Area clutter is then represented as shown in Eq. 2.34:

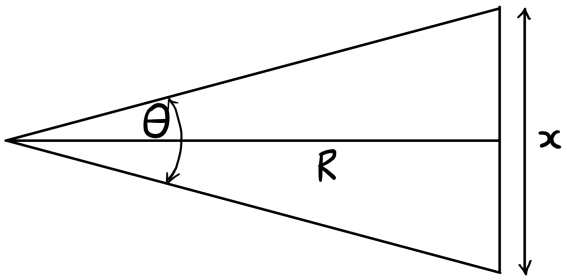

Figure 2.8: A diagram indicating the subtension length x at a distance R for a beamwidth of θ.

$$\sigma = \sigma^0 A \tag{2.34}$$

where A is the clutter patch area in m^2 [47, p. 471].

The NRCS allows for the comparison of the degree of scattering from a surface by normalising for the area of the measurement. The calculation of NRCS is achieved by combining Eq. 2.16 and Eq. 2.34 and rearranging for σ^0 to give Eq. 2.35:

$$\sigma^0 = \frac{P_r (4\pi)^3 R^4}{P_t G_r G_t {\lambda_r}^2 A} \tag{2.35}$$

A quantity related to the NRCS is the noise equivalent sigma zero (NESZ), which is calculated by using the receiver noise instead of P_r in Eq. 2.35. This value is the sensitivity limit of the instrument i.e. gives the lower bound on the NRCS level which can be measured.

The clutter cell area, A, is defined by the beam footprint. Formulae for this value belong to two categories, classified as either beamwidth limited or range resolution limited. This classification depends on whether the subtension length[2] enclosed by the elevation beamwidth (as shown in Fig. 2.8) or the range resolution length is greater when projected to ground range. These two cases are illustrated in Fig. 2.9. In all further discussion the beamwidths referred to are **two-way**, since in this scenario the same antenna transmits and receives, and thus the observed response for any scattering element within a patch (and therefore the patch itself) will be the self-convolution of the antenna pattern i.e. the two-way response. It is also assumed that the illuminated area of the footprint has a sharply defined edge, whereas in reality the antenna pattern is a continuously varying function.

From Fig. 2.8, the subtension length x enclosed by an angle θ is derived as shown in Eq. 2.36, which is a useful relation for the derivation of both clutter patch areas. In the following derivations, the observation grazing angle γ is as defined in Fig. 2.3, i.e.

[2]The counterpart length to a subtended *angle*.

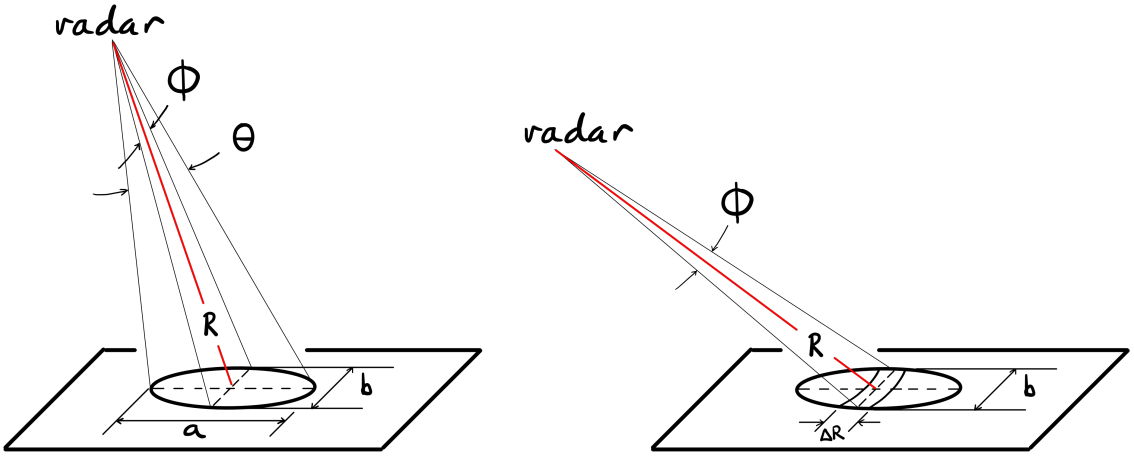

Figure 2.9: Beamwidth limited (left) and range-gate limited (right) beam footprints. The ellipses represent the two-way −3 dB antenna pattern contour.

the angle measured from the boresight ray to the surface plane.

$$x = 2R\tan(\theta/2) \tag{2.36}$$

Considering first the beamwidth limited case, the area A_b can be defined as that of an ellipse with the major axis a and minor axis b. The clutter patch area is then derived as shown in Eq.2.37:

$$\begin{aligned} A_b =& \frac{\pi}{4}ab \\ \approx& \frac{\pi}{4}\left(2R\tan\left[\frac{\theta_2}{2}\right]\csc[\gamma]\right)\left(2R\tan\left[\frac{\phi_2}{2}\right]\right) \\ \approx& \pi R^2\tan\left(\frac{\theta_2}{2}\right)\tan\left(\frac{\phi_2}{2}\right)\csc(\gamma) \end{aligned} \tag{2.37}$$

For the range resolution limited case, the area A_r enclosed by two arcs and the sides of the beam ellipse can be approximated as a rectangle. The clutter patch area is then derived as shown in Eq. 2.38:

$$\begin{aligned} A_r \approx& 2R\tan\left(\frac{\phi_2}{2}\right)\Delta R\sec(\gamma) \\ \approx& 2R\tan\left(\frac{\phi_2}{2}\right)\Delta R_g \end{aligned} \tag{2.38}$$

where the expression for the ground range resolution from Eq. 2.14 has been substituted into the equation. To determine which equation to use at a given grazing angle, the expressions for A_b and A_r are set to be equal and the resulting expression solved for the critical grazing angle γ_c, as shown in Eq. 2.39:

$$\begin{aligned}
\pi R^2 \tan\left(\frac{\theta_2}{2}\right)\tan\left(\frac{\phi_2}{2}\right)\csc(\gamma_c) &= 2R\tan\left(\frac{\phi_2}{2}\right)\Delta R\sec(\gamma_c) \\
\pi R\tan\left(\frac{\theta_2}{2}\right)\csc(\gamma_c) &= 2\Delta R\sec(\gamma_c) \\
\frac{\sec\gamma_c}{\csc\gamma_c} &= \frac{\pi R\tan(\theta_2/2)}{2\Delta R} \\
\tan(\gamma_c) &= \frac{\pi R\tan(\theta_2/2)}{2\Delta R}
\end{aligned} \tag{2.39}$$

Since with increasing γ_c the area tends to A_b, in the case where the left hand side in Eq. 2.39 is greater the beamwidth limited form in Eq. 2.37 should be used, and the range limited form in Eq. 2.38 when the inequality is reversed.

For small beamwidths, small angle approximations can be applied such that $\tan(\theta) \approx \theta$, $\sin(\theta) \approx \theta$, and $\cos(\theta) \approx 1$ for angles <10° (and when the unit of angle used in the formulae is the radian). The clutter patch areas in this case can be further approximated as Eq. 2.40 and Eq. 2.41:

$$A_b \approx \frac{\pi R^2}{4}\phi_2\theta_2\csc(\gamma) \tag{2.40}$$

$$A_r \approx R\phi_2\Delta R_g \tag{2.41}$$

with the limiting condition becoming Eq. 2.42:

$$\tan(\gamma_c) = \frac{\pi R\theta_2}{4\Delta R} \tag{2.42}$$

For low grazing angles (<10°), the small angle approximation can be applied again such that $\csc(\gamma) = 1/\gamma$ and $\sec(\gamma) = 1$, hence the clutter patch areas become Eq. 2.43 and Eq. 2.44:

$$A_b \approx \frac{\pi R^2\phi_2\theta_2}{4\gamma} \tag{2.43}$$

$$A_r \approx R\phi_2\Delta R \tag{2.44}$$

with the limiting condition of Eq. 2.45.

$$\gamma_c \approx \frac{\pi R\theta_2}{4\Delta R} \tag{2.45}$$

The derivations above follow those in Nathanson [21, p. 72] with additional clarifications. There are however some differences in the results, namely the form of Eq.

2.39 in Nathanson neglects the factor of $\pi/2$ and the factor of $1/2$ for the elevation beamwidth. The approximated form in Eq. 2.44 is also found in Nathanson [21, p. 274].

Other texts make various errors which will be noted here:

- **Currie et al. [48, p. 10]:**
  - The one-way beamwidth is incorrectly used throughout.
  - Eq. (1.33) applies the small angle approximation to the wrong parameter from what is indicated in the text (applied to azimuth beamwidth rather than to the grazing angle), but is otherwise correct.
  - Eq. (1.34) neglects to apply the small angle approximation at all.
  - Fig. (1.4) states the grazing angle condition with the incorrect inequality symbol.
- **Currie et al. [35, p. 192]:**
  - Fig. (5.1), the factor of 2 should be in the denominator in the grazing angle condition.
  - Fig. (5.2), the beam shape factor for the azimuth term should be in the denominator, and similarly the factor of 2 should be in the denominator of the grazing angle condition.
  - Eq. (5.20) states the grazing angle condition with the factor of 2 in the numerator, this should be in the denominator.
- **Richards et al. [34, p. 169]:**
  - Paragraph 4 of Section (5.1.3.1) suggests that both the beam limited and range resolution limited clutter patch area cases were 'considered' in Section (2.13), however these have been omitted from that section.
  - Eq. (5.7) erroneously states the use of one-way beamwidths according to the definition of symbols, however a later statement in the section states these values should be the two-way beamwidths.
  - Equations (5.9) and (5.10) state the range resolution limited area using $\csc(\gamma)$ rather than $\sec(\gamma)$.
  - Equations (5.11) and (5.12) are missing a factor of π and the factor of 2 in the numerator should be in the denominator.
- **Ward et al. [49, p. 323]:**

– The range resolution limited area is correctly stated in Eq. (12.7), however in the adjoining paragraph the authors state the use of the one-way beamwidth rather than two-way.

Skolnik [47, p. 471] derives only the range resolution limited case, does not state the use of the two-way beamwidth, and does not explicitly state the use of the small angle approximations when producing Eq. (13.4) but otherwise agrees with the derivation above.

Wetzel [36, p. 15.8] states the correct formulae for both beamwidth and range resolution limited cases in Equations (15.8) and (15.9), however these equations assume a symmetric beam since no distinction is made between azimuth and elevation beamwidths. They also assume a narrow beamwidth and apply the small angle approximation without statement, do not provide the grazing angle condition, and do not state that the beamwidth should be two-way. They note however that in the approximation of a clearly defined edge to the antenna pattern, the area tends to be overestimated by 1 or 2 dB.

Rosenberg and Watts [13, p. 196] correctly state the range resolution limited equation in Eq. (6.7) but do not explicitly state the use of the small angle approximation for narrow beamwidths.

The radar used in this research has a fine range resolution and narrow beamwidth, and as such the equation for the range resolution limited area will be used. Considering again Eq. 2.38, it can be seen that the area is directly proportional to the range (but not to R^2). Thus using Eq. 2.34 the dependence of the NRCS on range for the range resolution limited beam footprint is Eq. 2.46:

$$\sigma^0 \propto R^3 \tag{2.46}$$

and the received power shown in Eq. 2.47:

$$P_\mathrm{r} \propto R^{-3} \tag{2.47}$$

2.1.10 Doppler measurement

Results of Doppler measurement are not discussed at any length in this thesis. The radar developed as part of this work (as described in Chapters 4 and 5) was however designed specifically to be a coherent instrument, and Doppler results are shown in other references connected with this thesis, so an overview of the theory of Doppler measurement is included here.

The measurement of the Doppler frequency shift in a radar return allows the radial velocity of a scatterer to be determined. The relation between scatterer radial velocity v_r and the measured Doppler frequency f_D which is often used in radar applications is shown in Eq. 2.48:

$$f_D = -\frac{2v_r f_0}{c} \tag{2.48}$$

and is valid for velocities $v_r \ll c$ [34, p. 274]. The v_r for a scatterer receding from the radar is defined as positive to be consistent with the scatterer range increasing. The Doppler frequency in Eq. 2.48 is then defined with a negative term since for receding targets the frequency shift is negative. The Doppler offset is mathematically expressed in the time domain signal as shown in Eq. 2.49:

$$x_D(t, f_D) = s_t(t)\exp(2j\pi f_D t) \tag{2.49}$$

where $s_t(t)$ is the transmitted radar signal.

The Doppler frequency offset is measured from data by calculating the phase variation across successive chirps at the same range and angular position to compare the displacement change for the same scatterers. The measurement of f_D can be achieved using a Fourier transform (FT), typically performed with the FFT algorithm.

Given that the resolution of an FT increases with the observation period, this is what limits the achievable Doppler resolution. In practice, this period is measured as the coherent processing interval (CPI), composed of a number of successive chirps, N_c. The measured chirps must be coherent for phase comparison to be meaningful. The number of chirps in a CPI is determined by the relation $N_c = \text{CPI} \cdot \text{CRF}$, where the CRF is the chirp repetition frequency (the inverse of the chirp repetition interval (CRI)). The Doppler resolution, Δf_D, is then given in Eq. 2.50:

$$\Delta f_D = \frac{1}{\text{CPI}} \tag{2.50}$$

The chirp repetition frequency (CRF) is the sampling rate for the Doppler frequency, and by similar argument as used for the maximum unambiguous range, the maximum unambiguous Doppler frequency which can be detected is CRF/2. The maximum unambiguous velocity is then given in Eq. 2.51 [34, p. 301].

$$v_{max} = \frac{\text{CRF}c}{4f_0} \tag{2.51}$$

It is often useful to measure how the Doppler frequency evolves as a function of time, in which case a joint time-frequency analysis is required. A common method for

doing this is with the short-time Fourier transform (STFT), implemented as an FFT across some time window that is stepped along the data set [34, p. 645].

2.1.11 Elements of radar hardware theory

This section will describe the generic implementation of a basic coherent FMCW homodyne radar, which is illustrated in Fig. 2.10. In brief, the functions of the subsystems are as follows:

- **Clock**: this oscillator provides a constant frequency signal which is used to time synchronise other components.
- **Divider chain**: this uses the clock oscillator input to derive the CRF for the chirp generator, and to derive the analogue to digital converter (ADC) sampling clock frequency and the trigger frequency which is used to trigger the chirp and ADC acquisition.
- **Chirp generator**: this component produces the chirp signal.
- **Transmitter**:
  - The mixer is used to up convert the chirp against a higher frequency oscillator.
  - The frequency multiplier increases the frequency of the chirp signal to the desired transmission frequency.
  - The bandpass filter removes frequency harmonics introduced by both the mixer and the multiplier.
  - The amplifier increases the signal level of the upconverted chirp signal.
  - The antenna transmits the signal.
- **Receiver**:
  - The antenna receives the signal reflected from the scene.
  - The multiplier down converts the received signal against a copy of the transmitted waveform, where this is the defining feature of a homodyne system.
  - The amplifier in the IF chain increases the signal level of the down converted signal.
  - The low pass filter removes the high frequency components of the down converted signal to prevent aliasing.

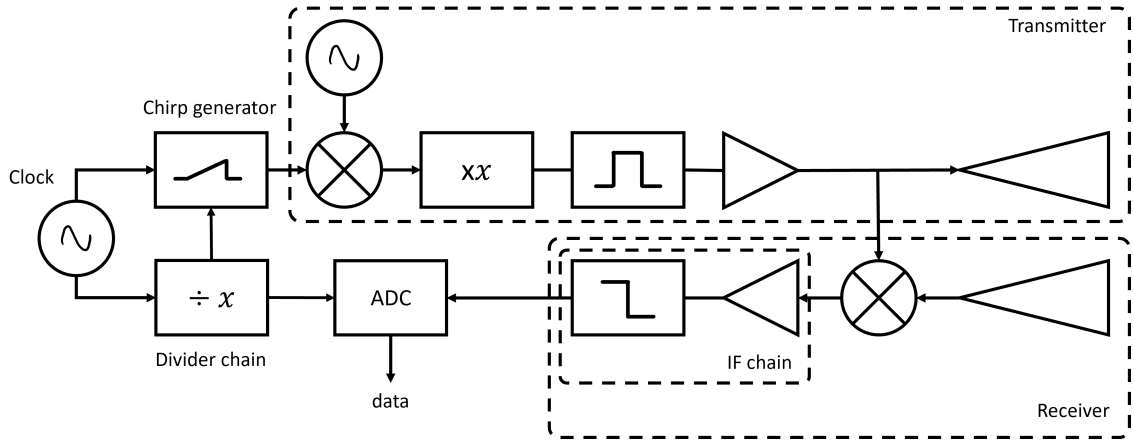

Figure 2.10: Generic architecture of a coherent FMCW homodyne radar.

- **ADC**: samples the down converted signal to produce data.

This structure has evolved to solve problems that arise in radar system design, notably:

- The signal chirp is created at a lower frequency (baseband) which is then upconverted and multiplied to reach the transmission centre frequency (passband). In general signal synthesis becomes more challenging at higher frequencies, so by first generating a chirp at baseband the chirp can be more linear, the process is more cost effective, and this provides a more modular design where the same chirp generation technology can be used to reach a higher carrier by adding further multiplication stages. Chirp linearity is the primary concern for FMCW radars, since the ranging principle in Eq. 2.7 depends on the chirp rate s being regular and predictable, where otherwise this increases range uncertainty and thus compromises range resolution. Contemporary radars generally use direct digital synthesis (DDS) boards to achieve easily programmable and highly linear chirps. A drawback of the frequency multiplication approach is that this increases phase noise as shown in Eq. 2.63 below.
- The transmitter amplifier increases the transmitted signal level, which as shown in Eq. 2.16, then increases the received signal and thus instrument sensitivity.
- Separate antennas reduce the power coupled directly from the transmitter to the receiver, which is known as transmit-receive leakage. As the receiver is designed to be as sensitive as possible, leakage from the transmitter can easily overwhelm the receiver causing either saturation or damage. The alternative to dual antennas is using a single antenna with a circulator, which saves on antenna costs and design complexity. This does however increase transmit-receive leakage relative to a dual antenna system and can also be difficult to engineer at high frequency. Dual antenna systems are however susceptible

to a reduction in signal level due to parallax at short range, as well as from misalignment of the antennas if these have narrow beamwidths.

- Homodyne operation performs dechirp on receive in analogue hardware. For high frequency radar (10s or 100s of GHz), this demodulates the signal by using the transmitted waveform as the mixer local oscillator (LO) input and produces a much lower frequency (10s of MHz) as IF. This greatly reduces the sampling rate requirement of the ADC which would otherwise prohibitive.
- The IF chain primarily amplifies the IF signal from the receiver mixer which is typically very low power. The amplified signal then occupies the full dynamic range of the ADC such that the signal is very much greater than the ADC noise, and the amplified receiver noise is also somewhat higher than then ADC noise, such that the dynamic range is not limited by the ADC noise at either extreme.
- The clock signal which is used for chirp generation is also used to derive the trigger signal for ADC data acquisition to ensure that these are synchronised. This ensures coherent operation.

The analogue signals generated and manipulated by the radar hardware are eventually digitised for further processing at the end of the IF chain by the ADC. For an adequate sampling rate, the Nyquist criterion states that the minimum rate f_s required to fully reconstruct a sampled signal without aliasing is as shown in Eq. 2.52:

$$f_s = \frac{1}{T_s} > B_2 \tag{2.52}$$

where T_s is the sampling period and B_2 is the *double-sided* signal bandwidth [34, Eq.(14.4)]. For a signal centred at 0 Hz and a double-sided spectrum bandwidth of B_2, the highest frequency component is $B_2/2$. This allows Eq. 2.52 to be reformulated in terms of maximum frequency, $f_{\mathrm{IF,max}}$, shown in Eq. 2.53:

$$f_s > 2f_{\mathrm{IF,max}} \tag{2.53}$$

where the $f_{\mathrm{IF,max}}$ sets the *maximum instrumented range* of the radar, beyond which ADC sampled IF becomes aliased. The relationship between f_s and the maximum instrumented range $R_{\mathrm{max,I}}$ is shown in Eq. 2.54.

$$R_{\mathrm{max,I}} = \frac{f_s c}{4s} \tag{2.54}$$

As mentioned in Subsection 2.1.1, the IF is a product of the chirp rate and the delay time as shown in Eq. 2.6 and so long range, high bandwidth systems have a high maximum IF which needs to be accounted for when specifying an ADC.

2.1.12 Phase noise

A significant concern in FMCW radar engineering is the phase noise of the transmitter and the degradation this can cause in the receiver sensitivity. This is because reflected phase noise can introduce strong range side lobes for bright targets which can obscure weaker signals. Phase noise is the random variation of phase in a given signal, expressed mathematically for a single tone as Eq. 2.55:

$$V(t) = V_0 \sin(2\pi f_0 + \phi(t)) \tag{2.55}$$

for a signal $V(t)$, nominal amplitude V_0, nominal frequency f_0, and phase noise $\phi(t)$ [50, p. 1]. The effect of phase noise is the spreading of the power of a single tone over adjacent frequencies, where the phase noise of a component is measured as a value normalised to the centre (or carrier) frequency level and represented as a power spectral density (PSD) function of the offset from carrier, defined as $\mathcal{L}(f)$.

The phase noise is transmitted as part of the radar waveform and so is also reflected back to the receiver from scatterers. When using some form of the transmitted waveform for down conversion (such as in the homodyne architecture), the phase noise of the received signal is mixed with that of the transmitted signal. This causes an interference effect known as *phase noise cancellation* which can cause strong range side lobes from scatterers [51, Fig. (10)], but can also be used to mitigate them [51, Section III B]. The reason why both situations can occur is because the effect is a function of the difference in signal path length between the range to the scatterer and the LO path to the receiver mixer, as measured from the point that these signal paths diverge in the radar architecture. This effect is well documented [51], [52], [53], [54], [55].

In general, the receiver mixer LO path is both fixed and much shorter than the scatterer range and thus is often approximated to be 0 m. The cancellation effect is then given as a function of the scatterer range, which maps to an IF frequency. An additional complication is that since the effect is due to the radar behaving like an interferometer, the phase noise cancellation is also a function of frequency, and since frequency in an FMCW radar is swept, this then modulates the cancellation level. When down converted the frequency sweep also maps to an IF frequency, so care must be taken not to confuse the IF frequency corresponding to the range to the scatterer and the IF frequency corresponding to a given range bin. For the sake of clarity, the former quantity is expressed as a range R and the latter as f_{IF}.

From Cooper et al. [51], the reflected transmitter phase noise PSD (in linear units) from a target at range R which is detected in the IF at frequency f_{IF} is derived to be Eq.

2.56[3]:

$$P_\phi(R, f_{\mathrm{IF}}) = \left\langle |\tilde{\Phi}_a(f_{\mathrm{IF}})|^2 \right\rangle \cdot 4\sin^2(2\pi f_{\mathrm{IF}} R/c) \tag{2.56}$$

The function $\tilde{\Phi}_a(f_{\mathrm{IF}})$, as shown in Eq. 2.57, is defined:

$$\tilde{\Phi}_a(f_{\mathrm{IF}}) = \mathcal{F}(a(t)\phi(t)) \tag{2.57}$$

where $\tilde{\Phi}_a(f_{\mathrm{IF}})$ is the Fourier transform of the time domain phase noise voltage function $\phi(t)$ under some windowing function $a(t)$, where the PSD[4] of this function is the phase noise spectrum $\mathcal{L}(f)$ as shown in Eq. 2.58:

$$\mathcal{L}(f_{\mathrm{IF}}) = \left\langle |\tilde{\Phi}_a(f_{\mathrm{IF}})|^2 \right\rangle \tag{2.58}$$

which in practice is a *measured* quantity. Eq. 2.56 can then be re-factored to give Eq. 2.59:

$$P_\phi(R, f_{\mathrm{IF}}) = \mathcal{L}(f_{\mathrm{IF}}) \cdot M(R f_{\mathrm{IF}}) \tag{2.59}$$

where $M(R, f_{\mathrm{IF}})$ is the modulation due to the interferometric effect, as shown in Eq. 2.60:

$$M(R, f_{\mathrm{IF}}) = 4\sin^2\left(2\pi f_{\mathrm{IF}} \frac{R}{c}\right) \tag{2.60}$$

where this produces a characteristic lobed pattern in the reflected phase noise.

In reality, determining the $P_\phi(R, f_{\mathrm{IF}})$ in a radar IF signal from a measurement of system $\mathcal{L}(f_{\mathrm{IF}})$ is not quite so straightforward. Firstly the $\mathcal{L}(f_{\mathrm{IF}})$ must be integrated from a PSD to the power per IF bin resolution bandwidth, Eq. 2.8, by multiplying by a factor g given by Eq. 2.61:

$$g(t_{\mathrm{c}}) = \frac{1}{t_{\mathrm{c}}} B_{\mathrm{w}} \tag{2.61}$$

where this includes the gain from the window noise bandwidth B_{w}. Additionally, if the signal for which the $\mathcal{L}(f_{\mathrm{IF}})$ is measured is subject to frequency multiplication before being transmitted, then the phase noise is also multiplied by this process, corresponding to a gain factor for $\mathcal{L}(f_{\mathrm{IF}})$ of Eq. 2.62:

[3]Where $m/T_{\mathrm{s}} \to f_{\mathrm{IF}}$ since $\Delta f_{\mathrm{IF}} = 1/T_{\mathrm{s}}$ and m is the IF bin number, and $\tau_b \to 2R/c$ in Eq. (6), as per the notation of the paper.

[4]Where from [56, Eq. (1.3.10)], this is defined as $\phi(\omega) \coloneqq \lim_{N\to\infty} \left\langle 1/N |\mathrm{DTFT}(y(t))|^2 \right\rangle$, in the notation of the source.

$$h_{\mathrm{PN,lin}}(n) = n^2 \tag{2.62}$$

where $h_{\mathrm{PN,lin}}$ is the linear phase noise multiplication gain, and n is the multiplication factor. This equation is often presented on the decibel scale as shown in Eq. 2.63.

$$h_{\mathrm{PN}}(n) = 20\log_{10}(n) \quad [\mathrm{dB}] \tag{2.63}$$

A phase noise data fitting model was defined by Cooper [54, Eq. (2)] in the decibel scale as shown in Eq. 2.64:

$$\hat{P}_{\phi}(R, f_{\mathrm{IF}}) \coloneqq C_1(f_{\mathrm{IF}}) + 10\log_{10}(M(R, f_{\mathrm{IF}})) + C_2 f_{\mathrm{IF}} + C_3 \exp\left(\frac{-{f_{\mathrm{IF}}}^2}{C_4^2}\right) \quad [\mathrm{dB}] \tag{2.64}$$

where C_1 is the phase noise power as shown by Eq. 2.65.

$$C_1 = \mathcal{L}(f_{\mathrm{IF}}) + 10\log_{10}(g(t_{\mathrm{c}})) + h_{\mathrm{PN}}(n) + K \quad [\mathrm{dB}] \tag{2.65}$$

The additional elements of the model parameterised by C_2, C_3, and C_4 were added in [54] to improve the fit to data. Fitting the model to data and then solving for $\mathcal{L}(f_{\mathrm{IF}})$ for a given f_{IF} produces a value close to that measured for $\mathcal{L}(f_{\mathrm{IF}})$ using a typical test set. It should be noted that since $\mathcal{L}(f_{\mathrm{IF}})$ is defined as relative to the carrier (dBc) then the value of the signal peak K from the scatterer at R must be added to C_1 to give the correct level.

For multiple scatterers or area scattering, phase noise is reflected from a continuum of ranges. This causes many superimposed phase noise patterns which incoherently sum, resulting in an overall increase in the noise floor, washing out the modulation pattern [54, Fig. (4b)].

The best way to mitigate this effect is to choose an LO source with minimal phase noise, and which is also as close to the carrier frequency as possible to minimise the contributions from both $\mathcal{L}(f_{\mathrm{IF}})$ and the frequency multiplication factor n respectively. Stable sources at high millimetre-wave and sub-THz frequencies are not available commercially [51], thus minimising the oscillator phase noise necessarily becomes the primary concern.

This concludes the essential radar theory needed to understand the radar development process, sea clutter measurements, and analysis which follow in later chapters. The following two sections of this chapter cover concepts related to the sea, and then a summary of the published research on microwave frequency and Ka-band radar sea clutter.

2.2 The sea

This section explains the features of sea surfaces, how these surfaces form, and the factors which affect this process. This is followed by a discussion on how the sea surface is characterised, and how these surfaces can be simulated. The framework for describing the sea surface which is presented then provides the context for the discussions of sea clutter in later sections.

2.2.1 Features of the sea surface

Sea surfaces consist of wave structures over a broad range of scales. These can have a number of different sources such as the tides or seismic events, however this thesis only considers waves created by the wind. The main features of the wind generated sea surface are:

- **Capillary waves**: these are short wavelength ripples forming the fine structure of the sea surface. When a strong wind is blowing these waves may have sharpened features such as in Fig. 2.11a, quickly becoming rounded in lighter winds as shown in Fig. 2.11b. These waves quickly dissipate in the absence of wind. A conventional value for the upper wavelength limit is given as $\lambda_w = 2.5$ cm in Rosenberg and Watts [13, p. 4], but definitions for the regions may differ [57, Appendix A]. The lower wavelength limit has been measured to be approximately 7 mm, after which point the spectral density falls steeply for most wind speeds [58, p. 11543].
- **Gravity waves**: these waves have wavelengths of anything greater than $\lambda_w = 5$ cm [13, p. 4]. These waves form the bulk structure of the sea surface and can propagate much further than capillary waves. The local area of actively wind-driven gravity waves is called the wind sea. Gravity waves are shown in Fig. 2.11c and 2.11d.
- **Swell**: gravity waves which have propagated away from the wind sea of their origin are known as swell. Swell can hence be present in the absence of wind, and due to the interactions of waves with each other swell tends to have long wavelengths [59, p. 288]. An image of swell is shown in Fig. 2.11e. The wavelength of swell waves is generally defined as being anything greater than that which can be supported by the present wind conditions (and thus will increase with sea state).
- **Whitecaps**: these waves are defined by some of the wave detaching from the bulk surface or the crest collapsing such that air becomes mixed with the water.

This is preceded by the wave growing in height and sharpening until its shape can no longer be supported by the internal forces of the wave, leading to breaking. There are a number of different causes for this process, but all are related in that the top of the wave moves faster than the bottom which eventually disrupts the wave structure. Whitecaps are shown in Fig. 2.11f.

A superposition of the listed features produces a sea surface. There is considerable structure to the surface of the sea, but due to the multiple complex processes which generate it, it can appear chaotic and is often described statistically.

2.2.2 Generation of waves by the wind

The generation of wind waves on the sea is not completely understood nor totally experimentally verified [60]. However, the current accepted theories are from Phillips [61], Belcher and Hunt [62], and Miles [63]. The first has been determined to be the best current explanation for the growth of capillary waves, and the latter two for the growth of short and long wavelength gravity waves, respectively.

In the theory presented by Phillips [61], the generation of waves on the sea is driven by the flow of faster moving air over the surface of the water. The turbulent flow of air over the interface causes random pressure fluctuations, forming small ripples (wavelets) on the water's surface [60, p. 42] [61, p. 427]. If the velocity of the pressure fluctuations of the air and the ensuing wavelets is the same as that of another wave on the surface, a resonant forcing effect occurs and energy is transferred to the wave, causing it to grow. This is the source of capillary waves, which have a phase velocity[5] determined by the restoring force of surface tension.

In an extension of a theory originally presented by Jeffreys [64], Belcher and Hunt [62] proposed a mechanism whereby wave crests produce a 'sheltering' effect such that air on the leeward side of the wave is at a lower pressure than on the windward side. This again results in a resonant forcing mechanism between the oscillatory shape of the waves and the resulting pressure differential when wind blows over them. This is thought to be the mechanism by which capillary waves grow to eventually be gravity waves - waves of sufficient mass such that the dominant restoring force is gravity - and has been found to best describe the growth of gravity waves when their wavelengths are short [60, p. 42].

The growth of longer wavelength gravity waves is then thought to be explained best by the theory presented by Miles [63], where energy is coupled from the wind to surface waves by shear flow instabilities (Kelvin-Helmholtz instabilities) occurring at a

[5] Phase velocity, as usually defined: $v_p := \omega/k = f\lambda$.

(a) Capillary and gravity waves.

(b) Capillary waves from a light breeze.

(c) Gravity waves.

(d) Gravity waves.

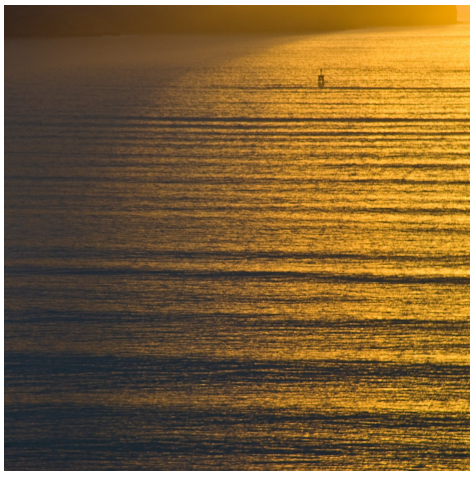

(e) Swell.

(f) White caps.

Figure 2.11: Photographs of different sea surface features shown with other objects for scale. Reproduced with thanks to Dr David Macfarlane, except for the image of swell which was adapted from Phillip Capper [CC BY 2.0], via Wikimedia Commons.

height above the wave surface where the wind speed and the phase velocity of the wave are matched. These theories all have limitations and are not perfectly corroborated, where this is an ongoing area of research [60, p. 42].

Over time, the gravity waves caused by the wind in a patch of sea interact with each other to form longer wavelength waves [65, p. 7] [59, p. 288]. Given enough time and distance (known as duration and fetch), these interactions along with numerous loss mechanisms such as wave dissipation on shorelines, balance the driving force of the wind, resulting in an equilibrium known as a fully-developed sea.

Whitecaps in deep water form as gravity waves are steepened by the wind, where breaking occurs when the height to wavelength ratio is ~0.17 [66, p. 96]. In high winds the tops of waves can also be blown off, creating additional spray in the air and on the water, which can appear similar to whitecaps from steepening. Whitecaps in shallow water form due to shoaling, whereby the wavelength of waves coming into shore is reduced. This occurs as the group velocity[6] of water waves decreases with depth in shallow water. The reduced wavelength leads to an increase in height and steepening of the front face of the wave (since the seabed at a shoreline slopes upwards), until eventually the wave breaks, typically occurring when the ratio of the height to the water depth exceeds 0.8 [66, p. 97] [59, pp. 293–295]. Shoaling waves are can also be known as littoral waves when they occur in the littoral (or coastal) zone.

2.2.3 Factors affecting the generation of wind waves

The physical parameters affecting wind wave formation, as described in Young [67, p. 83], are:

- **Wind velocity** relative to the wave velocity.
- **Water depth** in the patch of sea, and how this varies.
- **Fetch**, or the length of the patch of sea, determined as the distance over which a wind blows with an approximately continuous direction and speed.
- **Width** of the patch of sea, perpendicular to the fetch.
- **Duration**, how long the wind has been blowing over the patch of sea.

These parameters encompass the energy input, dissipation, and boundary conditions which then govern the behaviour of the body of water.

[6] Group velocity, as usually defined: $v_g := \partial\omega/\partial k$.

2.2.4 Characterising the sea

A system for describing the sea surface is useful for relating the observed conditions to other measurements, and for recording how the sea changes over time and in response to other factors of the environment. Three main descriptors can be used to define the conditions measured at sea: wind velocity v_w, significant wave height (SWH), and sea state (SS).

2.2.4.1 Wind velocity

Wind velocity is often used as a descriptor since this can be easily measured with an anemometer, and has traditionally been of interest for sailing. Since the wind provides the energy which drives waves, its velocity is clearly linked to the resulting sea surfaces, however it is an indirect measurement since the correlation of wind velocity input to sea surface output is not totally straightforward. Wind takes time to affect the water's surface, so the duration of the wind blowing over a surface needs to be measured. The fetch over which the wind is in contact with the water is also important, since the interface between the moving wind and waves it generates mediates energy transfer.

These additional parameters then mean the measurement is no longer localised in space or in time, which makes it more difficult to perform accurately. It also cannot be used to describe swell, since swell can be present in the absence of wind. It should be noted however that wind creates transient sea surface features such as capillary waves, whitecaps, and sea spray, and so *local wind velocity* is always a key measurement parameter in describing the sea surface.

2.2.4.2 Significant wave height

Significant wave height was historically defined as the mean height of the highest third of waves measured over some time period, represented as $H_{1/3}$. This definition is still sometimes used, however it has been shown that this quantity is related to four times the standard deviation of the surface displacement, ζ:

$$H_{1/3} = 4\langle\zeta^2\rangle^{1/2} \tag{2.66}$$

where this is the generally utilised method of calculating SWH from wave measurements since it uses a standard statistical measure of the distribution of wave heights [59, p. 277]. The difference between the heights derived from the two methods is very minor.

Significant wave height is an attractive way to characterise the sea surface since, like

wind velocity, it is quantitative but is additionally direct and localised. It is, however, typically difficult to measure as equipment such as wave buoys or gauges need to be deployed and recovered from the sea, and the limitations of these instruments mean that they may not be able to measure the fine structure of capillary waves on the surface.

2.2.4.3 Sea state

Sea state is a description of the sea surface on both qualitative and quantitative scales, with benefits to both approaches. It is often determined by observing what sea features are visible and/or by visual estimation of SWH. It is also used as a quantitative parameter derived from a measurement of the SWH or of the trio of wind velocity related parameters.

When describing the sea state qualitatively, the main benefit is that it is quick and easy to make an estimate of local conditions which can be recorded as a single value without describing in detail what the surface looks like. The drawback is that since it is qualitative, it is to some degree subjective, and can be difficult to estimate consistently. When instead described quantitatively, such as by measuring SWH, a scale can then be used to relate this to what surface features are expected to be seen in a convenient way.

Sea states are described with scales, namely either the Douglas or the World Meteorological Organisation (WMO) scale. These have been subject to various revisions and so when considering historical measurements quoting a particular scale it is necessary to be aware of the contemporary definition of the scale. Sea clutter research typically uses the Douglas scale, where the most current version is reproduced in Table 2.2 from Rosenberg and Watts [13, p. 4].

Some noted inconsistencies in the literature on sea states:

- In Ward et al. [49, p. 20] (published 2006) the Douglas scale is incomplete and does not match with that in Rosenberg and Watts [13].
- The Douglas scale presented in Ward et al. [49] instead matches the WMO scale presented in Rosenberg and Watts [13].
- The Douglas scale presented in Nathanson [21, p. 270] (published 1991) which is referenced by Ward et al. [49, p. 20] consequently does not match the the scale presented in Rosenberg and Watts [13].
- The Douglas scale in Nathanson [21] matches an older definition in Owens [68, p. 723] (published 1982), and interestingly the WMO scale definition in the same book matches well with the Douglas scale presented by Rosenberg and Watts [13].

SS	Description	$H_{1/3}$ [m]	v_w [m s^{-1}]	Fetch [km]	Duration [h]
0	Glassy	-	0	-	-
1	Calm	0.0 to 0.1	0 to 3	-	-
2	Smooth	0.1 to 0.5	3 to 6	50	5
3	Slight	0.5 to 1.25	6 to 7.5	120	20
4	Moderate	1.25 to 2.5	7.5 to 10	150	23
5	Rough	2.5 to 4.0	10 to 12.5	200	25
6	Very rough	4.0 to 6.0	12.5 to 17	300	27
7	High	6.0 to 9.0	17 to 25	500	30
8	Very high	9.0 to 14.0	>25	-	-
9	Phenomenal	14.0+	$\gg$25	-	-

Table 2.2: Douglas sea state scale as shown in Rosenberg and Watts [13, page 4].

The Beaufort scale is often used for estimating wind conditions from observations of the environment, and so can be used to relate sea state to wind speed. It is however not generally used for sea scattering research, but is shown in Fig. 2.12 to further illustrate the scale of sea conditions.

The descriptions of sea state and its links to wind velocity presented here are for open and deep water. For littoral (or near-shore) waves this is less well defined. Due to shoaling the SWH and thus the sea state can be said to increase in this region, compared to what might be observed in open water. This would however be an approximation, as some aspects e.g. the shape of littoral waves are not necessarily the same as those in deep water.

2.2.5 Simulating sea surfaces

Another way to characterise the sea is in terms of the power spectrum of the water wave frequencies, obtained by Fourier analysis of a wave height time series. The power spectrum can then be used to reconstruct the sea surface in a simulation. These models are used by wave tanks to generate physically realistic sea surfaces, and can also be used to simulate the interaction of EM radiation with the sea surface to model radar sea clutter. Numerous functions have been fitted to measured power spectra to create empirical models parameterised in terms of other observed variables such as wind speed. This subsection shows some examples from the literature as a brief overview.

2.2.5.1 Pierson-Moskowitz spectrum

The Pierson-Moskowitz (PM) spectrum is commonly mentioned in the literature and is one of the most basic models, formulated assuming a fully developed sea [59, p. 285] [70]. The spectrum is represented by the function:

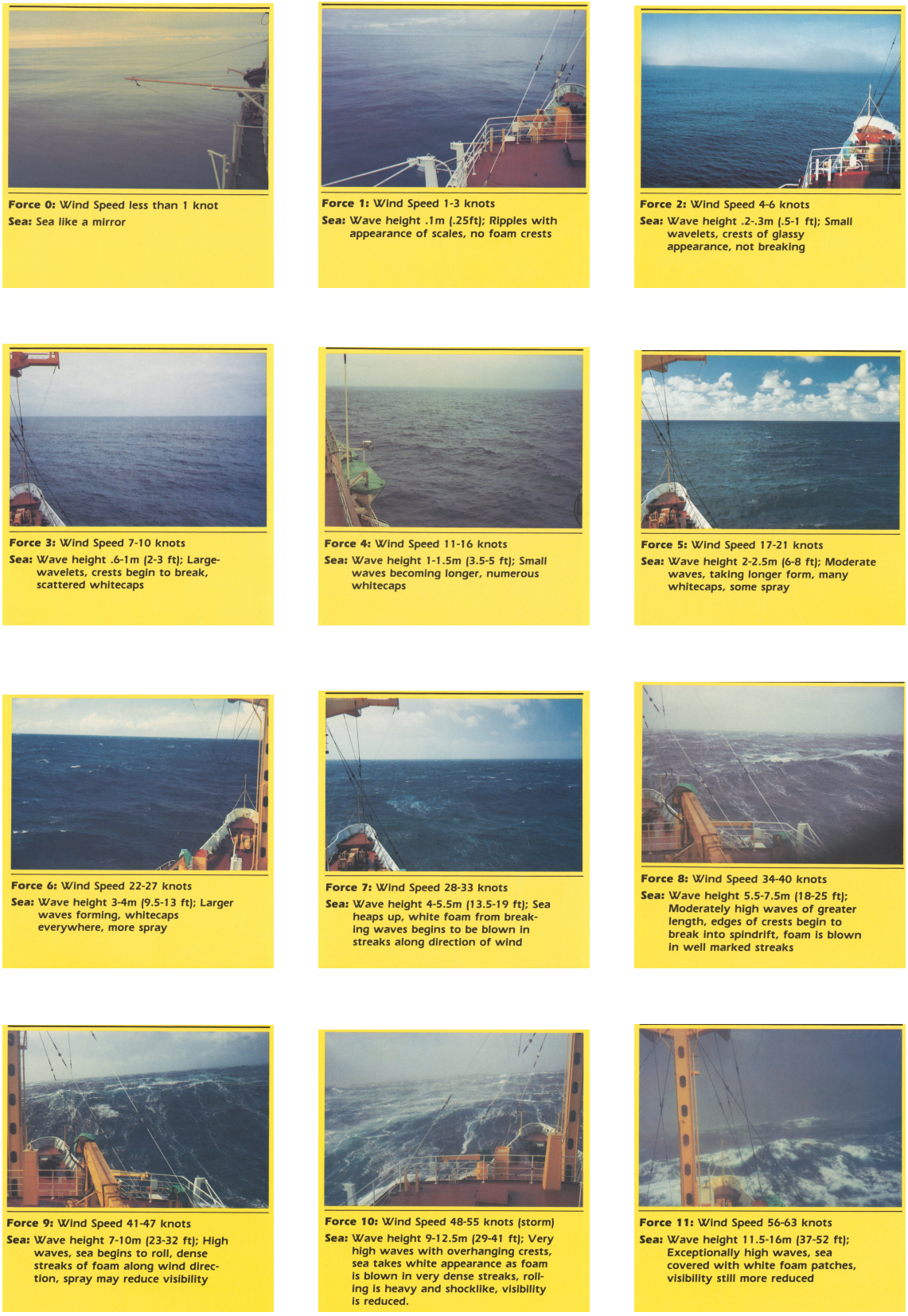

Figure 2.12: The Beaufort wind scale. Adapted from the National Oceanic and Atmospheric Administration [69].

$$S_{\mathrm{PM}}(\omega, U_{19.5}) = \frac{\alpha g^2}{\omega^5} \exp\left[-\beta \left(\frac{\omega_0}{\omega} \right)^4 \right] \tag{2.67}$$

Where the parameters are defined for this section only as:

- $S_{PM}(\omega, U_{19.5})$: the PM spectrum function [$\mathrm{m^2\,s\,rad^{-1}}$].
- ω: water wave angular frequency [$\mathrm{rad\,s^{-1}}$].
- g: gravitational acceleration, 9.81 $\mathrm{m\,s^{-2}}$.
- α: fitting parameter for intensity of value 8.1×10^{-3} [unitless].
- β: fitting parameter for shape of value 0.74 [unitless].
- ω_0: is a frequency parameter equal to $g/U_{19.5}$ [$\mathrm{s^{-1}}$].
- $U_{19.5}$: is the wind speed at an anemometer height of 19.5 m.

2.2.5.2 JONSWAP spectrum

The formulation of the PM spectrum assumes a fully-developed sea and that there are no wave-wave interactions. This is in general unrealistic, thus other spectra have been developed such as the Joint North Sea Wave Observation Project (JONSWAP) spectrum [65]. It was determined that the sea is never fully-developed, with the spectrum continuing to change through wave-wave interactions. They thus modified the PM spectrum:

$$S_{\mathrm{J}}(\omega, U_{10}, F) = \frac{\alpha g^2}{\omega^5} \exp\left[-\frac{5}{4} \left(\frac{\omega_p}{\omega} \right)^4 \right] \gamma^r \tag{2.68}$$

$$r(\omega, U_{10}, F) = \exp\left[-\frac{(\omega - \omega_p)^2}{2\sigma_J^2 \omega_p^2} \right] \tag{2.69}$$

where the constants are defined in this section only as:

$$\alpha(U_{10}, F) = 0.076 \left(\frac{U_{10}^2}{Fg} \right)^{0.22} \tag{2.70}$$

$$\omega_p(U_{10}, F) = 22 \left(\frac{g^2}{U_{10} F} \right)^{1/3} \tag{2.71}$$

$$\gamma = 3.3 \tag{2.72}$$

$$\sigma_J(\omega, \omega_p) = \begin{cases} 0.07 & \omega \leq \omega_p \\ 0.09 & \omega > \omega_p \end{cases} \tag{2.73}$$

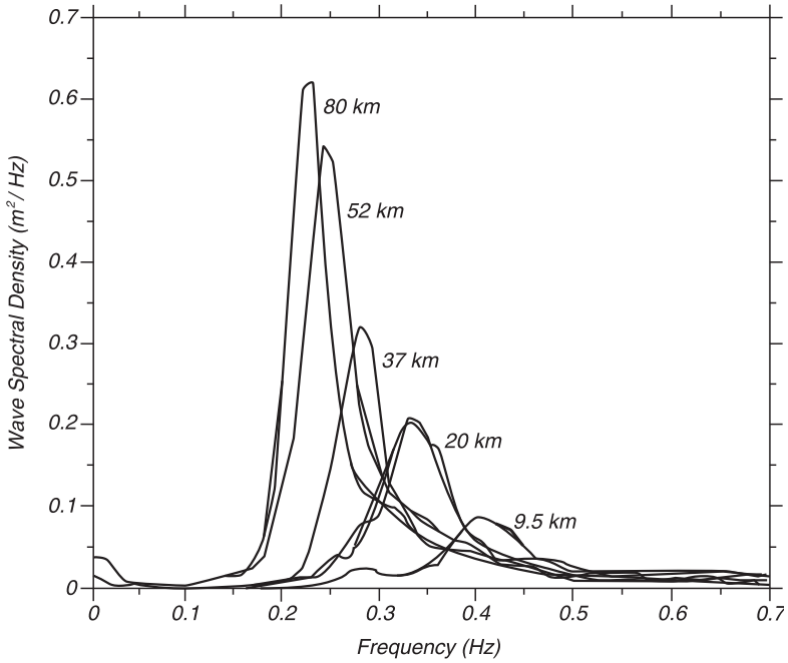

Figure 2.13: JONSWAP spectrum fitted to data, reproduced from Stewart [59, p. 287], as an adaptation from Hasselmann [65]. Note that this spectrum is given as a function of frequency rather than the angular frequency, as was the case in the original definition.

and where these parameters are defined for this section only as:

- $S_J(\omega)$: the JONSWAP spectrum [$\mathrm{m^2\,s\,rad^{-1}}$].
- ω: the water wave frequency [$\mathrm{rad\,s^{-1}}$].
- F: the fetch [m].
- $\omega_p(U_{10}, F)$: the peak frequency of the wave spectrum [$\mathrm{rad\,s^{-1}}$].
- $\sigma_J(\omega, \omega_p)$: the FWHM of the spectrum peak [$\mathrm{rad\,s^{-1}}$].
- U_{10}: the wind speed at a height of 10 m.

as defined in Hasselmann [65].

2.2.5.3 Bretschneider spectrum

Another model is the Bretschneider spectrum (also derived for fully developed seas), where this was formulated with the aim of incorporating only the direct wave properties of $H_{1/3}$ and wave spectrum peak frequency ω_p independent of wind speed, fetch or duration:

$$S_B(\omega, H_{1/3}, \omega_p) = \frac{5}{16} {H_{1/3}}^2 \frac{\omega_p^4}{\omega^5} \exp\left[-\frac{5}{4}\left(\frac{\omega_p}{\omega}\right)^4 \right] \tag{2.74}$$

where the other parameters are defined for this section only as:

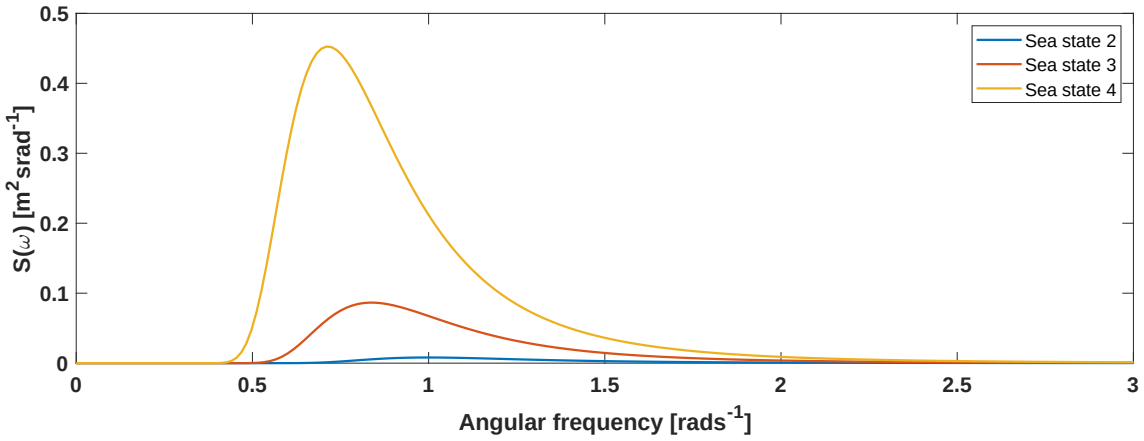

Figure 2.14: The Bretschneider spectrum as a function of sea state [72].

- $S_B(\omega, H_{1/3}, \omega_p)$: the Bretschneider spectrum [$\mathrm{m^2\,s\,rad^{-1}}$].
- ω: the water wave frequency [$\mathrm{rad\,s^{-1}}$].

The Bretschneider spectrum is fitted to data by inputting these parameters and varying the constants. This form of the spectrum is matched to the PM spectrum [71], where a plot of the Bretschneider spectrum as a function of sea state is shown in Fig. 2.14.

2.2.5.4 Spreading functions

The spectra shown above can be used to simulate a sea surface by utilising a suitable angular spreading function to generate a 2D surface from a 1D spectrum [73][74][75]. This is computed:

$$S_{2D}(\omega, \omega_p, \theta_w) = S(\omega)D(\omega, \omega_p, \theta_w) \tag{2.75}$$

where $D(\omega, \omega_p, \theta)$ is a spreading function, such as the Mitsayasu [74] function:

$$D(\omega, \omega_p, \theta_w) = \frac{\Gamma(s+1)}{2\sqrt{\pi}\Gamma(s+0.5)}\left[\cos^2\left(\frac{\theta_w - \theta_0}{2}\right)\right]^s \tag{2.76}$$

$$s(\omega, \omega_p) = \begin{cases} 9.77(\omega/\omega_p)^{-2.5} & \omega \leq \omega_p \\ 6.97(\omega/\omega_p)^5 & \omega > \omega_p \end{cases} \tag{2.77}$$

where the parameters are defined for this section only as:

- $S_{2D}(\omega, \omega_p, \theta_w)$: the 2D wave surface [m].
- $S(\omega)$: the wave spectrum [$\mathrm{m^2\,s\,rad^{-1}}$].
- ω: the water wave frequency [$\mathrm{rad\,s^{-1}}$].

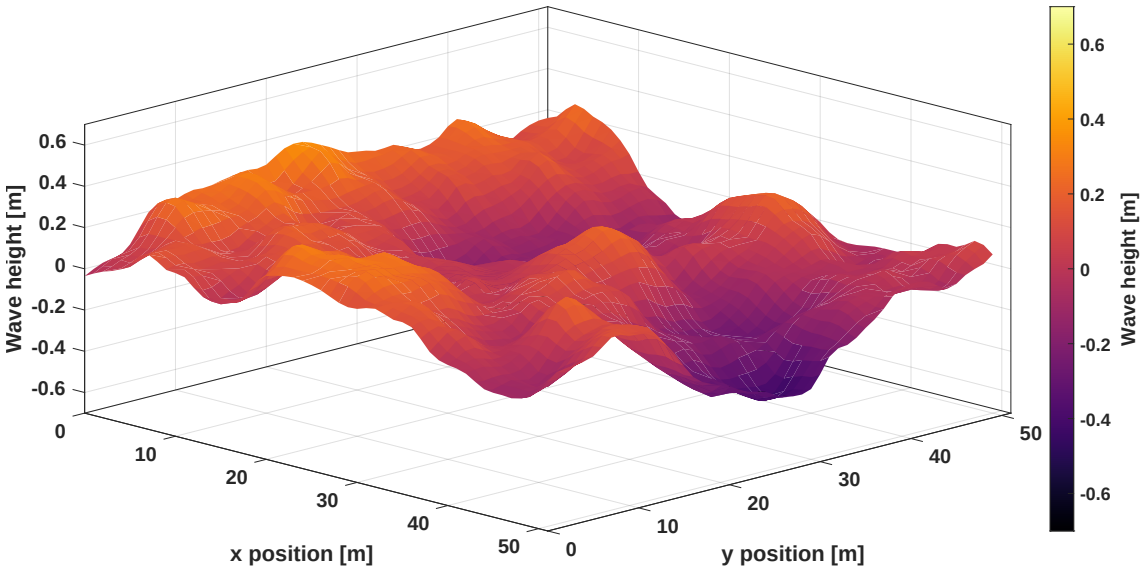

Figure 2.15: A sea surface simulated using the WAFO toolbox with the Bretschneider spectrum and the Mitsayasu spreading function [72].

- θ_w: the water wave direction [rad].
- Γ: the gamma function [unitless].
- θ_0: the wind direction [rad].
- ω_p: the peak frequency of the water wave spectrum [rad s^{-1}].

MATLAB® toolboxes are available which simulate sea surfaces using these methods such as WAFO [76] and WafoL [77], where an example of the surfaces which can be generated using WAFO are shown in Fig. 2.15.

This concludes this section covering information regarding the sea, where the following section will use this context to review sea clutter amplitude statistics up to Ka-band frequencies.

2.3 Sea clutter amplitude statistics up to Ka-band

This section outlines how the sea surface scatters EM radiation to produce the characteristic effects detected with radar at microwave and Ka-band frequencies. It also shows the effect of different environmental and radar system parameters on the scattering observed, and several models which have been developed to describe empirical results. This discussion is limited to Ka-band and below where the majority of radar sea clutter research has been performed to date. The following chapter then discusses the available research on sea clutter amplitude statistics above Ka-band, where these are the frequencies most relevant to this thesis.

Sea clutter is also often characterised in terms of its Doppler statistics, however this aspect of sea clutter is not covered here since this is not the focus of the analysis in this thesis, but is detailed in several texts in the field including Ward et al. [49] and Rosenberg and Watts [13].

2.3.1 Motivation for the study of sea clutter

The utility of studying sea clutter is explained well in Ward et al. [49, p. 7] and similarly in Rosenberg and Watts [13, p. 6], where some elements are paraphrased here. In essence, measurements of radar sea clutter can be used to both produce empirical models and to inform the development of physical models, where these describe sea clutter in different conditions. These models are invaluable in the development of radars operating at sea, and are used for the following purposes:

- **Performance definition**: the modelling of what performance is needed to achieve a sensing goal under different conditions, where this can be used to define the performance of a new system or upgrades to an existing one.[7]
- **System performance modelling**: the analysis of how well a radar with a given specification will perform under different conditions.[8]
- **Algorithm development**: the production and assessment of the performance of processing designed e.g. for target detection, where models can be used to produce synthetic data.
- **Performance assessment**: the analysis of how well the system works by comparison to expected performance in different conditions.
- **Operator training**: the use of simulations of radar behaviour in different conditions for the training of end users of the radar systems.

2.3.2 Describing sea clutter

The description and features of sea clutter which are of interest in radar development are well outlined in Ward et al. [49, p. 17] and Rosenberg and Watts [13, p. 5], and are paraphrased here. Sea clutter signals on a fine scale consist of discrete 'spike' events in space and time. As such, sea clutter analysis may consider both:

- the distributed returns from a *particular area* (either from averaging returns from such an area or from large beam footprints) termed as referring to the *bulk features* in this thesis,

[7] Asking the question: 'I want to detect that, what performance do I need?'.
[8] Asking the question: 'I have this system, what performance do I get?'.

Feature	Descriptor
Backscatter intensity/amplitude	Mean σ^0
Backscatter intensity variation	Intensity distribution in terms of σ^0
Amplitude variation in time	Temporal correlation
Amplitude variation with position	Spatial correlation

Table 2.3: Sea clutter bulk features and descriptors.

- the discrete amplitude *signal peaks* themselves, referred to as *sea spikes* or *clutter spikes* in the general literature, defined as large amplitude excursions above the mean level [13, p. 42].

The bulk features and descriptors of sea clutter are summarised in Table 2.3. Clutter spike signals are given special consideration since they cause the most trouble for radar sensing as they may appear target-like to a detector. The degree to which the clutter spikes are evident, and the appropriate statistical treatment, depends on the available resolution of the radar system and the environmental conditions. Sea spikes may be seen to correspond to individual wave features if the sensor resolution is high enough, where three distinct scattering mechanisms have been identified and are explained in the following subsection.

Clutter spikes are usually identified by the level of the signal (σ^0) and its duration, and also by polarisation dependence as explained in the following section. As clutter spikes constitute the backscatter from the sea, their behaviour then naturally determines the bulk features which encapsulate their collective behaviour.

2.3.3 Scattering mechanisms and clutter spikes

Three primary scattering mechanisms have been identified as the cause of microwave sea clutter, each contributing backscatter returns of a particular type. These scattering types are named Bragg, burst, and whitecap, and are detailed in the following subsections.

2.3.3.1 Bragg scattering

Bragg scattering is caused by the constructive interference of reflected EM waves from water waves of twice the wavelength, similar to x-ray diffraction in crystals from which it inherits its name [47]. The condition for this scattering is derived using the diagram in Fig. 2.16. Constructive interference of the EM waves is achieved when the path difference between the rays from the radar to the two scatterers is an integer number of half wavelengths of the radar emission λ_r. The spacing between the two scatterers will

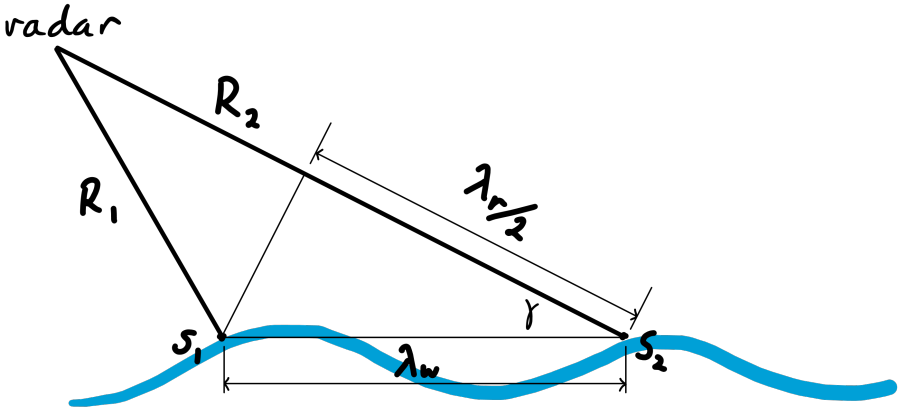

Figure 2.16: Diagram showing the condition for constructive interference of radiation from two scattering centres separated by the water wavelength. Adapted from [78].

be the water wavelength λ_w, and then taking the integer number as one, the condition for constructive interference is derived as shown in Eq. 2.78:

$$\lambda_w = \frac{\lambda_r}{2} \sec(\gamma) \tag{2.78}$$

which rearranged for λ_r is:

$$\lambda_r = 2\lambda_w \cos(\gamma) \tag{2.79}$$

where Eq. 2.79 is the commonly stated form of the equation [78], [79, p. 842]. It should be noted that the equation for Bragg resonance in x-ray diffraction instead has a dependence on $\sin(\gamma)$, as the coherent scattering originates from the crystal lattice layer beneath the surface, whereas for water waves only the surface is considered. Equivalently, the water's surface functions as a Littrow configuration diffraction grating [80].

The graph in Fig. 2.17 shows the required water wavelength needed for the Bragg resonance condition as a function of radar frequency, f_r. The wavelength limits for gravity and capillary waves are also shown, indicating that Bragg resonance from gravity waves only occurs for radars with carrier frequencies of ~4 GHz and below, whilst capillary waves producing Bragg scattering are well documented at X-band [49, pp. 29, 35, 37]. Given the spectral density of capillary waves falls beyond approximately 7 mm [58, p. 11543], this implies a limit to Bragg scattering from capillary waves of ~22 GHz after which point the intensity of backscatter would be expected to decrease.

Bragg scattering is illustrated in Figures 2.18 and 2.19, which were collected with a radar with the following specifications:

- Carrier frequency of 9.75 GHz (X-band).

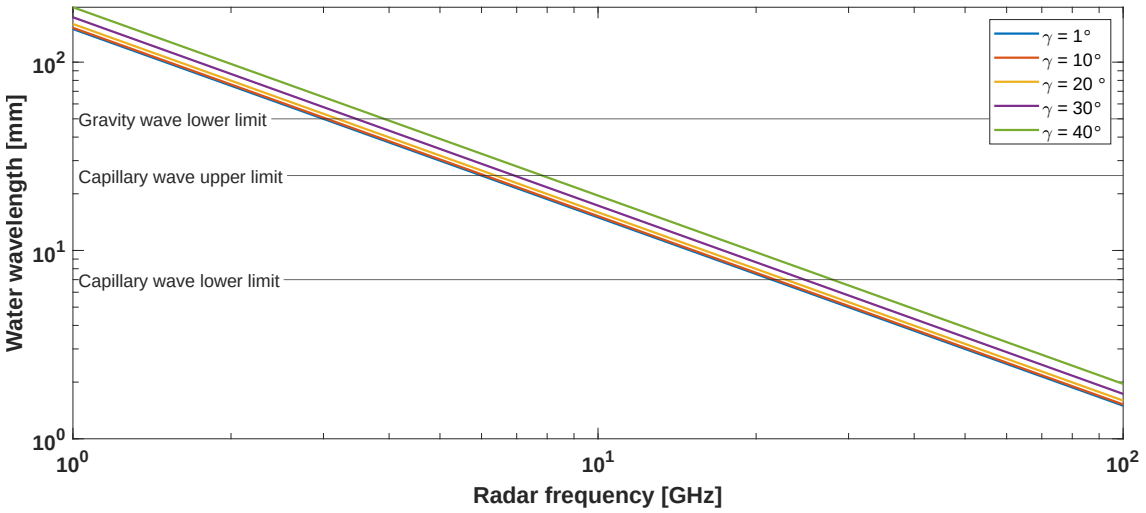

Figure 2.17: Graph of Bragg resonance water wavelength versus radar carrier frequency as determined by Eq. 2.79.

- A pulse bandwidth of 100 MHz, producing a range resolution of ~2 m.
- A transmitter pulse rate of 1 kHz alternating between V and H.
- Two receiver channels for simultaneous reception in V and H, such that each linear polarisation combination of VV, HH, VH, HV is recorded at a frequency of 500 Hz.

Bragg scattering is typically identified as having the following features, displayed in Figures 2.18 and 2.19:

- The NRCS is greater in VV than in HH, although Bragg scattering is generally observed in both polarisations [49, pp. 36–27].
- The signals have a rapidly varying, noise-like character in time series data [49, pp. 36–27] which appears more smoothly varying in range-time-intensity (RTI) plots in comparison to burst or whitecap scattering.
- The duration of Bragg scattering can be many seconds [49, p. 37].
- Temporal correlation[9] times are ~10 ms [81].
- The backscatter originates from many scattering centres in a resolution cell, producing speckle statistics [49, p. 36].
- Bragg scattering is of a lower amplitude than burst or whitecap, where for example a threshold of five standard deviations above the mean distinguishes between Bragg scattering and true clutter spikes [82, p. 4558].

[9] Autocorrelation of the signal with respect to time.

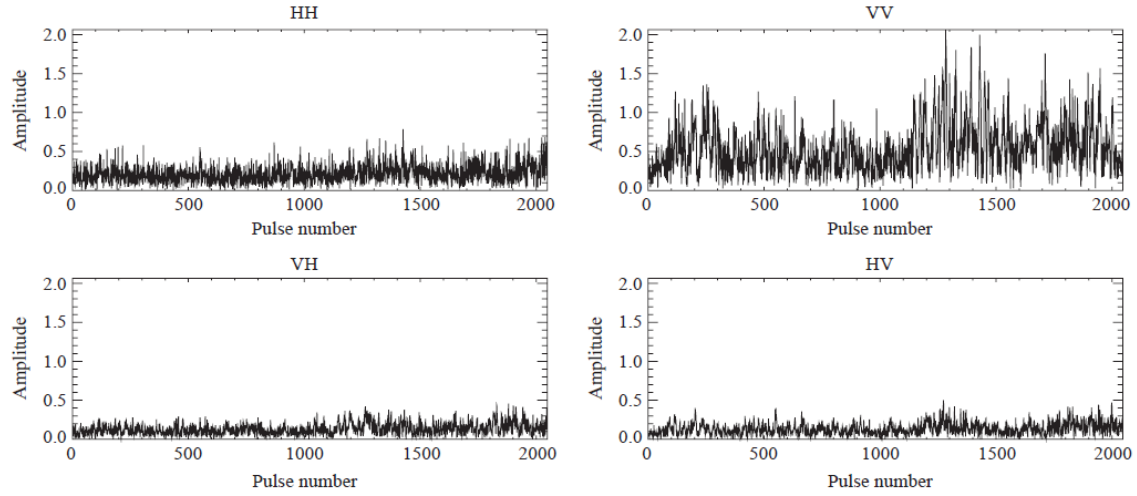

Figure 2.18: Time series data of Bragg scattering at X-band in different linear polarisations observed pulse-to-pulse over a time of 4 s. Bragg return is seen to be greatest in VV. The two cross polar channels are very similar as would be expected due to reciprocity. In general, the signal appears as noise-like. Adapted from Ward et al. [49, p. 37].

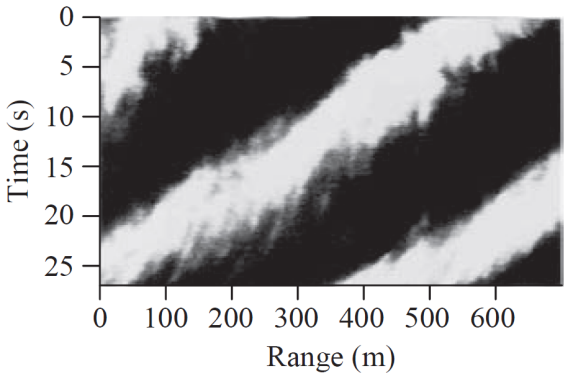

Figure 2.19: RTI of sea swell showing smoothly modulated Bragg scattering at X-band. Adapted from Ward et al. [49, p. 29].

The smooth modulation from Bragg scattering together with the other two spike mechanisms produce the non-Gaussian amplitude statistics associated with sea clutter when analysed in bulk. The non-Gaussian statistics are considered ‘spiky’ due to the occasional large amplitude excursions they describe, and due to this the backscatter signals due to Bragg resonance are often called Bragg spikes, despite in fact not being spiky [49, p. 34].

2.3.3.2 Burst scattering

In burst scattering, rays are forward scattered from a patch of sea in front of a wave and then focussed back to the radar by the curved front face of the approaching wave.

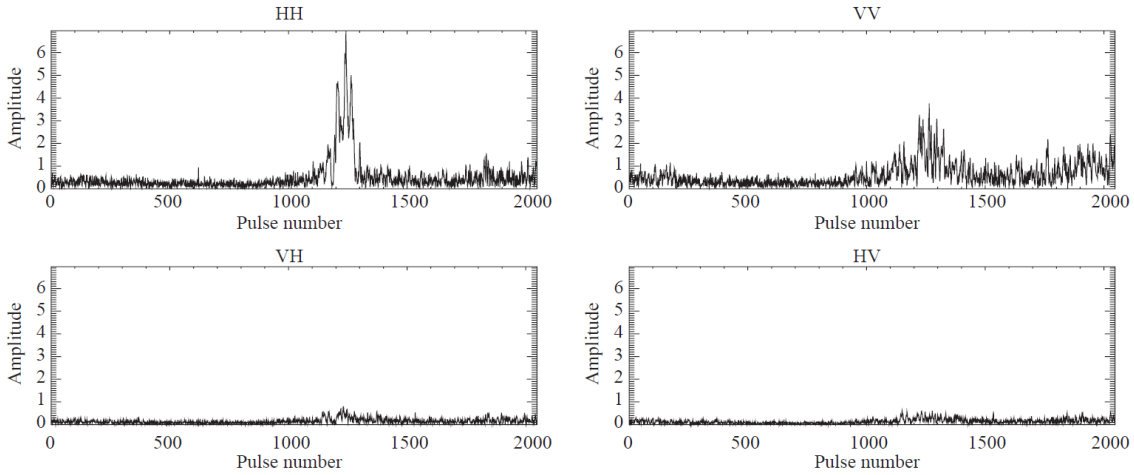

Figure 2.20: Time series data of spike scattering at X-band in different linear polarisations observed pulse-to-pulse over a period of 4 s. Spike returns are overwhelmingly stronger in HH, where the returns seen here in VV are from Bragg scatter. Adapted from Ward et al. [49, p. 39].

This multipath effect enhances HH backscatter intensity. This effect is not seen in VV due to the suppression of forward scattering by the Brewster effect [49, p. 36] [83, pp. 2457–2459]. This is most pronounced when the wave is steep, and generally requires waves to be steepening towards the radar. An example of burst scattering is shown in Fig. 2.20, where it is typically identified by the following features:

- Burst scattering is mainly only observed in HH due to the suppression of the multipath enhancement effect in VV.
- Discrete, high amplitude spikes in time series data which fluctuate less than Bragg and whitecap scattering.
- Burst spikes have a typical duration of <200 ms [49, p. 36].
- Burst scattering has relatively long temporal correlation times of >80 ms [81].

2.3.3.3 Whitecap scattering

Whitecap scattering is caused by the roughened, foamy surfaces of the breaking waves from which it takes its name. This results in diffuse and intense backscatter as shown in the time series data of whitecap scattering in Fig. 2.21. Whitecap scattering is identified by the following features:

- The σ^0 is approximately equal in HH and VV due to the diffuse nature of the scattering, and is also sometimes detectable at a lower level in VH and HV during high copolar scattering [49, p. 39].

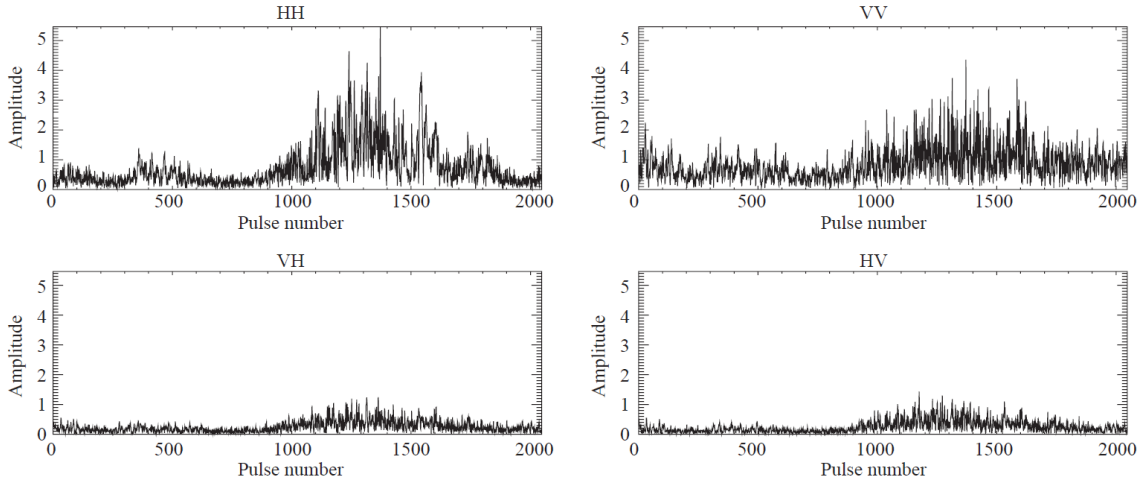

Figure 2.21: Time series data of whitecap scattering at X-band in different linear polarisations observed pulse-to-pulse over a period of 4 s. Returns are approximately equal for both HH and VV, and are of a noise-like character. Adapted from Ward et al. [49, p. 41].

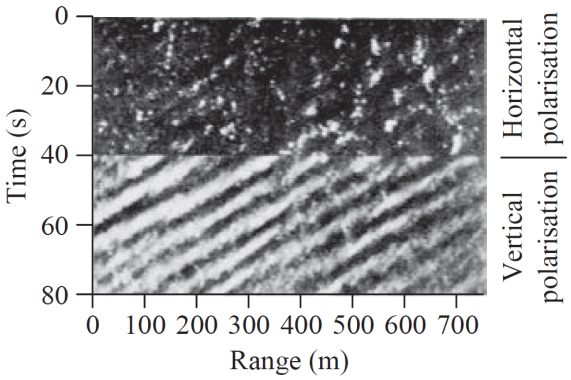

Figure 2.22: RTI plots from X-band radar, collected at SS 3, 30° to upwind, $\gamma = 1°$. Burst and whitecap scattering are visible as the shorter and longer duration patches of signal in HH, with an undulating pattern caused by Bragg scattering visible in VV. Adapted from Ward et al. [49, p. 29].

- The signal is more noise-like than burst spikes, and higher amplitude than Bragg scattering [49, p. 38].
- Whitecap spikes last on the order of 1 s [49, p. 34].
- Very short temporal correlation times of ~5 ms [81].

An RTI plot featuring both burst and whitecap scattering is shown in Fig. 2.22, also showing the relative insensitivity of HH to Bragg scattering. A comparison of the time series signatures of the three scattering types is shown in Fig. 2.23.

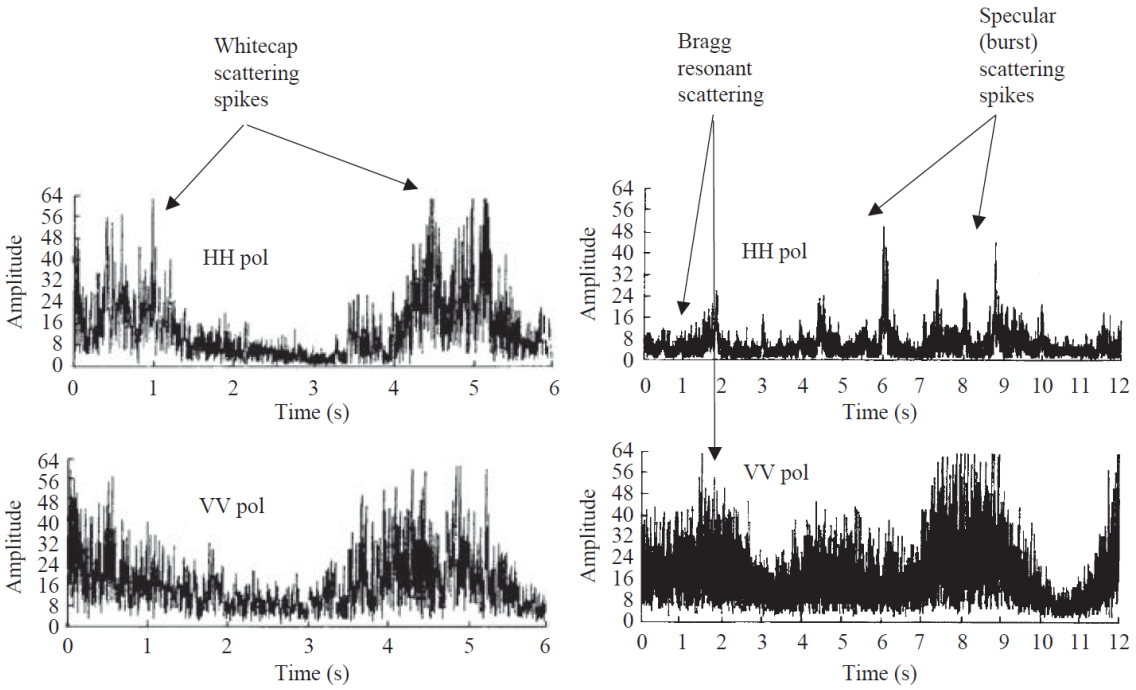

Figure 2.23: X-band time series data of SS 3, showing the three different scattering types and their relative intensities in both HH and VV. From Ward et al. [49, p. 35].

2.3.4 Factors affecting mean NRCS

The following subsection discusses the variation of the mean σ^0 as a function of two sets of parameters:

- **Radar parameters**: the radar carrier frequency, grazing angle, and polarisation.
- **Environmental parameters**: the sea state SS, wave direction ψ, wind speed v_w, and wind direction ξ.

The following trends of σ^0 are presented mostly as shown in Rosenberg and Watts [13], where they draw the distinction that many of the measurements these trends are based on did not specifically characterise the effects of anomalous propagation and multipath scattering on the backscatter. Thus the trends are presented as σ^0 combined with ${F_p}^4$, where F_p is the one-way propagation factor. It should be noted that this distinction is not always made as explicitly in the literature for similar plots [49, p. 22] [13, p. 18]. The work covered in this thesis does not include measurements of σ^0 separate from the propagation factor, so in general these are measurements of $\sigma^0 {F_p}^4$ but will be referred to as measurements of σ^0.

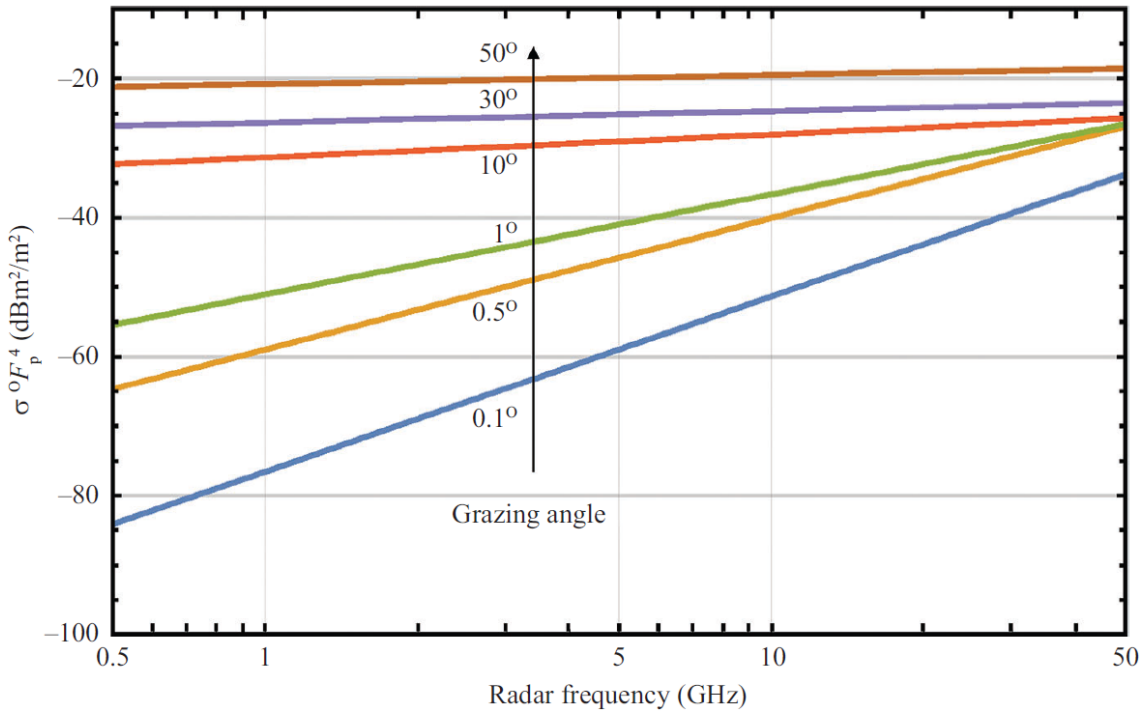

Figure 2.24: The variation of mean with radar carrier frequency for different grazing angles. From Rosenberg and Watts [13, p. 20], after the NRL model. Note that the NRL model as published by Gregers-Hansen et al. [84] uses data from Nathanson [21, pp. 275–278], implying that results beyond 35 GHz are extrapolated.

2.3.4.1 Radar carrier frequency

Figure 2.24 shows the trend of σ^0 as a function of radar carrier frequency at different grazing angles. As seen from graph, σ^0 is seen to increase as a function of carrier frequency, where this effect becomes less pronounced at higher grazing angles. This assertion is mentioned elsewhere by Wetzel [36, pp. 15.11–15.12], who writes that 'the frequency dependence of sea clutter at intermediate grazing angles is weak at microwave frequencies from L to K band'.

These curves are produced by the Naval Research Laboratory (NRL) model [84], based from data from Nathanson's tables [21, pp. 275–278]. The data from Nathanson does not distinguish between Ka-band and W-band results [21, p. 279] due to no discernible trend in the limited number of W-band results published at the time the book was written. It is expected however that there would be some distinction with increasing frequency. With that in mind, it should then be noted that the NRL model is likely only defined up to Ka-band, and Fig. 2.24 reproduced from Rosenberg and Watts [13, p. 20] showing a frequency axis up to 50 GHz is then an extrapolation of this model.

2.3.4.2 Grazing angle

Figure 2.25 shows the variation of σ^0 with grazing angle for both HH and VV. This trend divides into three regimes:

- **0° to 10°** the LGA or interference region,
- **10° to 45°** the medium grazing angle or plateau region,
- **45° to 90°** the high grazing angle or specular region.

In the low grazing angle region, EM wave propagation is heavily dependent on multipath effects and wave shadowing plays a major role [13, p. 17], and the sea can be considered to mostly direct energy away from the radar [21, p. 281]. The low grazing angle region is of most interest to the STREAM project since that is the observation geometry of small, surface bound craft.

In the second region, both HH and VV increase approximately linearly with grazing angle. Nathanson [21, p. 282] mentions a fit to this region shown in Eq. 2.80:

$$\sigma^0 = \beta \sin(\gamma) \tag{2.80}$$

Where β is a fitting parameter. This is known as the constant gamma model in the literature (as gamma is used as the fitting parameter). Nathanson suggests this is a good fit to data for $\gamma = 3°$ to $60°$, and that additionally Barton [85] suggests the lower grazing angle limit can be calculated by Eq. 2.81:

$$\gamma_c = \frac{\lambda_r}{4\pi\sigma_h} \tag{2.81}$$

Where γ_c is the critical grazing angle below which multipath and shadowing begins to affect σ^0, and σ_h is the root mean square (RMS) wave height. NRCS for HH is less than VV in general up to approximately the start of the third region at 45°.

In the final region, σ^0 for both HH and VV is approximately the same and increases rapidly, and scattering is said to be quasi-specular [49, p. 21] and potentially of very high intensity [21, p. 281].

2.3.4.3 Polarisation

Polarisation makes a profound difference to collected radar sea clutter data, as seen in Figures 2.18, 2.19, 2.20, 2.21, 2.22, and 2.23. As shown in Fig. 2.25, mean σ^0 at low and medium grazing angles VV tends to be significantly greater than HH. Since Bragg scattering is greater in VV, this suggests that Bragg scattering is the dominant mechanism in this regime, which is also asserted by Watts et al. [87] when discussing

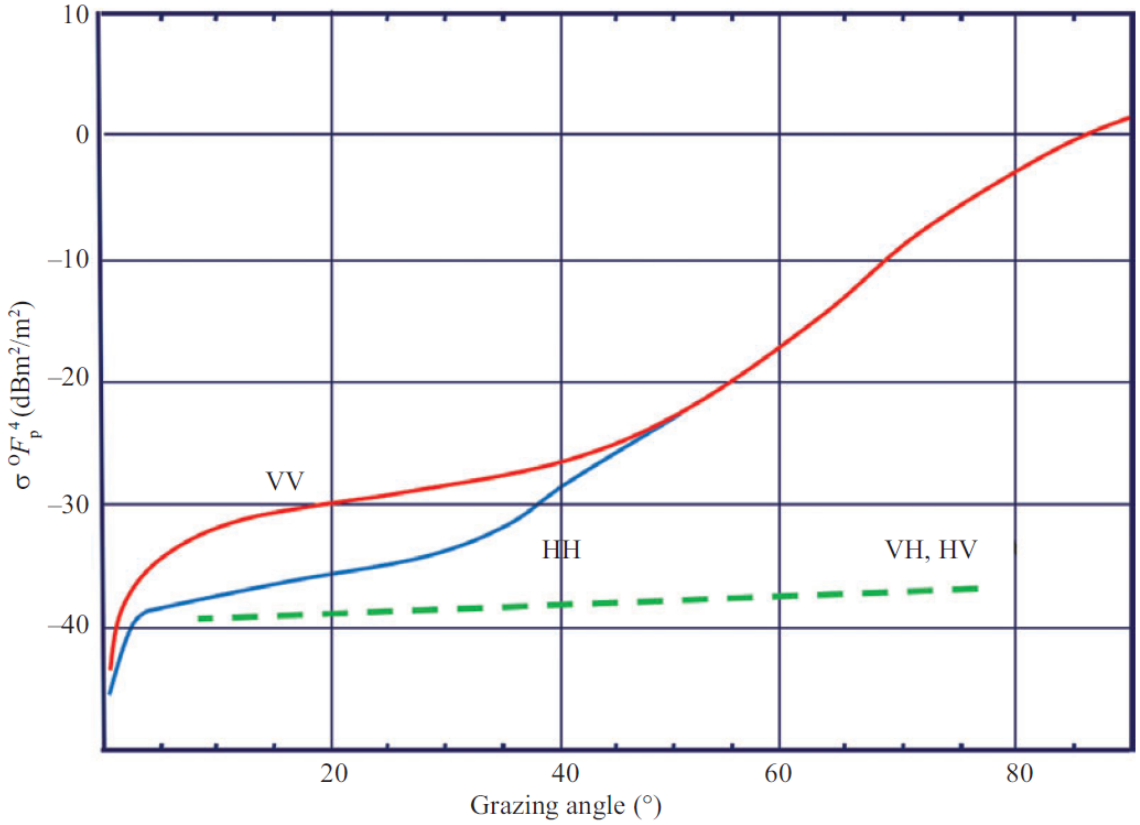

Figure 2.25: 'Mean backscatter variation with grazing angle at a wind speed of 7.7 m s^{-1}' for a radar at X-band, adapted from [86].

medium grazing angles, where they write that at X-band backscatter in this region comes mostly from resonant scattering from small ripples, i.e. Bragg scattering.

It has been noted experimentally that in certain conditions HH returns exceed VV [88]–[90], which cannot be caused by the Bragg mechanism, and is likely due to burst scattering since this is suppressed in VV thus creating the observed disparity. Additionally, Wetzel [36, p. 15.11] notes that the gap between HH and VV returns at low grazing angles decreases with increasing carrier frequency, and that some data at X-band has shown HH exceeding VV at γ<2° in 'moderate to strong wind speeds'.

2.3.4.4 Sea state, wind speed, and wind direction

Rosenberg and Watts [13, p. 18] provide Fig. 2.26, and state that the power law model in Eq. 2.82 is often used to estimate the fully developed sea state from the wind speed at a height of 10 m.

$$v_w = 3.18SS^{0.8} \tag{2.82}$$

In general it can be seen that the backscatter increases with wind speed and sea state. It

is expected that Bragg scattering dominates at low sea states, whilst burst and whitecap scattering will become dominant at higher sea states as larger waves and breaking waves appear, although the effect that burst scattering has on the mean σ^0 appears to be subordinate to the effect of whitecap scattering [49, p. 36]. With regards to a direct relationship between sea state and sea clutter, Rosenberg and Watts [13, p. 17] note that even though the sea state is usually used to describe conditions, its relation to backscatter is not necessarily straightforward. To illustrate this, they describe the case of strong local wind beginning to blow over the sea, producing a very rough surface but only small wave heights. This will likely produce strong backscatter, since a radar can be sensitive to the small scale roughness of the surface which is not necessarily described by sea state. Ward et al. [49, p. 22] also make this point, adding that a large swell with no wind will produce low backscatter intensity. Despite this ambiguity, sea state is generally used as an input parameter in empirical models of sea clutter given its ubiquity in describing the sea.

The dependence of NRCS on wind direction ξ at X-band is shown in Fig. 2.27 for a variety of grazing angles. The radar line of sight relative to the wind direction is defined as being 0° when looking upwind, where from the plot it can be seen that in general the σ^0 is greatest in this direction. In the low grazing angle regime, the mean σ^0 tends to be lowest downwind, whereas for medium grazing angle and above it is lowest crosswind [13, p. 18]. Wind direction is generally used as a proxy for wave propagation direction, ψ, however this of course is not necessarily the case in nature, where results in the case of non-matching directions will produce some averaging of the scattering due to either the prevailing wave shapes or the wind induced ripples. For simplicity, the discussion here will only consider the case of matching wave and wind directions. The radar line of sight is similarly defined relative to the wave direction as 0° towards the direction of approach. Nathanson [21, p. 284] states that the variation of mean σ^0 is explained by the angle of the wave slopes being steepest upwind, and that the variation cannot be detected at very low and very high grazing angles, and is reduced for high sea states. Additionally, due to burst scattering, HH returns are expected to be higher than VV for higher sea states when looking in the direction of the origin of breaking waves (often upwind) which has been observed experimentally [90].

2.3.5 Factors affecting NRCS distribution

As well as affecting the mean, the *distribution* of σ^0 is also influenced by the factors above. In general, parameters which increase the degree of burst or whitecap scattering will produce more non-Gaussian statistics, considered to be spiky. To summarise these

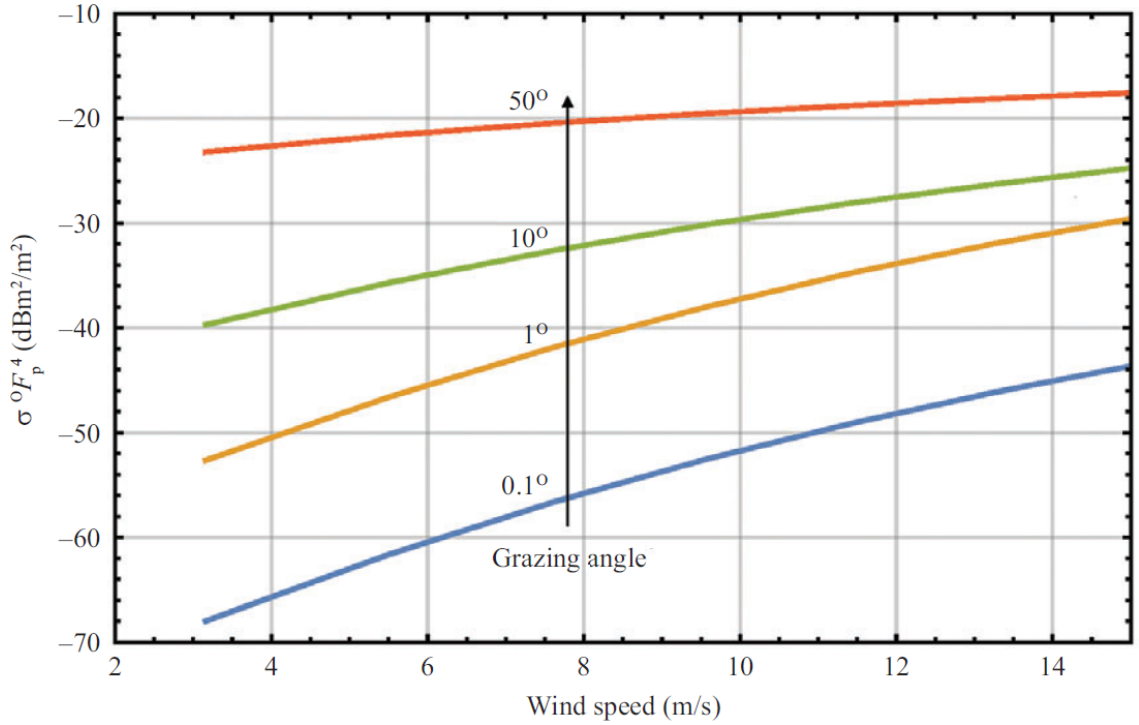

Figure 2.26: Graph showing the variation of mean σ^0 with wind speed. Data collected at X-band in VV. From Rosenberg and Watts [13, p. 19].

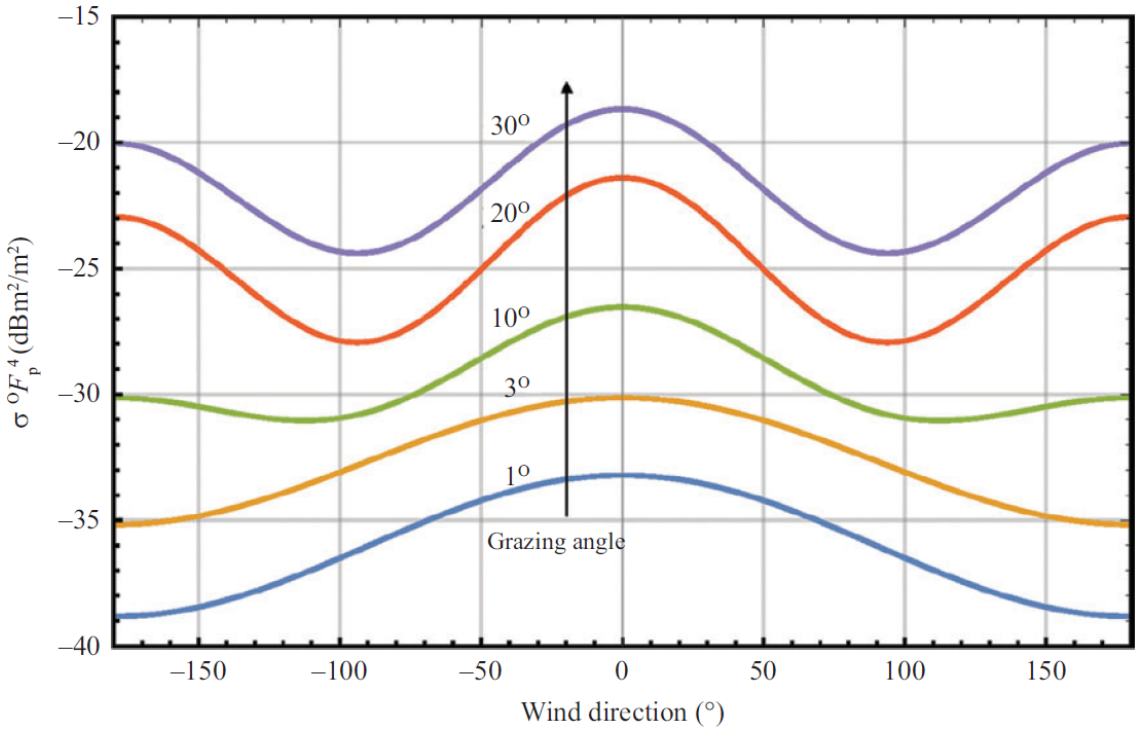

Figure 2.27: Graph showing the variation of mean σ^0 with wind direction. Upwind is defined as 0°. Data collected at X-band in VV for SS 4. From Rosenberg and Watts [13, p. 19].

effects:

- **Sea state:** at higher sea states, more breaking waves will be observed. This will increase spikiness due to whitecap scattering [13, p. 43]. It has also been noted that spikiness is weakly increasing with sea surface roughness for grazing angles of 20° and 40° [87, p. 243]. Ward et al. state however that 'no significant statistical trend has been established for the variations of spikiness with sea state, wind speed or aspect angle relative to wind direction' [49, p. 31], although this may have been true at time of publication, the state of the art has progressed in the intervening 15 years to the statement published in Rosenberg and Watts [13, p. 43].
- **Polarisation:** HH is seen to be spikier than VV [49, p. 31], as burst scattering is overwhelmingly only seen in HH [13, p. 43].
- **Grazing angle:** lower grazing angles produce spikier data, especially in HH [49, p. 31] [87, p. 243] [13, p. 44]. This is interesting to note, since less spiky Bragg scattering is more present at lower grazing angles. The conclusion is that although the impact on the mean σ^0 of burst spikes in this grazing angle range is small, even one spike will lengthen the tail of the distribution.
- **Range resolution:** for a coarse range resolution, many scatterers are present in a single resolution cell. In this case, sea clutter distributions are equivalent to speckle and have Gaussian statistics [49, p. 24], and are modelled acceptably by a Gaussian distribution because of the central limit theorem [13, p. 15], where in effect the scattering has been spatially averaged. A fine range resolution then conversely produces spikier statistics, as individual parts of the wave are resolved in more detail [49, p. 25] [13, pp. 5–6]. This is also supported by empirical results mentioned by Ward et al. [49, p. 31], and also Watts et al. [87, p. 243].
- **Angular resolution:** by analogy with range resolution, it is expected that a coarser angular resolution will produce some degree of spatial averaging, and reduce clutter spikiness, and vice versa.
- **Swell:** sea clutter amplitude spiking is increased by swell, with the largest increase observed in up or down-swell directions [49, p. 31] [87, p. 243].

2.3.6 Empirical models for mean NRCS

The physical models for sea clutter are not fully reliable, and so for the radar design purposes as outlined in Subsection 2.3.1, empirical models are used instead. Models of mean σ^0 are the most mature and have been developed from 'many thousands of

measurements' [13, p. 8]. One of the best resources of compiled measurements are Nathanson's tables [21, pp. 275–278], numerous models having been based on these values. The quirks of this compilation should however be noted: all the results have been averaged for wind/wave direction; no distinction is made between Ka-band and W-band results as explained in Subsection 2.3.4.1; and which sea state scale is being used is not initially clear. To expand on this last point, the scale in Nathanson's tables runs from 0 to 6 and is not explicitly named, whereas the scale printed on page 270 runs from 1 to 8. The latter is identified as an older version of the Douglas sea state scale (omitting the beginning 0) in Owens [68, p. 723]. It would then be reasonable to assume that the scale in the tables is also this older version of the Douglas scale. The tables have been cited as the Douglas sea state scale in Ward et al. [49, p. 20] and match the scale printed there. An inconsistency arises however when comparing this table to the Douglas scale printed in Rosenberg and Watts [13, p. 4], which appears to be the older WMO scale as printed in Owens [68, p. 723] and in Ward et al. [49, p. 20].

Of the numerous empirical models listed in Rosenberg and Watts [13, p. 108], two noteworthy examples will be reproduced here which are both valid in the low grazing angle regime.

2.3.6.1 The GIT model

The Georgia Institute of Technology (GIT) model (developed in 1978 [91]) is unique in that it was developed to predict σ^0 values 1 to 100 GHz. Given that there would naturally have been fewer W-band data of the sea at that time than at lower frequencies, the trust in this upper range is diminished. It is however still the only model specifically defined to this frequency range, and so is included here. Additionally, it is defined up to average wave heights $\bar{H}$ of 3.5 m, grazing angles 0.1° to 10°, all wind/wave directions, and is fitted only to data which did not show signs of anomalous propagation, and thus does not show good agreement with Nathanson's data, particularly at low sea states. The model here is reproduced from Rosenberg and Watts [13, pp. 109–111].

The mean σ^0 in decibels for HH and VV is modelled as the piecewise functions:

$$\sigma^0{}_{\mathrm{HH}} = \begin{cases} 10\log_{10}(\lambda_{\mathrm{r}}\gamma^{0.4}a_{\mathrm{GIT}}b_{\mathrm{GIT}}c_{\mathrm{GIT}}) - 54.089 & 1 \leq f_{\mathrm{r}} < 10 \\ 10\log_{10}(\lambda_{\mathrm{r}}\gamma^{0.547}a_{\mathrm{GIT}}b_{\mathrm{GIT}}c_{\mathrm{GIT}}) - 54.381 & 10 \leq f_{\mathrm{r}} < 100 \end{cases} \tag{2.83}$$

$$\sigma^0{}_{\mathrm{VV}} = \begin{cases} \sigma^0{}_{\mathrm{HH}} - 1.73\ln(\bar{H}+0.015) + 3.76\ln(\lambda_\mathrm{r}) \\ \qquad + 2.46\ln(\gamma+0.0001) + 22.2 & 1 \le f_\mathrm{r} < 3 \\ \sigma^0{}_{\mathrm{HH}} - 1.05\ln(\bar{H}+0.015) + 1.09\ln(\lambda_\mathrm{r}) \\ \qquad + 1.27\ln(\gamma+0.0001) + 9.7 & 3 \le f_\mathrm{r} < 10 \\ \sigma^0{}_{\mathrm{HH}} - 1.38\ln(\bar{H}) + 3.43\ln(\lambda_\mathrm{r}) \\ \qquad + 1.31\ln(\gamma) + 18.55 & 10 \le f_\mathrm{r} < 100 \end{cases} \tag{2.84}$$

where the multipath or interference factor a_{GIT} is defined:

$$a_{\mathrm{GIT}} = \frac{\sigma^4_{\mathrm{GIT}}}{1+\sigma^4_{\mathrm{GIT}}} \tag{2.85}$$

and where the multipath roughness parameter σ_{GIT} is defined for an assumed Gaussian distribution of wave heights as:

$$\sigma_{\mathrm{GIT}} = \frac{(14.4\lambda_\mathrm{r}+5.5)\gamma\bar{H}}{\lambda_\mathrm{r}+0.015} \tag{2.86}$$

The sea is assumed to be fully developed with matching wind and wave propagation directions, aligned with the azimuth pointing angle ϕ_w, defining the sea direction factor as:[10]

$$b_{\mathrm{GIT}} = \begin{cases} \exp(0.2\cos(\phi_\mathrm{w})(1-2.8\gamma)(\lambda_\mathrm{r}+0.015)^{-0.4}) & 1 \le f_\mathrm{r} < 10 \\ \exp(0.25\cos(\phi_\mathrm{w})(1-2.8\gamma)(\lambda_\mathrm{r}+0.015)^{-0.33}) & 10 \le f_\mathrm{r} < 100 \end{cases} \tag{2.87}$$

and where the wind speed factor is defined:

$$c_{\mathrm{GIT}} = \begin{cases} \left[\frac{1.94\upsilon_\mathrm{w}}{1+\upsilon_\mathrm{w}/15.4}\right]^{1.1(\lambda_\mathrm{r}+0.015)^{-0.4}} & 1 \le f_\mathrm{r} < 10 \\ \left[\frac{1.94\upsilon_\mathrm{w}}{1+\upsilon_\mathrm{w}/15.4}\right]^{1.93(\lambda_\mathrm{r}+0.015)^{-0.04}} & 10 \le f_\mathrm{r} < 100 \end{cases} \tag{2.88}$$

The average wave height $\bar{H}$ is defined in terms of $H_{1/3}$ as:

$$\bar{H} = H_{1/3}/1.6 = 0.00452{\upsilon_\mathrm{w}}^{2.5} \tag{2.89}$$

and where relationships between wind speed and sea state may also be derived for in

[10] Note the additional brackets around azimuth pointing angle compared with the printed version in Rosenberg and Watts [13, Eq. (4.8)] - these have been confirmed when examining a publication by the authors of the GIT model [92].

Polarisation	a_{NRL}	b_{NRL}	c_{NRL}	d_{NRL}	e_{NRL}
HH	-73.0	20.78	7.351	25.65	0.00540
VV	-50.79	25.93	0.7093	21.58	0.00211

Table 2.4: Curve fitting parameters for the NRL model [84].

terms of the SWH:

$$H_{1/3} = 0.00724 {v_{\text{w}}}^{2.5} \tag{2.90}$$

$$H_{1/3} = 0.049 SS^{2.6} \tag{2.91}$$

where v_{w} is the wind velocity 10 m above the surface[11] and SS is the Douglas sea state [84]. If the sea is fully risen then simply wind speed may be used as an input, otherwise wind speed and wave height should be measured separately as independent inputs to the model [92].

2.3.6.2 The NRL model

The NRL model [84] was designed by fitting to Nathanson's tables such that it was in agreement with the largest available collection of measurements. The results of this model were obtained by minimising the mean absolute deviation for grazing angles 0° to 60°, sea states from 2 to 6, and frequencies from 0.1 to 35 GHz, and is included here as the state of the art for these ranges. The model here is reproduced from Rosenberg and Watts [13, pp. 118–119] The fitted function is expressed:

$$\begin{aligned}\sigma^0(\gamma, f_{\text{r}}, SS) =& a_{\text{NRL}} + b_{\text{NRL}} \log_{10}(\sin(\gamma)) + \frac{(27.5 + c_{\text{NRL}}\gamma)\log_{10}(f_{\text{r}})}{(1 + 0.95\gamma)} \\ &+ d_{\text{NRL}}(1 + SS)^{1/2 + 0.085\gamma + 0.033 SS} + e_{\text{NRL}}\gamma^2\end{aligned} \tag{2.92}$$

Where γ is grazing angle, SS is sea state, and f_{r} is radar frequency [GHz]. The parameters used for curve fitting are shown in Table 2.4.

2.3.7 Empirical models for NRCS distribution

Models for the distribution of σ^0 have similarly been developed from empirical data, taking the form of probability distributions. Numerous functions have been proposed, including the log-normal (LN) and Weibull distributions, however the most successful

[11] Rosenberg and Watts suggest 10 m as a standard height, although acknowledge this varies and that it is only an approximate relationship [13, p. 108].

is the K-distribution. This (along with the LN distribution) is a type of compound distribution, wherein the mean of one distribution is itself a random variable with a secondary distribution. An extension of the K-distribution is the K+noise, which models sea clutter in the presence of non-negligible receiver noise. Further models including K+Rayleigh, Pareto, KK, KA, and tri-modal discrete (3MD) have been developed to account for the effects of sea spikes in lengthening the distribution tail [13, pp. 31–32]. Since the focus of this thesis is not the modelling of sea clutter, only the K-distribution is presented here, where the derivation is largely sourced from Ward et al. [49] and Rosenberg and Watts [13], both of which have further information on additional models.

2.3.7.1 The K-distribution

The K-distribution is formulated by modulating the distribution for scattering from capillary waves, known as speckle, with another distribution for gravity waves, known as texture. In general, a speckle distribution is produced when the contributions from an ensemble of many scatterers within a footprint interfere with each other. It also serves as the simplest model of sea clutter backscatter, but is only valid when the range resolution is coarse enough to contain multiple uniformly distributed scatterers within a footprint, which requires that the range resolution is greater than the sea wavelength [13, p. 28]. In the case of fine range resolution, and thus in the context of the K-distribution, speckle is defined as a 'temporal or fast varying component' which 'relates to the Bragg scattering from wind-driven capillary waves' [13, p. 29]. In both cases, it has Gaussian statistics and a probability density function (PDF) for square-law detectors expressed by Eq. 2.93:

$$\mathbb{P}_s(q|\langle q\rangle) = \frac{1}{\langle q\rangle}\exp\left(-\frac{q}{\langle q\rangle}\right) \tag{2.93}$$

for an intensity, q, subject to the mean intensity, $\langle q\rangle$, as shown in both Ward et al. [49, p. 76] and Rosenberg and Watts [13, p. 28].

When considering fine range resolution systems or low grazing angles, the effect on the PDF of the larger scale modulation of gravity waves described by the texture PDF needs to be accounted for. Texture is defined as the 'varying local intensity' which 'captures the effect of the resolved sea surface structure due to waves or swell' [13, p. 29]. A good fit to the texture PDF has been determined to be the gamma distribution shown in Eq. 2.94:

$$\mathbb{P}_t(\langle q\rangle|b,\nu) = \frac{b^\nu}{\Gamma(\nu)}\langle q\rangle^{\nu-1}\exp\left(-b\langle q\rangle\right) \tag{2.94}$$

described by a shape parameter, ν, and a scale parameter, b, both defined as greater than zero [49, p. 76] [13, p. 33], and where the gamma function is represented as Γ. Evidence for speckle being a good fit to the model shown in Eq. 2.93 and for texture fitting to Eq. 2.94 is based on the results of many experimental measurements [93].

The distribution for q is then derived by averaging the speckle PDF in Eq. 2.93 over all values of $\langle q \rangle$ by performing the integration shown in Eq. 2.95:

$$\mathbb{P}_{\mathrm{K}}(q|b,\nu) = \int_0^\infty \mathbb{P}_{\mathrm{s}}(q|\langle q \rangle)\mathbb{P}_{\mathrm{t}}(\langle q \rangle|b,\nu)d\langle q \rangle \tag{2.95}$$

producing the K-distribution as shown in Ward et al. [49, p. 76] and Rosenberg and Watts [13, p. 31]. Note that in the former the integration limits are neglected, however these are recovered when considering the speckle PDF is defined with limits between 0 to ∞ [49, p. 24]. This expression evaluates to Eq. 2.96:

$$\mathbb{P}_{\mathrm{K}}(q|b,\nu) = \frac{2b^{\frac{\nu+1}{2}} q^{\frac{\nu-1}{2}}}{\Gamma(\nu)} \mathcal{K}_{\nu-1}\left(2\sqrt{bq}\right) \tag{2.96}$$

where $\mathcal{K}$ is a modified Bessel function of the second kind of order $\nu - 1$ [49, p. xix] [13, p. 34], the symbol giving the K-distribution its name. The values for b and ν are dependent on radar parameters and environmental conditions [93]. The formula for the K-distribution shown in Eq. 2.96 is given in Ward et al. [49, p. 76]. This differs from the version shown in Rosenberg and Watts [13, p. 34] in that this is the expected distribution from a single pulse or equivalently 'single-look'. Rosenberg and Watts show the form of the distribution derived in the 'multi-look' case, where this is obtained by 'the non-coherent integration of N-independent speckle samples' [13, p. 30]. The multi-look case assumes that each speckle sample drawn from the distribution shown in Eq. 2.93 is not correlated with any other, which is achieved either by frequency agility or by 'a sufficiently large time interval between pulses' [13, p. 29]. The latter causes decorrelation via the 'relative motion of the scatterers' [49, p. 26]. Furthermore, the sampling of speckle is assumed to occur at a fast enough rate such that variations from texture can be ignored in the formulation of the speckle PDF, being included later when compounding the two distributions as before using Eq. 2.95. The sum of the intensity samples then drawn from Eq. 2.93 can then be expressed as Eq. 2.97:

$$Q = \sum_{n=1}^{N} q_n \tag{2.97}$$

where N is the number of pulses which are integrated and q_n is each sampled intensity value. This then results in the PDF for multi-look speckle given in Eq. 2.98:

$$\mathbb{P}_{\mathrm{s,m}}(Q|\langle q\rangle, N) = \frac{Q^{N-1}}{\langle q\rangle^{N}\Gamma(N)} \exp\left(-\frac{Q}{\langle q\rangle}\right) \tag{2.98}$$

which produces the multi-look K-distribution PDF shown in Eq. 2.99:

$$\mathbb{P}_{\mathrm{K,m}}(Q|b, \nu, N) = \frac{2}{Q}(bQ)^{(N+\nu)/2}\frac{1}{\Gamma(N)\Gamma(\nu)}\mathcal{K}_{\nu-N}\left(2\sqrt{bQ}\right) \tag{2.99}$$

This ends this section covering the behaviour of radar sea clutter amplitude statistics up to Ka-band, these frequencies being where most of the work on sea clutter research has taken place. The following chapter will review the literature on sea clutter above Ka-band, where relatively few measurements have been made and the characteristics of sea clutter are less well understood.

3

Sea Clutter Amplitude Statistics Above Ka-Band

THE main objective of this project, as outlined in Chapter 1, is to investigate the properties of sea clutter in the high *mm-wave and sub-THz* regimes. The following is an overview of the available research into sea clutter amplitude statistics above Ka-band. Given the low quantity of data in this frequency region, these are listed as summaries of either results collated in textbooks (historical measurements from the 1980s or earlier) or individual articles of research, *with this author's comments in italics.*

As also specified in Chapter 1, this project is specifically concerned with LGA clutter. However, some results from other grazing angle regimes are discussed with the caveat that these will at best provide ballpark estimates of LGA sea clutter, where their primary utility is limited to an indication of possible trends and to provide some degree of context. Some works include results from frequencies at Ka-band or below which were made at the same time as those above, and where appropriate these are discussed for comparison with the higher frequency measurements which are of primary interest.

Articles on the topic produced during the STREAM project are included in this summary, except for a preliminary work on 207 GHz sea clutter by the author [26] which is covered in Chapter 7, together with further results on sea clutter amplitude statistics at that frequency. This discussion is also limited to results for amplitude statistics, however papers covering primarily Doppler results are also collected here for reference without further review.

3.1 Historical measurements published in textbooks

Wetzel in Skolnik [36, p. 15.20] reports work by Wiltse (1957) [94] at 49 GHz and by Rivers (1970) [95] and Ewell (1979) [92] at 95 GHz. The latter two both link to a

research programme carried out by the GIT in the 1970s, finding HH and VV NRCS values of ∼−40 dB for a grazing angle of 1°.

Nathanson [21, pp. 275–279] cites the same work by Rivers [95], refers to Wetzel [36, p. 15.20], and also to work by Dyer et al. (1977) [96]. These data points were used in the production of Nathanson's tables, the issues of which have been discussed previously. These values suggest LGA NRCS values between −50 to −30 dB for sea states 1 to 3 and grazing angles 1 to 10° with no clear pattern between VV and HH. **Long** (2001) [97, pp. 372–378] reproduces Nathanson's tables with additional notes.

Currie and Brown [35, pp. 228–234] also reference the Rivers [95] report, along with work from Trebits et al. (1980) [98]. They present a summary table comparing NRCS for microwave and mm-wave for different conditions which is reproduced in Table 3.1. The results from Trebits et al. are for a SWH of 0.8 m (Douglas sea state 3) at 95 GHz for grazing angles of 1 to 5°. Upwind NRCS was found to be the highest and downwind the lowest, with the HH return being greater than VV, and where HH was ∼−30 dB upwind and varying ∼15 dB due to wind direction and 1 to 2 dB between polarisations, although HH and VV were approximately equal. No clear trend was established for the NRCS versus grazing angle. The amplitude distributions in HH and VV were of approximately equal width. In terms of frequency, the Rivers results showed that the NRCS was generally less at 95 GHz than at 9.5 GHz for both polarisations. **Currie et al.** (1992) [48, pp. 168–174] contains the same material as Currie and Brown [35].

Characteristic	Microwave	Millimetre-wave
Mean, low grazing angle	$\sigma^0_{HH} < \sigma^0_{VV}$	$\sigma^0_{HH} > \sigma^0_{VV}$
Mean, high grazing angle	$\sigma^0_{HH} \approx \sigma^0_{VV}$	$\sigma^0_{HH} \approx \sigma^0_{VV}$
Standard deviation, all grazing angles	$\sigma^0_{HH} > \sigma^0_{VV}$	$\sigma^0_{HH} \approx \sigma^0_{VV}$
Wind direction, high grazing angle	$\sigma^0_{UPWIND} \approx \sigma^0_{CROSSWIND} \approx \sigma^0_{DOWNWIND}$	
Wind direction, all other grazing angles	$\sigma^0_{UPWIND} > \sigma^0_{CROSSWIND} > \sigma^0_{DOWNWIND}$	
Frequency, mean values	$\sigma^0_{10\ GHz} < \sigma^0_{35\ GHz}; \sigma^0_{10\ GHz} > \sigma^0_{95\ GHz}$	
Frequency, standard deviation	$\sigma^0_{10\ GHz} < \sigma^0_{35\ GHz} < \sigma^0_{95\ GHz}$	

Table 3.1: Comparison of NRCS behaviour for microwave and mm-wave clutter from Currie and Brown [35, p. 230].

Kulemin (2003) [99] presents the results of a small number of Russian language papers which are not widely available. These suggest an NRCS upwind to crosswind ratio of 5 to 6 dB, increasing to 10 to 15 dB for low sea states [99, p. 196] at 'millimeter wavelengths'. *This is assumed to be 75* GHz *given the further results that are summarised in the plots in Figure 4.12 on page 205,* which show the variation of NRCS with grazing

angle and wind direction. The caption is somewhat ambiguous, but it is assumed that the final clause is erroneous. When examining the description of the results in text it states that the experimental results show good agreement with the model, and that the lines represent the model and the symbols the measured values – line 3 is taken to be 75 GHz and thus the circles are the measurements also at 75 GHz. On that assumption, the following conclusions are drawn considering grazing angles greater than 1°:

- The modelled NRCS increases from −43 to −38 dB for angles 1 to 7°, with measured values showing a variation between −40 to −35 dB in this range.
- NRCS decreases with increasing frequency.
- NRCS increases with wind speed and then saturates at ∼10 m s^{-1} at −35 dB.
- The saturation of NRCS happens at a higher wind speed for higher frequency. This contradicts the statement made on page 194.

3.2 Additional publications

3.2.1 *Remote Sensing of the Sea Surface at 94 GHz*, Makaruschka and Essen (1990) [100]

This paper presents the results of measurements made with a 94 GHz radar in HH polarisation of the sea for different wave directions and grazing angles. The sea state during data collection is not stated. Figures 4.1 and 4.2 from the paper are reproduced in Fig. 3.1, these being two RTI plots, Fig. 3.1a for upwind and Fig. 3.1b described either as 'more cross wind direction' or 'downwind'. The former shows more clutter features than the latter, which would then correspond to a greater NRCS in the upwind direction. The latter plot is described in text as having the radar beam parallel with the wave fronts, which would indicate this is crosswind. This data then implies that fewer spikes are seen in the crosswind direction, and that the NRCS can be expected to be lower.

Reproduced again in Fig. 3.1 are Figures 4.5 and 4.6, which present the variation of NRCS with the azimuth angle (wave direction) and with grazing angle (presented as depression angle, which at the maximum range considered of 1500 m may be slightly different), respectively. When discussing reflectivity, the text refers to RCS, however from the figures it can be seen that in fact these are correctly presented as NRCS values. Figure 3.1c shows a linear fitted trend for NRCS with azimuth angle, where this increases to a maximum upwind (at 120° in the plot) of −39 dB for a grazing angle of 1.2° from a downwind value of −48 dB (minimum at 30° 'azimuth' of −51 dB,

which corresponds to crosswind). The plot also indicates that the gradient of this trend becomes steeper for increasing grazing angle, and that the overall reflectivity was higher at 0.66° than at 1.2°, however since below 1° the role of shadowing and ducting becomes much more important this is not necessarily indicative of a broader trend at LGA. Figure 3.1d again shows the trend of NRCS decreasing with grazing angle, with the gradient of the trend becoming steeper at some wave directions, however the variation is not clear from the plot and is not stated in the text. The authors made comparisons of measured NRCS with the GIT model and concluded there was a good match, *however this cannot be verified given the sea state is not given. The good match is interesting to note considering the GIT model was formulated with data excluding anomalous propagation (see Subsection 2.3.5), which is highly likely at the grazing angle of these measurements.*

3.2.2 *Measurements of radar backscatter from the ocean surface at 94 GHz as a function of wind speed, direction and the modulation by the ocean waves during the SAXON-FPN experiment.*, Fuchs (1993) [101]

This paper presents the results of sea clutter measurements of the North Sea between 1990 and 1992 with a 94 GHz radar taken at a grazing angle of 45°. Given that the results are at medium grazing angle (MGA) the results are not reviewed in detail here. The general trends revealed that the NRCS was found to increase with wind speed for both upwind and crosswind directions, and that the NRCS dependence on wind speed at W-band was more pronounced than at Ka-band and below.

3.2.3 *Polarimetric multifrequency SAR measurements over sea at millimeterwave frequencies*, Boehmsdorff et al. (1997) [102]

This publication shows results from data collected by the MEMPHIS synthetic aperture radar (SAR) imaging sea surfaces and ships in HH polarisation at a grazing angle of 20° and with a range resolution of 1 m. The radar operates at both 35 GHz and 94 GHz simultaneously. The paper presents SAR imagery for both frequencies but does not present any significant quantitative analysis. Qualitatively it is observed that at 94 GHz the wake from the stern of the vessel is more pronounced indicating a greater reflectivity from foam. At both frequencies the wave crests are discernible over all azimuth angles, indicating that the scattering from the crests is somewhat isotropic, although a numerical analysis indicated that there is a variation of approximately 5 dB

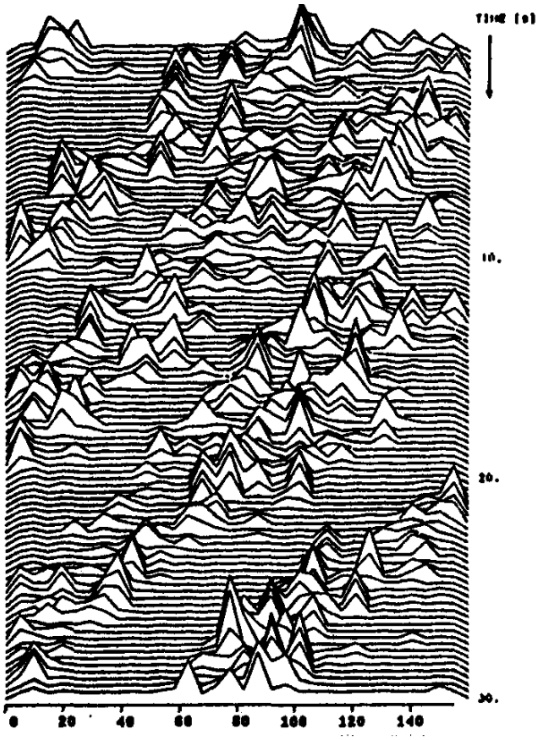

(a) Makaruschka and Essen (1990) [100] Figure 4.1.

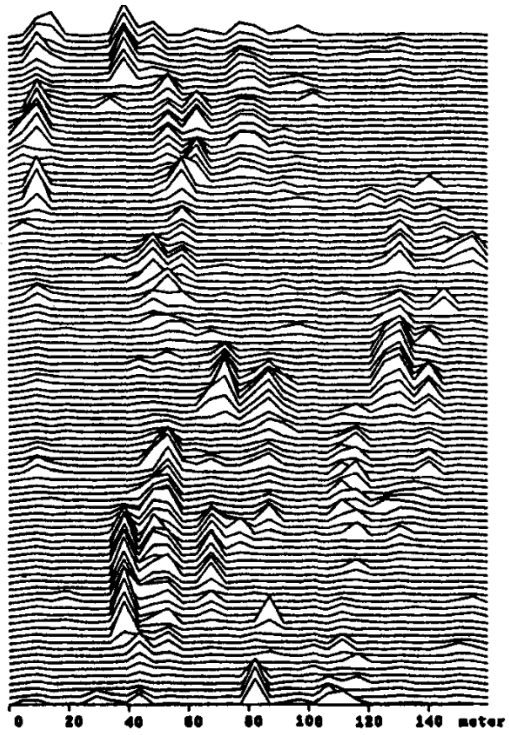

(b) Makaruschka and Essen (1990) [100] Figure 4.2.

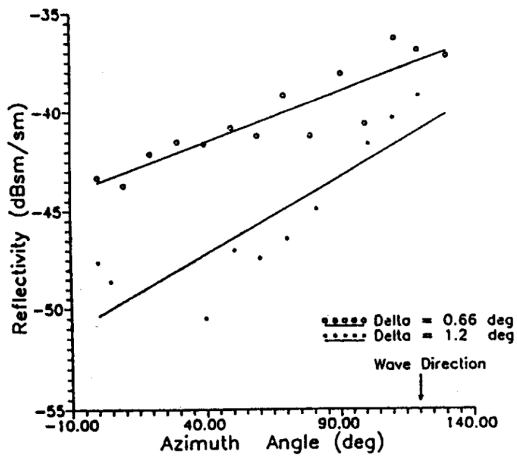

(c) Makaruschka and Essen (1990) [100] Figure 4.5.

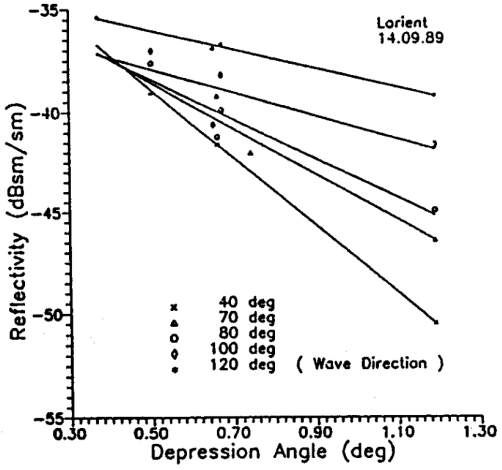

(d) Makaruschka and Essen (1990) [100] Figure 4.6.

Figure 3.1: Figures from Makaruschka and Essen (1990) [100].

between upwind, downwind, and cross-wind.

3.2.4 *Sea surface and ship observation with MEMPHIS*, Boehmsdorff et al. (1998) [103]

This paper presents the results of further measurements using the MEMPHIS radar to investigate MGA SAR imaging of disturbances of the sea surface at 35 and 94 GHz. Measurements in sea state 5 were made at a grazing angle of 37.5° and are reviewed briefly. The research indicates there are significant differences between the two frequencies: 35 GHz measurements are similar to X-band where Bragg scattering is still observed as significant, but at 94 GHz this effect is diminished due to a lack of short wavelength capillary waves, *as is indicated by the plot in Fig. 2.17 and discussed in [58, p. 11543]*. It is also reported, however, that at 94 GHz the NRCS in VV is consistently stronger than in HH, with the ratio being up to 10 dB, and more evident at low sea states – *this is exactly the behaviour seen for Bragg scattering at low frequencies, but is at odds with what is expected as possible from the wave spectrum. It should also be noted that the Bragg scattering equation given in this paper is incorrect, see Eq. 2.79, however the Bragg resonant water wavelength of 2.2* mm *for 94* GHz *at a grazing angle of 45° is correct.* The facet scattering model is suggested as an alternative to Bragg scattering, where the plate size required for specular scattering at W-band would be in the region of 1 mm, and that facets larger than this are physically reasonable. This model is presented as consistent with the observed decrease in backscatter when looking away from upwind.

The 94 GHz NRCS as a function of wind/wave direction indicates returns are greatest upwind and that downwind produces a consistently lower peak, with minima in the signal found at crosswind as shown in Figure 3.2. Comparing 94 GHz to 35 GHz, it was observed that at W-band the upwind to downwind σ^0 ratio increases. The same conclusion from [102] that rough, foamy surfaces from ship wakes are well detected at W-band is stated again.

3.2.5 *Millimetre-wave radar measurements from laboratory surface waves*, Connan et al. (1999) [104]

This research used a 94 GHz radar to observe waves generated in a tank both mechanically and by wind. Measurements were made with a range resolution of 5 cm, VV polarisation, and at a grazing angle of 55 to 60°. Interestingly, measurements were made with and without capillary waves, where it was determined that most of the observed scattering at mm-waves was due to the capillary waves and that without them the rapid fluctuations in the time series were greatly reduced. *This suggests that*

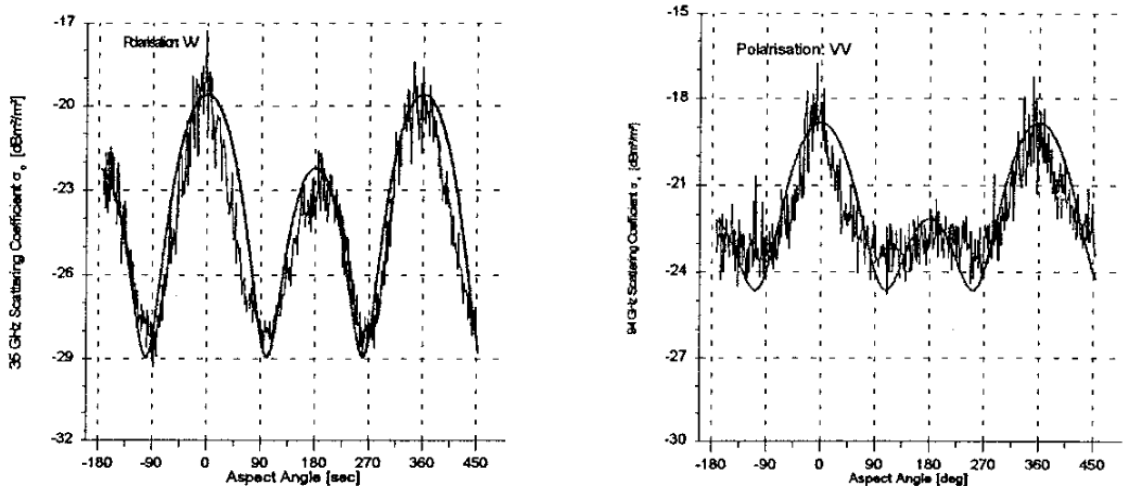

(a) 35 GHz. (b) 94 GHz.

Figure 3.2: Variation of σ^0 with wind/wave direction (upwind = 0°) for the MEMPHIS SAR observing sea state 5 in VV polarisation [103].

capillary waves may still have an impact on backscatter at these frequencies, even if this is not caused by the Bragg mechanism. For mechanically generated waves, periods of backscatter lasting 0.25 s were observed. Given that these measurements were made in the MGA regime, it is possible that these qualitative observations may differ significantly from those observed at LGA. The publication also contains results of Doppler analysis.

3.2.6 *Doppler spectra of laboratory wind waves at low grazing angle*, Lamont-Smith (2000) [105]

In this paper, researchers from QinetiQ performed a series of measurements of wind generated waves in a wind-wave tank using radars ranging in frequency from 3 GHz to 94 GHz with range resolutions of 30 cm. The exact grazing angle is not stated, other than that measurements were made at LGA. Measurements were made in both HH and VV polarisations, however the research is mainly focused on investigating the behaviour of Doppler signatures. The results applicable to the discussion on amplitude behaviour are that Bragg scattering in HH polarisation was seen to be more pronounced at lower frequency, and that 'Bragg resonance appeared to be the dominant scattering mechanism in VV over all the radar frequencies measured, even for millimetric radars' *despite the conclusions of [103]*, with Bragg resonant Doppler returns detected from water waves with wavelengths of 1.5 mm up to 50 mm.

3.2.7 *Experimentally motivated model for low grazing angle radar Doppler spectra of the sea surface*, Walker (2000) [106]

This paper describes the further analysis of measurements taken with the same apparatus as in [105] to develop a model for LGA Doppler sea clutter. It is stated that measurements at grazing angles between 3 to 24° were made, however only measurements at 6° are presented, and measurements at 94 GHz are omitted.

3.2.8 *W-band radar backscattering at low grazing angles measured in a wave tank at various wind speeds*, Schlick et al. (2002) [107]

Presented in this publication are measurements made in a wind-wave tank at the University of Hamburg with the goal of comparing the returns at 10 GHz and 94 GHz. The instruments had a range resolution of 5 cm, and backscatter was investigated for grazing angles in the range 7.5 to 20° for VV, HH and VH polarisations over a range of wind speeds 2 to 10 m s^{-1} exclusively in the upwind direction.

The results shown in Fig. 3.3 indicate that the NRCS at W-band was greatest in VV at all sampled wind speeds, the authors concluding that this is evidence that Bragg scattering is the dominant mechanism observed. They provide further evidence for this hypothesis in that the ratio of VV to HH was seen to decrease with grazing angle. This is the expected behaviour with grazing angle for Bragg dominant scattering, since Bragg scattering enhances VV polarisation returns but burst scattering favours HH, where the latter becomes more apparent at larger grazing angles. Scattering in VH polarisation was found to be as high as HH at some wind speeds, indicating that other mechanisms as well as Bragg scattering are important at LGA. They suggest that the dominant scattering is consistently from capillary waves, where at lower wind speeds these are due to bound capillary waves (capillary waves generated by steepening gravity waves) whereas at wind speeds above 5 m s^{-1} they are freely propagating. The paper also presents further Doppler analysis.

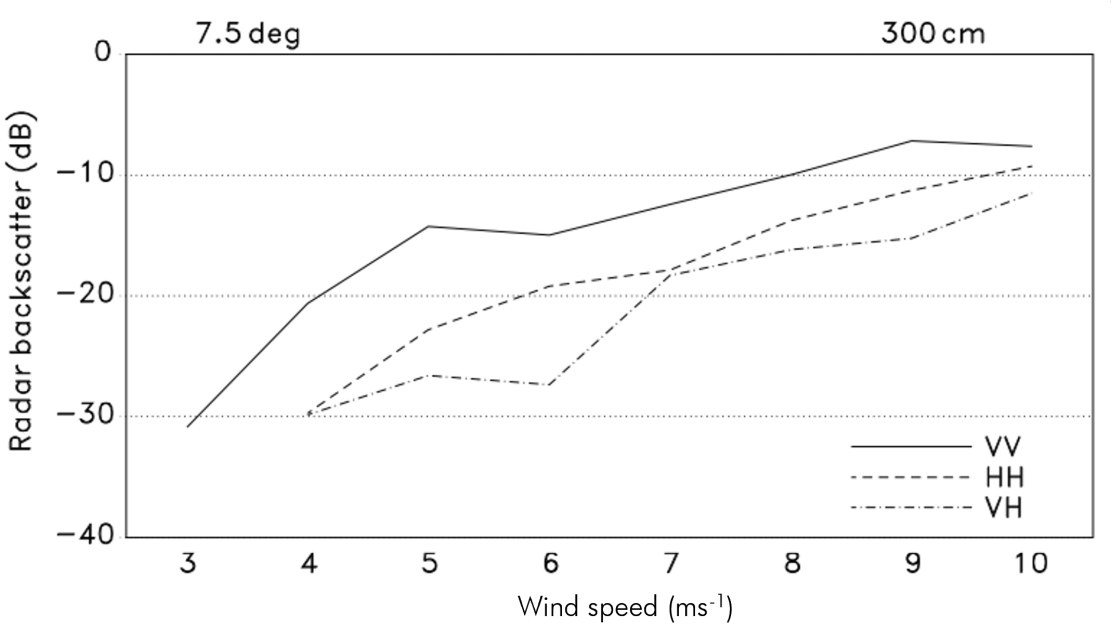

Figure 3.3: The variation of NRCS with wind speed as measured by Schlick et al. [107], at a grazing angle of 7.5° and a range resolution of 300 cm. Note that the paper erroneously shows the abscissa label as 'Range (cm)'.

3.2.9 *Investigation of the variability of Doppler spectra with radar frequency and grazing angle*, Lamont-Smith (2004) [108]

This paper presents further results from the same set of experiments run by QinetiQ as shown in Walker [106], discussing the effect of grazing angle on Doppler spectra. The paper only covers Doppler results but should be considering when reviewing Walker [106] as some results at W-band are included.

3.2.10 *Measurements of Ocean Surface Backscattering Using an Airborne 94-GHz Cloud Radar – Implication for Calibration of Airborne and Spaceborne W-Band Radars*, Li et al. (2005) [109]

Measurements were made of ocean surface backscatter at 94 GHz to allow for its use as a calibration reference by satellite sensors. Observations were made from an airborne platform at a high grazing angles from 68 to 90° with a range resolution of 150 m. Given the extreme grazing angle, the results from this study are unlikely to bear much relevance to the LGA case but the publication is listed here for completeness.

3.2.11 *Nested Radar Systems for Remote Coastal Observations*, Bell et al. (2006) [110]

This research compared the use of X-band and 77 GHz radar for littoral zone bathymetric mapping by measurement of surface water wavelengths. Waves were measured to have a SWH of 2 m further offshore by a wave buoy, with radars placed on the shoreline close to the water. From a photograph of the 77 GHz radar set up, it is estimated that the sensor is at a height of ∼1 m above sea level, and that the minimum range is 50 m from Fig. 3.4. The maximum range is stated to be 200 m. Using Eq. 2.15, the grazing angle is then estimated to vary between 0.3 to 1.1°. Wave heights at the shore are also estimated to be of a Douglas sea state of 3 from the photograph of the trial set up.

The main observation of note is that at 77 GHz only the foam line or front faces of the breaking waves were visible in plan position indicator (PPI) measurements. This may be in part due to the relatively low sensitivity of the 77 GHz system (given the 200 m maximum range), but its SNR was not specified. A comparison of the data at the two different frequencies is shown in Fig. 3.4, where the overlaid data from X-band and 77 GHz show contiguous wave features. *This does not immediately indicate the assertion that only the foam line or wave crest is visible in the data since they both appear similar (and X-band would be expected to pick up signal between crests), but it is possible that during data collection the 77* GHz *radar signal may have been observed to be at noise floor in between crests whereas the X-band system was at some level above this.*

3.2.12 *Remote sensing of the sea surface by millimeterwave SAR*, Essen et al. (2006) [111]

Further measurements made with the MEMPHIS SAR at 35 GHz and 94 GHz, at range resolutions of 75 cm and 20 cm (following upgrades since the previous publications listed here). Observations are made over a variety of wind/wave directions at a grazing angle of 37.5° (MGA). This paper repeats the summary of the results of NRCS variation with wind/wave direction published in Boehmsdorff et al. [103] by the same group, as summarised above.

Several SAR images of the sea surface are presented in the paper and are reproduced in Fig. 3.5. Figures 3.5a and 3.5b compare images made at 35 GHz and 94 GHz with a range resolution of 1.5 m in VV polarisation. They show the same wave patterns at both frequencies, however at 94 GHz the wave crests appear better resolved, suggesting that at this frequency scattering occurs from smaller areas of the wave near the crest, where small facets are aligned most favourably to produce backscatter. Observations

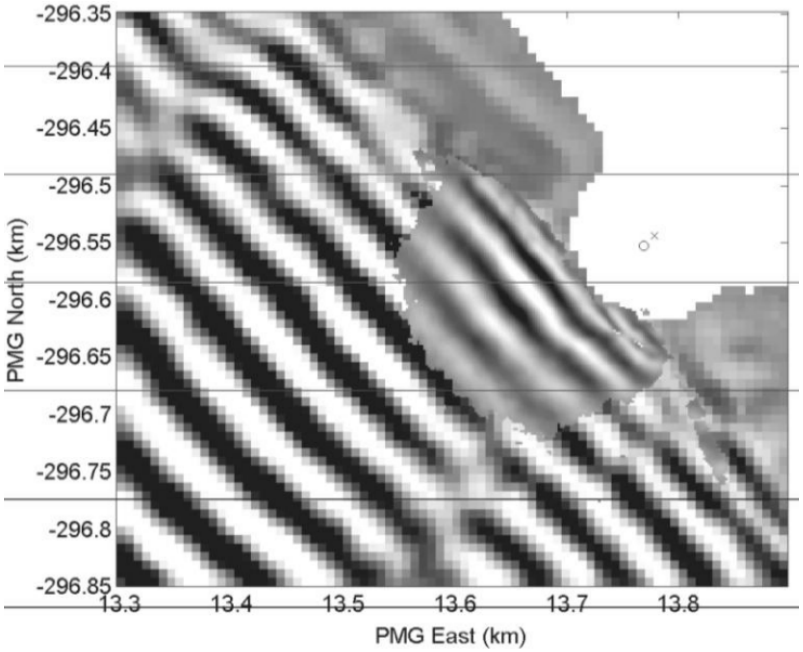

Figure 3.4: Overlaid radar data from X-band and 77 GHz of waves approaching the shore, from Bell et al. [110]. The X-band radar is marked by an 'x', where the data at this frequency extends much farther in range than the mm-wave radar, which is marked with a 'o'.

at different wave directions produce the same type of pattern, which implies that the W-band scattering is relatively isotropic. Figures 3.5c and 3.5d show SAR images at both frequencies for a range resolution of 20 cm. The linear structures of the waves again appear better resolved at 94 GHz, indicating that scattering lobes for 35 GHz are broader given that the range and cross-range resolutions at both frequencies are the same.

The paper also presents NRCS histograms, showing that for 20 cm range resolution at 94 GHz the dynamic range is 23 to 24 dB where the distribution peaks at −32 dB which is 5 dB lower than at 35 GHz, and that the samples are K-distributed *but does not present the parameters used for fitting*. Two histograms of 35 GHz data with either 20 cm or 75 cm range resolution are also compared, where the lower resolution data fits to a normal distribution *as is expected by the central limit theorem*. The mean value of the distribution is found to remain constant at −27 dB, however the dynamic range of the lower resolution data is reduced to 18 dB, where this is mostly due to a 5 dB reduction in the maximum NRCS observed when compared to 20 cm range resolution, this being −11 dB at 20 cm resolution.

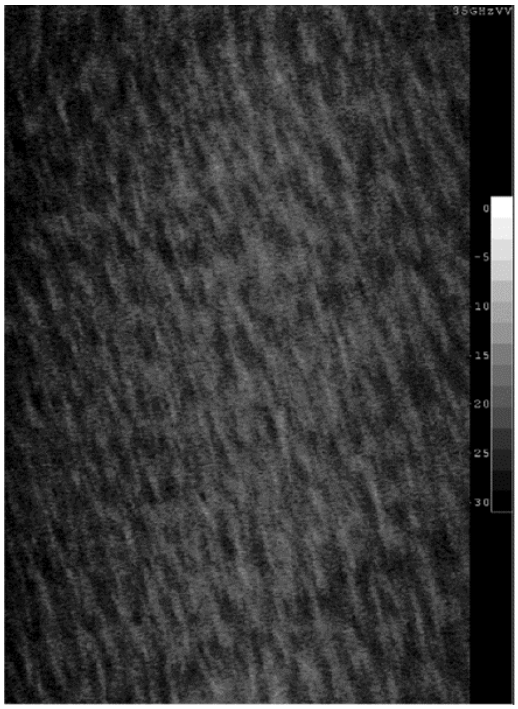

(a) Essen et al. (2006) [111] Figure 4, 35 GHz SAR data at 1.5 m range resolution.

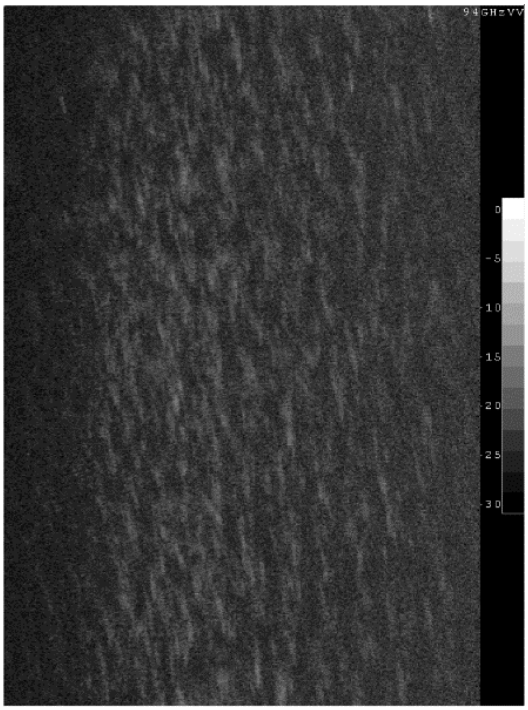

(b) Essen et al. (2006) [111] Figure 4, 94 GHz SAR data at 1.5 m range resolution.

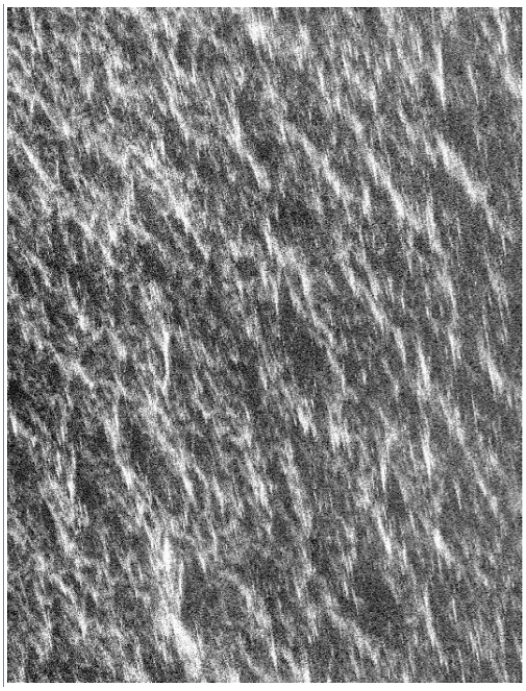

(c) Essen et al. (2006) [111] Figure 5, 35 GHz SAR data at 0.2 m range resolution.

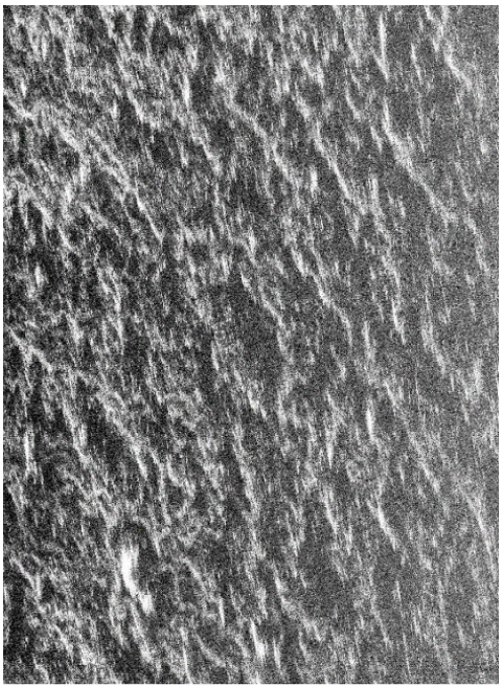

(d) Essen et al. (2006) [111] Figure 5, 94 GHz SAR data at 0.2 m range resolution.

Figure 3.5: Figures from Essen et al. (2006) [111] showing SAR imagery in VV polarisation.

3.2.13 *High resolution millimeterwave SAR for the remote sensing of wave patterns*, Essen et al. (2007) [112]

A further paper on MEMPHIS measurements at 35 GHz and 94 GHz to determine sea clutter amplitude statistics and investigate the difference between range resolutions of 75 cm and 20 cm. The figures and material are mostly the same as presented by the same group previously in Essen et al. [111] and are summarised above. The conclusion of the paper asserts that at low range resolution Bragg scattering is contributing to scattering, but that at high resolution it does not due to the high resolution statistics being K-distributed. *This is a misunderstanding, since the K-distribution is specifically formulated to include Bragg scattering. Furthermore, the lower limit on range resolution for Bragg scattering to still occur would be half the Bragg resonant water wavelength. Since at W-band the 20* cm *range resolution of the radar is approximately an order of magnitude greater than this lower limit, it would be expected that Bragg resonance is not limited by the range resolution.*

3.2.14 *Measurements of the Doppler spectra of breaking waves*, Lamont-Smith et al. (2007) [113]

The fourth paper derived from the set of measurements by QinetiQ first detailed in [105], this publication analysed the Doppler spectra of breaking waves with measurements up to 94 GHz. The results focus on Doppler analysis, however the RCS was shown to scale according to the relation $\sigma \propto \lambda_r^{1.5}$, explained as an enhancement to scattering due to the angle of steeper waves to the radar beam being more favourable to backscatter and having front faces more closely approximating parabolae. The average backscatter was observed to vary only by a few dB with either grazing angle (between 3 to 24°) or wave direction *although the range for the latter is unspecified and given this was not mentioned as a variable in prior publications based on these experiments, may be an error confusing it with the other experiments summarised in this paper.*

3.2.15 *94-GHz Tarsier radar measurement of wind waves and small targets*, Leonard et al. (2011) [114]

Simultaneous measurements of the water's surface at a reservoir were taken by QinetiQ with a Tarsier 94 GHz radar and a 9.4 GHz Raymarine Pathfinder system with the aim of directly comparing clutter and target returns. The 94 GHz data is for a range resolution of 0.3 m and the 9.4 GHz data at 7.5 m. Various targets of opportunity were measured in the water and shown with PPI plots, as well as RTI plots of directly approaching

waves. The text describes a 'clear qualitative improvement in the signal-to-clutter level' for the data gathered with the 94 GHz radar, *although there is no quantitative assessment of the difference nor discussion of which parameters contribute to the improvement.* The abstract indicates that 94 GHz clutter histograms are presented in the body of the work *however this seems to be an error.* Some Doppler data is shown.

3.2.16 *An Improved Empirical Model for Radar Sea Clutter Reflectivity*, Gregers-Hansen et al. (2012) [84]

The main focus of this paper is the presentation of the NRL model for sea clutter, as previously discussed in Subsection 2.3.5. In addition to this, 94 GHz measurements by NRL using the WARLOC radar are presented. These were made at a very low grazing angle (0.5°) of the sea for a 12 kn wind in sea state 2 to 3 and a range resolution slightly greater than 1 m. They report extremely spiky data equivalent to one significant return per 80 m^2. A K-distribution was fitted to NRCS data and produced a shape parameter of $\nu = 0.03$, where the authors state that this is very low compared to data at low frequencies, and corroborates results at lower frequencies indicating finer resolution produces spikier data. The measured distribution indicates that for a $\mathbb{P}_{fa} = 10^{-6}$ the required threshold would be 30 dB above the mean level, with $\mathbb{P}_{fa} = 10^{-2}$ for 10 dB above mean level. The mean RCS plus noise was measured as −36.8 dBsm with a noise level of −80 dBsm. The clutter patch area is stated as 6 m^2, indicating that the mean NRCS of the measured area was −44.6 dB. An RTI plot corresponding to a section of the data from which the mean is calculated is also shown, showing multiple scattering events varying in duration from 10s of milliseconds to several seconds.

3.2.17 *Littoral Sea Clutter Returns at 94GHz*, Stove et al. (2014) [115]

This paper describes results from sea clutter measurements made in the littoral zone using the SAFIRE 94 GHz radar, in linear and circular polarisations, at a grazing angle of 2°, and a range resolution of approximately 0.13 m. Measurements were made from the shore of waves with heights consistent with sea state 3. The publication also reports some older data from an unpublished source which is reproduced in Table 3.2, made by Barrett, Booth, and Stove as part of work at Philips in 1986.

Figure 3.6 shows a typical HH polarised PPI where only whitecap returns were visible, corroborating results in Bell et al. [110]. The dynamic range for the image is ∼15 dB. As shown here and in other measurements, no returns above the noise floor

of −37 dB were seen to come from between wave crests, where most of the returns were observed to come from whitecaps which were ∼10 dB greater than the average return.

The NRCS values for VV and HH were reported as −22 dB for whitecap returns and −30 dB for a mean over the full wave. Following a later calibration of the radar, these values were found to be in error, with the correct values being −12 dB for the wave crests and −20 dB for the mean value over the full wave, the revision being published in [26]. No significant difference was observed between the mean levels of VV and HH, *which suggests white-cap scattering was dominant with Bragg and burst scattering minimal assuming low frequency trends hold.* The discussion states that the results support the mean LGA NRCS in SS 3 being <−30 dB, *however given the updated calculation of the mean being −20* dB *this is clearly no longer the case, with NRCS being much greater than expected.* Measurements made in circular polarisation generally showed a reduced return power compared to either linear polarisation, however the strongest returns were approximately equivalent in NRCS, indicating spikier data in circular polarisation.

The analysis of the amplitude distributions showed that HH has a longer-tailed (spikier) distribution than VV, continuing the trend from low frequencies. Fits to the K-distribution indicated ν values of 0.1 to 0.2. *Curiously, this is much higher than for a far smaller resolution cell at 94 GHz compared to [84].*

Grazing angle	Sea state	NRCS [dB]
1°	3 to 4	<−30
3°	1 to 2	−40
3°	3 to 4	−29
10°	3 to 4	−29

Table 3.2: Previously unpublished 94 GHz sea clutter backscatter values shown in Stove et al. [115], made by Barrett, Booth, and Stove as part of work at Philips in 1986.

3.2.18 *Characterization of Surface Radar Cross Sections at W-Band at Moderate Incidence Angles*, Battaglia et al. (2017) [116]

This paper presents airborne measurements of NRCS at 94 GHz made in VV and HH over water in the Great Lakes region, made for grazing angles between ∼28 to 90°. The range resolution is between 15 to 150 m. The results discussed here are for the lower limit of the grazing angles measured, as these will be most similar to the LGA regime. These results show that the NRCS increases with wind speed, and that the median HH

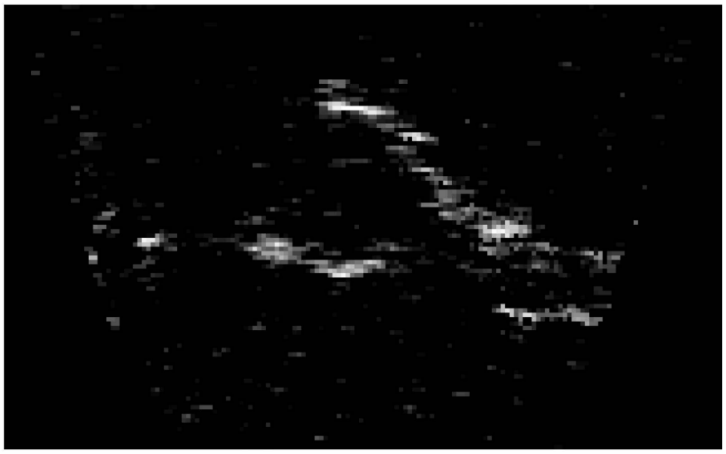

Figure 3.6: SAFIRE 94 GHz PPI in HH for a range between 40 to 65 m, sea state 3, indicating that only the wave crests are detected by the radar [115].

NRCS is greater than in VV by approximately 5 to 10 dB. The dependence on wind direction shows a maximum upwind, minima crosswind, and a maximum downwind which is approximately 5 dB less than upwind. The total variation is approximately 7 dB.

3.2.19 *Measurements of Sea Clutter at Low Grazing Angle in Mediterranean Coastal Environment*, Fabbro et al. (2017) [117]

Further measurements with MEMPHIS 35 GHz and 94 GHz in the Mediterranean, however only the 35 GHz results are reported.

3.2.20 *Radar Propagation Experiment in the North Sea: The Sylt Campaign*, Danklmayer et al. (2018) [118]

Further MEMPHIS measurements at 9.6 GHz, 35 GHz and 94 GHz in the North Sea, with 94 GHz results again unreported.

3.2.21 *W-band Littoral Low Grazing Angle Sea Clutter Measurement*, Weidong Hu et el. (2019) [119]

Researchers from the Beijing Institute of Technology used a stepped frequency radar from 91.5 to 97.5 GHz at range resolution of 15 m to measure clutter amplitude statistics in a sea state of 1 to 2 and at a grazing angle of 1.2°. The NRCS for wave peaks was measured to be −24.5 dB, where the authors assume that the average value is lower

with reference to Stove et al. [115]. *If it is assumed that the difference between the NRCS from the wave peaks and across the whole wave is the same as in Stove et al., then the average value in this case will be 8* dB *lower at ∼−32* dB*, however the difference in sea states between the two measurements should be kept in mind.* Measurements were made in both HH and VV, *but the NRCS estimate does not state which polarisation was used for this measurement.* Histograms of HH and VV data are shown which indicate that HH has a longer tail. *This follows the trend for low frequencies resulting from multipath/Brewster angle effects.*

3.2.22 *First Airborne Measurements With a G-Band Differential Absorption Radar*, Roy et al. (2022) [120]

This work presents measurements made with the VIPR radar of ocean surfaces at a frequency of 167 GHz. These measurements were made at grazing angles of 62 to 90° and so LGA results can be expected to differ greatly, however they are included here as they represent the first measurements of sea clutter at G-band, and the highest carrier frequency measurement of sea clutter prior to work published by the author [26]. At the lowest grazing angle, the measurements record an average NRCS of ∼−20 dB for a sea state of 0 to 1 (described as very calm with glassy patches of water). The results also show that the NRCS decreases over the grazing angle range measured *which is expected from prior results at lower frequencies.*

3.2.23 *Amplitude Characteristics of Littoral Sea Clutter Data at K-band and W-band*, Rahman et al. (2022), [22]

This was the first publication from the STREAM project which presented measurements of sea clutter. Measurements were made at 24 GHz (HH) and 94 GHz (circular polarisation), with range resolutions of 60 cm and 20 cm respectively. The trial was conducted at the beach in St Andrews, Scotland, in the littoral zone. The sea state was of a maximum of 1, however larger waves were observed breaking closer to shore which would be compatible with sea state 2 or 3, from visual estimation.

The data showed that returns were dominated by sea spike events, where mainly the crests of waves were visible, as shown for 94 GHz data of whitecaps in Fig. 3.7. *This is similar to the observations made by Bell et al. [110].* At 94 GHz, the scattering from smooth areas of the sea surface was observed to be below the NESZ value of the radar of −65 dB.

The NRCS values of the data were analysed by first categorising them in terms of being either Bragg, burst, or whitecap scattering. The results for both frequencies are

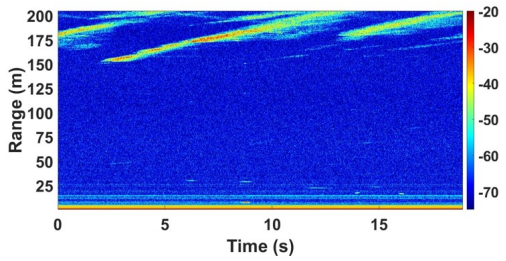

(a) Rahman et al. [22] Fig. 2a.

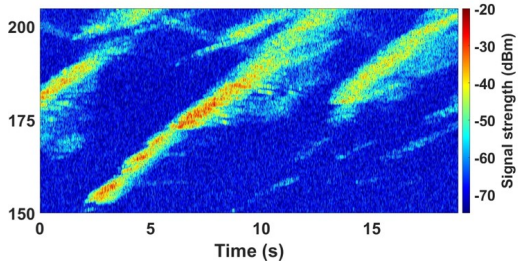

(b) Rahman et al. [22] Fig. 2b.

Figure 3.7: Figures from Rahman et al. [22], showing data collected at 94 GHz of breaking waves (whitecaps).

collected in Table 3.3, where it should be noted that whitecap scattering measurements were made at $\gamma = 1.3°$ whereas Bragg and burst were observed at $\gamma = 3°$. Direct comparison of these results is complicated by the fact that these were measured in different polarisations, however the returns in circular polarisation at W-band were comparable or higher than those in HH at K-band.

Scattering which qualified as Bragg according to the methodology in [121] was observed, however as previously stated the spectral density of the required resonant water waves is likely to be too low at 94 GHz *[58, p. 11543] for any significant Bragg scattering to be observed. The observed backscatter may instead be caused by another mechanism, such as rough surface scattering (RSS), but this is difficult to determine from this data since both HH and VV data were not measured (where VV would be enhanced over HH in the case of Bragg scattering).*

f_0 [GHz]	Pol.	σ^0, Bragg [dB]	σ^0, burst [dB]	σ^0
24	HH	−47	−30	−17
94	Circular	−48	−26	−12

Table 3.3: Measured values of NRCS at 24 and 94 GHz from Rahman et al. [22]. Note that the values for Bragg and burst scattering where measured at $\gamma = 3°$, whereas for whitecap scattering the measurements were made at $\gamma = 1.3°$. The results show that Bragg scattering levels are very similar at both frequencies, and that burst and whitecap scattering was somewhat greater at 94 GHz.

3.2.24 *Amplitude Distribution of Low Grazing Angle G-band Littoral Sea Clutter*, Vattulainen et al. (2023), [26]

The results of this publication, presenting results from data measured at 207 GHz, are covered later in Chapter 7 together with further results from that frequency.

3.2.25 *Doppler Characteristics of Sea Clutter at K-band and W-band: Results from the St Andrews and Coniston Water Trials*, Rahman et al. (2023), [25]

Further measurements made during the STREAM project in both St Andrews and at Coniston Water. These results are from data measured with the same radars as discussed in Rahman et al. (2022), [22], and present the Doppler statistics of data from the same trial.

3.3 Conclusions

These publications provide some indication of the behaviour of sea clutter above Ka-band, however many suffer from a lack of contextual information regarding the sea and measurement conditions. This makes it difficult to draw quantitative conclusions from the data presented, but some estimated trends are described here to summarise the findings of the collected publications. These can then be compared with results from Ka-band and below.

3.3.1 Estimated values for mean NRCS

The measured values for mean NRCS are summarised in Table 3.4. These come with a considerable number of caveats, however the general trends indicate that values averaged over one or more full waves will lie within the range −50 to −20 dB.

3.3.2 Variation with frequency

The data from Nathanson [21] would suggest that NRCS increases with frequency within the microwave range, and thus models based on this data such as the NRL model show the same, as shown in Fig. 2.24. This might then conceivably be expected to continue into W-band, however this is difficult to determine definitively from the limited number of results available. Other sources instead find a decrease with frequency, including Currie and Brown [35], Kulemin [99], Essen et al. [111], and Lamont-Smith et al. [113], the latter describing the variation of RCS as $\sigma \propto \lambda_r^{1.5}$.

Several papers have postulated that Bragg scattering will be greatly diminished or non-existent at W-band due to the lack of Bragg resonant water wavelengths of sufficiently short wavelength. Since Bragg scattering produces a spatially and temporally distributed return, the idea that this mechanism is absent is supported by observations that only wave crests were visible in data gathered by Bell et al. [110], Essen et al. [111],

Publication	f_0[GHz]	γ [°]	SS	Pol.	σ^0 [dB]
Skolnik [36]	95	1		HH, VV	∼−40
Nathanson [21]	94[a]	1 to 10	1 to 5	-	−50 to −26[b]
Kulemin [99]	75	1 to 7	-	-	−40 to −35
Makaruschka [100]	94	1.2	-	HH	−51 to −39[c]
Essen [111]	94	37.5	5[d]	-	∼−32[e]
Gregers-Hansen [84]	94	0.5	2 to 3	-	∼−45[f]
Stove [115]	94	2	3	HH, VV	−20[g]
Stove (Philips) [115]	94	1 to 10	1 to 2, 3 to 4	-	−40, −30[h]
Weidong Hu [119]	94	1.2	1 to 2	-	∼−32[e,i]
Rahman [22]	94	1.3 or 3	2 to 3	Circ.	−48 to −12[j]

Notes: [a] conflated with 35 GHz results, [b] averaged over wind/wave direction, [c] lowest crosswind, highest upwind, [d] sea state inferred from the presentation of these results with measurements of variation with wave direction where the sea state was given in [103], [e] polarisation not specified for result, [f] RCS and resolution cell size given in the paper used to calculate NRCS, [g] corrected mean values, [h] lower value for lower sea state range, [i] mean value calculated by assuming an 8 dB reduction from measurements of crests only, [j] lower value from $\gamma = 3°$ and greater value collected at $\gamma = 1.3°$ where these are for Bragg (approaching waves) and whitecap scattering (receding waves) – see Table 3.3.

Table 3.4: Summary of W-band NRCS measurements, values assumed to be for upwind/approaching waves unless otherwise stated.

Stove et al. [115], and by Rahman et al. [22], which suggest a major contribution to backscatter comes from the rough, foamy surfaces of breaking waves or from steepened wave crests. Connan et al. [104] found that capillary waves are the greatest source of scattering in wind-wave tank experiments. All of this evidence suggests that fine-scale rough water surfaces produce the greatest backscatter, implying that reflectivity at higher frequencies may see an increased sensitivity to local wind.

Lamont-Smith [105] contradicts the theory that Bragg scattering ceases at W-band by claiming that in VV polarisation Bragg scattering is dominant at all frequencies, whereas for HH it is reduced. It is possible that RSS was mistaken for Bragg scattering at higher frequencies, however this does not explain the disparity in polarisation since this could reasonably be expected to be polarisation independent. Boehmsdorff et al. [103] and Schlick et al. [107] also suggest Bragg scattering-like behaviour is still observed, as VV polarised returns are seen to be greater than HH, and that this ratio decreases with increased grazing angle. The former publication does not make this conclusion however, instead discussing how Bragg scattering becomes impossible due to the lack of water waves of a sufficient wavelength, even though the evidence is possibly contradictory. Rahman et al. [22] categorise some returns as Bragg by applying a cited methodology to the time series data, however it is possible that this category may suit other backscatter mechanisms such as RSS.

If Bragg scattering does indeed cease at mm-wave frequencies, this will cause a significant departure in terms of scattering behaviour from that seen at microwave frequencies. It has potential implications for the applicability of the K-distribution since the speckle characteristics are derived from the Bragg scattering phenomenon. It is possible however that RSS will simply replace this and provide similar speckle behaviour, albeit with potentially different parameters. Without Bragg scattering, it would be expected that VV scattering would be diminished, and the trend of VV exceeding HH at LGA would be reversed at some critical frequency, which is predicted when extrapolating some sea clutter models such as the NRL model [84].

3.3.3 Variation with grazing angle

The general observation from Table 3.4 is that the NRCS increases with grazing angle in the LGA regime. This indicates a development in understanding since the publication of Currie and Brown [35], where it was stated that no clear trend had been established at frequencies above Ka-band. Additionally, Makaruschka and Essen [100] observed that the variation with wind/wave direction became more pronounced with increasing grazing angle, and Schlick et al. [107] found that the VV to HH ratio decreases with increasing grazing angle. This last finding is also seen at microwave frequencies as shown in Fig. 2.25, as well as the general increase in NRCS with grazing angle, where this latter point implies the need for high sensitivity instruments to make LGA measurements of sea clutter.

3.3.4 Variation with sea state and wind speed

Referring again to Table 3.4, it is noted that NRCS increases with sea state when examining individual pieces of work which recorded a range of sea states. It is also noted however, that the trend becomes less consistent when comparing all measurements together; the two results from Stove et al. [115] showing a 10 dB discrepancy for sea states 3 to 4 for instance, and these both exceeding measurements by Essen et al. [111] at a much higher grazing angle and sea state, where these factors would both be expected to increase backscatter when considering results from microwave frequencies. It would be expected however, that the lack of consistency is likely due to experimental or environmental differences, where in fact the real trend would show an increase in NRCS with sea state and wind speed, as suggested by results from Fuchs [101] and Kulemin [99]. The need for accurately calibrated radars when making sea clutter measurements cannot be understated given the numerous other parameters which can affect results.

At microwave frequencies, NRCS is universally observed to increase with sea state and wind speed at LGA, as shown in Fig. 2.26. Bragg scattering dominates at low sea states, and thus if indeed there is no Bragg scattering at W-band and above then this could be expected to cause a suppression in sea clutter relative to microwave frequencies. If there is an increased sensitivity to local wind as explained above, then this may weaken the correlation between sea state and backscatter at W-band and above for the reasons explained in Subsection 2.3.4.4.

3.3.5 Variation with polarisation

The trend of NRCS with polarisation in W-band remains unclear from the data. Wetzel in Skolnik [36], Nathanson [21], and Stove et al. [115] found no significant difference between HH and VV for similar measurement conditions. Currie and Brown [35] observes that HH may be 1 to 2 dB greater than VV. Boehmsdorff et al. [103] and Schlick et al. [107] observed VV was greater than HH by up to 10 dB in the former publication.

At Ka-band frequencies and below the contribution from Bragg scattering is very strong at LGA, and as explained above if this no longer plays a role above Ka-band then it can be expected that VV returns will be comparatively suppressed. As mentioned in Subsection 2.3.4.3 the gap between HH and VV returns narrows with increasing frequency in the microwave region. It is expected that this trend will continue until at some frequency the mean value in HH will be greater than in VV at LGA, however more data are needed to prove this.

3.3.6 Variation with wind/wave direction

The highest values for NRCS are universally recorded upwind/in the direction of approaching waves. The NRCS is then seen to vary sinusoidally with wave direction, where minima are seen at crosswind and a lower maximum is observed downwind. The only dissent to this trend is from results reported in Currie and Brown [35] and shown in Table 3.1, which indicated that the crosswind reflectivity was greater than downwind. This is unlikely to be correct, since by naïve intuition it can be reasoned that the most favourable condition for backscatter would be from a surface which is at the highest grazing angle (ideally normal incidence). This surface is most likely to occur when looking upwind, and then secondarily when looking downwind, since waves present steepened crests in these direction and look somewhat similar in both directions. Looking along the crests of waves, i.e. crosswind, decreases the projected area for scattering, and thus NRCS. At microwave frequencies, the response with

wave/wind direction is typified by Fig. 2.27, where the results from mm-wave show a similar trend except for those from Currie and Brown [35].

Currie and Brown [35] suggest a total variation of ~15 dB with wave direction for sea state 3, and Makaruschka and Essen [100] also suggest a similar value of 12 dB, but do not give the sea state. Kulemin [99] finds a similar value of 10 to 15 dB for for low sea states (presumably below 4), but find a lower value of 5 to 6 dB for higher sea states which is possibly corroborated by Boehmsdorff et al. [102] with a value of 5 dB for an unspecified sea state. In a subsequent publication, Boehmsdorff et al. [103] find that the variation increases at 94 GHz compared to 35 GHz.

3.3.7 Amplitude distribution trends

The amplitude distribution is seldom reported and is a function of range resolution as well as the other parameters typically considered. Stove et al. [115] and Weidong Hu et al. [119] measured the distribution to be spikier in HH polarisation than VV. Stove et al. fitted K-distributions to the data with shape parameters ν 0.2 to 0.3, which are interestingly greater than the value of 0.03 fitted to data from Gregers-Hansen et al. [84] for a range resolution an order of magnitude larger. The latter discrepancy is probably due to the very low grazing angle of 0.5° for the NRL data, which can be expected to increase spikiness. Additionally, Essen et al. [111] report that the clutter appears roughly K-distributed and that the distribution had a dynamic range of 23 to 24 dB for a range resolution of 20 cm.

At microwave frequencies, HH is similarly seen to be spikier than VV. The values for shape parameter ν seen for mm-wave are very low compared to microwave, however this could be due to both the frequency and the finer range resolution more easily achievable at mm-wave and above.

This chapter reviewed the trends in sea clutter amplitude statistics above Ka-band, which will provide context for the later analysis of G-band sea clutter. The next chapter discusses the design of the new G-band radar built during this project. This begins with the final element of the literature review summarising the prior art of radar in this frequency range, which is then followed by the design specifics of the new radar.

4

G-band Doppler Radar Design

THIS chapter discusses the development of a new 207 GHz Doppler radar named 'Theseus'[1] produced as part of this Ph.D. It first discusses the motivation for developing an instrument operating in the sub-THz region, and then presents a literature review on G-/Y-band systems to contextualise the technological achievements. The final section then presents the design of the radar system and its antennas. The results of the characterisation and final testing of the system are then shown in Chapter 5. Some of the substance of this chapter has been adapted from two publications on the radar system, Vattulainen et al. (2022) [23] and Vattulainen et al. (2024) [29], mainly in Sections 4.1 and 4.2, but otherwise indicated where appropriate.

As will be shown in the review of G-/Y-band systems in Section 4.2, radars operating in this frequency range with any significant Doppler measurement capability remain a rarity. The specific implementation of the radar described in this chapter and Chapter 5 as a solid-state and field-ready instrument is yet more novel, where the measurement capability is expected to be of increasing importance as interest in this frequency region for radar uses grows.

The design and development of this radar was a collaborative effort between the author and his supervisors Prof. Duncan A. Robertson and Dr Samiur Rahman. Specifically, the survey of G-/Y-band radars presented in Section 4.2 was produced by the author; the system performance modelling shown in Subsection 4.3.1 was undertaken by the author; the radio frequency (RF) architecture of the system described in Subsection 4.3.3 was designed by Prof. Duncan A. Robertson; the design of the Gaussian optics lens antennas (GOLAs) presented in Subsection 4.3.5 was produced by Dr Samiur Rahman; the data processing software describe in Subsection 4.3.4 was developed by

[1]The radar was developed in several iterations which reused parts from an older instrument, where subsequent revisions replaced further components until very little of the original remained, like the Ship of Theseus.

Dr Samiur Rahman; and the mechanical designs for the antennas and radar enclosure shown in Subsection 4.3.6 were produced by the author.

4.1 Motivation for radar at G-band

Operating at G-band (140 to 220 GHz) provides the general benefits of resolution gains, sensitivity to surface texture, and more compact sensor sizes associated with sub-THz instruments as outlined in Chapter 1. As such, there is a growing interest in sensing in this region, including applications like meteorology, security screening, environmental sensing, target detection, and situational awareness – these latter two cases being the primary motivations of this thesis. As shown in Fig. 2.5, at the upper end of G-band lies an atmospheric attenuation window (often known as the '220 GHz window') on the upper flank of the water absorption line at 183 GHz, where aiming for operation in this region will reap the benefits associated with this frequency regime whilst mitigating the deleterious effect of the atmosphere on SNR. The lowest absorption in this window occurs at ~213 GHz for any significant humidity, and so operating near this frequency is preferable. Referring also to Table 2.1, the 220 GHz window is also within the overlapping Y-band, however for brevity this thesis will refer only to G-band when discussing this region.

As explained in Chapter 1, the renewed interest is in part being driven by an increasing availability of key signal generating components as a result of the drive towards sub-THz frequencies for 6G communications. Research and development of radar systems at these frequencies had previously been hampered by the lack of affordable components and their modest performance, and as such there is a comparative lack of data in most areas of phenomenological research at G-band. As such, the development of this instrument was motivated by the need to gather data of sea clutter and marine targets at sub-THz frequencies for the STREAM project, but also as a general purpose instrument to carry out research at these frequencies as interest continues to increase. These data can be used to guide the design of future instruments and thus should be valuable for others working in this field.

4.2 G-band radar prior art

Components generating signals near the 220 GHz window use either G-band or Y-band waveguide for transmission. Working in either frequency band poses similar technological challenges, thus instruments operating in either G- or Y-band near the 220 GHz window are included in this review.

4.2.1 Early G-/Y-band radars

The oldest published radar system operating in this frequency region found during this review dates from 1981 and was published by Nemarich et al. [122][2]. That radar system operated at both 140 GHz and 225 GHz (with two different front-ends), and was used to measure the backscatter from falling snow and the RCS of a tank. A subsequent publication featuring the same system describes measurements of falling snow and rain in Nemarich et al. [123]. Each transmitter in this system was based on a pulsed extended interaction oscillator (EIO) vacuum tube.

Other radars similarly based on these vacuum tubes have been published:

- 1987: a 140 GHz instrumentation radar for general phenomenology studies, published in Currie and Brown [35, p. 58].
- 1988-1989: a 215 GHz system used for measuring backscatter from trees and fog, as well as absorption by clouds [124] [125] [126].
- 1990-1991: a 225 GHz radar making polarimetric measurements of trees and natural surfaces [127] [128] [129].
- 1991: the first coherent radar at 225 GHz, used for research into target detection and the Doppler signatures of vehicles [130].

The research in these publications was motivated by the increased sensing potential at these frequencies, as discussed above and in Chapter 1. Additionally, Mead et al. [126] explains that smaller sensor sizes at these frequencies are beneficial for airborne platforms – similarly limited in size and weight as small and medium-sized ASVs – as well as more sensitive to small hydrometeors. The general theme is of initial phenomenological research exploring the sensing possibilities at these frequencies, made newly accessible by high power vacuum tubes.

4.2.2 Published instruments since 2007

After the flurry of publications in the late 1980s, there is a significant gap in publishing until 2007, when a 220 GHz radar for inverse synthetic aperture radar (ISAR) and concealed object detection was presented. That application was no doubt stimulated by the increased awareness of terror threats to public safety, precipitating the need for through clothing imaging to detect weaponry and suspicious packages. That radar is especially noteworthy as being the first FMCW G-band radar, made practicable by newly developed millimetre-wave monolithic integrated circuit (MMIC) chips used

[2] It is possible that other systems may pre-date this publication but were not widely reported.

Year	f_0 [GHz]	Mode	Application	Doppler	Ref.
2008	228	FMCW	monitoring of vital signs	no	[136]
2009	228	CW	monitoring of vital signs	no	[137]
2010	190	FMCW	concealed object detection	no	[138]
2012	200	SFCW	general purpose	no	[139]
2012	200	SFCW[a]	concealed object detection	no	[140]
2013	240	FMCW	imaging, material characterisation	no	[141]
2013	140	FMCW	ISAR imaging	yes	[142]
2014	215	FMCW	imaging, interferometry	yes	[143]
2014	200	SFCW	concealed object detection	no	[144]
2014	220	SFCW	ISAR imaging	yes	[145]
2014	215	SFCW[a]	situational awareness	no	[146]
2016	220	FMCW	concealed object detection	no	[147]
2016	240	FMCW	imaging, concealed object detection	no	[148]
2016	222	SFCW[a]	environmental phenomenology	no	[149]
2017	220	FMCW	SAR imaging	no	[150]
2017	238	pulsed	cloud-profiling	no	[151]
2017	228	FMCW	environmental phenomenology	no	[152][c]
2018	170[b]	FMCW	DAR	no	[153]
2019	220	pulsed	InISAR volumetric imaging	yes	[154]
2022	199.5	pulsed	Doppler cloud-profiling	yes	[155]
2023	223	FMCW	situational awareness	no	[16][c]

Notes: [a] VNA based radars, [b] the centre frequency of this system was changed to this value in subsequent publications, [c] different iterations of the same system.

Table 4.1: A summary of the G-/Y-band solid-state radars developed since 2008.

for a frequency doubler, LNA, and a subharmonic mixer at 220 GHz [131] [132] [133]. The benefits of solid-state components precipitated renewed interest in this frequency band as larger bandwidths are more easily achieved at high frequency and in FMCW operation. Previous vacuum tube based instruments also suffered from the general limitations of that technology, in that they are expensive, bulky, heavy, and have significant power and cooling overheads as well as more limited lifetimes, making the continued development and maintenance of these radars more difficult to justify.

A steady flow of solid-state systems then followed until the present day in various configurations, as shown in Table 4.1. The only vacuum tube based radar recently developed is ViSAR, a 235 GHz SAR system capable of generating high resolution imagery at video rates. In that case, the system sought to capitalise on the shorter aperture baselines required at this frequency to decrease frame latency. That necessitated the use of a travelling wave tube source for sufficient link-gain given that the instrument was intended for an airborne platform [134] [135].

Newer solid-state systems listed in Table 4.1 of particular interest include two for meteorological measurements: the VIPR differential absorption radar (DAR) utilising the rapid change in atmospheric loss near the 183 GHz water absorption line to estimate humidity within clouds by comparing the signal levels between transmission at 167 GHz and 174.8 GHz [153] [156] [157] [120]; and the Doppler cloud-profiling radar GRaCE, which is designed to measure the vertical wind speeds and drop size distributions of rain for lower rain rates and drop sizes than was previously possible at lower frequencies [155].

Notably with regards to the motivation of the STREAM project, there has been research into the use of G-/Y-band radar for terrestrial situational awareness. The latest publication is of a 223 GHz mechanically scanned imaging radar proposed as a future alternative to lidar sensing in terrestrial autonomy [16]. This publication builds on previous work from the same group in developing the radar and in the characterisation of different surfaces such as roads and buildings [146] [149] [152].

To the author's knowledge, this review represents the full extent of the published reports of systems operating in the G-/Y-bands. Despite the enormous sensing potential of this frequency region, there are still comparatively few radars designed in this range due to the challenges in SNR and expense outlined above. As signal generating components become more widely available and the THz-gap closes however, exploitation of this band will inevitably increase and so phenomenological research in this band now is of great value. Of the summarised systems above, only a small fraction are coherent with a high enough CRF or pulse repetition frequency (PRF) to measure significant Doppler velocities [134] [135] (a vacuum tube-based design) [142] [143] [145] [154] [155] (solid state radars), indicating a clear opportunity for research on Doppler phenomenology especially.

4.3 Radar design

The system design began by identifying the required performance specification and features for the instrument. The main goal of the instrument was to measure sea clutter and marine targets, where it was expected that in terms of signal level the limiting factor would be the NRCS of the sea surface since the RCS of targets is generally much greater. The NRCS was estimated from measurements made by Stove et al. [115] and Nathanson's tables [21, pp. 275–278] to be ∼−30 dB at 94 GHz, where this was the closest available measured frequency at the time. Additionally, it was estimated that a maximum Doppler velocity of $\sim \pm 5\ \mathrm{m\,s^{-1}}$ would be sufficient to measure the signatures of waves and most marine targets without aliasing. This estimate was based

on published X-band measurements, such as are shown in Rosenberg and Watts [13, Section 2.5].

To be in keeping with the majority of the literature, measurements of sea clutter should ideally be made of sea surfaces for deep water in the open sea to be most consistent with the definition of sea state. Due to the estimated range of the instrument being much less than a typical marine radar, to achieve this condition the sensor would need to be mounted on a vessel. This approach would however be both logistically difficult to achieve and would make the data analysis more complicated, as the effects of the motion of the platform on the data would be difficult to compensate. For these reasons it was decided that measurements of the sea would be made from the shore, where locations with deep water nearby were desirable to provide the best compromise. It was also reasoned that given the intended application, measurements closer to shore in the littoral zone would still be very relevant for situational awareness. As such, good candidate trial locations would be places such as harbours or quays, as these provide good access for vehicles and areas to set up equipment whilst also having deep water nearby. The drawback to these structures is that they are often quite high above the water. Since for this application it was desirable to measure sea clutter at LGA, and given the relationship between γ and h shown in Eq. 2.15, maximising the range would add additional flexibility to choice of trial location, as well as providing increased sensitivity at closer ranges.

4.3.1 System performance modelling

Given the multiple parameters which influence sensitivity, and knowing that sensitivity will decrease with range as shown in the radar range equation (Eq. 2.16), the radar performance is modelled in terms of clutter to noise ratio (CNR) and SNR and how these vary with range. This analysis first considers CNR since this is expected to be the limiting factor, as explained above. The CNR can then be used to define the required system performance such that measurements of sea clutter can be made at an acceptable range. The CNR, $\mathcal{C}$, is defined in Eq. 4.1:

$$\mathcal{C} = \frac{P_c}{N_r} \tag{4.1}$$

for a clutter power P_c (as measured at the output of the receiver) and a receiver noise power of N_r (equivalent to N_{out} in Eq. 2.23). The clutter power is expressed in Eq. 4.2:

$$P_c = \frac{P_t G_t G_r {\lambda_r}^2 A_r L_{at} \sigma^0 G_{rec}}{(4\pi)^3 R^4} \tag{4.2}$$

where A_r is the range-gate limited beam footprint area approximated by Eq. 2.44, valid for small beamwidths and low grazing angles as is the case for the application in question, and G_{rec} is the linear gain of the receiver (and is equivalent to G_{lin} in Eq. 2.23). The other parameters in Eq. 4.2 are as defined as for the RRE in Equations 2.16 and 2.34.

The approximate antenna gain resulting from one-way azimuthal beamwidth can be derived using the definitions of antenna gain (Eq. 2.31) and directivity, and the approximation for beam solid angle (Eq. 2.29). Combining these expressions results in Eq. 4.3:

$$G_A = DL_A = \frac{4\pi L_A}{\Omega_A} \approx \frac{4\pi L_A}{\phi_1 \theta_1} \tag{4.3}$$

where assuming that the beam is symmetric i.e. $\phi_1 = \theta_1$, and using the relation between the one-way and two-way beamwidths $\phi_2 = 1/\sqrt{2}\phi_1$, the antenna gain can be expressed in terms of the the two-way beamwidth as shown in Eq. 4.4:

$$G_A \approx \frac{2\pi L_A}{{\phi_2}^2} \tag{4.4}$$

Combining Equations 4.2, 2.44, and 4.4 then gives the expected clutter return power for the range-gate limited case for small beamwidths and low grazing angles, shown in Eq. 4.5:

$$P_c \approx \frac{P_t {\lambda_r}^2 \Delta R {L_A}^2 L_{at} \sigma^0 G_{rec}}{16\pi {\phi_2}^3 R^3} \tag{4.5}$$

where the gain of the transmit and receive antennas has been assumed to be equal. Here it is noted that the dependence on range from Eq. 2.44 gives Eq. 4.5 a $1/R^3$ relationship. Equation 4.5 and the expression for receiver noise given by Eq. 2.23 (where here $N_{out} = N_r$) are then substituted into Eq. 4.1 to give Eq. 4.6:

$$\mathcal{C} \approx \frac{P_t {\lambda_r}^2 \Delta R {L_A}^2 L_{at} \sigma^0}{16\pi (F-1) k_B B_N T_0 {\phi_2}^3 R^3} = \beta_C \frac{L_{at}\sigma^0}{R^3} \tag{4.6}$$

noting that the terms for receiver gain, G_{rec}, cancel. The radar system constant for clutter performance β_C is then defined by Eq. 4.7:

$$\beta_C = \frac{P_t {\lambda_r}^2 \Delta R {L_A}^2}{16\pi (F-1) k_B B_N T_0 {\phi_2}^3} \approx \frac{\mathcal{C} R^3}{L_{at}\sigma^0} \tag{4.7}$$

The value of the system constant can then be used to guide the values that the system parameters can take when constrained by the required CNR at a given range for clutter

with a specific NRCS.

Some of these parameters can now be defined:

- λ_r: the frequency should be as close as possible to the atmospheric window discussed above (with a minimum close to 213 GHz). For this model, this is set to be 207 GHz, where the technological reasons for this exact value are explained later in Subsection 4.3.3.
- ΔR: ideally a fine range resolution is used as may be required for marine autonomy. This was chosen to be 7.5 cm (equivalent to a signal bandwidth of 2 GHz).
- ϕ_2: the beamwidth was chosen to be similar to another radar used for field trials so that comparison of data would be more straightforward. The target value was set to be 1.41° (or 2° one-way beamwidth). For Eq. 4.7, this is expressed in radians.
- L_A: the antenna loss will be minimised as much as possible, however a nominal expected value of 1 dB is assigned.
- T_0: the reference temperature, which is taken to be the standard value of 290 K.
- L_{at}: this is calculated for a pressure at sea level of 101325 Pa, temperature of T_0, and a relative humidity of 60% which is equivalent to a water vapour density of 8.60 g m^{-3}, calculated using Eq. (D.2) in Speirs [44, p. 295].

The approximate value for the noise bandwidth B_N can also be determined from the required v_{max}. The minimum CRF needed for a $v_{max} = \pm 5$ m s^{-1} can be determined from Eq. 2.51 to be ~13.81 kHz. The CRI is the inverse of the CRF as discussed in Subsection 2.1.10, and thus CRI $\approx$ 72.41 µs. This implies a maximum t_c of 72.41 µs since by definition CRI $\geq t_c$. From Eq. 2.54, the sampling rate also depends on the required $R_{max,I}$ and ΔR. For a nominal maximum range of 150 m, the range resolution specified above, and an estimated sampling rate of 80 MHz (where this is a plausible but not excessive sampling rate for an ADC) then t_c is further narrowed down to a minimum value of ~50 µs. The IF FFT resolution, Δf_{IF}, is then derived from the inverse of the chirp time as shown in Eq. 2.8, for a maximum value of ~20 kHz. As shown in Eq. 2.25, B_N is then determined from Δf_{IF} by specifying a window function and thus a noise bandwidth factor, B_w, which for this model is taken to be 2.0045 as for the −92 dB Four-Term Blackman-Harris window [158, p. 105]. This gives the final noise bandwidth estimate of $B_N \approx 40$ kHz.

The remaining parameters are then constrained by the system constant, their exact realised values depending on the performance and affordability of components. Given

the estimated NRCS of −30 dB and a desired minimum CNR of 10 dB at a range of 100 m, this indicated a necessary system constant value of $\beta_C = 100.6$ dB, as shown by the curve in Fig. 4.1. After accounting for the approximately fixed parameters listed above, the remainder is ∼−18.5 dB, meaning that a ratio of $P_t/(F-1)$ (designated as a figure of merit) greater than this is needed for the desired performance. The system constant was then used to model the CNR with range via Eq. 4.6, where this curve is also shown in Fig. 4.1.

Given that targets are also of interest, a similar system constant can be defined in terms of the SNR, $\mathcal{S}$. The SNR is first defined as shown in Eq. 4.8:

$$\mathcal{S} = \frac{S}{N_r} \tag{4.8}$$

where the output signal power from the receiver due to a target is S. The system constant, β_S, is then introduced in the same manner as shown in Eq. 4.6, giving Eq. 4.9:

$$\mathcal{S} \approx \frac{P_t {\lambda_r}^2 {L_A}^2 L_{at} \sigma}{16\pi(F-1)k_B B_N T_0 {\phi_2}^4 R^4} = \beta_S \frac{L_{at}\sigma}{R^4} \tag{4.9}$$

noting that for targets, the range dependence is R^{-4}. The system constant is defined for SNR as:

$$\beta_S = \frac{P_t {\lambda_r}^2 {L_A}^2}{16\pi(F-1)k_B B_N T_0 {\phi_2}^4} \approx \frac{\mathcal{S}R^4}{\sigma L_{at}} \tag{4.10}$$

relating to the system constant for clutter as:

$$\beta_S = \frac{\beta_C}{\Delta R \phi_2} \tag{4.11}$$

For the value of β_C at 100 m, this gives $\beta_S \approx 128$ dB. Assuming an RCS of 0 dBsm, the SNR is then modelled using Eq. 4.9, and also shown in Fig. 4.1. The curve suggests an SNR of ∼47.3 dB at 100 m, indicating good performance for measuring targets is also achieved with the performance needed to satisfy the CNR requirements.

In addition to the Doppler sampling and sensitivity requirements discussed above, the additional features needed for the instrument were:

- **Configurable polarisation:** clutter and target phenomenology require the measurement of the response to different polarisations, where for this radar these were chosen to be configurable as HH, VV, VH, or HV. It was decided that this would be achieved by physically changing the antenna orientations and

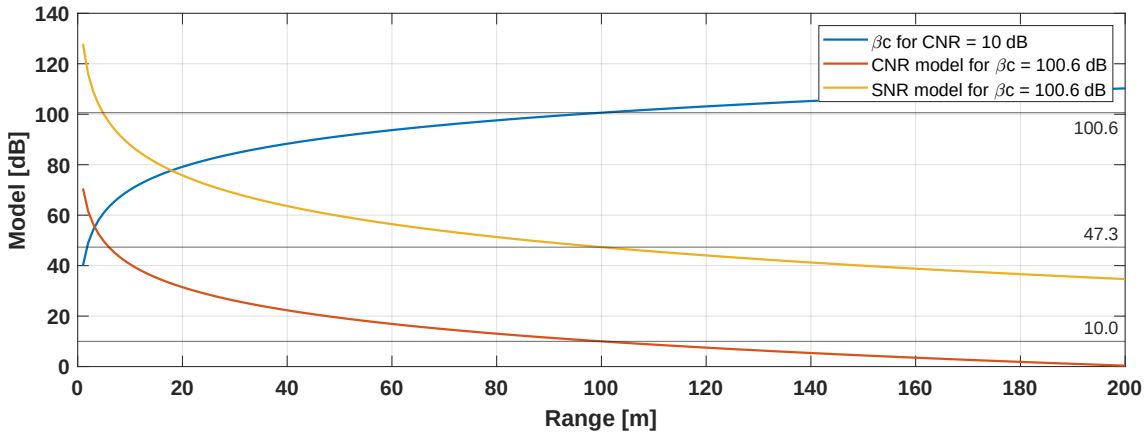

Figure 4.1: Plot showing modelled curves against range for the system constant for clutter, β_C, for an NRCS of −30 dB and a CNR of 10 dB, and the resulting CNR and SNR curves for a $\beta_C = 100.6$ dB as needed to produce a CNR of 10 dB at 100 m.

then connecting these with either a waveguide straight or 90° section, such that a circulator was not necessary and thus a loss term for this component was not included in the model shown in Fig. 4.1.

- **Flexibility in centre frequency:** not strictly necessary for the application, but additional flexibility for exploring the change in target and clutter response with frequency is a bonus.
- **Low power consumption:** choosing a low power consumption design reduces system complexity and logistics for field deployment.
- **Compact with full enclosure:** originally designed to fit within the yoke of a 2-axis gimbal, a relatively small size was necessary for easier manoeuvrability during field trials. A full enclosure provides some degree of weather protection and RF shielding for the system.
- **Switchable internal and external triggering:** the radar needed the capability to switch between triggering modes for collecting data in both staring and scanning modes. Staring mode data collection was to be achieved using an coherently related trigger signal derived from the core oscillator of the chirp generator. The scanning mode trigger signal would then be derived from an external azimuth scanning mechanism to ensure correct sampling as a function of angle.

Given the complexity and high degree of interdependence of the features and numerous performance characteristics, there are many different trade-offs to consider when designing such a system. The summary here then presents an abridged version of the design process, where in reality this involved iteration of designs in response to different design challenges becoming apparent during the development process.

4.3.2 Waveform design

The final waveform design was required for setting the sampling rate, f_s, of the ADC and to determine the maximum instrumented range, $R_{max,I}$. This was predominantly guided by the desired measurement performance for v_{max}, $R_{max,I}$, and ΔR. This description is presented as a chain of steps, however similar to the performance modelling shown in Subsection 4.3.1, in reality this process was not as linear as described and included some iteration of the free parameters to arrive at the final optimised values shown.

The design process began by specifying the clock frequency for the DDS board used to generate the chirp. A 3.5 GHz oscillator was chosen for this design, which determined the digital ramp generator (DRG) frequency for the DDS board model to be used (Analog Devices AD9914) as shown in Eq. 4.12.

$$f_{DRG} = f_{CLK}/24 \tag{4.12}$$

The first of two coherency requirements stipulates that the sampling frequency f_s is required to be an integer fraction of the DRG update rate f_{DRG}, such that:

$$f_s = \frac{f_{DRG}}{n}, \quad \text{for } n \in \mathbb{Z} \tag{4.13}$$

and where additional boundaries on f_s are imposed by the desired v_{max} of $\pm 5\ \mathrm{m\,s^{-1}}$. As shown above, this is introduced via Eq. 2.51, shown again here for convenience:

$$v_{max} = \frac{\mathrm{CRF}c}{4f_0}$$

where the v_{max} limits the CRF, which in turn limits t_c and then f_s. As reasoned above, v_{max} sets a lower bound on the CRF of ~13.81 kHz, and thus an upper bound on the CRI of CRI $\approx$ 72.41 µs. This further implies a maximum bound on t_c, since CRI $\geq t_c$, where in this case t_c must be less than the CRI due to a short period of dead time between chirps required by the DDS board of ~1 µs.

Next, the desired $R_{max,I}$ and ΔR were used to determine the approximate number of range bins per measurement. This relationship is shown in Eq. 4.14:

$$R_{max,I} = N_{FFT}\Delta R = \frac{N_{FFT}c}{2B_S} \tag{4.14}$$

For the desired performance of $R_{max,I} \approx 150$ m and $\Delta R \approx 0.075$ m (from $B_S = 2$ GHz), this implied an $N_{FFT} \approx 2000$. To increase the efficiency of the FFT used to process the data, the number of samples per chirp i.e. in a single ranging measurement was chosen to be a power of two, namely 4096. Each range cell corresponds to a double sided

bandwidth measurement, however only real samples are collected in this design (not I-Q), and thus the negative frequency half of the FFT spectrum is discarded, hence the number of range cells is half the number of samples i.e. $N_{\text{FFT}} = 2048$. For a bandwidth of 2 GHz and thus a range resolution of ~0.075 m, the maximum instrumented range is then ~153.5 m.[3]

The N_{FFT} then imposes a minimum bound on f_{s} via the relationships shown in Equations 2.53 and 2.8, repeated here for convenience:

$$f_{\text{s}} > 2f_{\text{IF,max}}$$

$$\Delta f_{\text{IF}} = \frac{1}{t_{\text{c}}}$$

and additionally Eq. 4.15:

$$f_{\text{IF,max}} = \Delta f_{\text{IF}} N_{\text{FFT}} \tag{4.15}$$

which are combined together to give Eq. 4.16:

$$f_{\text{s}} > 2f_{\text{IF,max}} = 2\Delta f_{\text{IF}} N_{\text{FFT}} = \frac{2N_{\text{FFT}}}{t_{\text{c}}} \tag{4.16}$$

The inequality in Eq. 4.16 along with the maximum bound on t_{c} from above of ~71.46 μs then determined the minimum desired f_{s} to be 57.359 MHz. The impact of the choice of f_{s} on $R_{\text{max,I}}$ is also seen directly in Eq. 2.54. The sampling frequency is also subject to a second coherency constraint with respect to the CRF as shown in Eq. 4.17:

$$\text{CRF} = \frac{f_{\text{s}}}{m}, \quad \text{for } m \in \mathbb{Z} \tag{4.17}$$

and where also the achievable f_{s} is upper bounded ultimately by budget, since a greater sampling frequency increases the cost of ADC cards. This latter consideration, along with the coherency constraints, defined a final sampling frequency of $f_{\text{s}} = 79.5494$ MHz. The corresponding t_{c} determined by Eq. 4.16 was then 51.49 μs. The short period of dead time gave a minimum CRI of ~52.49 μs, which along with the coherency constraint in Eq. 4.17 produced a realised value of CRI = 67.59 μs, where the integer in Eq. 4.17 was chosen such that the realised CRI was as close as possible to the minimum whilst still being either greater than or equal to this value, as this

[3]The actual range resolution is very slightly less than 0.075 m as the speed of light is $<3 \cdot 10^8$ m s^{-1}, making the true maximum instrumented range slightly less that $2048 \cdot 0.075 = 153.6$ m.

maximised the CRF and thus the achievable v_{max} to be 5.3568 m s^{-1}.

4.3.3 System architecture

The first iteration of this design was published in [23], where following subsequent upgrades the final version of the design was published in [29]. The design reuses core elements of a previous instrument published in [147].

The system block diagram for the Theseus radar is shown in Fig. 4.2. In keeping with the Motivation in Chapter 1 and the requirement for low power consumption, the radar was developed as an FMCW design. The instrument was divided into six subsystems: the chirp generator, transmit chain, receive chain, antennas, IF chain, and divider chain. The frequency multiplication scheme of the radar is summarised in Table 4.2. The radar is capable of operation at centre frequencies of either 201 GHz or 207 GHz, named low and high band respectively.

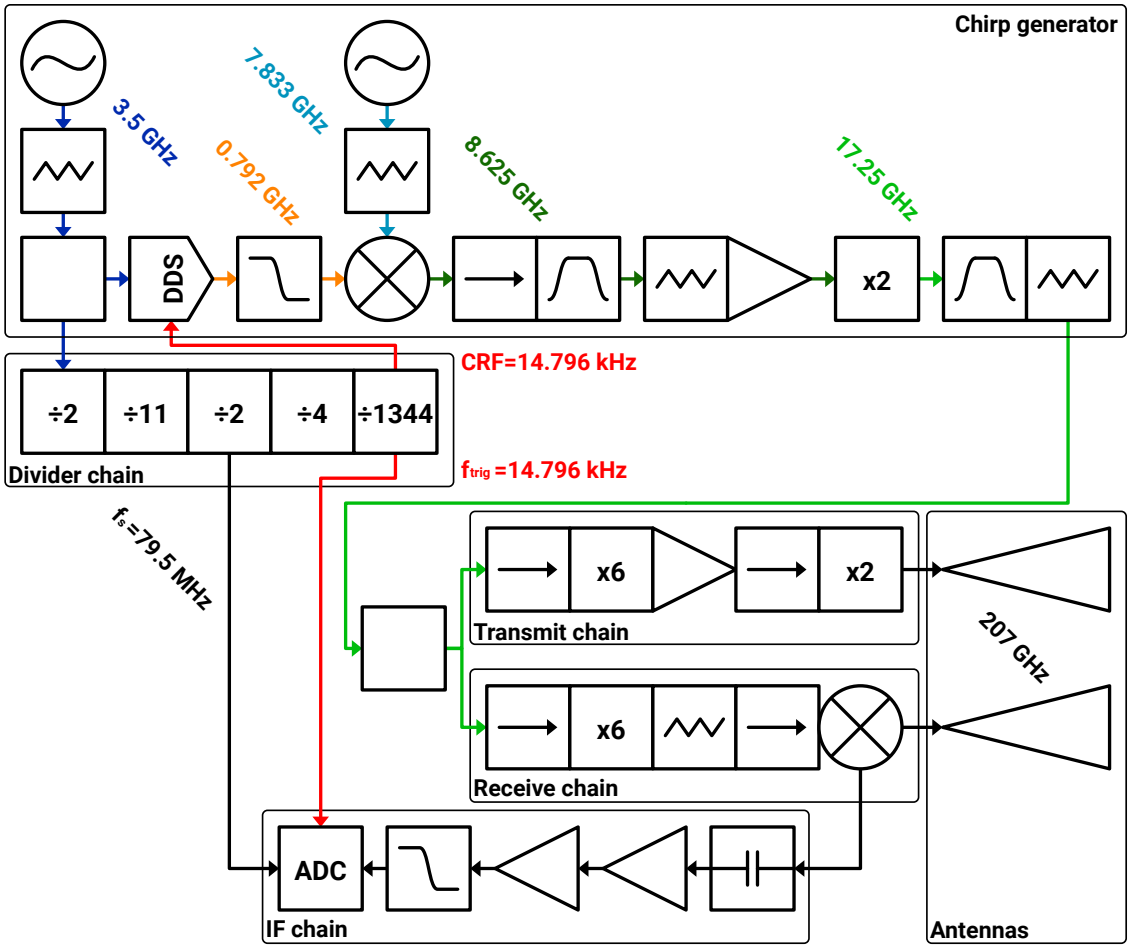

Figure 4.2: The block diagram for the Theseus radar, where the annotations indicate the output frequency from key stages for a final centre frequency of 207 GHz.

		Low band [GHz]			High band [GHz]		
Stage	Factor	f_{min}	f_0	f_{max}	f_{min}	f_0	f_{max}
f_{DDS}	-	$0.500\dot{3}$	0.542	$0.583\dot{6}$	$0.750\dot{3}$	0.792	$0.833\dot{6}$
f_{mix}	2	$8.\dot{3}$	8.375	$8.41\dot{6}$	$8.58\dot{3}$	8.625	$8.\dot{6}$
f_{CG}	6	$16.\dot{6}$	16.75	$16.8\dot{3}$	$17.1\dot{6}$	17.25	$17.\dot{3}$
f_{RF}	2	200	201	202	206	207	208

Table 4.2: The frequency multiplication scheme of the Theseus radar for low and high band operation. Values for f_{mix} are derived by upper sideband mixing with an LO frequency of 7.833 GHz.

4.3.3.1 Chirp generator

A description of the chirp generator was first published in Vattulainen et al. (2022) [23]. This was subsequently upgraded to the version published in Vattulainen et al. (2024) [29], where the material in this subsection expands on that presented there. The chirp generator consists of:

- Microwave Dynamics DRO-1000-03.50 3.5 GHz dielectric resonator oscillator (DRO).
- 10 dB attenuator.
- ATM P214 power splitter.
- Analog Devices AD9914 DDS board.
- Mini-Circuits VLF-1200 low-pass filter (LPF).
- Avantek DBX-1221 mixer.
- Nexyn NXOS-0783-01761 7.833 GHz DRO with 6 dB attenuator on mixer LO.
- ATM ATi 6-12 isolator.
- Aaren cavity band-pass filter (BPF) AT22F-A238-AF 8.3 to 9.6 GHz.
- 4 dB attenuator.
- Mini-Circuits ZX60-183-S+ amplifier.
- Analog Devices Hittite HMC814LC3B frequency doubler.
- Aaren cavity BPF AT22F-WT481-AF 15.4 to 17.5 GHz.
- 6 dB attenuator.
- Aaren AT30A-124180J-2-AF power splitter.

The LFM chirp waveform is created using a DDS board clocked from a 3.5 GHz DRO stable local oscillator (STALO), generating the chirp frequencies shown in Table 4.2. The bandwidth of the DDS signal f_{DDS} at this stage is $83.\dot{3}$ MHz. Chirp generation with a DDS board produces very linear and low phase noise waveforms which prevents degradation of the range and Doppler resolutions. This signal is filtered to remove

harmonics produced by the DDS signal generation process.

The LFM waveform is then upconverted with a 7.833 GHz Nexyn NXOS-0783-01761 DRO STALO using the upper sideband, expressed mathematically in Eq. 4.18:

$$f_{\text{mix}} = f_{\text{DDS}} + f_{\text{LO}} \tag{4.18}$$

The previous iteration of the design published in Vattulainen et al. [23] used lower sideband mixing on a Micro Dynamics DRO-1000-05.56 5.567 GHz DRO with an additional doubling stage in the chirp generator. That was replaced with the Nexyn model to reduce the transmitter phase noise, which was found to be problematic when observing bright scatterers. The details of the upgrade are included in Section 5.3.3.

To minimise transmitter phase noise resulting from frequency multiplication (see Eq. 2.63), the upconversion STALO frequency should be maximised. Since the ×6 multipliers in the transmit and receive arms accept an input of ~17 GHz, ideally the STALO frequency would be ~16 GHz such that after upconversion the input signal to the multipliers approaches the maximum. In this instance however, the Nexyn unit was already available to use, and the convenience and cost saving was deemed to be an acceptable compromise.

Following upconversion, the mixer output signal f_{mix} is filtered, amplified, and frequency multiplied by a factor of 2 to produce the output signal from the chirp generator f_{CG}. The filtering stages remove harmonics which are introduced during mixing and frequency multiplication, ensuring signal purity. The chirp generator amplification stage ensures that the signal level supplied to both the transmit and receive chain multipliers is high enough to drive them at saturation after being split equally between the two arms. The bandpass filter after the mixer has a lower passband edge of ~8.3 GHz, which then imposes a minimum frequency output limit of ~16.6 GHz on the chirp generator.

4.3.3.2 Transmit chain

The design of the transmit chain was first described in Vattulainen et al. (2022) [23] and again covered in Vattulainen et al (2024) [29]. The transmit chain consists of:

- Innowave 11831S-1 isolator.
- Quantum Microwave QMC-MX6-10F10 ×6 frequency multiplier.
- Spacek Labs SPW-10-20 power amplifier (PA).
- Micro Harmonics Corporation FR100M2 isolator.
- Virginia Diodes Inc. (VDI) D200 frequency doubler.

In the transmit chain, the output of the chirp generator drives one of two identical Quantum Microwave ×6 frequency multipliers which produce an output in the high W-band range. These multipliers are driven at saturation to minimise the variability of output power during the chirp frequency sweep. On transmit, a Spacek Labs PA is used to maximise the signal power at W-band. The availability of PAs which can output signals with a power over 20 dBm much beyond 100 GHz is extremely limited, where components providing performance beyond that of the Spacek model are subject to breakpoints in cost, bulk, and power consumption which are prohibitive. This then becomes the limiting factor in the final output power of the system, as the VDI varactor doubler later in the chain can accept higher input powers than can be produced by the PA. Since the power output of the PA also drops with increasing frequency, this imposes an upper limit on the maximum viable centre frequency when considering the CNR modelling above. Due to this limitation, the centre frequency of the radar is set to 207 GHz for an upper band edge of 208 GHz in high band rather the ideal centre of ~213 GHz. The results of the measured output power with frequency for the PA are shown in Subsection 5.1.5.

At the output of the PA is a Micro Harmonics isolator which prevents reflected power from the doubler damaging the PA. The VDI doubler represents the state-of-the-art, and multiplies the W-band signal to G-band. This type of doubler can typically accept drive powers in the range 500 to 1000 mW (27 to 30 dBm), however this unit has been optimised to run at the lower drive level produced by the PA without significant loss of efficiency. The transmitted signal frequency f_{RF} has then undergone a total multiplication factor of ×24 since the output from the upconversion mixer. Given the limitation on minimum frequency due to the BPF in the chirp generator mentioned above, the minimum accessible frequency for the radar is ~200 GHz which defines the lower edge of the low band range.

4.3.3.3 Receive chain

The receive chain was first described in Vattulainen et al. (2022) [23] and again covered in Vattulainen et al (2024) [29]. The receive chain consists of:

- Innowave 11831S-1 isolator.
- Quantum Microwave QMC-MX6-10F10 ×6 frequency multiplier.
- Quantum Microwave QMC10-ATT04 WR-10 4 dB waveguide attenuator.
- Micro Harmonics Corporation FR100M2 isolator.
- Farran SPM-05-0002 G-band sub-harmonic mixer (SHM).

As mentioned above, the split signal coming from the chirp generator to the receive

chain is also frequency multiplied by a factor of ×6. The output from the multiplier is attenuated by 4 dB before passing through another Micro Harmonic isolator on the LO input of a Farran SHM used for homodyne detection with the second harmonic. The resulting IF frequencies have a bandwidth equal to f_{DDS}. The isolator prevents reflections from the SHM causing damage to the multiplier or from producing ringing in the DC response of the SHM as the frequency is swept. The attenuator is used to level set the drive power to the SHM to ensure it is not damaged by excessive power or subject to loss of conversion efficiency due to being LO-starved. The choice of the SHM to perform de-chirp on receive means that a second frequency multiplication stage is not required to produce the mixer LO signal. This design choice is in common with many other systems in this frequency range, such as published in Cooper et al. [159] and Muppala et al. [16], and reduces the cost and complexity of this system by replacing a second doubler and G-band mixer.

4.3.3.4 IF chain

The IF chain is first described in detail in Vattulainen et al. (2024) [29]. The IF chain consists of:

- Mini-Circuits BLK-18 DC block.
- Wenteq Microwave Corp. ABL0050-00-3310 LNA.
- Mini-Circuits ZFL-500HLN amplifier.
- Mini-Circuits SLP-30 LPF.

The primary purpose of the IF chain is the amplify the signal from the receiver to best utilise the −1 to + 1 V dynamic range of the ADC. The maximum IF was first determined from the desired sampling frequency of 79.5494 MHz to be 39.7747 MHz according to Eq. 2.53. This then dictated the required operational frequency range of the components in the IF chain. A Mini Circuits BLK-18 DC-block is used to initially filter out large DC signals which would otherwise either saturate or damage the amplifiers in the IF chain. This is then followed by a Wenteq Microwave Corp. ABL0050-00-3310 LNA and a Mini Circuits ZFL-500HLN. The LNA is first in the chain to minimise additional receiver noise. The second amplifier provides further gain and was chosen to minimise harmonics near saturation. Finally, a Mini Circuits SLP-30 LPF with a nominal roll-off frequency of 32 MHz is used to prevent aliasing of the IF signal which would lead to range ambiguity. This is necessary since the maximum IF frequency bin set by the FFT is 41.$\dot{6}$ MHz[4] but the ADC card is configured to sample a maximum frequency of ∼39.8 MHz.

[4] Half the baseband chirp bandwidth.

4.3.3.5 Divider chain

A description of the design and function of the divider chain was first published in Vattulainen et al. [23]. The divider chain consists of:

- Analog Devices Hittite HMC432 frequency divider, factor of 2.
- Analog Devices Hittite HMC394LP4 frequency divider, factor of 11.
- Analog Devices Hittite HMC394LP4 frequency divider, factor of 2.
- Analog Devices Hittite DC1075B-A frequency divider, factor of 4.
- Programmable divider circuit, factor of 1344.

The divider chain is designed to produce the clock signals used by the DDS board and the ADC. All the clock signals are derived by frequency division from the same f_{CLK} signal produced by a Microwave Dynamics 3.5 GHz DRO at the beginning of the chirp generator to ensure coherent operation.

First the sampling frequency f_{s} is derived for the ADC. The three frequency divider boards at the start of the chain divide the clock signal by a total of 44, where the HMC432 divider is used first as this accepts a higher input frequency than the HMC394 boards. The latter boards have configurable division ratios whereas the first only performs a division by 2. HMC394 boards are capable of any division ratio from 2 to 32 and so the remaining frequency division by a factor of 22 could be performed by a single unit, however the mark space ratio is also changed by the same factor. The ADC requires a 50/50 mark space ratio for the sampling clock, and so by using a second HMC394 with a division ratio of 2 following the division by 11, the required ratio is restored in the output signal.

After the f_{s} frequency is tapped off from one of the outputs of the second HMC394, the signal from a secondary output is further divided. The programmable divider cannot accept signals >20 MHz, and so the DC1075B-A board is used to first divide by 4. The final division is performed by the programmable divider circuit which is based on an Atmel ATmega168-PU microcontroller integrated circuit (IC), previously mentioned in [160] and [23]. This is an 8-bit microcontroller with 16 kB of flash memory that runs up to a 20 MHz clock frequency. The division factor q is set using Eq. 4.19:

$$q = 2(a+1) \cdot 2^{2(b+1)}, \quad \text{for } a,\ b \in \mathbb{Z} \tag{4.19}$$

where a takes values between 0 to 63 and b takes values between 0 to 3. This results in a range of values from 8 to 32768 which can be further extended by the use of an integrated pre-scaler with values of 1, 8, 64, 256, or 1024. The output signal from the

programmable divider is then used to trigger both the ADC and DDS, the trigger signal being exactly equal to the CRF to maintain coherence.

4.3.4 Data processor

The output signal from the IF chain is digitised by a Spectrum ADC, model M2p.5940-x4 (1 channel, 80 MS/s SE & DIFF, 16 bit A/D, PCI Express). This was chosen as the sampling frequency of 80 MHz allows for the desired sampling frequency of 79.5494 MHz. The ADC card is installed in a Cincoze fanless PC, model DS-1302 (i5-10500TE 4.50 GHz 6 core CPU, 16 GB RAM, 512 GB SSD, Win10, 1 TB SSD), where this unit was chosen due to its compact size and passive cooling, features which are convenient for field trial work. The radar control code which runs on the PC is implemented in Lab-Windows/CVI, and displays processed range profiles and Doppler spectra in real-time whilst also saving raw data. The control code is multi-threaded across 4 processing cores in the PC, where the paralellised code has dedicated threads for data acquisition and processing, with capture occurring continuously. The control code plots the range profile for each chirp to a user interface, alongside a range-Doppler plot produced from 64 consecutive chirps.

The radar data presented in this thesis in Chapters 6 and 7 were post-processed from raw data saved from the ADC output, the processing procedure being explained in Section 5.2.

4.3.5 Antenna design

The antenna design summarised here was first published in Vattulainen et al. (2022) [23] with further details and measurement results published in Vattulainen et al. (2024) [29].

The radar uses two identical antennas to separate transmit and receive channels. This is to provide sufficient isolation which can be an issue in FMCW designs, as explained in Subsection 2.1.1. The extra space required by a second antenna was justified by the simplicity and low cost of the solution. This is in comparison to a G-band circulator which would also incur additional losses and negatively impact both the transmit power and the receiver noise figure due to transmit-receive leakage. A final one-way beamwidth of ~2° was desired to provide sufficient gain to fulfil the CNR and SNR requirements as outlined above but without being too narrow such that accurate instrument pointing became difficult. The gain produced by one of these units would then be ~39 dBi, calculated using Eq. 4.3 and assuming an antenna loss of ~1 dB.

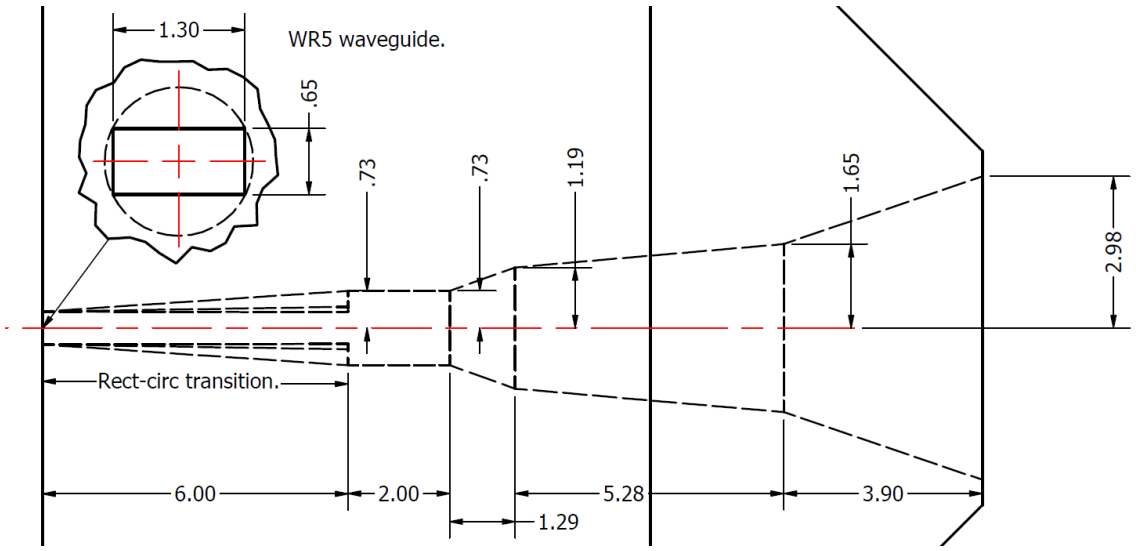

Figure 4.3: The internal profile of the 207 GHz linearly approximated spline horn based on designs by Granet et al. [161], with units in mm.

Initially, smooth-walled horn antennas were considered for the design as the research group at the University of St Andrews has prior experience in designing and manufacturing these in-house, however it was determined that for the required gain these would be too long to fit inside the enclosure. A GOLA design was then selected as the gain of a much shorter horn could be enhanced with the use of a lens, where both elements could still be manufactured in-house. A symmetric antenna pattern was chosen due to manufacturing considerations and for equal beam footprint sizes in HH and VV polarisations. The antenna polarisation can then be changed by rotating each unit 90°, as the input is supplied from a rectangular waveguide which imposes a linear polarisation. Connection to the transmit and receive chains is achieved with either a straight or 90° twist section of G-band waveguide, depending on polarisation.

4.3.5.1 Horn design

The GOLA feedhorn is based on smooth-walled spline horns derived from designs published by Granet et al. [161]. Each spline curve in the original profile is approximated with a straight line resulting in the design shown in Fig. 4.3. The design was developed as an appropriately scaled down version of a design already proven at W-band, consisting of a transition from rectangular WR-5 waveguide to a short section of circular waveguide, followed by three conical flared sections of different opening angle.

The design was developed using MATLAB®, CST Studio Suite® (CST), and the mode-

Parameter	Value
Beam waist radius	1.3 mm
Beam waist distance behind aperture	−3.8 mm
Directivity	19.3 dBi
One-way −3 dB beamwidth	19° (both planes)
LG_{00} coupling	98.7%
S_{11} (CORRUG)	−38.5 dB
S_{11} (CST)	−25.1 dB

Table 4.3: Outputs of various horn parameters from CORRUG and CST simulations of the final horn design at 207 GHz. The negative beam waist distance indicates this was located behind the aperture.

matching software CORRUG[5]. The initial design was first produced using CORRUG, which is capable of rapidly simulating designs thus shortening the time between iterations, however it is only capable of simulating circularly symmetric profiles and so the rectangular-to-circular transition and circular waveguide section were omitted at this stage. These together provide the impedance matching for the antenna and were optimised later. MATLAB® was used to interface with the CORRUG software and sweep over the frequency range of interest whilst recording output parameters and beampatterns. Critical output values at 207 GHz are shown in Table 4.3. Simulations were performed for the whole of G-band (140 to 220 GHz), where the values in the table are calculated for that whole range, the horn having a wideband response.

After initial simulations showed that the profile performed as expected, CST was used to further optimise the design and to verify the beampattern. The horn profile was recreated in CST along with the rectangular-to-circular transition and the circular waveguide section, and a parameter sweep was performed to determine the lengths of these two additional sections which would minimise the S_{11} and produce the optimum antenna patterns. The final simulated S_{11} from CST was −25.1 dB, as shown in Table 4.3. S_{11} values below −20 dB are classed as acceptable, so the simulated value shows good performance. The simulations were performed using 65% Cu brass, which was used as the final antenna material.

4.3.5.2 Lens design

The lens design was produced in MATLAB® using equations from Goldsmith [162] for a planar-spherical lens. Aspherical lens designs were considered but simulations showed more favourable results for simple spherical lenses thus these were used for

[5]CORRUG - SMT Consultancies http://www.smtconsultancies.co.uk/index.php

the final antenna. The typical GOLA design process begins with the lens and the feed design then follows, however since the feedhorn was essentially a scaled version of a design already proven at W-band this was made first, where the final decision on the lens design also took this resulting beam pattern into consideration.

From the specified beamwidth, the approximate directivity was calculated using Eq. 2.29. The beamwaist ω_0 was then calculated beginning with an expression for the effective aperture A_e shown in Eq. 4.20:

$$A_\mathrm{e}\Omega_A = {\lambda_\mathrm{r}}^2 \tag{4.20}$$

with Eq. 4.21, this is related to the beamwaist:

$$A_\mathrm{e} = 2\pi{\omega_0}^2 \tag{4.21}$$

using the definition of directivity from Eq. 2.29, these expressions are combined to give Eq. 4.22[6]:

$$D = \frac{4\pi A_\mathrm{e}}{\lambda_\mathrm{r}} = \frac{8\pi^2{\omega_0}^2}{{\lambda_\mathrm{r}}^2} \tag{4.22}$$

which can then be rearranged for ω_0:

$$\omega_0 = \sqrt{\frac{D{\lambda_\mathrm{r}}^2}{8\pi^2}} \tag{4.23}$$

this allows the calculation of the beamwaist for a lens given the required directivity or beamwidth. The beamwaist was calculated to be $\omega_0 = 16.55$ mm for a directivity $D = 40.13$ dB.

The beamwaist is then used to define the lens diameter. Since there are many interconnected parameters for this antenna design, the diameter was used as a fixed constant to narrow down the search for possible options. The rule of thumb given by Goldsmith is that the aperture radius should be at least three times the beamwaist radius such that sufficient power is captured by the aperture (for simple systems) [162, p. 339], and where here we assume that the beamwaist is an acceptable approximation for the beam radius at the aperture. The antenna diameter was additionally constrained in that both units needed to fit side-by-side in the enclosure. This led to the chosen aperture diameter to be 56 mm, which is $3.38\omega_0$ and thus satisfies the rule given by Goldsmith. Maintaining this constraint was also convenient for the design process,

[6]Note that beginning with the approximation for far field divergence angle (beamwidth) $\theta_0 \simeq \lambda/\pi\omega_0$ [162, p. 24] and the common approximation for beam solid angle $\Omega_A \approx \theta_1\phi_1$ [46, p. 25] produces a different result and is not recommended.

Thickness [mm]	Focal length [mm]	$\theta_{ET}[^\circ]$	Edge taper [dB]
10	57.4	26.0	−14.63
18	40	35.0	−22.23
28	36.4	37.6	−25.25

Table 4.4: Different lens thickness options, resulting focal lengths, and edge taper values.

where keeping one factor constant was helpful to limit the number of possible solutions.

The curved profile of the lens could then be calculated using Eq. 4.24 [163] (in cylindrical coordinates) by specifying the lens arc curvature radius R_l:

$$z_l = \frac{C \cdot \vec{r}^2}{\sqrt{1 - \vec{r}^2 \cdot C^2}}, \quad \text{where } C = \frac{1}{R_l} \tag{4.24}$$

where z_l is the displacement in the z direction and $\vec{r}$ is the lens profile radial position vector. A number of different lens options were explored by varying R_l. The origin for the lens is defined by the equation to be at the centre of the tangent to the spherical surface, thus the thickness of the lens could be calculated using the same formula by evaluating z_l at the edge of the lens $|\vec{r}| = 28$ mm.

The optics formula for a spherical lens shown in Eq. 4.25 was used to calculate the focal length l_f for the different lenses:

$$l_f = \frac{R_l}{n_l(n_l - n_a)} \tag{4.25}$$

where n_l and n_a are the refractive indices of the lens material and of air, respectively. The lens material was chosen to be high density polyethylene (HDPE), with a refractive index of 1.51 at 207 GHz as measured by the group at the University of St Andrews. The results for three different lens thickness values are presented in Table 4.4. Also included here are values for the edge taper, which is calculated using Eq. 4.26:

$$\theta_{ET} = \arctan\left(\frac{d_l}{2l_f}\right) \tag{4.26}$$

where θ_{ET} is the angle to the edge of the aperture from the focal distance and d_l is the diameter of the lens. The edge taper value can then be read off at this angle from the simulated beam pattern of the feedhorn.

In making a decision on which option to use, it was considered that a thinner lens requires a longer focal length and increases the edge taper value, whereas a thick lens incurs additional dielectric losses. A higher edge taper value also narrows the

beamwidth, but at the cost of higher sidelobes. A low edge taper value of <−20 dB was in practice desirable since this prevents cavity resonance effects within the metallic tube housing the lens-horn assembly affecting the performance of the antenna. This was also compatible with a short focal length and thus keeping the antennas compact enough to fit inside the enclosure. The 18 mm thick lens was chosen for the final design as the best compromise. The resulting lens design is shown in Fig. 4.4.

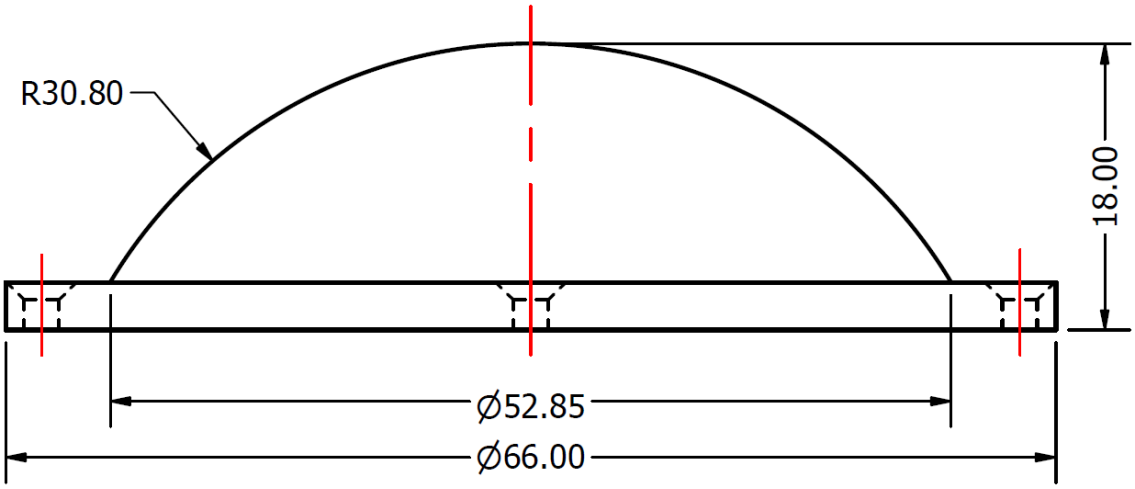

Figure 4.4: The profile of the dielectric lens used for the GOLA antennas. The lens is rotationally symmetric and fabricated from HDPE. Note that the lens diameter was slightly reduced from the nominal 56 mm by the addition of the mounting flange.

The directivity of the GOLA was then simulated by CST to be 39.35 dBi with a gain of 38.87 dBi at 207 GHz, which was within the expected ballpark from previous calculations. This indicates an antenna loss of 0.48 dB. The simulated beam pattern for the GOLA is presented in Chapter 5 for comparison with measured results. The simulated S_{11} of the GOLA was less than for the standalone horn, being −32 dB. These simulations were run without the cylindrical enclosure (tube) of the GOLA to reduce computational load.

4.3.6 Mechanical design

The mechanical designs shown here for the antennas and the radar enclosure were developed by the author using the computer aided design (CAD) package Autodesk Inventor and manufactured by the University of St Andrews Mechanical Workshop.

4.3.6.1 Antennas

The manufacture of the internal profile of a horn required it to be turned from brass as several sections which were then screwed together. This design is shown in Fig. 4.5, as

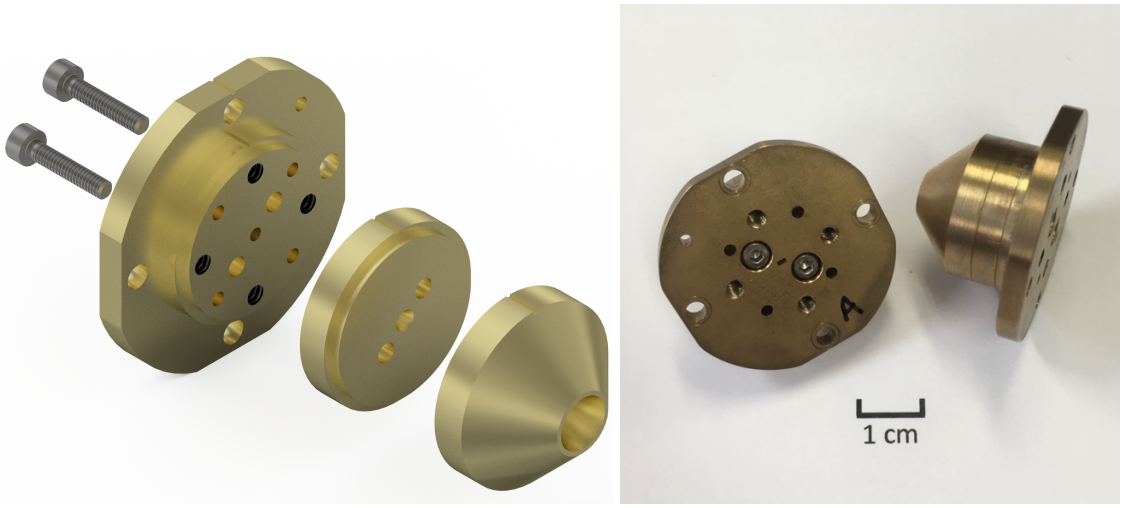

(a) (b)

Figure 4.5: (a) An exploded view CAD rendering of the GOLA horn and (b) a photograph of both manufactured units with scale, first published in Vattulainen et al. [23].

both the CAD model and the finished horns. The first section (leftmost) contains the rectangular-to-circular transition and the section of circular waveguide, the second section contains the first two conical flares, and the final section the last flare. To ensure co-location of the profile between sections, a concentric lip was machined into the edge of one flat face, which would fit into an opposing groove, as can be seen in Fig. 4.6a. The edge of the full aperture was also chamfered on the outside surface to prevent the formation of edge currents which would degrade the beampattern.

The mechanical design of the GOLAs is shown in Fig. 4.6, consisting (from left to right) of the horn, the end cap, the tube, and the lens. A flange was added to the first section of the horn to allow mounting to the rest of the GOLA and leave the face with the waveguide flange pattern proud of the surface. The horn is attached to the end cap with screws and a waveguide dowel to ensure concentricity and that the horn is mounted to the GOLA in consistently the same orientation. The end cap then mounts to the tube similarly with screws and a locating dowel. A further concentric groove on the end cap fits a lip on the tube, again to ensure concentric location of the horn with the tube. The tube then acts as a spacer for the remaining focal length required for correct focusing of the beam from the horn onto the lens. The GOLA tube and end cap were machined from aluminium, where the cavity was lined with a layer of microwave absorbing foam to reduce any possible resonance effects resulting from the cavity. The tube could alternatively been made from plastic, greatly reducing any possibility of reflections within the cavity and thus resonance, however aluminium was preferred as this would prevent any chance of coupling between the antennas which may have otherwise occurred through transmissive plastic.

The lens itself is mounted with four countersunk screws to aid with concentric location, where the previous lip and groove method was not used here since the fragility and flexibility of the plastic would make this less effective. As shown in Fig. 4.4, the final diameter of the lens was somewhat reduced from the initial specification of 56 mm due to the addition of the mounting flange, however given the significant edge taper this was not expected to make a considerable difference to the final beam pattern. The lens was manufactured from a single piece of HDPE with a smooth finish (no additional impedance matching by e.g. blazing).

4.3.6.2 Radar enclosure

The enclosure was originally designed to fit within a 2-axis gimbal yoke, which constrained the total volume of the instrument, however the final design also needed to maximise the internal volume available to house the signal components and antennas. To satisfy both of these requirements, an octagonal housing design was developed as this allowed a greater internal volume than a square box whilst not requiring any curved sides which are more complicated to manufacture. Additionally the overall weight of the instrument needed to be minimised to comply with the weight limits of the gimbal and also as the radar was to be field deployable. For this reason the housing was made from aluminium. For ease of manufacture, the enclosure was made from multiple sections of flat plate which were bolted together rather than being milled from a solid block. This latter option was used for the AVTIS-2 radar [164] which was designed to be mounted in an identical gimbal, however the time taken to mill the component was prohibitive. An exploded view of the construction of the enclosure is shown in Fig. 4.7. The construction also allows for the removal of individual plates to better access the components at the sides of the housing for maintenance.

Due to the large number of components and the necessity of reasonable spacing to allow for assembly and access, careful consideration was given to the placing of components. To accommodate the large but flat DDS board, a shallow compartment was made at the bottom of the enclosure using the large central plate shown in Fig. 4.7. The DDS board was then mounted to the underside of this plate. The rest of the chirp generator components were mounted onto a vertical plate shown in the top left of Fig. 4.8. Similarly, the IF and divider chains were also mounted to a plate, seen in the bottom right of Fig. 4.8. The use of these plates allowed for sub-assembly of these systems outside of the enclosure before mounting in the full enclosure, making things easier. To accommodate the varying heights of input and output ports, recesses were cut into the plates for each component.

As can be seen in Fig. 4.8, the centre of the top compartment contains both the

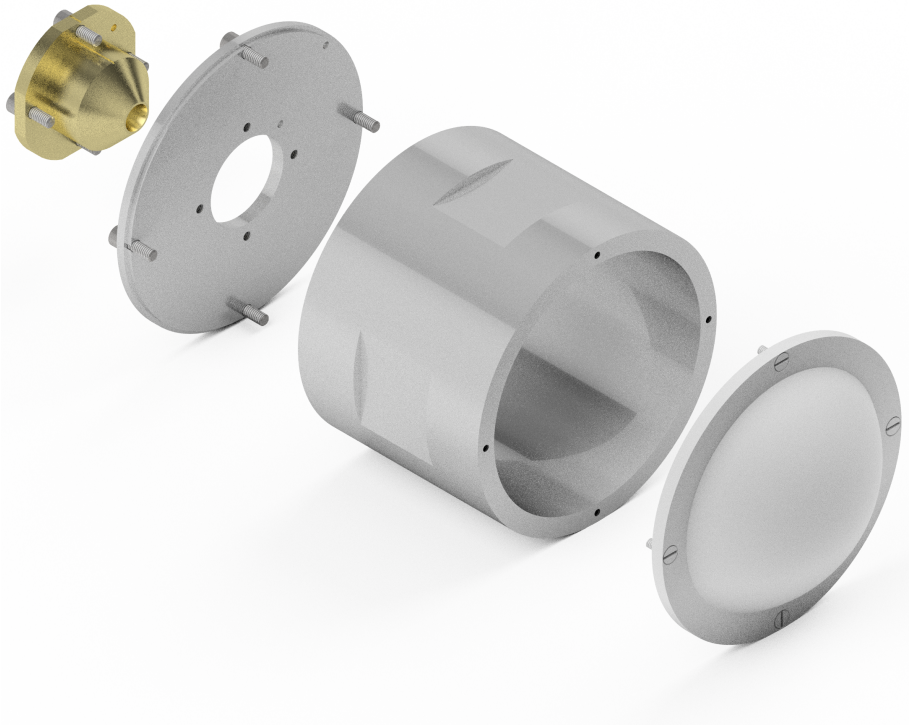

(a)

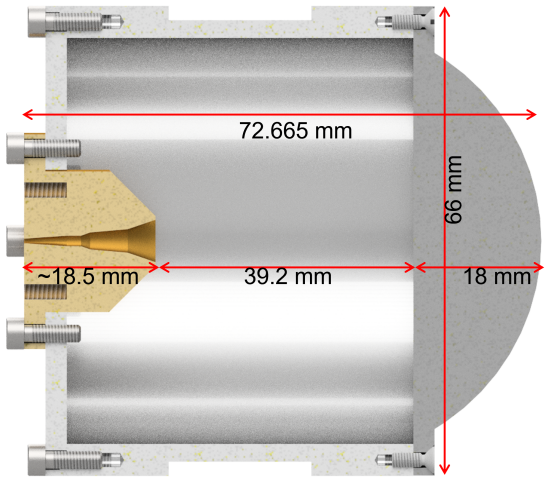

(b)

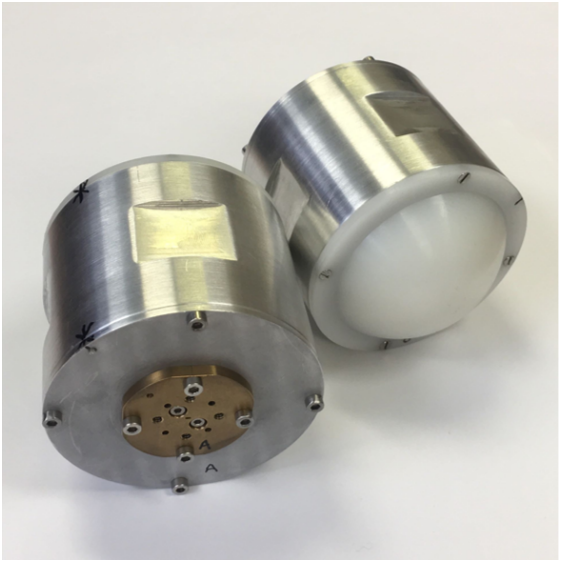

(c)

Figure 4.6: (a) An exploded view CAD rendering of the full GOLA mechanical design, showing (left to right) the horn, end cap, tube, and lens, (b) a CAD rendering of a GOLA with annotation indicating critical dimensions, and (c) both manufactured units. The absorber lining is omitted from the CAD models. Figures (b) and (c) were first published in Vattulainen et al. [23].

transmit and receive chains which are mounted on aluminium blocks for heatsinking. The antennas are mounted such that they are vertically centred on the instrument, and equally spaced from the horizontal mid-line. Numerous holes are cut through the internal plates to allow for routing of power lines and signal cables. All the required voltage regulator boards are mounted to the walls of the enclosure for better heatsinking, where many of the board are located in the bottom compartment.

The lid contains several ports for connecting signal cables to allow the input and output of information, as well as a switch for selection of internal or external triggering. A USB port is used to interface and control the DDS board via a computer, and power to the instrument is supplied via a single 8-core cable also connecting through the lid. For additional thermal management, there are two back-to-back heatsinks attached to the lid, with an internal fan to aid air circulation. A large port in the lid is used to access the internal cavity and antennas for switching between polarisations by unbolting waveguide connections, rotating the antennas, and substituting the waveguide links with either a straight or 90° twisted section as appropriate.

This chapter first presented a review of the published G-/Y-band radar systems to date. This was followed by a detailed summary of the design of the Theseus G-band radar, with the context of the considerations for each design choice which was made. The following chapter reports the characterisation of the key radar sub-systems and the radar as a whole.

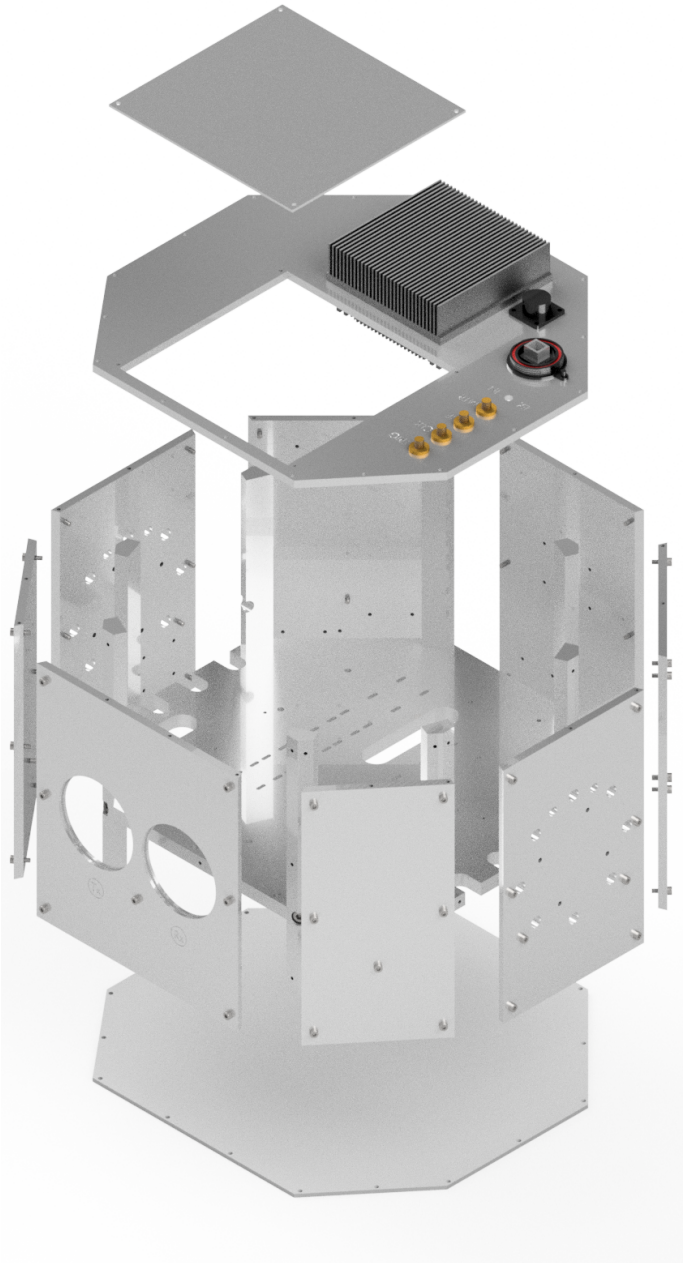

Figure 4.7: Exploded view of the radar enclosure showing construction from multiple aluminium plates.

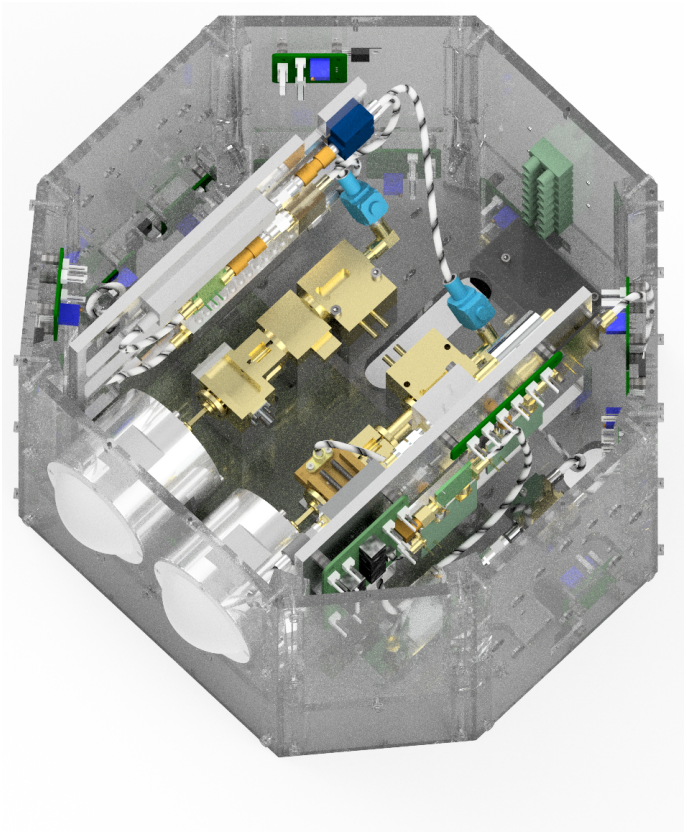

Figure 4.8: Internal view of the top compartment of the enclosure showing mounted system components. The lower compartment contains the DDS board and voltage regulators, where cabling between the two compartments is fed through several ports in the dividing plate.

5

G-band Doppler Radar Characterisation

In this chapter, the measurements and characterisation of the G-band Doppler radar built as part of this Ph.D. are reported. The first section describes the measurements and results for each radar subsystem, the second section describes the radar range processing used to perform measurements, and the third section details the results for the system as a whole.

The design and development of this radar was a collaborative effort between the author and his supervisors Prof. Duncan A. Robertson and Dr Samiur Rahman. All of the work detailed in this chapter was completed by the author, except the following elements:

- The data for the CST simulation of the G-band standard gain horn (SGH) pattern in Fig. 5.3 were produced by Prof. Duncan A. Robertson.
- The simulated data for the GOLA (horn and the full antenna) in Subsection 5.1.1 were provided by Dr Samiur Rahman.
- The measurement of the spurs from the new chirp generator configuration presented in Fig. 5.9 was made by Prof. Duncan A. Robertson, where previously the same measurement had been made for the original configuration by the author.
- The data for the chirp generator phase noise results presented in Fig. 5.13 were measured by Prof. Duncan A. Robertson.
- The data for the SHM LO drive power optimisation shown in Fig. 5.19 were measured by Prof. Duncan A. Robertson and the author.
- The data for the receiver noise figure results shown in Fig. 5.21 were measured by Prof. Duncan A. Robertson and the author.

- The data for the range calibration results in Figures 5.32, 5.34, were measured by Dr Samiur Rahman and the author.
- The data investigating the change in signal power due to antenna flexing presented in Fig. 5.35 were measured by Dr Samiur Rahman and the author.
- The measured data of the radar noise floors at low and high band Fig. 5.36 were collected by Dr Samiur Rahman and the author.
- The data for the phase noise measurements in Fig. 5.37 were measured by Dr Samiur Rahman and Prof. Duncan A. Robertson, SR and DAR, where the model fitting of curves was performed by Dr Samiur Rahman.

This chapter details numerous novel aspects of radar development of interest, where the general implementation of a radar instrument at this frequency remains a rarity as previously explained in Chapter 4. Other achievements include:

- The successful in-house development and fabrication of GOLAs for use from 200 to 208 GHz.
- The demonstration of the performance of the SHM for use in radar and how to optimise this for the design.
- The presentation of results for the output power of the W-band solid-state PA.
- The measurement of the transmitter power using a freespace power meter, where this uncommon approach was required due to the technical challenges associated with developing instruments in this frequency range. These measurements demonstrated the capability of the VDI doubler for use in this instrument, both in terms of the final output power achieved and the high efficiency of its operation due to the prior optimisation of this unit for the expected output power range from the W-band PA by the manufacturer.
- Results of measurements of the phase noise of the instrument, which emphasise the impact of phase noise on the eventual performance and its specific concern in this frequency regime.

5.1 Subsystem characterisation

5.1.1 Antenna results

5.1.1.1 S_{11} measurements

The S_{11} as a function of frequency for each horn and of the assembled GOLAs was measured to ensure this was below the desired limit of −20 dB. This was the first test

conducted on the antennas as the S_{11} is a good indicator of any serious manufacturing issues which might impair the beam pattern and gain. The latter two measurements require more effort to set up, so the S_{11} measurement is a good way to eliminate defective units before investing more time in their evaluation.

The S_{11} of the horns was first simulated in CST as part of the design process outlined in Subsection 4.3.5. Measurement sweeps over the whole of G-band were then conducted using an Anritsu ME7808B vector network analyser (VNA) with a G-band V05VNA2-T/R extender head made by Oleson Microwave Laboratories Incorporated (OML Inc.). The antenna under test (AUT) was terminated into an absorbing cone beam dump such that only reflections from the AUT were recorded.

The results of these measurements are shown in Fig. 5.1. The data for both horns, units A and B in Fig. 5.1a, indicate that the measured S_{11} values are very similar at low band with a maximum deviation of ∼1.5 dB, whilst being slightly more divergent at high band with a deviation of up to ∼5 dB. Overall, the S_{11} is <−23 dB at low band and <−24 dB at high band. The match of horn A to simulation at high band is very good, but in general the curves for units A and B do not match simulation particularly well, although the average levels are similar. The S_{11} was optimised for frequencies at high band, so this could be the reason that the match at these frequencies is good for unit A, however this could simply be a coincidence. The machining tolerances at the scale of WR-5 waveguide (1.2954 mm by 0.6477 mm) are very tight and are likely to be the cause of the significant deviations over most of the range.

The data for the GOLA measurements are shown in Fig. 5.1b, plotted with the simulated horn data in lieu of that for the GOLAs as the simulation time for the full antenna was prohibitive. In general it was expected that the GOLA S_{11} would follow that of the horn and so the data for the horn measurements are also overlaid, showing this is indeed the case. There is an additional variation caused by a standing wave cavity effect due to the reflections from the GOLA lens, tending to degrade performance. The S_{11} is still however <−20 dB over both the low and high band ranges, fulfilling the desired performance criteria. The S_{11} results for horn A and GOLA A were first published in Vattulainen et al. (2022) [23].

5.1.1.2 Beam patterns

Beam pattern measurements were carried out to verify the expected beamwidths in both E- and H-planes, and to check the position and level of any sidelobes.

The measurement set-up is shown in Fig. 5.2. The experiments were performed using both the radar transmit and receive chains to access the required frequency range. Accurate beam pattern measurements rely on good on-axis alignment between

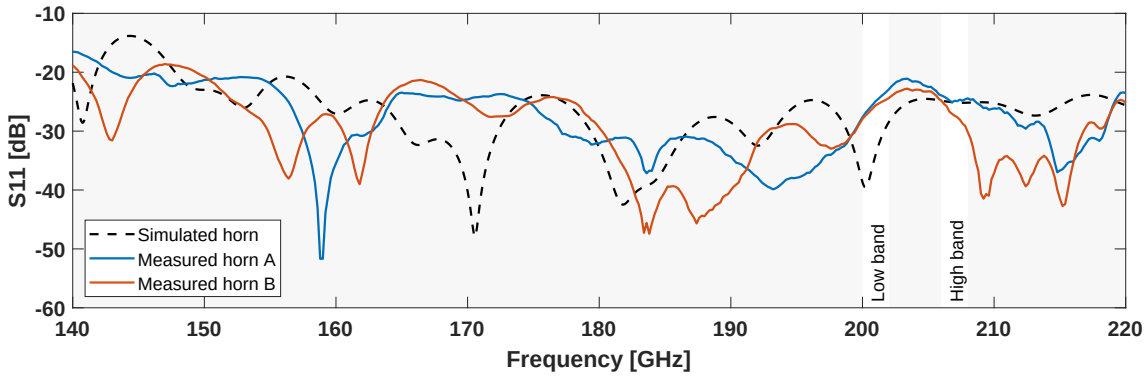

(a)

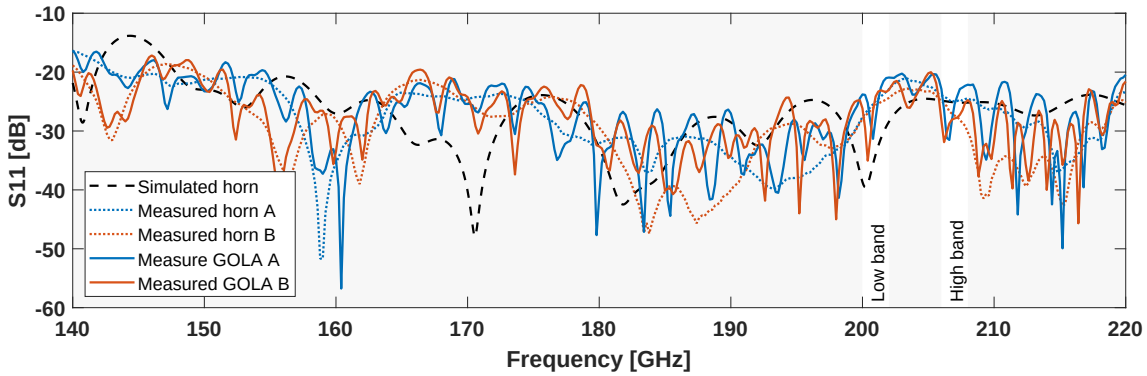

(b)

Figure 5.1: (a) S_{11} measurements of both GOLA horns plotted with data from a CST simulation, where the measured S_{11} for both units is <−22 dB at low band and <−24 dB at high band. (b) S_{11} measurements of both fully assembled GOLAs, plotted alongside the simulated and measured data for the horns. The GOLA data shows a cavity effect imposed on the trend for each horn, producing an overall S_{11} which is <−20 dB for low and high band.

the transmit antenna and the AUT, so that the beam is correctly sampled. To help with this, the chosen transmit antenna was a G-band pyramidal SGH which produces a fairly wide mainlobe to provide plane wave illumination and ensure the required distance between the SGH and the AUT was minimised by this being limited by the far field distance (FFD) of the AUT only. The measured beam patterns in the E- and H-planes and CST simulation of the SGH antenna used are shown in Fig. 5.3, with all data for a frequency of 207 GHz. The gain of this unit was measured to be 21.48 dBi at 207 GHz and 21.62 dB at 200 GHz. The beam patterns were measured with the same procedure as for the GOLAs (detailed below in this subsection) and the gain was measured by the gain substitution method (detailed below in Subsection 5.1.1.3) with reference to a Flann Microwave G-band SGH with serial number SN221703.

The SGH then has a well defined and measured gain which agrees with simulated values. This was used to check the received IF power level was approximately as

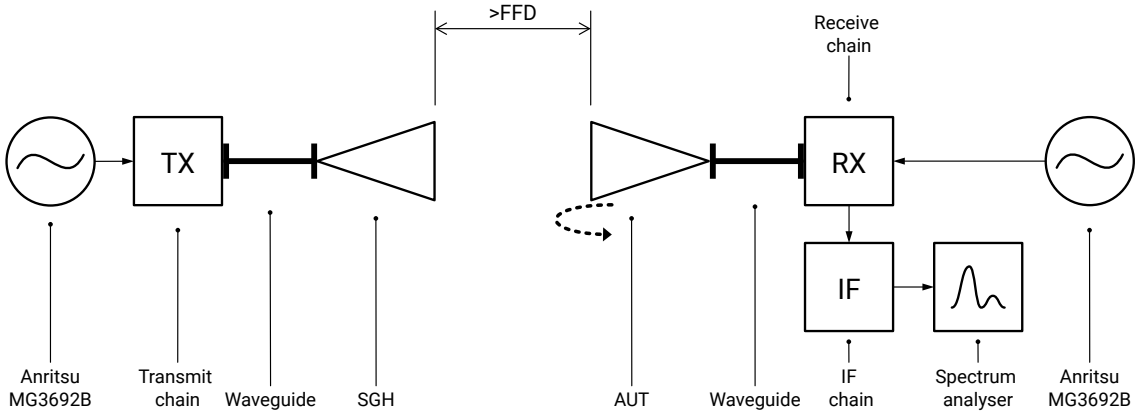

Figure 5.2: Diagram of the beam pattern measurement apparatus.

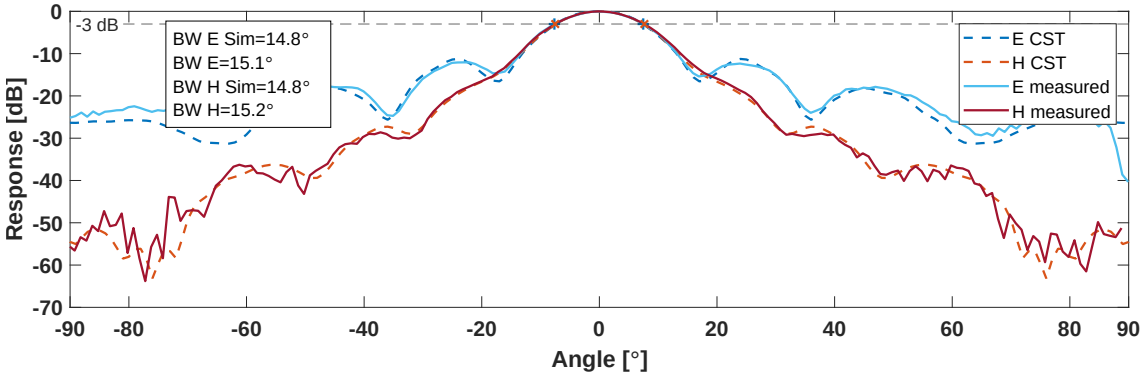

Figure 5.3: Measured and simulated beam pattern of pyramidal G-band SGH at 207 GHz.

predicted by the link-gain, shown in Eq. 5.1:

$$P_{\mathrm{IF}} = \frac{P_{\mathrm{t}} G_{\mathrm{t}} G_{\mathrm{r}} \lambda_{\mathrm{r}}{}^{2} G_{\mathrm{rec}}}{(4\pi)^2 R^2} \tag{5.1}$$

where P_{IF} is the received power at the IF chain output, and G_{rec} is the receiver gain. For this test, a second SGH was used for the receiver so that both G_{t} and G_{r} were well defined, where this second horn has a near identical pattern to the first and a measured gain of 21.71 dB at 207 GHz and 21.96 dB at 200 GHz. The measurements were carried out at a range greater than the FFD for the antennas, as given by Eq. 2.27. The antenna aperture was 6.70 by 8.43 mm, where the largest dimension was used to calculate $R_{\mathrm{ff}} = 0.098$ m. The gain check with two known antennas was performed to help eliminate any errors and to optimise the measurement set up, to ensure that measurements of beam pattern and gain were successful.

The drive signal for each chain was provided by separate Anritsu MG3692B signal generators. The signal from the synthesiser for the transmitter was set to provide the test frequency for the AUT after ×12 frequency multiplication in the transmit chain.

The signal generator for the receiver was set at a 5.8$\dot{3}$ MHz offset from this, such that after ×12 multiplication this produced a signal which was 70 MHz higher. This allowed straightforward measurement of the IF signal with an HP8591E spectrum analyser, where the measurement span was limited to exclude the DC spike and a very low resolution bandwidth of 3 kHz was used to reduce the instrument noise floor and thus maximise the dynamic range of the measurement. The spectrum analyser has a greater dynamic range than a power meter, this being useful for measuring the low level edges of the antenna pattern, and additionally since the experiment measures relative power levels only the comparative lack of amplitude accuracy using a spectrum analyser was not an issue. On the IF port of the receiver SHM there was an IF chain consisting of a DC block, a Wenteq ABL0050-00-3310 LNA, and a LPF with an cut-off above 70 MHz.

The AUT was mounted on a stand attached to a turntable. This was programmed to incrementally scan and measure the IF signal to record this as a function of azimuth angle. The angular range of interest was −90° to +90°, and so the measurements were made with a small buffer of 10° either side to allow for centring of the pattern after measurement. For horn measurements, the increment was a constant 1° which was sufficient for the broad antenna patterns, however for the very narrow GOLA beams the increment was reduced to 0.2° in the range −10° to +10° and 1° otherwise.

The test area was surrounded by microwave absorber sheets as much as possible to reduce multipath reflections, these being placed in particular around the transmit and receiver antennas which otherwise can cause problematic standing waves. The far field distance for the GOLA horns was ∼50 cm, and for the GOLAs was ∼4 m. To measure the E-plane response, both the transmit horn and the AUT were mounted such that the E-plane was horizontal (HH configuration) and the horizontal scan with the turntable recorded the pattern. To measure the H-plane, both antennas were rotated 90° such that they were in VV configuration, and scanning horizontally cut through the pattern in the H-plane. Data were collected at 200 GHz and 207 GHz, as these were the proposed centre frequencies for low band and high band, where the the low band centre was subsequently revised to 201 GHz after the measurements were completed. The difference between the patterns at the two frequencies will be insignificant enough to consider the pattern at 200 GHz equivalent.

The resulting apparatus for the horn measurements is shown in Fig. 5.4, and the apparatus for the GOLA measurements is shown in Fig. 5.5. The primary difference between the two set-ups is the increased distance between the antennas to account for the differing far field distances.

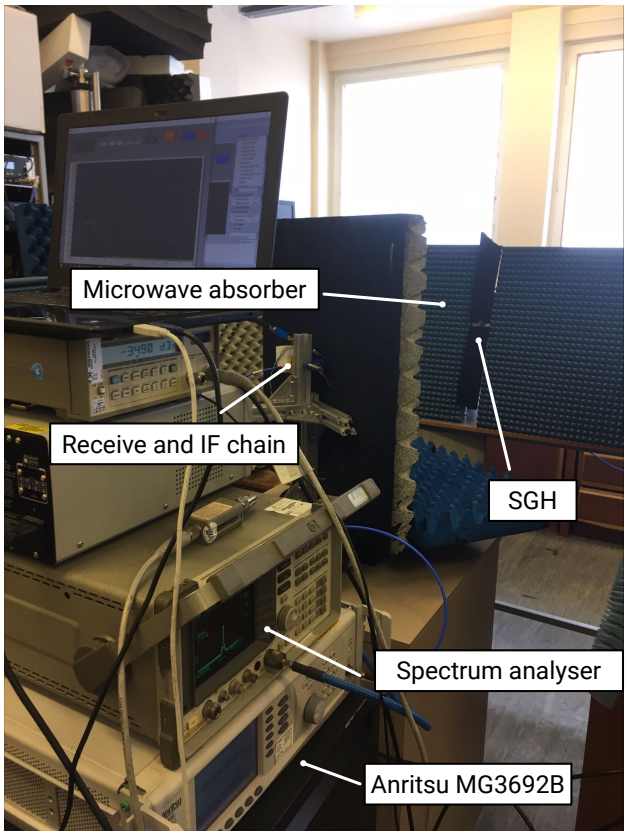

(a)

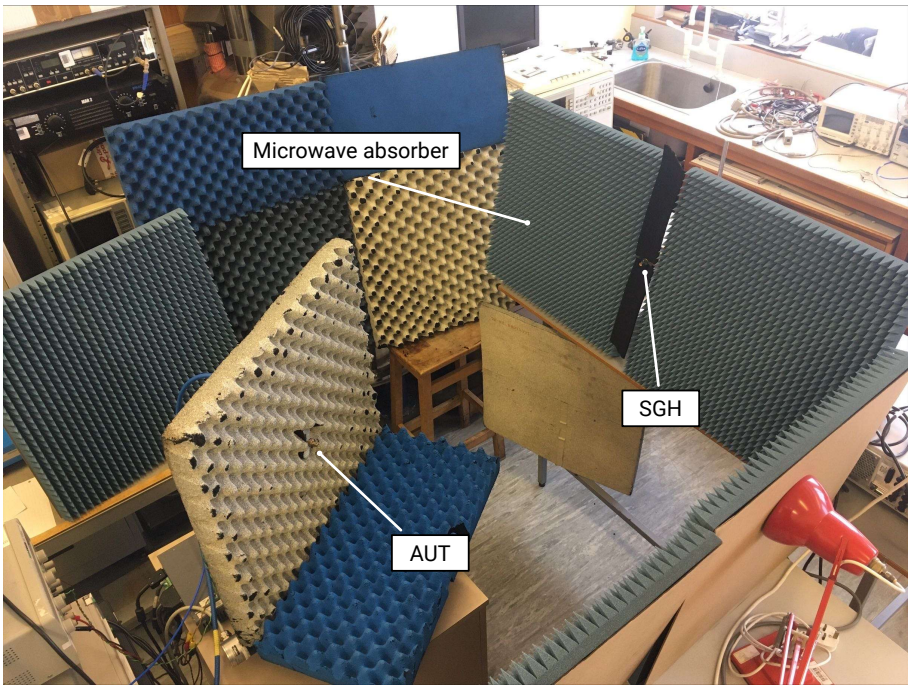

(b)

Figure 5.4: Annotated photographs of the apparatus used to measure the beam pattern and gain values of the GOLA horns.

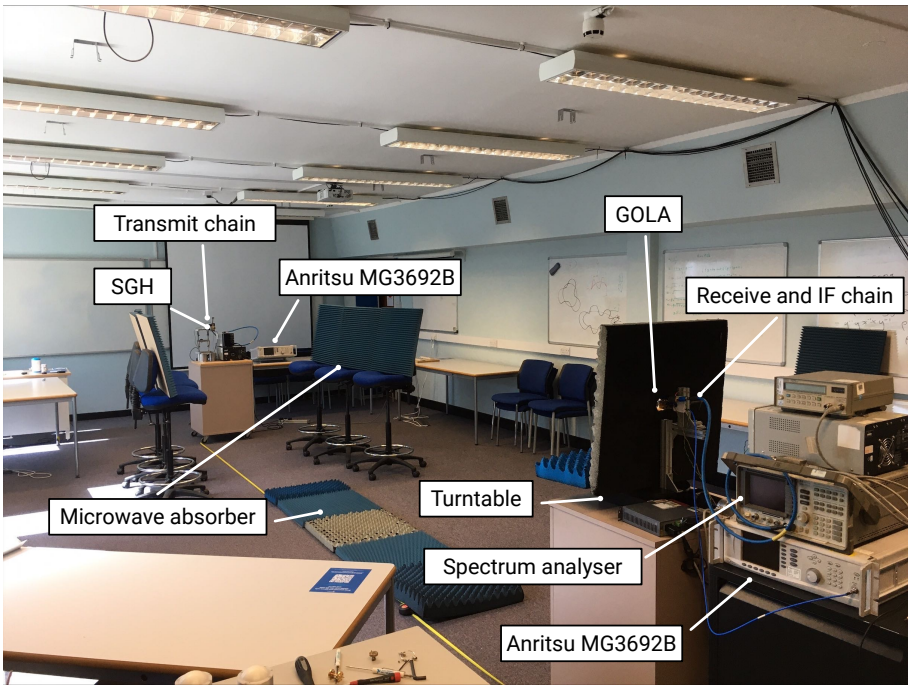

Figure 5.5: Annotated photograph of the apparatus used to measure the beam pattern and gain values of the GOLAs.

Horn beam pattern results

The horn beam patterns are presented in Fig. 5.6. The patterns for horn A show excellent main lobe agreement down to −30 dB at both 200 GHz and 207 GHz. Simulations from CST show the best agreement with measured values, which is not unexpected since the CORRUG simulations necessarily did not include the rectangular-to-circular transition or the circular waveguide section. Beyond 50° on either side multipath fluctuations become evident. At 207 GHz, the position of the null at ∼54° in the CST data matches well with the measurement, but the depth is lost due to multipath reflections.

The pattern for horn B similarly shows excellent agreement to −30 dB. E-plane data shows an additional null at −60°, which also appears for horn A, however this is assumed to be due to multipath reflections as no similar defect is seen at 207 GHz. The position of the nulls at 207 GHz gives a good match, however the shoulder of the mainlobe at −40° is lowered by ∼6 dB and by ∼4 dB at 200 GHz. Being so far off-axis and a relatively minor discrepancy however, this is not expected to impact the final performance of the GOLA.

From these results it can be seen that the horns are working as expected, with beamwidth values matching the simulated data very well. The simulated and measured beamwidth values as well as the percentage errors between them are shown in Table 5.1, where both units are near identical in performance.

GOLA beam pattern results

The GOLA beam pattern results for both units at 200 GHz are shown in Fig. 5.7. The results are very similar for both units, showing excellent agreement with simulation down to −15 dB, and good agreement to −45 dB in both E- and H-planes. As can be seen from Figures 5.7b and 5.7d which show detail of the mainlobes, these are fairly symmetrical at a level of −20 dB, but with the shoulder at ∼3° being more pronounced in H for unit A, and in E for unit B. A small spike is seen at ∼−18° for both units, where it is assumed this is due to multipath. The beamwidths for both units show a very good match to simulation.

The beam pattern results at 207 GHz for both GOLAs are presented in Fig. 5.8. Likewise to the results at 200 GHz, the mainlobe agreement is excellent to −15 dB and good to −45 dB, with the results for both units being nearly identical. Both units show a raised shoulder in both E and H, which is probably due to a small manufacturing error leading to the horn being slightly off axis relative to the lens. The small spike at ∼−18° seen in both H-plane cuts is again assumed to be a multipath reflection. Since this was also seen in the measurements at 200 GHz, this is more likely to be a reflection from the room than the actual antenna response.

These measurements showed that both GOLAs functioned as expected and were suitable for use in the radar, with no major problems detected. The simulated and measured beamwidth values as well as the percentage errors between them for both GOLAs at each frequency are shown in Table 5.2. At 200 GHz, unit B shows a closer match to simulation, whereas at 207 GHz both units are very similar, with errors in the region of 5% in E and 3% in H. In general the errors in the GOLA beamwidths are somewhat greater than for the horns. The additional percentage broadening of the mainlobe could be due to any number of small manufacturing imperfections such as the misalignment of the horn and the lens along the optical axis, or of the planar surface of the lens not being exactly perpendicular to this axis, and any small deviation of the manufactured lens profile from the simulated shape. Some uncertainty in the complex permittivity of the piece of HDPE used may also contribute to the difference between measured and simulated beamwidths, where this value can vary slightly between individual pieces of plastic. It was found during simulations by Dr Samiur Rahman that the beamwidth would change slightly even with a change in permittivity of 0.01. In general the sidelobe level is kept below −35 dB which is desirable for measurements of faint targets and clutter, as bright off-axis scattering picked up by sidelobes may increase the reflected transmitter phase noise collected by the receiver and degrade the instrument noise floor. Sidelobes can additionally cause imaging artefacts in PPI scans for example, and so reducing these as much as possible is beneficial to

f [GHz]	E_s [°]	E_m [°]	Err. E[%]	H_s [°]	H_m [°]	Err. H[%]
Horn A						
200	19.8	20.1	1.5	19.8	20.2	2.0
207	18.8	19.0	1.1	19.4	19.9	2.6
Horn B						
200	19.8	20.2	2.0	19.8	20.6	4.0
207	18.8	18.7	0.5	19.4	19.9	2.6

Table 5.1: Simulated (subscript s) and measured (subscript m) beamwidth values, and resulting percentage errors for the GOLA horns.

f [GHz]	E_s [°]	E_m [°]	Err. E[%]	H_s [°]	H_m [°]	Err. H[%]
GOLA A						
200	2.00	2.12	6.0	2.06	2.17	5.3
207	1.95	2.05	5.1	1.98	2.04	3.0
GOLA B						
200	2.00	2.13	6.5	2.06	2.10	1.9
207	1.95	2.07	6.2	1.98	2.03	2.5

Table 5.2: Simulated (subscript s) and measured (subscript m) beamwidth values, and resulting percentage errors for the GOLAs.

performance. The beam patterns for horn A and GOLA A at 207 GHz were first published in Vattulainen et al. (2024) [29].

5.1.1.3 Gain measurements

The final test of antenna performance was a measurement of gain, arguably the most important value as this is a major determining factor in the final radar sensitivity.

The gain for each AUT was measured by the *gain substitution* technique using the same apparatus as for the beam pattern measurements in Subsection 5.1.1.2, shown in Fig. 5.2. The gain substitution experiment is also a relative power measurement, and so measuring the signal level with a spectrum analyser is suitable.

The same pair of G-band SGHs were used as before, where the measured gain values for these are known at the frequencies of interest. The link-gain equation in Eq. 5.1 was again used to check the set-up was working as expected. The peak power response of the receive SGH was measured by carefully aligning the antennas such that the received power was maximal. Once the value for the SGH was recorded, this was swapped for the AUT, and without changing the positioning or other aspects of the apparatus, the received power was recorded. The gain of the AUT was then calculated using Eq. 5.2:

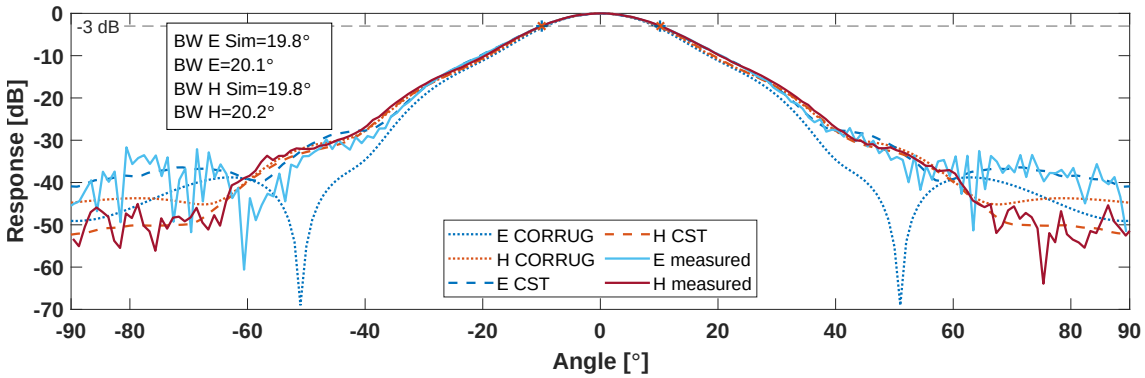

(a) Horn unit A at 200 GHz.

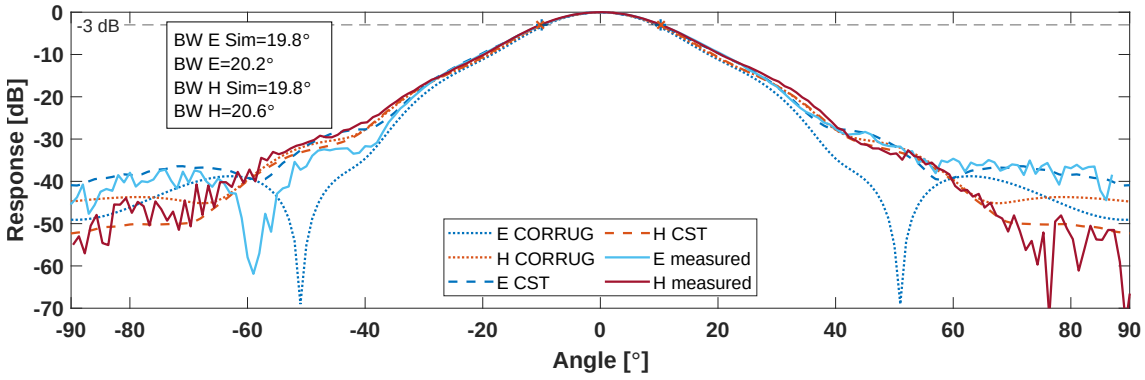

(b) Horn unit B at 200 GHz.

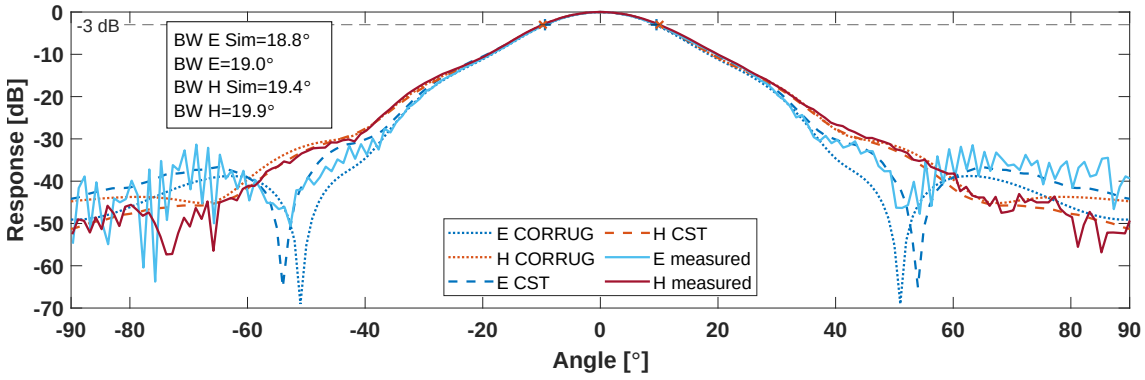

(c) Horn unit A at 207 GHz.

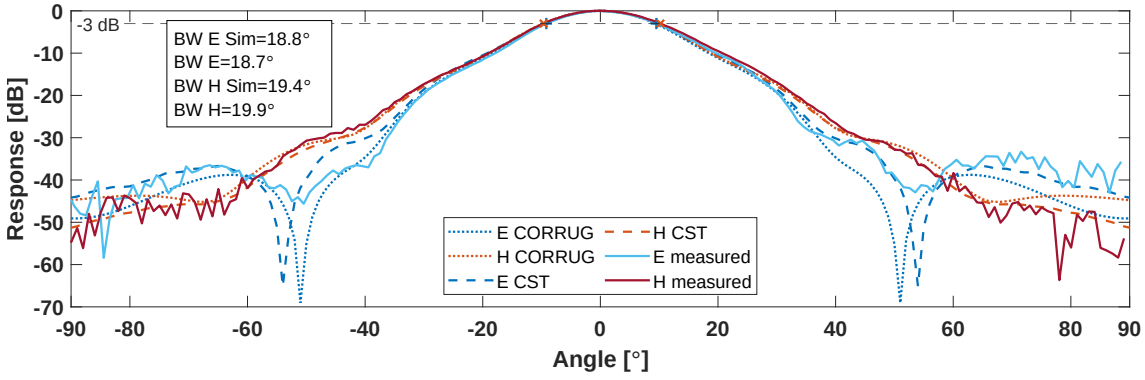

(d) Horn unit B at 207 GHz.

Figure 5.6: Horn beam patterns as simulated by both CORRUG and CST, plotted alongside the measured data of both horns A and B at 200 GHz and 207 GHz.

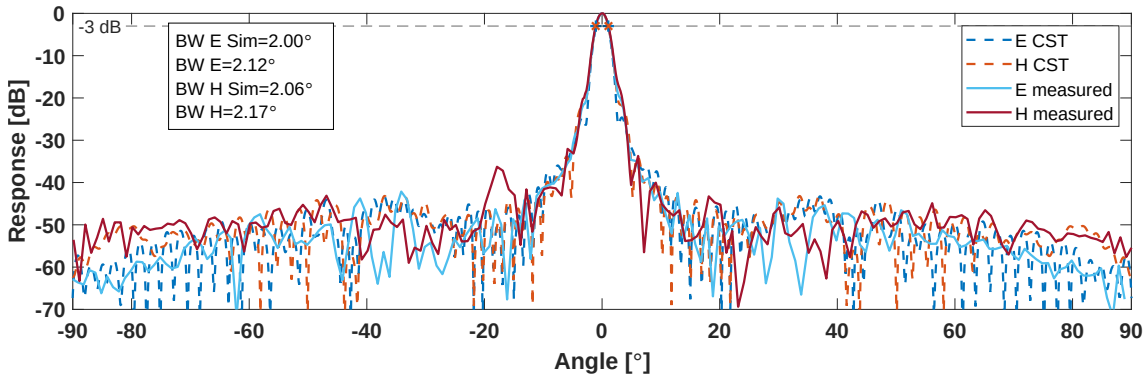

(a) GOLA unit A at 200 GHz.

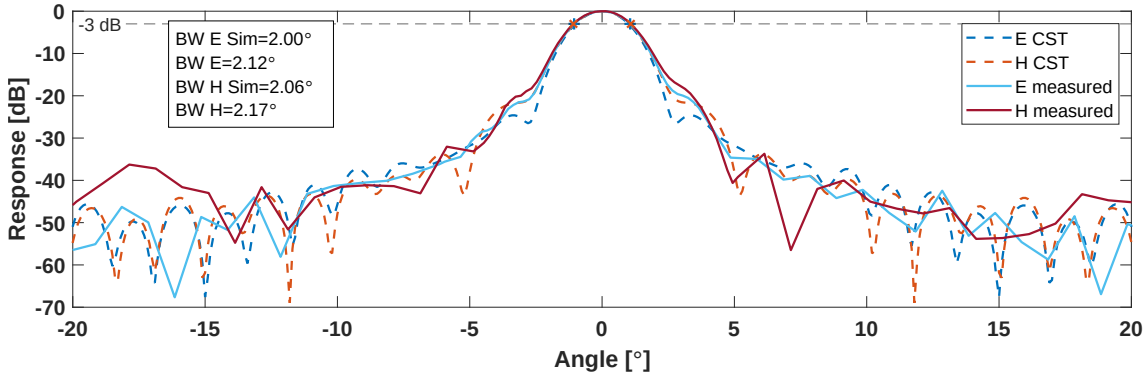

(b) Zoomed view of GOLA unit A at 200 GHz.

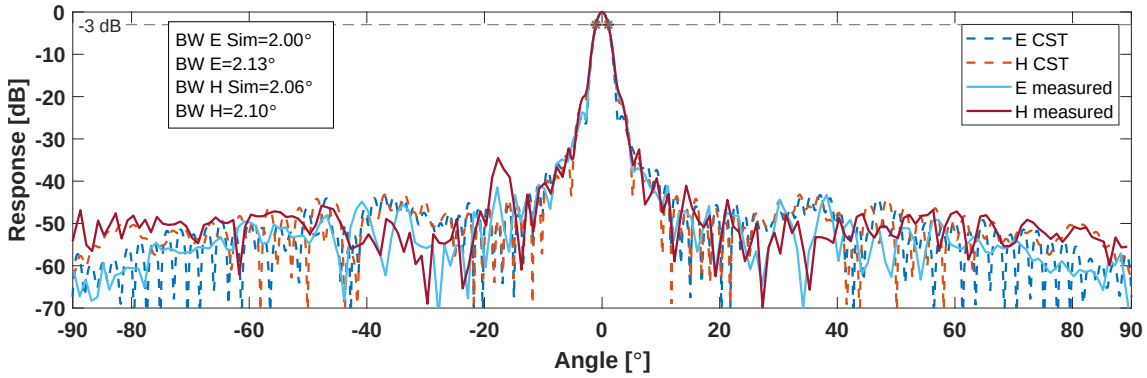

(c) GOLA unit B at 200 GHz.

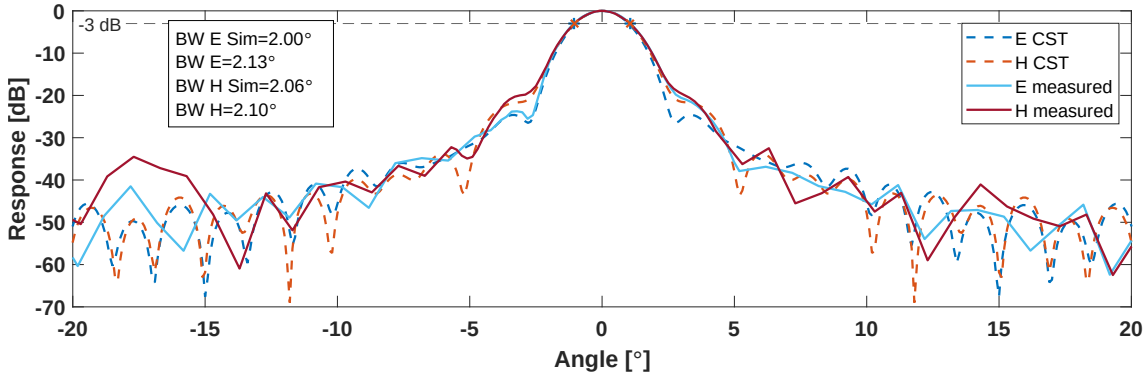

(d) Zoomed view of GOLA unit B at 200 GHz.

Figure 5.7: Beam pattern plots of CST simulations and measured data at 200 GHz for both GOLAs A and B.

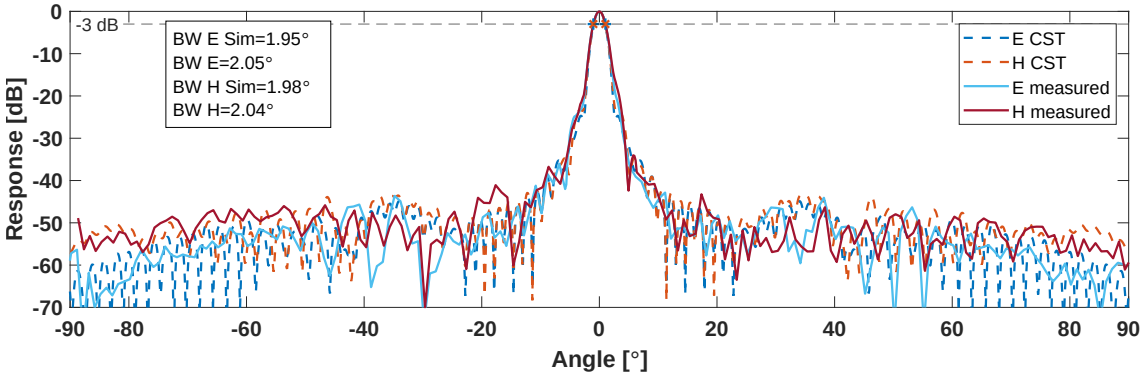

(a) GOLA unit A at 207 GHz.

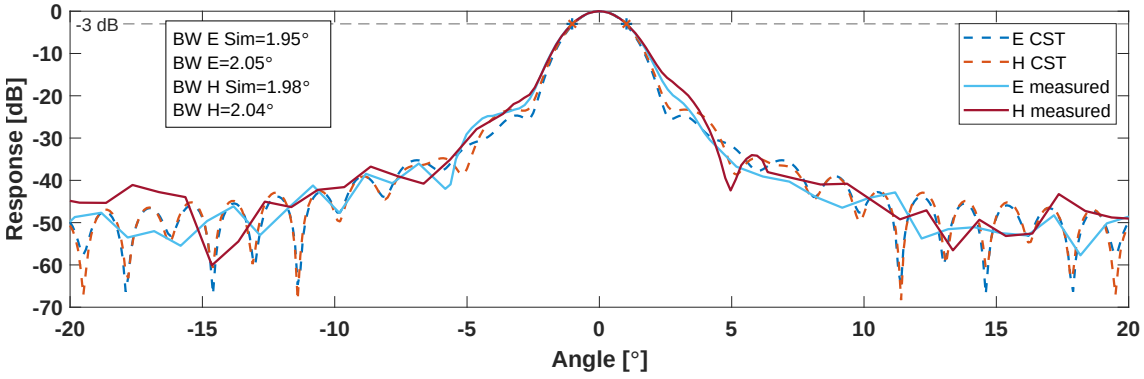

(b) Zoomed view of GOLA unit A at 207 GHz.

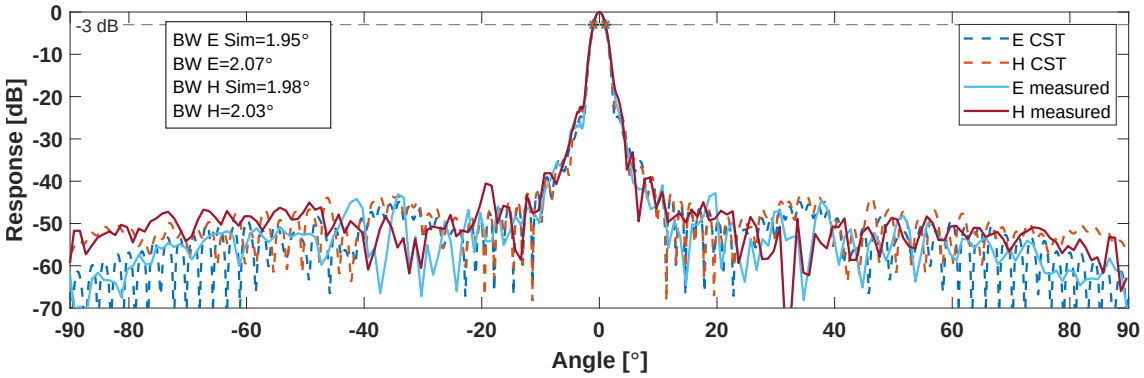

(c) GOLA unit B at 207 GHz.

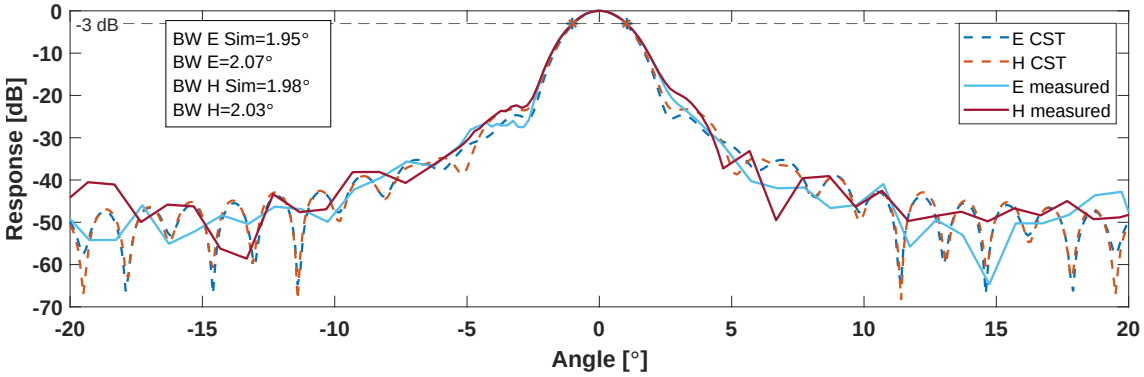

(d) Zoomed view of GOLA unit B at 207 GHz.

Figure 5.8: Beam pattern plots of CST simulations and measured data at 207 GHz for both GOLAs A and B.

$$G_{\mathrm{AUT}} = \frac{P_{\mathrm{m}} G_{\mathrm{ref}}}{P_{\mathrm{ref,m}}} \tag{5.2}$$

where P_{m} is the measured received power using the AUT, $P_{\mathrm{ref,m}}$ is the measured received power using the reference antenna, and G_{ref} is the known gain of the reference antenna.

The results of these measurements for each horn are shown in Table 5.3. The measured gain values G_{m} shown here *include the loss of the waveguide links* used to attach the horns and thus the GOLAs to the receive and transmit chains. The losses of the waveguide links were measured separately using the Anritsu ME7808B VNA with G-band V05VNA2-T/R extender heads, where these averaged to 0.25 dB at both low and high band. The losses quoted in the table are calculated using Eq. 5.3:

$$L = D_{\mathrm{s}} - G_{\mathrm{m}} \quad [\mathrm{dB}] \tag{5.3}$$

where the measured gain G_{m} is subtracted from the directivity predicted by CST, D_{s}, and where the equation is specified in the decibel form for ease of use with the values in the table.

The measured gain values of both horns agree very closely with simulation, as is expected considering that the beam patterns also show very good agreement. The gain of horn A is in general slightly higher, again reflected in the beam patterns, where the loss of 0.12 dB at 200 GHz is less than that of the waveguide link, indicating that the antenna performance slightly exceeds the CST prediction. The measured gain values of the GOLAs are almost identical. They fall short of the simulated gain by ∼0.8 dB (not including the waveguide loss), which is at least partly attributed to the uncertainty in the complex permittivity of the lens, as discussed previously. Overall however, both antennas show very good performance.

5.1.2 Chirp generator results

The characterisation of the chirp generator began by measuring the S-parameters of all the passive components using an Hewlett-Packard Ltd. (HP)8510 VNA for measurements up to 19 GHz. This testing confirmed that all of the components were within their specified performance values.

Testing of the active components then proceeded by first measuring the output power of the DROs using a power meter (e.g. HP438A) and a HP8481A sensor head. Oscillator output spectra were also checked with a HP8593A spectrum analyser to verify the frequency of the fundamental tone and to make sure that the harmonics were sufficiently low. The general procedure for testing the other active components was similar, where the aim was to ensure that the subsequent component in the signal

f [GHz]	E_s [°]	E_m [°]	H_s [°]	H_m [°]	D_s [dBi]	G_s [dBi]	G_m [dBi]	L [dB]
Horn A								
200	19.8	20.1	19.8	20.2	18.96	18.8	18.84	0.12
207	18.8	19.0	19.4	19.9	19.25	19.1	18.95	0.30
Horn B								
200	19.8	20.2	19.8	20.6	18.96	18.8	18.53	0.43
207	18.8	18.7	19.4	19.9	19.25	19.1	18.67	0.58
GOLA A								
200	2.00	2.12	2.06	2.17	38.98	38.50	37.44	1.54
207	1.95	2.05	1.98	2.04	39.35	38.87	37.87	1.48
GOLA B								
200	2.00	2.13	2.06	2.10	38.98	38.50	37.43	1.55
207	1.95	2.07	1.98	2.03	39.35	38.87	37.89	1.46

Table 5.3: Simulated (subscript s) and measured (subscript m) values, for both horns and GOLAs, of beamwidths in the E- and H-planes, directivity D, gain G, and loss L. Measured gain and loss values include the averaged loss from the waveguide lines (0.25 dB). The results for GOLA unit A were originally published in Vattulainen et al. (2024) [29].

chain had sufficient drive power, and that the output did not contain any unexpected spectral components. The latter test ensures that components are not malfunctioning or defective, and that unwanted spectral elements will be rejected by the appropriate filtering stages in the design used to control spectral regrowth and intermodulation products.

Due to the digital synthesis process, the DDS board signal output contains spurious signals at frequencies which change during a chirp. For the AD9914 board, the wide-band spur-free dynamic range is quoted as <-50 dBc [165]. It is important that the spurs be adequately low compared to the carrier to prevent degradation of the chirp signal purity. Since the chirp signal from the DDS inherently contains these spurs, maintenance of the chirp signal purity is achieved by avoiding frequencies where spurs are particularly prominent. Of specific concern are frequencies at which two or more spurs cross due to the potential for intermodulation products when these are used in mixing processes. To monitor this issue, the spectrum of the chirp output was recorded using a HP8593A spectrum analyser over the proposed range of DDS frequencies at fine increments. The result of this measurement for the range of DDS frequencies to be used by the radar 500.33$\dot{3}$ to 833.66$\dot{6}$ MHz is shown in Fig. 5.9. This did not show evidence of any significant spurs in this range, which verified that the frequency multiplication scheme as shown in Table 4.2 was viable.

The output spectrum of the final chirp generator doubling stage (HMC814LC3B) is shown in Fig. 5.10. This data is for the original chirp generator configuration prior to

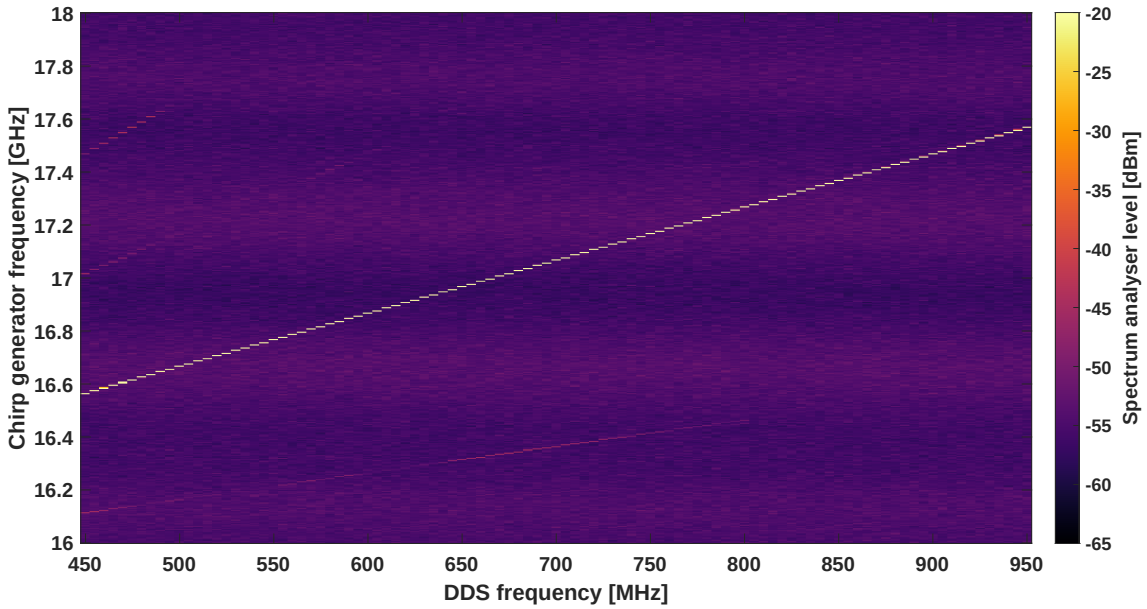

Figure 5.9: Measurement of the output spectrum of the chirp generator as a function of DDS frequency to check for the presence of any problematic DDS spurs or their intermodulation products. No significant spurs were detected over the entire range to be used for both low band and high band, the highest spur level being ∼−41 dBc at a chirp generator frequency of ∼17.6 GHz.

being upgraded, however is shown here as an example of the kind of measurements performed on other active components. Since the preceding components in the chain up to the ATM ATi 6-12 isolator remain the same in both designs, it is expected that the output spectrum at this point will be very similar. This measurement was produced by setting the DDS to chirp continuously over high band (see Table 4.2) whilst using a spectrum analyser to record the maximum signal amplitude spectrum (using 'maximum hold') over several chirps. This measurement shows the chirp centred at 17.25 GHz, as well as the harmonics of the chirp produced by the doubler and preceding amplifier (ZX60-183-S+). These products are filtered out by the subsequent BPF (AT22F-WT481-AF) where the passband of this filter is indicated in the plot.

The output power versus frequency was also recorded for the upgraded chirp generator and is shown in Fig. 5.11, measured at the output of the final BPF. This measurement was performed by recording the power level at each chirp increment using a power meter. This method is more definitive than that described above, since a power meter records signal amplitudes more accurately than a spectrum analyser, and since measuring the signal at a fixed frequency and then incrementing ensures that the measurements are properly synchronised. As the power meter measures the integrated power over a fixed bandwidth, this kind of measurement is only valid if prior verification of signal purity has been made and the signal does not include e.g.

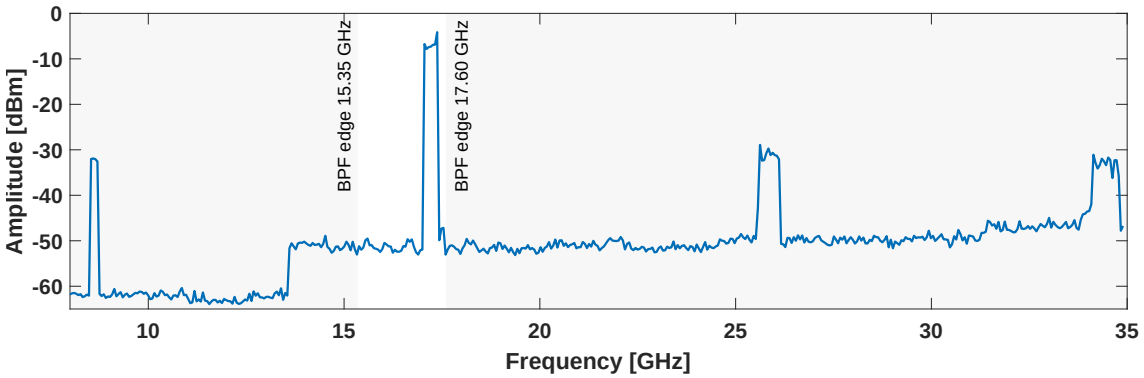

Figure 5.10: The output spectrum of the HMC814LC3B doubler for a signal chirping over high band as recorded by an HP8593A spectrum analyser, for the original chirp generator design. The step change in noise floor occurring at approximately 13.5 GHz is an inherent property of the spectrum analyser.

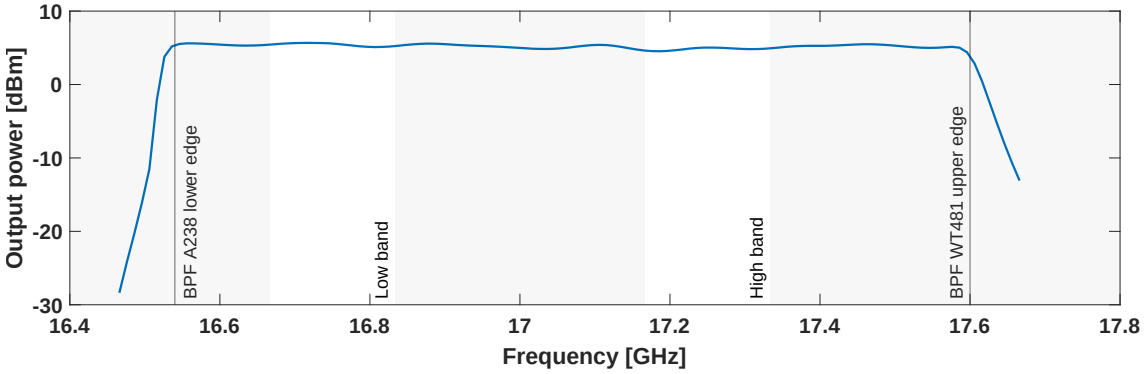

Figure 5.11: The upgraded chirp generator output power versus frequency, recorded at the output of the AT22F-WT481-AF BPF.

unwanted harmonics which contribute to the total signal level. By measuring at the output of the BPF, the unwanted harmonics shown in Fig. 5.10 are removed.

Figure 5.11 shows that the average output power for the chirp generator is 5.2 dBm, with a variation of ±0.3 dBm in the indicated low and high band ranges of 167 MHz. The band edges of the two BPFs in the chirp generator are also marked on the plot, showing the boundaries of the presently accessible bandwidth. To access frequencies below the low band limit of 200 GHz ($f_{CG} = 16.\dot{6}$ MHz), the AT22F-A238-AF BPF would need to be exchanged to a model with a wider passband, however for this project this was not necessary as measurements as close as possible to 213 GHz ($f_{CG} =$ 17.75 MHz) were desirable. The upper frequency limit of the chirp generator implies a maximum RF output frequency of ~211 GHz ($f_{CG} = 17.58$ MHz), however in practice the achievable power in this range is also limited by the output power of the W-band PA which tapers off steeply above 104 GHz ($f_{CG} = 17.\dot{3}$ MHz), as shown in Subsection 5.1.5.

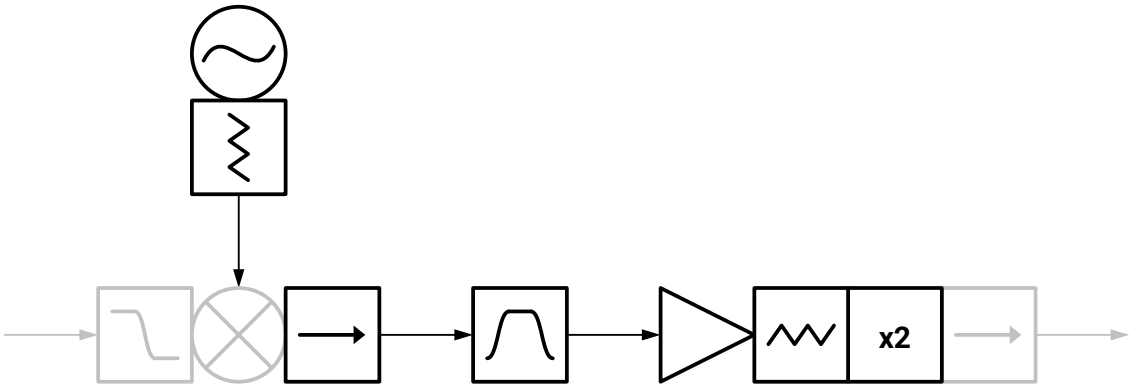

Figure 5.12: A block diagram showing the section of the chirp generator which was replaced during the upgrade to improve phase noise performance. Components belonging to the original design only are shown in black, whilst components which still remain in the present design are shown greyed out. On the left hand side of the diagram, the IF input to the Avantek mixer comes from the MC VLF-1200 filter (both grey) on the DDS board output. On the right hand side of the diagram, the MC ZX90-2-50 frequency doubler connects to the ATM ATi 6-12 isolator (grey) which remains part of the redesign.

5.1.2.1 Chirp generator upgrade

Reflected transmitter phase noise in FMCW radars can degrade the noise floor of the instrument, as explained in Subsection 2.1.12, described specifically by Equations 2.59 and 2.60. The effect was noted during early experiments involving the full radar system, where it was observed that bright targets or clutter were obscuring low level signals due to an increase in the instrument noise floor. These results are shown in Subsection 5.3.3, and indicated that improvements were needed to reduce the phase noise produced by the chirp generator.

A block diagram of the section of the original design which was replaced is shown in Fig. 5.12. The replaced components are shown in black. This section consisted of:

- Micro Dynamics DRO-1000-05.56 5.567 GHz DRO as mixer LO.
- 6 dB attenuator.
- Narda 4914 isolator.
- Aaren cavity BPF BP4479.16-625-12KS AT22F-A237-AF 4.166$\dot{6}$ to 4.791$\dot{6}$ GHz.
- Mini-Circuits (MC) ZRON-8G amplifier.
- 1 dB attenuator.
- MC ZX90-2-50 frequency doubler.

The benefits of the upgrade lie in substituting the Microwave Dynamics DRO-1000-05.56 DRO at 5.56$\dot{6}$ GHz with a Nexyn NXOS-0783-01761 at 7.83$\dot{3}$ GHz, which improved performance in two ways:

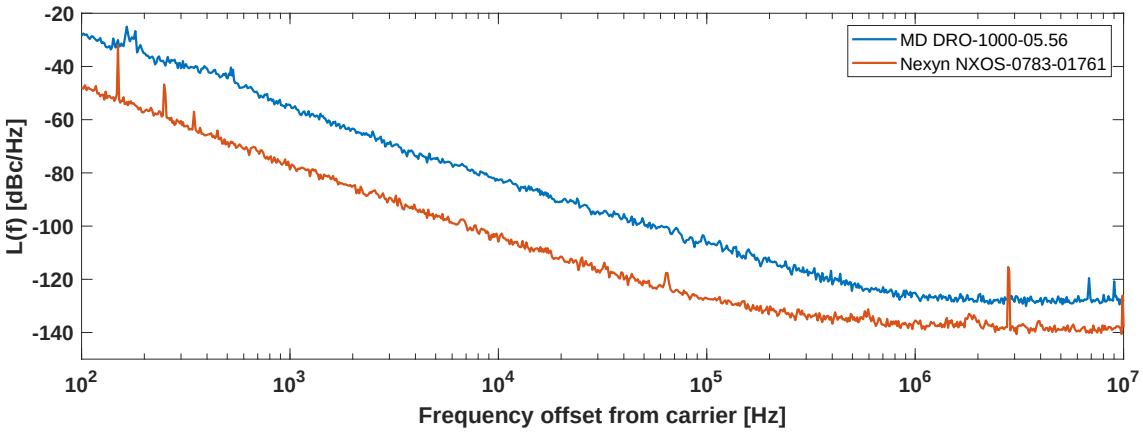

Figure 5.13: The measured chirp generator phase noise (f) as a function of offset frequency from the carrier, for both the original design using a Microwave Dynamics DRO-1000-05.56 upconversion LO and the upgraded system using a Nexyn NXOS-0783-01761 DRO.

- The LO frequency of the upconversion mixer was increased such that the MC ZX90-2-50 ×2 frequency doubler could be removed, thus improving phase noise performance by $20\log_{10}(2) = 6$ dB as governed by Eq. 2.63.
- The Nexyn DRO had a lower inherent phase noise than the Microwave Dynamics unit by approximately 15 to 20 dB according to the data sheet, which is then carried forward for the performance of the whole chirp generator.

In the original configuration shown in Fig. 5.12, a DDS chirp centred at 1.2545 GHz for high band operation was upconverted to 4.3125 GHz with the 5.567 GHz DRO using lower sideband mixing. The MC ZX90-2-50 frequency doubler then produced a signal at 8.6250 GHz, which is the same as the output from the Avantek mixer in the redesign.

The phase noise of the chirp generator was measured both before and after being upgraded, with these results shown in Fig. 5.13. This measurement was performed using a HP4352B phase noise analyser by downconverting the ~17 GHz chirp signal against a low phase noise reference DRO at 13.6 GHz. The results show an average reduction in phase noise of 21.5 dB for offset frequencies from 10^2 to 10^5 Hz from the carrier. The impact of this upgrade on the overall performance of the full radar is shown in Fig. 5.37 and described in Subsection 5.3.3.

5.1.3 IF chain

5.1.3.1 Compression curve and gain response

Figure 5.14 shows the compression curve for the full IF chain. This was measured by first characterising the input signal, produced using an HP8648D synthesiser set to

10 MHz and incremented in amplitude and measured using a power meter. This was then fed into the IF chain and the output similarly measured with a power meter. The output power versus the characterised input power level was then plotted, and a line fitted to the linear region of the gain curve, chosen as the data up to −40 dBm input power. This gives the linear or small signal gain as 54.4 dB, also shown in the chart. The divergence of the fit from the data was monitored to find the −1 dB point, where the data lagged below the expected gain by 1 dB. The measured −1 dB compression point was −36.8 dBm, with a maximum undistorted output power of 16.6 dBm. These results were previously presented in Vattulainen et al. (2024) [29].

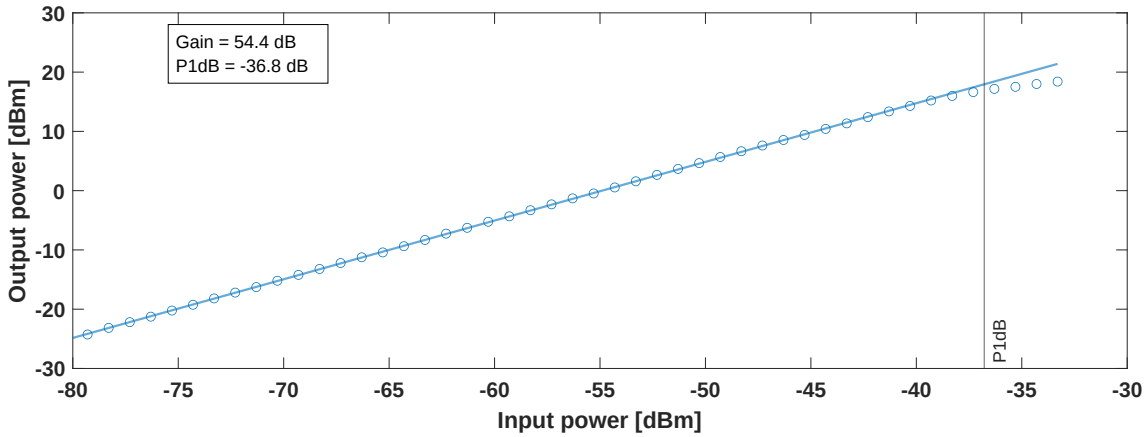

Figure 5.14: The compression curve of the final IF chain, with a linear fit to the data up to −40 dBm input power showing the small signal gain and the −1 dB compression point.

The IF gain as a function of input frequency is shown in Fig. 5.15. This measurement was conducted using a HP8648D signal generator as input, with the amplitude set such that the output signal level from the the IF chain was −10 dBm when measured with a power meter i.e. well within the linear gain region, for an initial frequency of 10 MHz. The amplitude of the input signal was then measured using a power meter. To collect the data of interest, the power meter was once again connected to the IF chain output and the signal level measured at several input signal frequency increments in the range of 0.01 to 50 MHz. The output power values were then adjusted to account for the input level, and plotted as a function of the input frequency to produce Fig. 5.15.

The low frequency behaviour from 0 to 0.5 MHz in Fig. 5.15 is a result of the DC-block frequency response. After this region there is a small rise between 0.5 to 5 MHz due to the MC ZFL500HLN which quickly decays to a more gentle slope of ∼2 dB between 5 to 32 MHz, also due to the ZFL500HLN, the Wenteq LNA gain being flat to ∼0.1 dB within this frequency range. The steep roll-off beyond 32 MHz is due to

the MC SLP-30 anti-alias LPF with a nominal cut-off frequency of 32 MHz. Excepting the desired filtering behaviour of the DC-block and the anti-alias filter, the frequency response would ideally be flat as this prevents an additional signal level range dependence on top of that expected from the radar range equation. This would be evident in e.g. RTI plots, and in extreme cases could make these more difficult to interpret correctly. The ∼2 dB change seen in this characterisation is however only a minor discrepancy and will not impair the functioning of the instrument whatsoever. In any case, the sensitivity of the radar is preserved since the IF gain amplifies the signal and noise level equally and evenly enough that there will be no issues in keeping the amplified signal within the dynamic range of the ADC. For measurements of RCS or NRCS, the variation of gain frequency response is included in the radar range calibration and accounted for in these calculations. These results were previously presented in Vattulainen et al. (2024) [29].

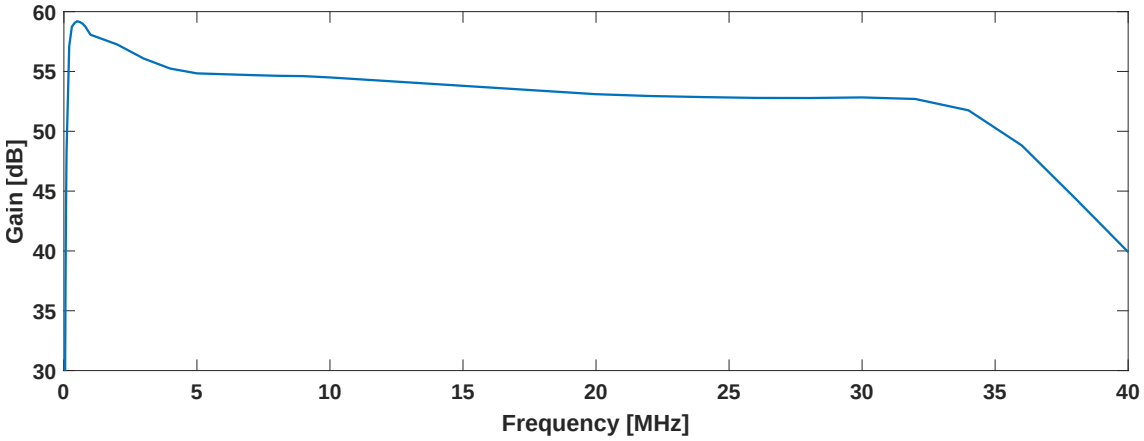

Figure 5.15: The frequency response curve of the IF chain. The low frequency cut-off below 0.5 MHz is due to the DC-block, and the high frequency cut-off due to the roll-off of the anti-alias filter at 32 MHz. The peak between 0.5 to 5 MHz and the gentle ∼2 dB slope of the curve between 5 to 32 MHz is primarily due to the ZFL500HLN amplifier.

5.1.3.2 IF chain amplifier harmonics

Initial testing of the radar revealed that significant harmonics were introduced by the IF chain. To reduce these, the second IF amplifier was changed from an MC ZFL500LN to an MC ZFL500HLN, which has both a higher −1 dB compression point and third-order output intercept point (OIP3), thus better harmonic performance. The plots in Fig. 5.16 illustrate the issue. The data for these graphs was obtained by measuring the amplitudes of the harmonics produced by each amplifier using an Rohde & Schwarz (R&S) FSP40 spectrum analyser. The 10 MHz input signal to the amplifier was supplied by an HP8648D signal generator filtered using an MC SLP-15

LPF to remove harmonics generated by the synthesiser. The input level was then incremented and the output level of the harmonics measured. The measurements of the ZFL500LN are retrospective and are not necessarily of the same unit as was used in the IF chain originally, however the data is believed to be fairly typical of this model. The data of the ZFL500HLN is of the unit used in the final IF chain of the radar.

Figure 5.16a shows the measurements as absolute decibel values for both amplifiers. This shows that the −1 dB compression point is greater for the ZFL500HLN, however the gain is slightly less (by ∼5 dB according to data sheet values). It can also be seen that the harmonics for the ZFL500LN model begin at a much lower input power level of ∼−55 dB, although a better comparison of the performance is given in Fig. 5.16b which shows the second and third harmonics plotted as decibels relative to the carrier. From this it can be seen that both the harmonics of the ZFL500LN are at a higher level with respect to the fundamental compared to the harmonics of the ZFL500HLN, where the second harmonic is −12.8 dBc at −10 dBm input power for the former, versus −46.7 dBc for the latter.

Figure 5.16c shows the output power level of the third-order intercept points of the amplifiers, this being the point at which the fit to the linear sections of the gain curves for the fundamental and the third harmonic cross. This is a common amplifier figure of merit, where a higher OIP3 corresponds to better harmonic performance. The value for the ZFL500HLN is indeed greater which confirms it as the better choice to reduce IF harmonics. The impact can also be seen in Fig. 5.37, where the data for the new configuration is taken with the upgraded IF chain.

5.1.4 Receive chain

5.1.4.1 Frequency multiplier characterisation

The characterisation of the receive chain began with measurements of the performance of both ×6 Quantum Microwave frequency multipliers with serial numbers 306 and 328. It was expected that their performance would differ slightly as the manufacturers data sheets indicated differing maximum power levels and current draws. Firstly a compression curve measurement was undertaken for each multiplier in much the same way as for the IF chain as explained in Subsection 5.1.3, using a fixed frequency input of 17.25 GHz, corresponding to a chirp generator frequency for the centre of high band. This was produced by an Anritsu MG3692B signal generator and attached to the multiplier input via a cable for which the loss was measured. The signal generator power was then incremented and the multiplier output power measured for each step using a power meter with a W-band waveguide sensor head model HPW8486A.

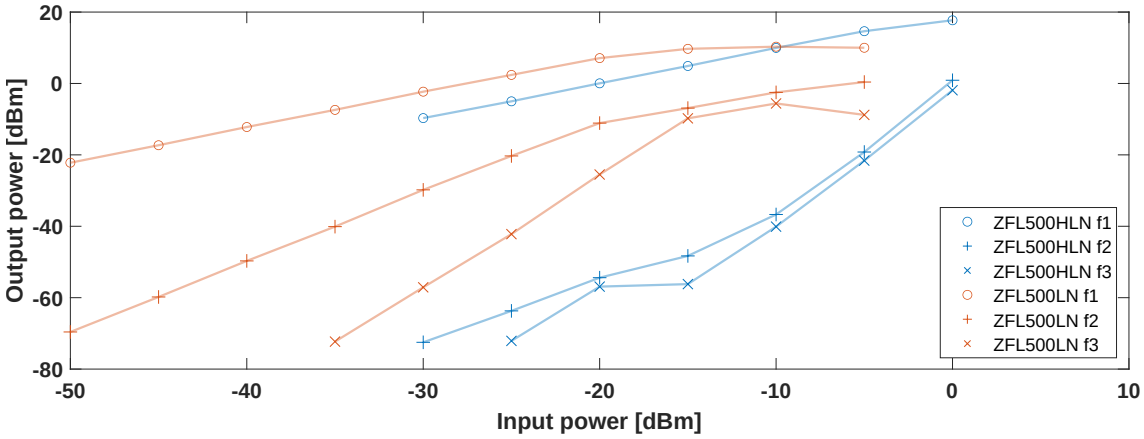

(a)

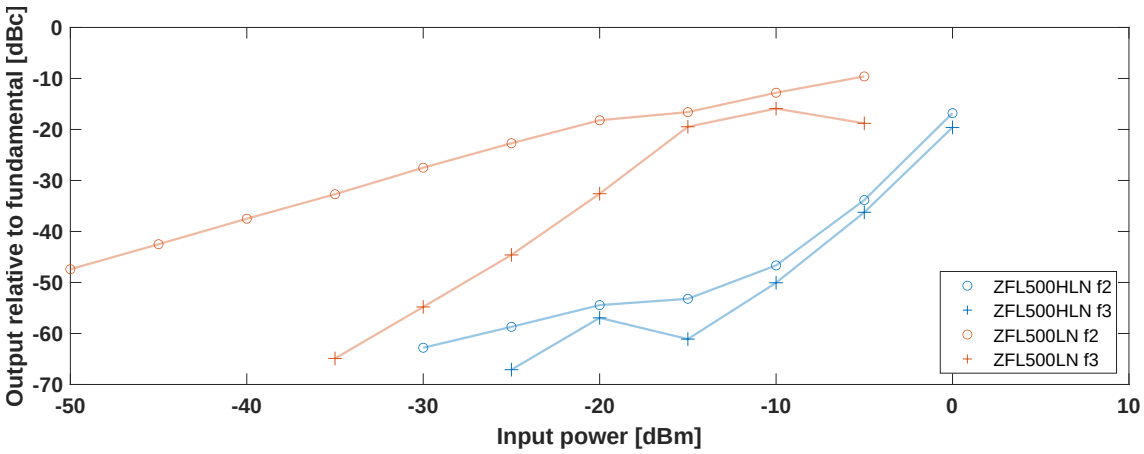

(b)

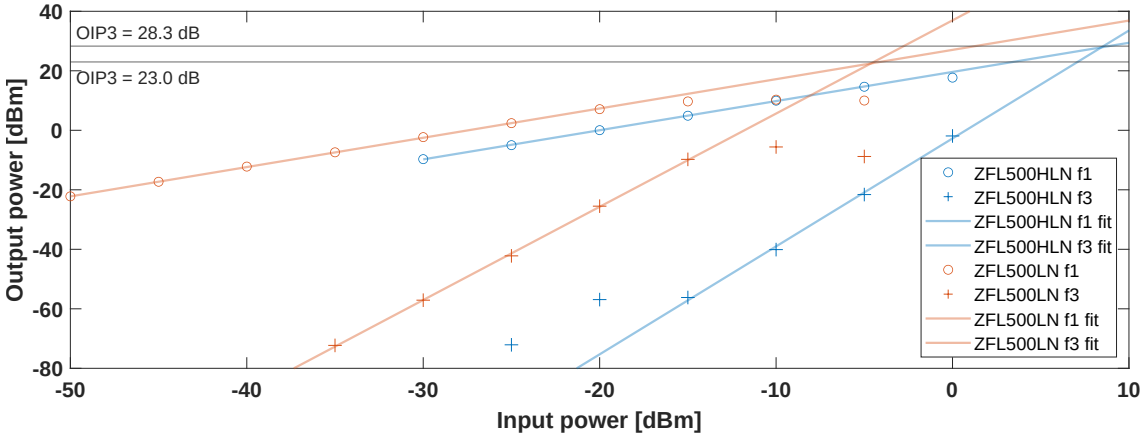

(c)

Figure 5.16: (a) The absolute measured power of the fundamental, second harmonic, and third harmonic for the ZFL500HL and ZFL500HLN amplifiers, (b) the signal level of the second and third harmonics relative to the fundamental tone, and (c) the fitted OIP3 values of each amplifier.

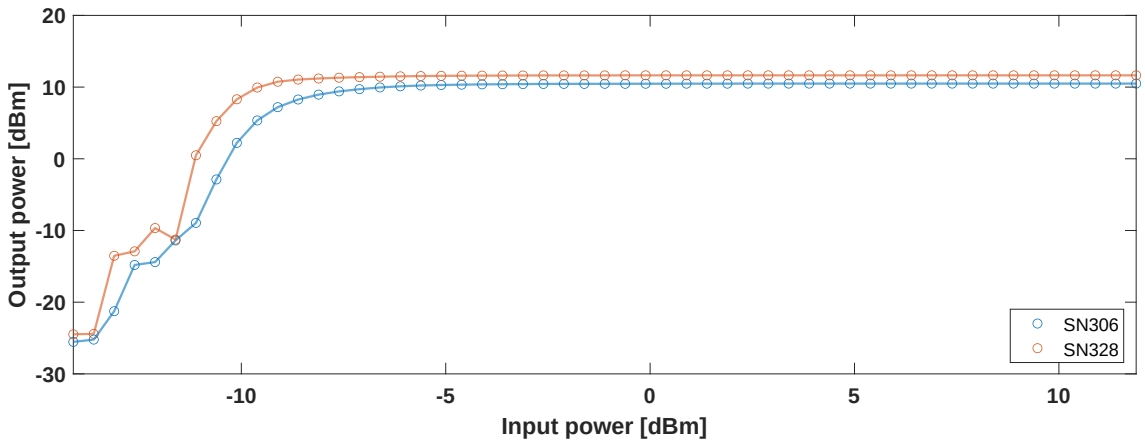

Figure 5.17: The compression curve measurements for Quantum Microwave QMC-MX6-10F10 ×6 frequency multipliers with serial numbers 306 and 328. Data were measured at a constant input frequency of 17.25 GHz. Saturation is achieved by ∼−5 dBm for both units, where the saturated level is 11.6 dBm for SN328 and 10.5 dB for SN306.

The data for the measurement are plotted in Fig. 5.17, where the input power level accounts for the cable loss and the output power measurement is adjusted according to the calibration of the meter head. The plot shows that the output power of both multipliers is saturated at an input signal of ∼−5 dBm. Unit 328 produces approximately 1 dB more output power than unit 306, the saturated levels being 11.6 dBm and 10.5 dBm respectively. It was anticipated that the LO drive to the SHM would require attenuation to be set to the correct level, and so the lower power unit was selected for use in the receive chain.

The frequency response of both multipliers was then measured, again in a similar way as the IF chain in Subsection 5.1.3. Here the Anritsu signal generator was set to a constant level well beyond saturation for the multipliers, and the frequency incremented whilst measuring the output power with a power meter in the same way as for the compression curve measurement. When conducting initial measurements of transmit chain, it was discovered that at certain frequencies a resonance effect between a multiplier and a subsequent component could produce a signal of up to 21 dBm at 90 GHz. A signal this large was much greater than expected, and is much greater than the allowed SHM LO input. It was then determined that this was a fault with these units and they were sent back to the manufacturer for repair, where it was discovered that a small absorber component within each multiplier was missing. This was then added to each multiplier, and the repaired units were measured again. The data for both sets of measurements are shown in Fig. 5.18, where the first run of measurements were taken with an input power level of 3.89 dBm, and a level of 4.25 dBm for the second run. This should not impact on the comparison between the measurements

however, since the input power level remained well within saturation in both cases.

The measurements for the repaired multipliers show average output powers of 11.5 dBm and 11.9 dBm for unit 328 at high and low band respectively, with a variation of ±0.1 dB. For unit 308, the output powers were 10.2 dBm and 10.9 dBm at high and low band, similarly with a variation of ±0.1 dB. The slight difference in output level between the measurements in Fig. 5.17 and Fig. 5.18 at corresponding frequencies is attributable to the repair of both units, where this caused the output of unit 328 to increase slightly whilst for unit 306 a decrease is seen. Both of the output power levels are acceptable to drive the subsequent components in the receive and transmit chains however, and it is more important that these units function reliably and without the resonance effect which could damage subsequent components than to maximise output power from the multipliers.

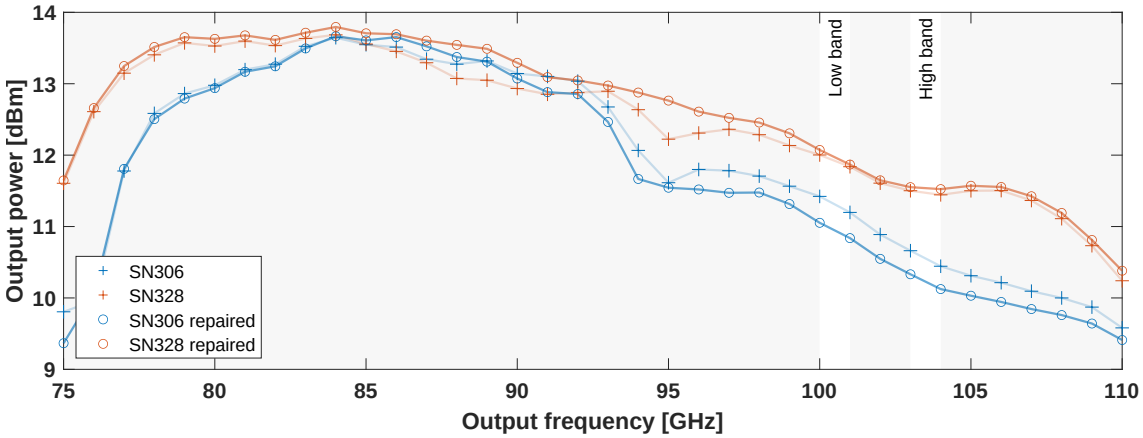

Figure 5.18: Frequency response measurements of both Quantum Microwave QMC-MX6-10F10 ×6 frequency multipliers across the whole of W-band. Two measurement runs are shown for each multiplier, before and after being repaired to resolve an unwanted signal spike at 90 GHz caused by a resonance effect. A slight change is observed in output power level before and after the repair, where the final average levels at high band are 11.5 dBm (SN328) and 10.2 dBm (SN306) and at low band these are 11.9 dBm (SN328) and 10.9 dBm (SN306).

5.1.4.2 Mixer LO level optimisation

The next two experiments aimed to optimise the LO drive to the SHM. The SHM requires an LO level between 2 to 6 mW (3 to 7.8 dBm) to function properly, where a low LO level worsens the receiver conversion loss and degrades sensitivity, whilst a drive level above the upper limit will damage the SHM. Since the multiplier output varies with frequency as shown in Fig. 5.18, preserving the maximum accessible frequency range for the receiver without damaging the SHM required setting the the

attenuation for the mixer LO so that it remained below 7.8 dBm over the greatest frequency interval which also encompassed high band.

The goal of the first experiment was to then determine the maximum LO attenuation level which would not increase the conversion loss significantly, since this would give the largest margin of safety. This was accomplished by monitoring the integrated IF power level of the mixer versus LO frequency for different levels of LO drive when receiving only free-space noise, which provided a constant input level to the RF port. Higher IF power levels would then indicate a lower conversion loss, where a saturation level would eventually be reached.

The experiment was conducted by varying the LO drive from the ×6 multiplier with serial number SN306 by using W-band waveguide attenuators either singly or combined to give 3, 4, 5, or 6 dB of attenuation. The W-band isolator between the attenuator and SHM (which adds ∼0.8 dB of attenuation) was included in the measurement since this was the configuration that the SHM would always be operated in. The resultant LO drive levels which were tested thus ranged from ∼3.4 to ∼6.4 dBm at high band and ∼4.1 to ∼7.1 dB at low band in increments of 1 dB, for waveguide attenuations of 6 to 3 dB. A small conical G-band horn was attached to the mixer RF port and terminated into an absorbing cone to ensure that the only input at this port was free-space noise. To protect the IF amplifiers, an MC BLK-18 DC-block was attached to the mixer IF port. This was followed by an MC SHP25 high-pass filter (HPF) with a cut-off of 25 MHz and an MC SLP450 LPF with a cut-off of 425 MHz, so that the IF noise signal had a well defined bandwidth. The frequency limits were motivated by the lower limit of the HP8481A sensor head (which measures down to 10 MHz) and the upper limit of the Wenteq amplifiers (∼500 MHz) used to increase the signal level. This sensor head was specifically chosen to provide the widest bandwidth for the measurement, as the IF noise power from free-space noise is very low. The two identical Wenteq Microwave Corp. ABL0050-00-3310 LNAs used to increase the signal level were chosen as they have a high gain of ∼33 dB, a low noise figure of ∼1 dB, were available, and have a very flat frequency response which would not introduce any bias to the measurement.

The results of this experiment are shown in Fig. 5.19. This clearly shows that the integrated power (and thus conversion loss) varies as a function of frequency, unfortunately showing a minimum at the lower edge of high band which can indicate that the noise figure of the mixer is worse at this frequency. The absolute conversion loss of the mixer itself cannot however be inferred from these values since they are only a relative measurements, and as they are also a function of the varying drive level from the ×6 multiplier. This measurement shows that the integrated IF power level

saturates for an LO level of ∼5.4 dB at high band and ∼6.1 dB at low band as achieved by using a 4 dB waveguide attenuator, where no real increase in performance is seen when using a 3 dB attenuator. The choice for LO attenuator should then be the 4 dB unit as this best satisfies the requirements on the LO drive explained above and gives the greatest safe operating frequency range.

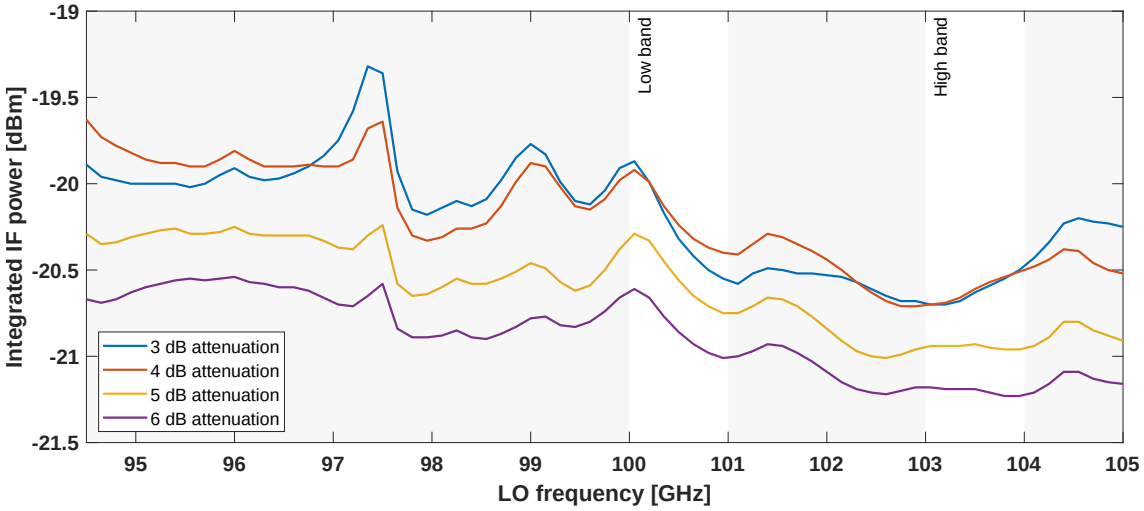

Figure 5.19: The results of four measurements of integrated IF power from the Farran SPM-05-0002 G-band SHM, as a function of LO signal frequency at four different attenuation levels on the LO. All the measurements were performed using Quantum Microwave ×6 frequency multiplier unit 306 along with a Micro Harmonics W-band waveguide isolator. Note that the attenuation value in the plot refers to the total from the waveguide attenuators only and does not include ∼0.8 dB attenuation caused by the isolator. These results indicate that the integrated IF power saturates for attenuators of 4 dB or less, resulting in LO drive levels of ∼5.4 dB at high band and ∼6.1 dB at low band. Attenuation greater than this should not be chosen so that the mixer conversion loss is minimised.

The goal of the second experiment was to then determine the resultant maximum accessible frequency range for the mixer LO which was within the safety limits when using the optimal attenuation level. This was accomplished by the same method used for the results in Fig. 5.18, where the output power was instead measured at the output of the W-band isolator i.e. at the LO input of the SHM. This measurement yielded the data in Fig. 5.20, which show that the minimum safe LO frequency is 95 GHz, or an RF frequency of 190 GHz. As discussed previously, in practice the radar does not operate at these frequencies in the present configuration due to the first BPF in the chirp generator, however this result confirms that the LO drive level set by the chosen attenuator is safe, and is useful in future if the centre frequency or bandwidth are changed. In the present design, the average LO drive level at high band was measured to be 5.9 dBm, and at low band was 6.6 dBm. It should be noted that had the resonance

issue with the ×6 multipliers not been detected and resolved, this could have destroyed the SHM, even with the attenuators in use.

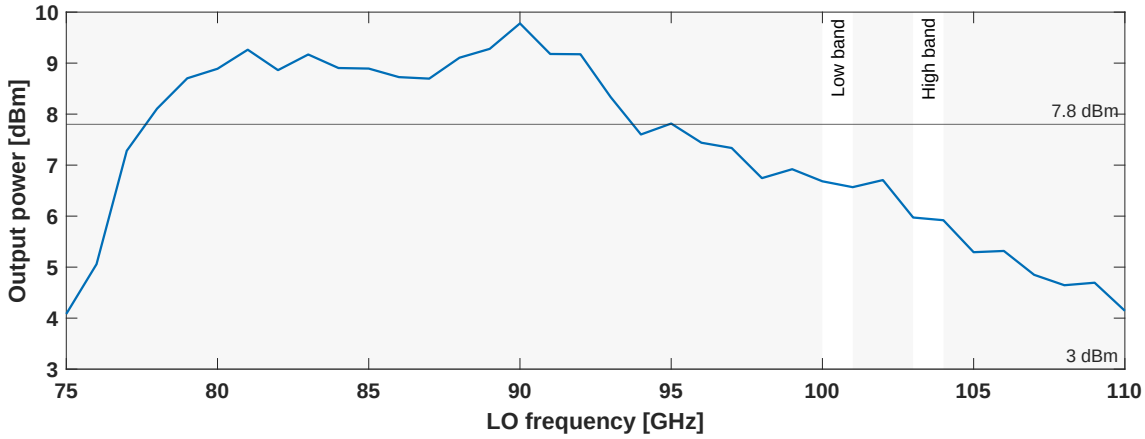

Figure 5.20: The LO drive level as a function of frequency at the input of the SHM, using a 4 dB waveguide attenuator. These results show that the LO drive remains within safe limits (indicated on the graph as 3 to 7.8 dBm) down to a signal frequency of 95 GHz. These results were first reported in Vattulainen et al. (2022) [23].

5.1.4.3 Noise figure

The next set of measurements was to determine the noise figure of the receiver, where these results were first published in Vattulainen et al. (2024) [29]. The noise figure is one of the key determining factors for sensitivity, as it describes the level of noise in the instrument. The double sideband (DSB) noise figure was measured using the Y-factor method for the full receiver, i.e. with the LO as supplied by the chirp generator, the radar antenna and waveguide link on the RF port, and the final IF chain on the IF port.

A Y-factor measurement involves recording the integrated IF power over a defined bandwidth whilst observing two broadband noise sources with different noise temperatures. In practice this can be achieved either with noise sources or, as in the case of the measurement made here, using black-body targets at two different known temperatures. The difference between the two power levels can then be used to calculate the Y-factor, and from that, the noise temperature of the device under test [45, p. 7.67]. The noise temperature T_N in terms of the noise power P_N is given in Eq. 5.4:

$$T_N = \frac{P_N}{k_B B_N} \tag{5.4}$$

where k_B is Boltzmann's constant and B_N is the noise bandwidth. The Y-factor y is then defined in Eq. 5.5 (as a ratio of linear powers), and can be used with Eq. 5.4 to express the noise powers of a hot and cold noise source P_H and P_C in terms of the noise

temperatures of the noise source and the noise temperature of the receiver, T_R:

$$y := \frac{P_H}{P_C} = \frac{(T_H + T_R)k_B B_N}{(T_C + T_R)k_B B_N} = \frac{T_H + T_R}{T_C + T_R} \tag{5.5}$$

Equation 5.5 can then be rearranged for T_R as a function of the noise source temperatures and the Y-factor, as shown in Eq. 5.6:

$$T_R = \frac{T_H - yT_C}{y - 1} \tag{5.6}$$

The noise temperature of the receiver can then be used to calculate the receiver noise figure $\mathcal{N}_r$ using Eq. 5.7:

$$\mathcal{N}_r = 10 \cdot \log_{10}\left(\frac{T_R}{290\ [\mathrm{K}]} + 1\right) \tag{5.7}$$

where the reference value for the temperature is taken as 290 K.

The Y-factor measurements were made using a HP8481A power meter sensor with the lowest frequency limit available of 10 MHz. This, along with the anti-alias LPF on the IF chain, defines the measurement bandwidth as 10 to 32 MHz. The 'hot' noise source used was a piece of microwave absorber at room temperature, and for the cold source a 45° mirror was used to observe a similar piece of Eccosorb AN72 microwave absorber immersed in liquid nitrogen. To measure the noise figure as a function of RF signal frequency, a set of power measurements were taken whilst incrementing the LO frequency and observing the hot source, and then a second set was taken at the same frequency steps immediately afterwards whilst observing the cold source. The difference between these two sets was then used to determine the Y-factor, and the procedure was repeated for a total of three runs.

The results of the experiment are shown in Fig. 5.21, along with the average of all three runs. This shows a generally good agreement between the three different runs of measurements, where the receiver noise figure average across low band is 12.1 dB, rising to 14.1 dB at high band. This indicates that the mixer conversion loss is indeed higher at high band compared to low band, as suggested by results in Fig. 5.19. Since the IF power could not be directly measured below 10 MHz, it is assumed that the noise is not significantly different than in the measured band of 10 to 32 MHz. In reality the noise may be slightly greater due to the rise in $1/f$ noise, so the measured noise figure may be a slight underestimate when considering the full IF band.

Since no direct measurement of the SHM conversion loss was practical, the conversion loss of the mixer L_c and the mixer noise figure $\mathcal{N}_{mix}$ were inferred from the noise figure of the receiver using the Friis formula for the total noise factor shown in

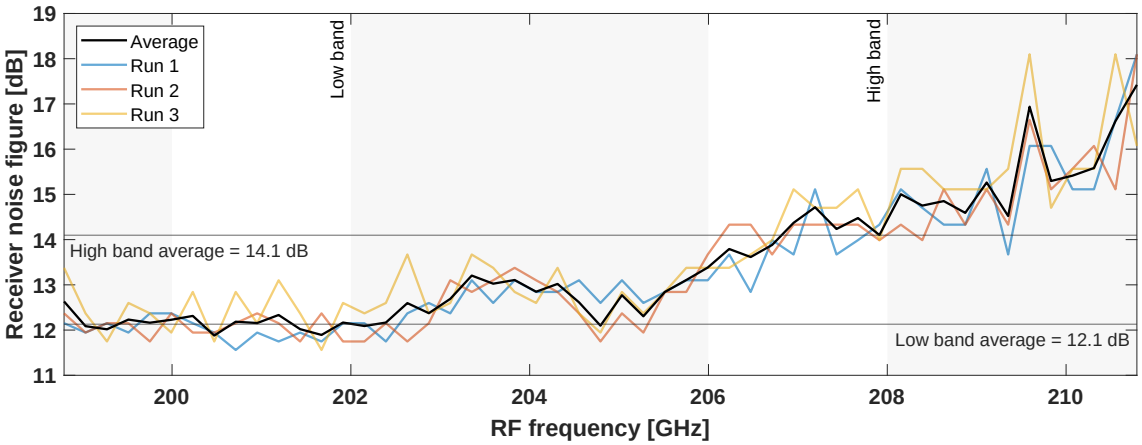

Figure 5.21: The noise figure of the full receiver measured using the Y-factor method. Three runs of data as a function of RF frequency were recorded and show good agreement. The average of the runs is also plotted, where the mean value across low band was 12.1 dB, rising to 14.1 dB at high band.

Eq. 2.26 of Section 2.1.6, reproduced here:

$$F_{\mathrm{t}} = F_1 + \sum_{i=2}^{Q} \left(\frac{F_i - 1}{\prod_{j=1}^{i-1} G_{\mathrm{lin},j}} \right)$$

where F_{t} is the total noise factor, F_{i} are the noise factors of each component, Q is the total number of components in the receiver chain, and $G_{\mathrm{lin},j}$ is the linear gain value of component j. This equation is reformulated from the long form given in [45, p. 7.27]. The equation was modelled in MATLAB® to produce the noise cascade model of the receiver shown in Fig. 5.22 with parameters in Table 5.4 calculated using each of the total average noise figures in low and high bands. Since the precise relationship between L_{c} and $\mathcal{N}_{\mathrm{mix}}$ is unknown, it was assumed that $\mathcal{N}_{\mathrm{mix}} = |L_{\mathrm{c}}|$ (in decibel units). Using this method, the mixer conversion loss was estimated to be −9.2 dB and −11.3 dB in low and high band respectively.

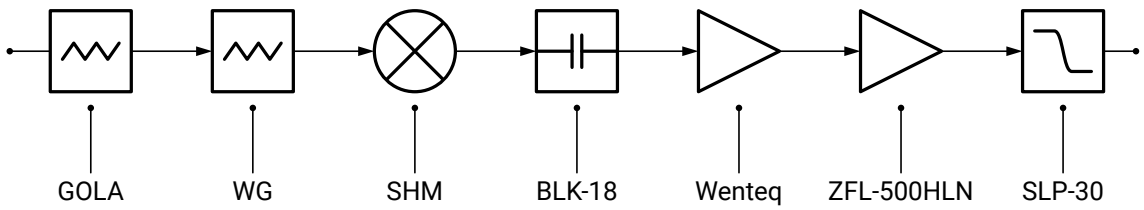

Figure 5.22: The receiver block diagram used for the noise cascade model. The parameters used for the modelling are shown in Table 5.4.

The implied conversion loss (and thus noise figure) of the mixer is worse than the values measured by the manufacturer, which were at worst ∼8 dB, however this is still

	GOLA	WG	SHM	BLK-18	Wenteq	ZFL-500HLN	SLP-30
Low band							
i	1	2	3	4	5	6	7
G	−1.30	−0.25	−9.2	−0.2	33.8	21.0	−0.2
G_{lin}	0.74	0.94	0.12	0.95	2400	126	0.95
$\mathcal{N}$	1.30	0.25	9.2	0.20	1.15	3.83	0.20
F	1.35	1.06	8.32	1.05	1.30	2.42	1.05
High band							
i	1	2	3	4	5	6	7
G	−1.23	−0.25	−11.3	−0.2	33.8	21.0	−0.2
G_{lin}	0.75	0.94	0.07	0.95	2400	126	0.95
$\mathcal{N}$	1.23	0.25	11.3	0.20	1.15	3.83	0.20
F	1.32	1.06	13.8	1.05	1.30	2.42	1.05

Table 5.4: The parameters of the noise cascade model of the receiver, listing the position (i), gain [dB] (G), linear gain (G_{lin}), noise figure ($\mathcal{N}$), and noise factor (F) of each component. A frequency of 10 MHz was assumed for the components in the IF chain. The mixer conversion loss was estimated from these values to be −9.2 dB and −11.3 dB in low and high band respectively. The results for high band were first published in Vattulainen et al. (2024) [29].

acceptable performance for use in the instrument. The discrepancy is likely due to the optimisation of the LO drive level, which for best performance should be performed for each LO frequency (this being the method followed by the manufacturer). This is however not practical for chirped operation, and thus degrades the overall performance. The noise figures of the other IF chain components are expected to be constant with power level and frequency (except of course the DC block and anti-aliasing filter) given their datasheet values, and their effects on the total noise figure will be overshadowed by that of the mixer due to either their comparatively low noise factor or position in the chain. The variation of the noise figure and thus conversion loss with frequency seen in Fig. 5.21 is then ascribed to the LO optimisation problem, where in contrast the manufacturer's measurements indicate the conversion loss is flat to ±∼0.5 dB. As a result, the total gain of the receiver (defined from the input port of the SHM to the output port of the IF chain) at low band is 45.3 dB, reducing slightly to 43.2 dB at high band, for an IF frequency of 10 MHz.

5.1.5 Transmit chain results

The first element of the transmit chain is the Quantum Microwave ×6 frequency multiplier SN328, the characterisation of which is shown in Figures 5.17 and 5.18. This unit was chosen over SN306 as it has the higher saturated power. The Spacek

W-band PA was to be driven with as much power as possible to maximise available power at W-band, since this would be the limiting factor for the final output level of the VDI doubler and thus the final transmit power. This subsection presents the achieved output power of the Spacek PA in the transmit chain and the output power of the VDI doubler, both as a function of frequency.

5.1.5.1 W-band power amplifier output power

This experiment was set-up with an Anritsu MG3692B signal generator providing the input signal to the Quantum Microwave ×6 multiplier at a level similar to that from the output of the chirp generator (i.e., enough to saturate the multiplier). The output of the multiplier was attached directly to the input of the Spacek PA. A Micro Harmonics W-band isolator SN035 was attached to the output of the PA, following the final configuration of the full chain and providing protection to the output port of the amplifier. The power levels were measured using a power meter with a HPW8486A W-band waveguide sensor head, where a 10 dB Quinstar QAF-10000 waveguide attenuator was used to reduce the signal level from the isolator to prevent damage to the meter head. The S_{21} of the attenuator was ∼−11.1 dB at low band and ∼−11.6 dB at high band. The measurement of amplifier output power was then carried out by incrementing the input frequency from the Anritsu synthesiser and measuring the power at each step.

The calibration of the meter head was then applied to the measured values, and the insertion loss of both the isolator and the waveguide attenuator were compensated for such that the data represents the power level directly from the output of the PA port. The isolator S parameter data used to apply the correction is provided in Fig. 5.23b as supplied by the manufacturer.

The results of the measurement are plotted in Fig. 5.24. This shows a level ∼>20 dBm over most of W-band, decreasing after 95 GHz to a minimum of 16 dBm at 110 GHz. The average across low band was 20.4 dBm, and across high band was 19.9 dBm. The roll-off is in part due to the performance of the PA itself but also due to the output of the ×6 multiplier also decreasing in this region as shown in Fig. 5.18. This is representative of the general reduction in performance seen for many solid state components operating at 100 GHz or above, it being very difficult to source components with output power levels in excess of 20 dBm. In this regard the Spacek model performs very well, especially considering the small package and modest cooling requirements which are easily met by good passive heat-sinking. The full transmit chain is shown on the bench in Fig. 5.25, where the Spacek PA is 2.36 cm by 2.87 cm. Each of these components save the isolator is attached to individual aluminium blocks which heat-sink to the enclosure, where only the block for the VDI doubler can be seen at

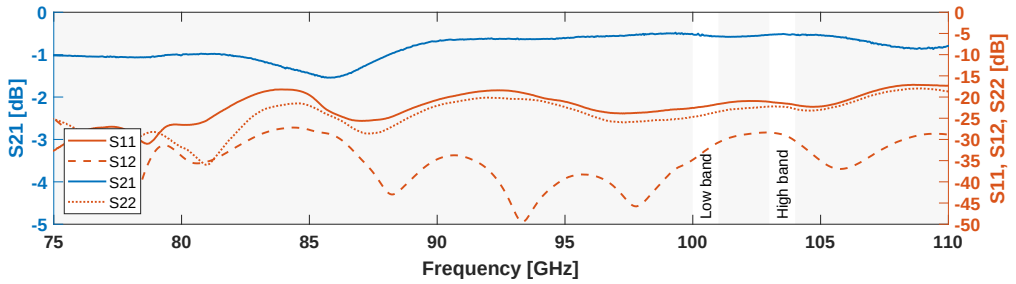

(a)

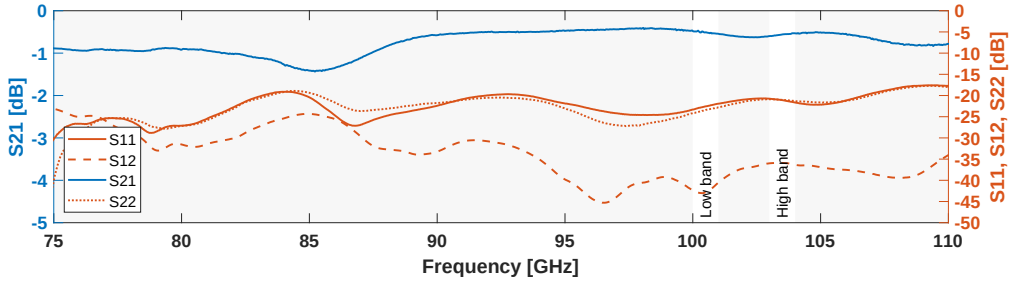

(b)

Figure 5.23: Micro Harmonics W-band isolator FR100M2 S parameters for (a) unit serial number -034 and (b) unit serial number -035, as provided by the manufacturer.

the angle of the photograph.

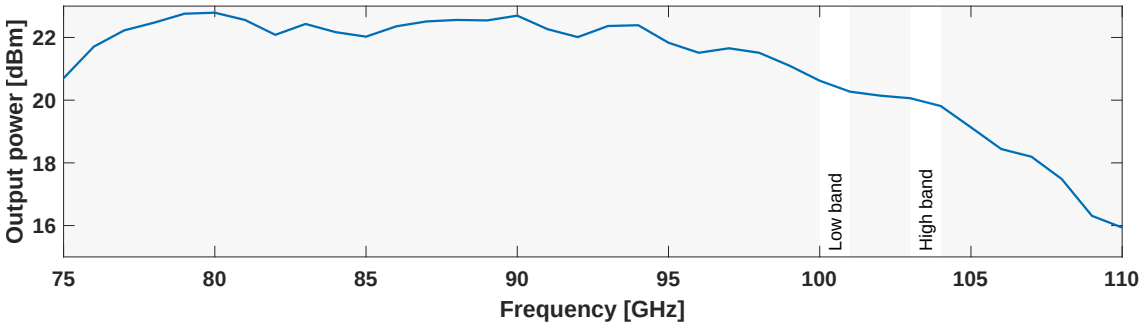

Figure 5.24: Measured output power as a function of frequency from Spacek Labs SPW-10-20 PA across W-band, as driven by the saturated output of a Quantum Microwave QMC-MX6-10F10 ×6 frequency multiplier. The output power is in excess of 20 dBm up to 103 GHz. The roll-off beyond 95 GHz is the combined effect of the output power of the ×6 multiplier falling and the performance of the amplifier itself.

Measurements of the PA gain as a function of frequency and of the compression curve were not made as these were not particularly relevant to the development of the radar. The main concern was the generation of adequate output power to drive the VDI doubler, and as such, testing in the configuration of the radar transmitter was deemed sufficient. Producing the maximum output power necessarily required that the amplifier output would be substantially compressed, however the inevitable harmonic distortion at this stage was not a concern since the doubler would itself add

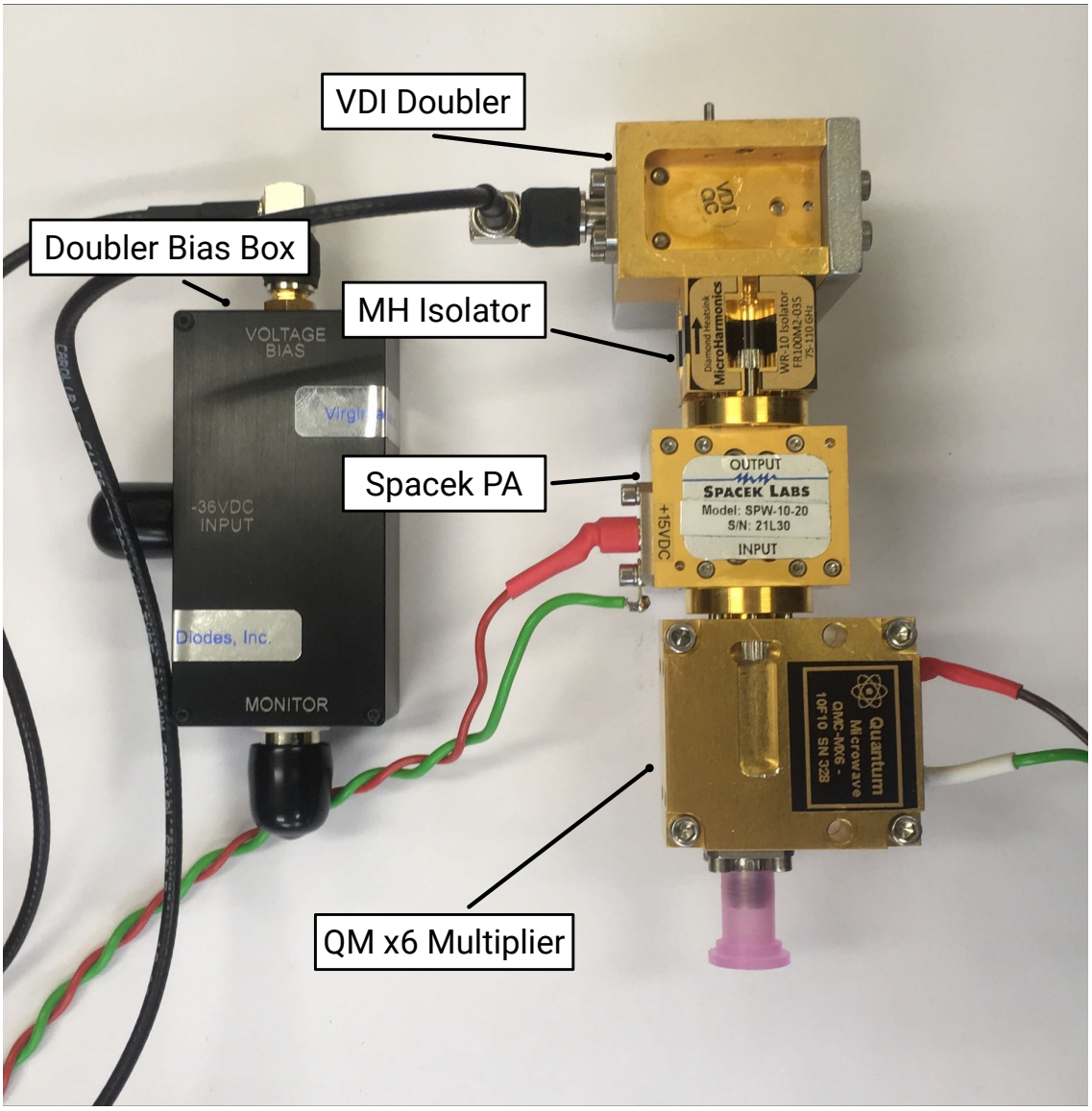

Figure 5.25: A photograph of the transmit chain components on the bench prior to integration into the radar enclosure. The Spacek PA is 2.36 cm by 2.87 cm.

harmonics in either case, and the potential for spectral regrowth or intermodulation products to degrade signal quality is less of a concern at the end of the signal chain than in the chirp generator. The results of the amplifier power measurement were previously published in Vattulainen et al. (2022) [23], however did not account for the insertion loss of the W-band isolator and thus those values are slightly lower than the output power values presented here.

5.1.5.2 Transmitter power

The measurement of the G-band transmit power required a more specialised apparatus than that used for W-band measurements, since no waveguide power meter was

available for the G-band frequency range. The key instrumentation used for this experiment was a Thomas Keating Ltd. (TK) free-space power meter[1] which is capable of measuring power over a large range of frequencies (from 30 GHz to 3 THz), but required a more complex apparatus and procedure than a typical power meter. A diagram of the set-up of the meter is shown in Fig. 5.26. The signal to be measured is generated by the transmit chain consisting of the Quantum Microwave ×6 multiplier, Spacek Labs PA, Micro Harmonics isolator, and the VDI doubler. The ×6 multiplier is driven by a signal from an Anritsu MG3692B synthesiser such that the multiplier output is fully saturated. The output of the doubler is coupled to free-space by a small copper G-band conical horn.

Inside the power meter head is a very thin metallised membrane in between two sheets of transparent material, forming a photo-acoustic cell. The membrane has an impedance equal to half that of free-space, and thus absorbs 50% of incident radiation (with 25% each transmitted and reflected) when the incident beam is at the Brewster angle. The change in pressure within the cell due to heating of the film and thus the air is measured by a pressure transducer inside the cell and a lock-in amplifier within the control box. For the lock-in amplifier measurement, the pressure signal and thus the heating of the film needs to be square-wave modulated, where the performance is optimised for low modulation frequencies of 10 to 50 Hz. To determine the power dissipated in the film by the beam, the anti-phase of the square-wave signal is used as input to the control box, which then alternately electrically heats the film to match the pressure caused by heating from the incident beam. The power dissipated by the electrical heating is determined by the known resistance of the film and by the control box which measures the voltage applied the film.

To operate the meter, the square-wave modulation of the incident signal is achieved by using a signal generator (in this case a HP33120A) to produce a transistor-transistor logic (TTL) control signal, set to 30 Hz for this measurement. This signal is split and used as the reference input for the power meter control box lock-in amplifier and as the control for an RF switch (Analog Devices HMC-C011) between the signal generator and the ×6 multiplier, turning the test signal on and off at a rate of 30 Hz. The reference and switching signals are arranged to be in anti-phase by selecting either the normally open or normally closed port to give the desired opposing phase to the control box signal. The final element of the apparatus is the coupling of power between the meter head and the conical horn. This is arranged such that the E-plane of the antenna pattern is at 55° incidence to the window of the meter, this being Brewster's angle

[1]Thomas Keating Ltd. website https://www.terahertz.co.uk/index.php?option=com_content&view=article&id=140&Itemid=443?option=com_content&view=article&id=140&Itemid=443

for that material, to ensure a known fraction of the energy is absorbed by the film as mentioned above. An accurate reading is then dependent on precise levelling of the meter with respect to the antenna so that the pattern is centred on the window, the E-plane is aligned exactly with the vertical axis of the meter, and the incidence angle is exactly 55°.

This set-up is clearly quite elaborate and is indicative of the challenges of G-band measurements. This is in recent years becoming easier as more convenient test equipment is designed for 6G communications technology development, notably up to 170 GHz at present with a power meter head from R&S [166] and up to 3 THz with a waveguide meter from VDI [167].

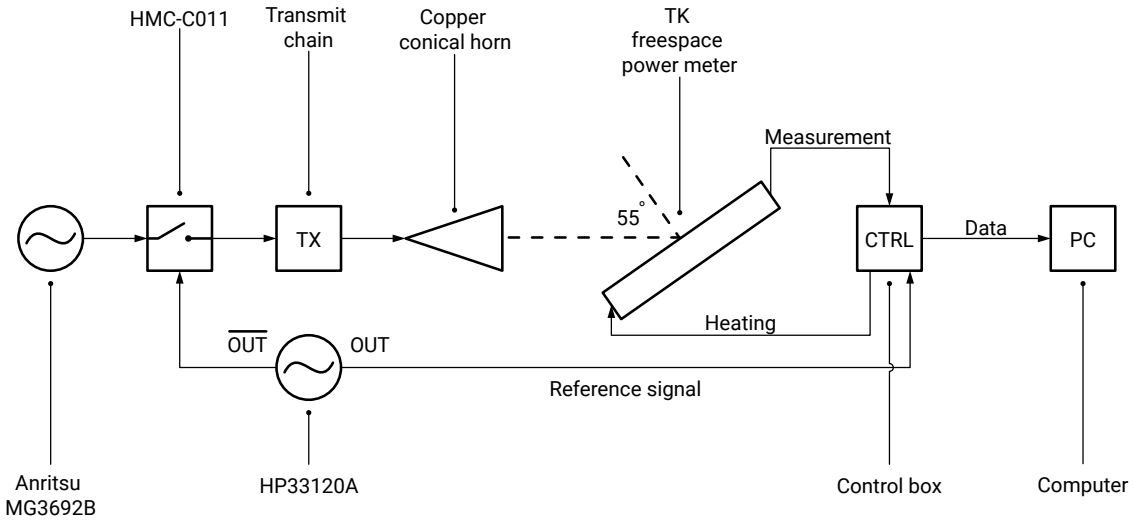

Figure 5.26: A diagram of the TK free-space power meter apparatus used to measure G-band power output. The H-plane of the antenna response is in plane with the page.

The averaged output power from two runs of measurements is shown in Fig. 5.27, where a loss of 0.2 dB was assumed for the copper conical horn and this was compensated for in the curve. Also shown in this plot is the doubler efficiency, calculated as the percentage between the output and input power levels in linear units. The input power level used is that from Fig. 5.24 with added attenuation due to the Micro Harmonics isolator.

The output power shows three distinct peaks, the highest coinciding with low band at an average level of 15.3 dBm and a maximum value of 15.4 dBm at 201.5 GHz. At high band, the average is slightly lower at 14.4 dBm. The power curve was used to inform the final decision on the frequency definitions of low and high band, chosen because they have a low variation in power level across the band, this being 0.13 dB at low band and 0.08 dB at high band. Low band was also defined as the region with the greatest output power, and high band the highest frequency region with a mostly

constant power level before the steep roll-off beginning at 208 GHz.

A good efficiency of 25% is achieved at ~198 GHz, which thereafter rises to a maximum of 36.2% at 202 GHz. The average in low band is 34.5% and at high band this is 31.9%. The excellent efficiency of >30% in low and high band is evidence of the specific optimisation of the doubler to work in this frequency range, and for this power level, where as mentioned previously they are typically designed to accept power levels of 27 to 30 dBm. The effect of the optimisation can additionally be seen in the lower efficiency and output power achieved at frequencies below 196 GHz, even though the drive level from the PA is approaching its maximum in this frequency region as seen in Fig. 5.24.

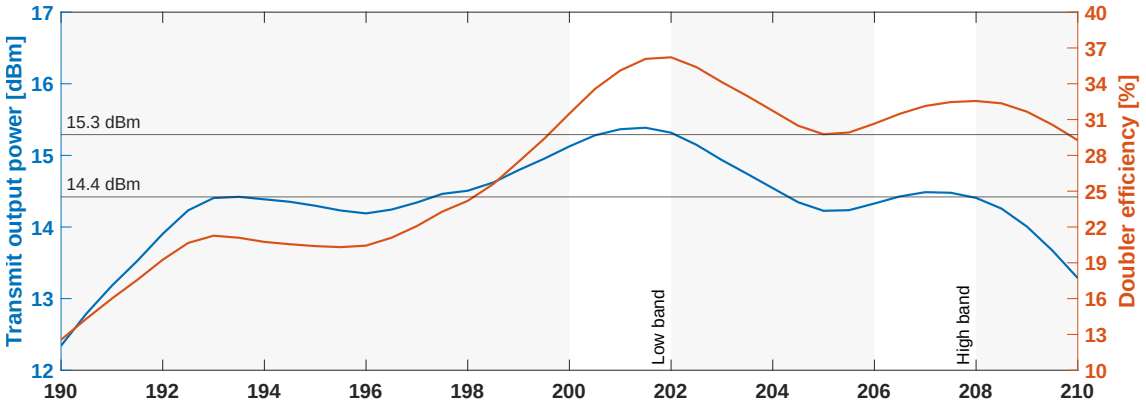

Figure 5.27: A plot of the measured transmitter power from the output port of the VDI doubler along with the efficiency of the doubler, on separate axes. The doubler output power was first published in Vattulainen et al. (2024) [29].

5.2 Radar range processing

The radar ADC records the IF chain output as voltage values which are saved as data files. The processing chain used to generate range profiles from this data is shown in Fig. 5.28. Data is first preprocessed to produce arrays of double precision floating point values from binary data files, which in the case of the Theseus radar are in the 'short' format. The ADC acquires 128 samples pre-trigger where these do not correspond to the measurement being made and must be discarded. The total samples acquired for each chirp is 4224, which after preprocessing is reduced to 4096, the expected number from the IF sampling plan described in Subsection 4.3.3. The rest of the range processing procedure is as follows:

- **Single chirp IF signal:** the preprocessed IF signal from a single chirp.

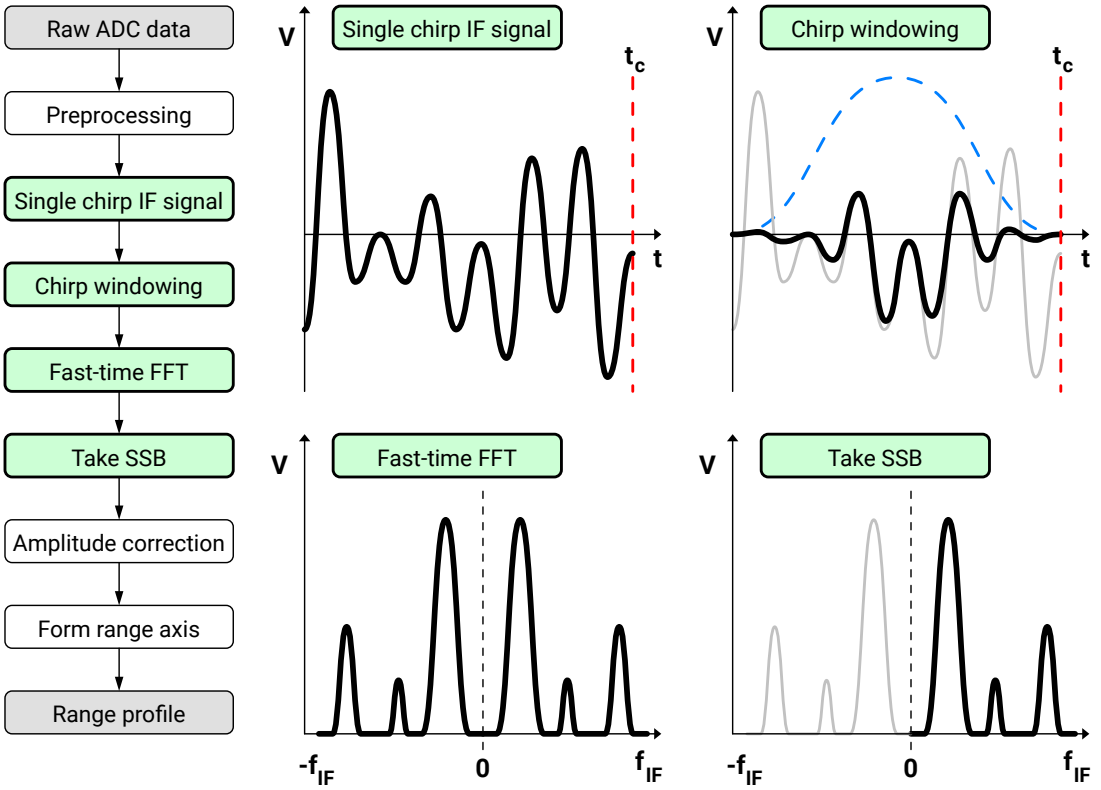

Figure 5.28: The FMCW range processing pipeline and diagrams of selected signal processing stages.

- **Chirp windowing:** a window is applied to the IF signal to suppress the spectrum side lobes. The exact window type depends on the measurement application.
- **Fast-time FFT:** a FFT is applied to the windowed chirp data along the fast-time/along-chirp dimension to extract frequency information.
- **Take single sideband (SSB):** the FFT produces a DSB spectrum, where in this step the image spectrum is removed as this does not correspond to a real range value.
- **Amplitude correction:** the data is transformed to decibels and the amplitude correction factor Ξ shown in Eq. 5.8 is applied to scale the data to units of dBm.
- **Form range axis:** the range-frequency relationship shown in Eq. 5.10 is used to transform the IF frequency axis to a range axis.

$$\Xi = -20\log_{10}(\Delta) - 3 + 30 - 10\log_{10}(50) - 20\log_{10}(n_S/2) - 20\log_{10}(G_w) \quad \text{[dBm]} \quad (5.8)$$

The factors contributing to Ξ are derived:

- $-20\log_{10}(\Delta)$: applies the ADC quantisation factor Δ to convert from the number of unique ADC values to V_{rms}. This is calculated in Eq. 5.9.

- −3: conversion from units of dB V_{rms} to dB W.
- +30: conversion from units of dB W to dBm.
- $-10\log_{10}(50)$: corrects for the 50 Ω input impedance of the ADC.
- $-20\log_{10}(n_S/2)$: corrects for the FFT gain.
- $-20\log_{10}(G_w)$: compensates for the IF windowing gain.

The ADC quantisation is calculated by dividing the total ADC range by the number of unique binary values it produces. The total range is −1 to + 1 V_{rms} and the number of bits is 16, thus:

$$\Delta = \frac{2}{2^{16}} \approx 3.0518 \cdot 10^{-5} \tag{5.9}$$

In practice, the windowing used is either a five term flattop window as described by Doerry [158, p. 192] or the '−92 dB Four-Term Blackman-Harris' window also catalogued by Doerry [158, p. 105], which are the default options for each family of windows in MATLAB®. The range-frequency relationship for the radar, used to convert the f_{IF} axis to the range axis, is determined by Eq. 2.7, and for the Theseus radar is given in Eq. 5.10:

$$R = \frac{f_{IF}c}{2s} = \frac{f_{IF}ct_c}{2B_S} = 3.859 \times 10^{-6}[\mathrm{m\,s^{-1}}] \cdot f[\mathrm{Hz}] \tag{5.10}$$

The radar is designed to be coherent and thus capable of Doppler measurements, but this workflow only describes the processing necessary for range profiles used in RCS and NRCS measurements which are the main results of concern in this thesis. For Doppler measurements, the standard slow-time processing over a CPI is performed [34, Section 17.5], but this is not discussed here.

5.3 System characterisation

A table summarising the results of the subsystem measurements and the defined radar parameters is shown in Table 5.5.

Using the values in Table 5.5, the realised performance of the radar versus the desired performance modelled in Subsection 4.3.1 can be evaluated. To do this, these parameters are used as inputs to the same modelling equations in that subsection and the results then compared. In Subsection 4.3.1, the right hand side of Eq. 4.7 was used to calculate the system constant β_C as 100.6 dB for the desired performance of $\mathcal{C} = 10$ dB at a range of 100 m for $\sigma^0 = -30$ dB. Using the measured radar parameters, the system constant was calculated to be 94.3 dB at high band and 97.3 dB at low band,

Parameter	Low band	High band
Transmit power	+15.3 dBm	+14.4 dBm
Receiver noise figure	12.1 dB	14.1 dB
Antenna gain	37.43 dBi (mean)	37.87 dBi (mean)
One-way antenna −3 dB beamwidth	2.13° (mean)	2.05° (mean)
Bandwidth/range resolution	2 GHz/7.5 cm	2 GHz/7.5 cm
Polarisation	HH, VV, HV, VH	HH, VV, HV, VH
CRF/CRI	14.796 kHz/67.59 µs	14.796 kHz/67.59 µs
Chirp duration	51.49 µs	51.49 µs
Sampling rate	79.55 MHz	79.55 MHz
Maximum unambiguous velocity	$\pm 5.36\ \mathrm{m\,s^{-1}}$	$\pm 5.36\ \mathrm{m\,s^{-1}}$
Maximum unambiguous range	153.5 m	153.5 m

Table 5.5: Measured and defined radar parameters.

where these values are 6.3 dB and 3.3 dB lower than desired, respectively, which is then passed on as the shortfall to the CNR at each band. This reduced the 10 dB CNR range to ∼63 m for high band and ∼78 m for low band for an NRCS of −30 dB.

The discrepancy is primarily due to a combination of insufficient transmitter power and high noise figure. For a $\beta_C = 100.6$ dB and using the realised parameters for the radar, the desired figure of merit $P_t/(F-1)$ is recalculated to be −23.3 dB at high band and −23.2 dB at low band. This is less than the estimate in Chapter 4 of ∼−18.5 dB due to the combined effect of the other measured values, meaning that the specification for transmitter power and noise figure was slightly more relaxed. When evaluating $P_t/(F-1)$ with the transmitter power values and noise factors however, this gives −29.5 dB at high band and −26.5 dB at low band. The discrepancy is ∼6.2 dB and ∼3.3 dB respectively, values which are approximately equal to the shortfalls noted above. Additionally, the antenna directivity was slightly lower and the antenna loss slightly greater than in the design calculations, both of which contribute to the somewhat degraded performance. The clutter measurement performance was still acceptable however, and given this sensitivity, the measurement of targets would still have a higher SNR due to the generally higher RCS. The ultimate performance of the radar was however determined by the measured radar range calibration curve and the system noise floor (with the added impact of the transmitter phase noise), where these results are presented in the following subsections, along with suggestions for improvements for system sensitivity.

The fully assembled radar is shown in Fig. 5.29, where this photograph was first published in [29]. Further photographs of the interior cavities of the radar are shown in Figures 5.30 and 5.31, where the key components and features have been labelled. This shows the compact arrangement of the internal components, power lines, and

signal cables. To interface the instrument with the control PC, the individual signal cables were bundled together into a control umbilical. A single cable feeds power to the instrument from a dedicated power supply unit.

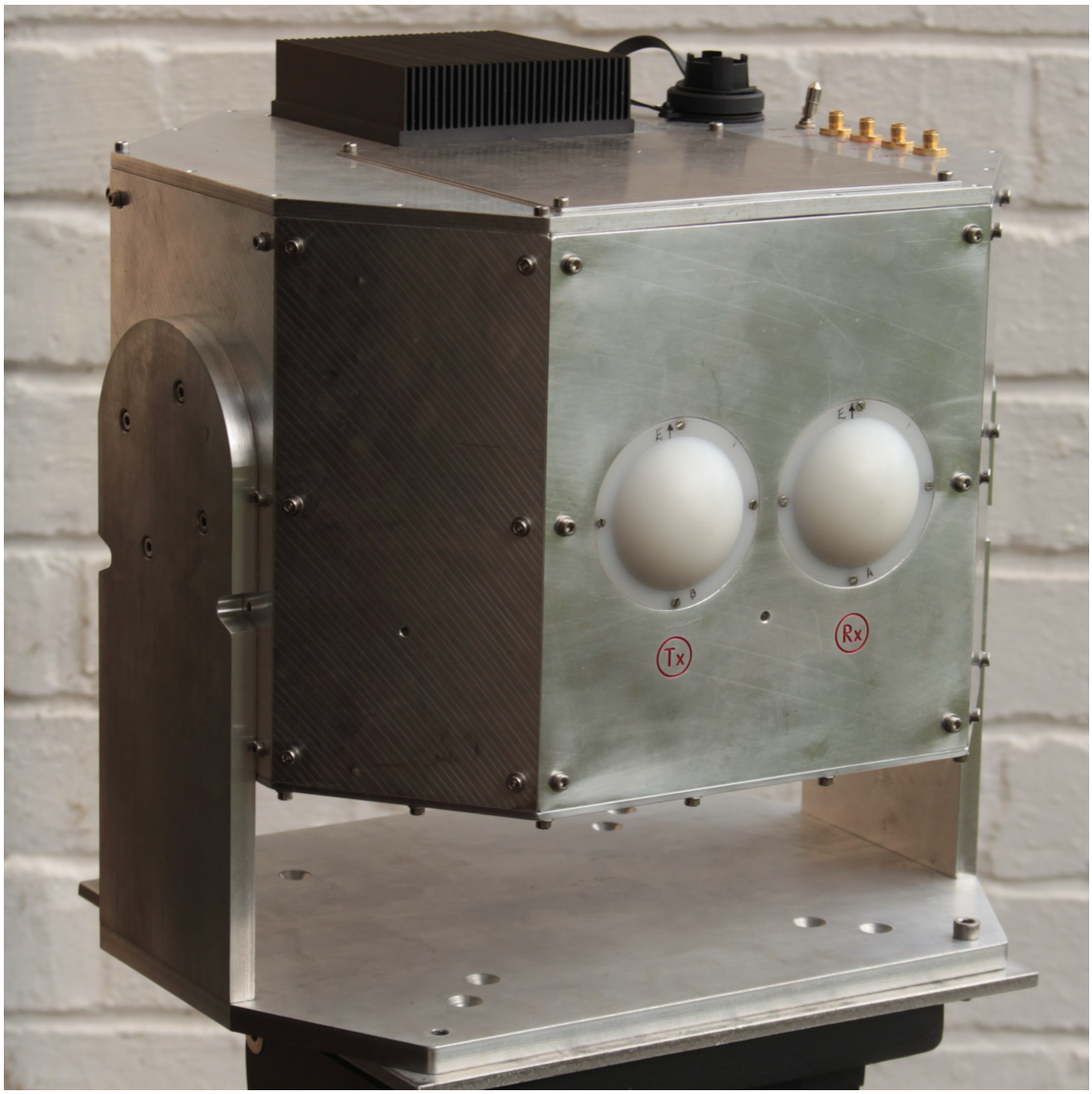

Figure 5.29: A photograph of the fully assembled Theseus radar mounted on a tripod where the twin GOLAs can be seen protruding from the front face. Through-bulkhead SMA connectors for the IF, clock, trigger, and motor control signals can be seen as the gold connectors at the top right of the photograph. Next to these is a switch to change between internal and external triggering, and a black USB connection port. The power cable connection point is obscured behind the black fins of the external heat-sink. Attached to the top face is a plate covering the port which allows access to the internal space, primarily for changing antenna polarisation.

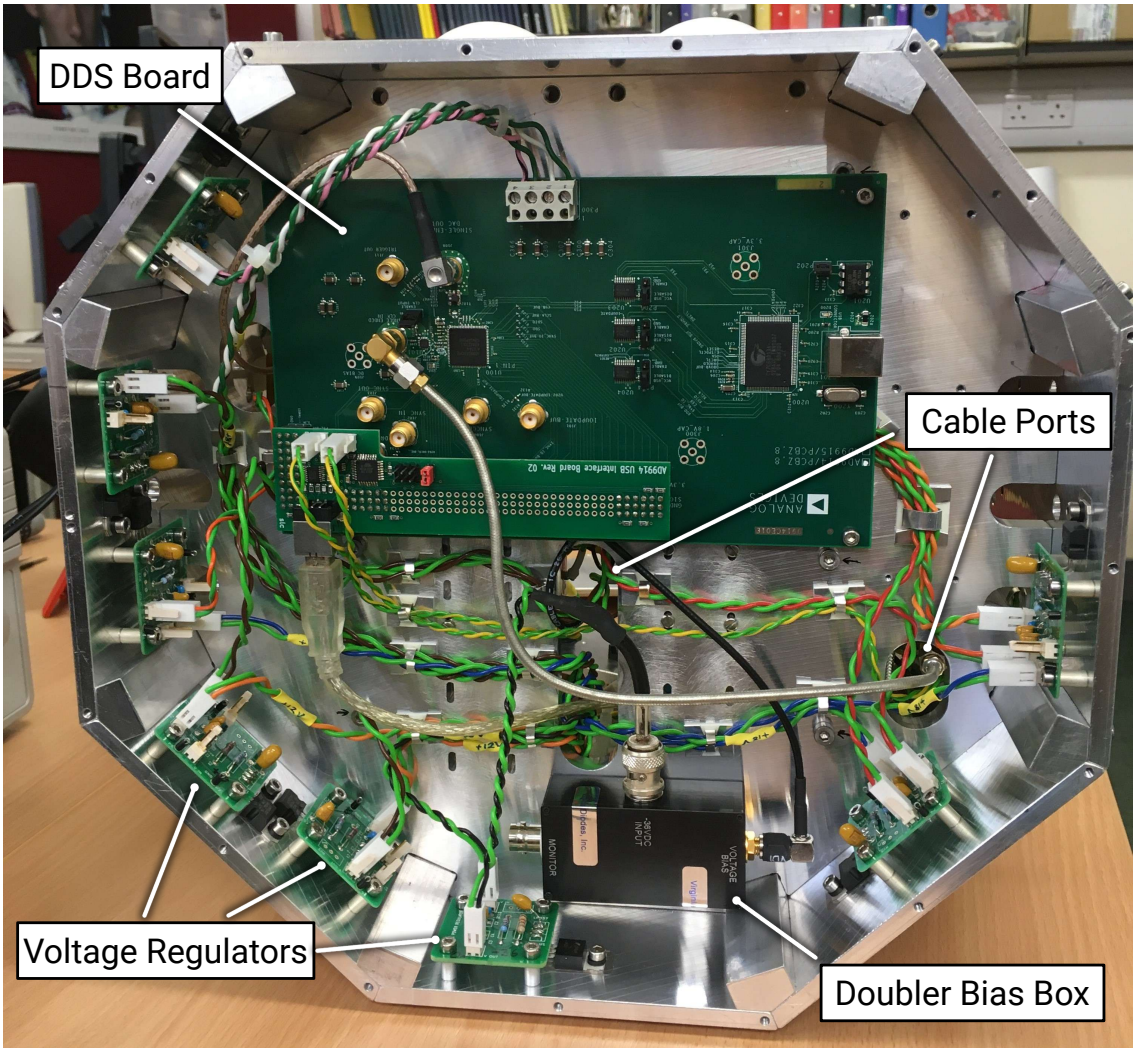

Figure 5.30: A photograph of the lower cavity of the Theseus radar, containing the DDS board and VDI doubler bias box attached to the internal plate, and numerous voltage regulator circuits mounted to the walls for direct heat-sinking to the environment. Several ports cut through the internal plate allow signal and power connections to be made between the lower and upper cavities.

5.3.1 Radar range calibration

The range calibration measurement tests the operation of the whole radar. The response of a calibrated target of known RCS can be predicted using the radar range equation Eq. 2.16 with the parameters measured for each subsystem above as listed in Table 5.5. The calibration curve is essential for the measurement of target and clutter reflectivity values, as it is used to control for the properties of the instrument itself when making such measurements.

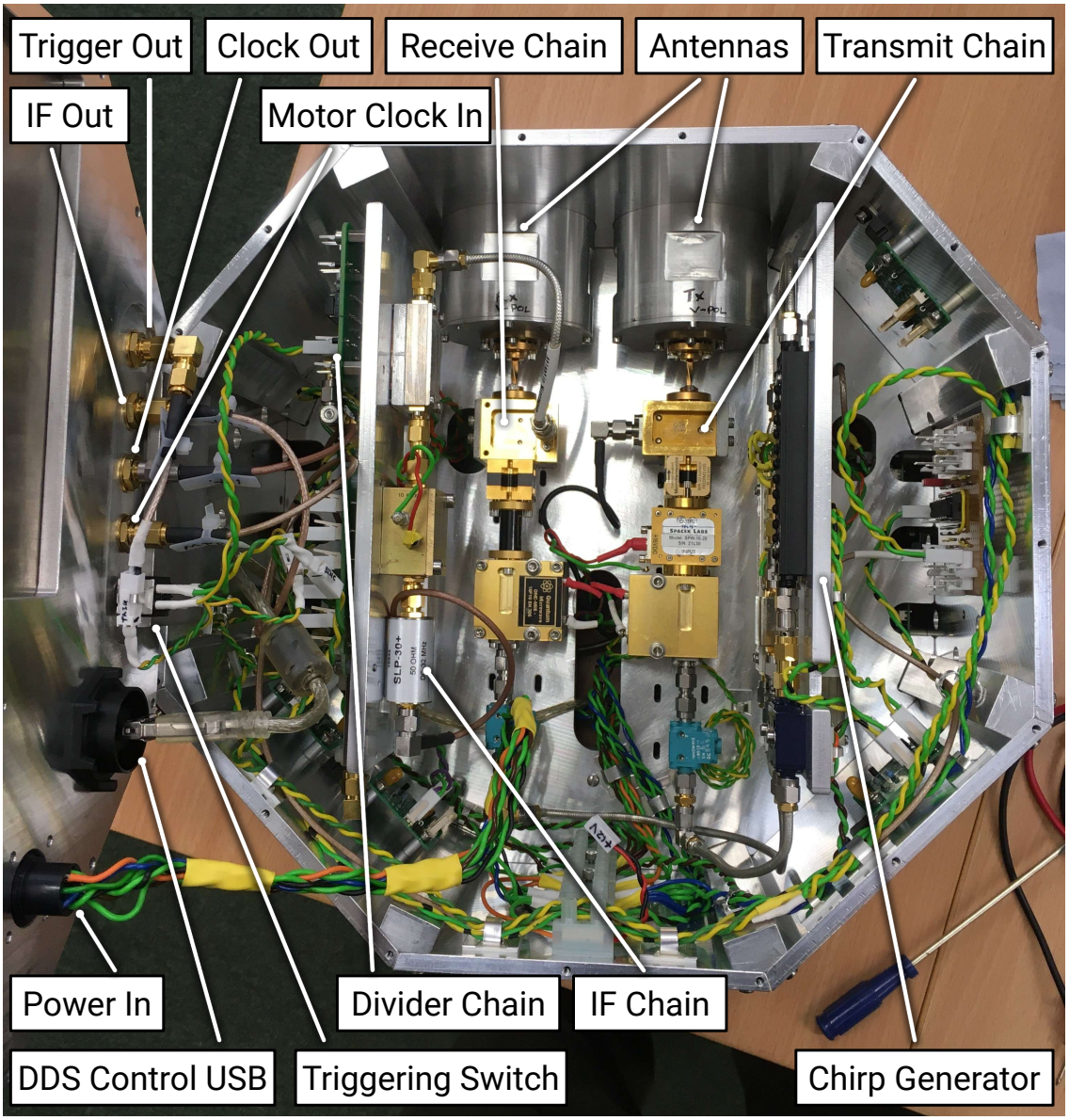

Figure 5.31: A photograph of the upper interior cavity of the Theseus radar. This chamber was split into three spaces by two interior plates which served to increase the area for mounting components. The divider chain was mounted in the left hand side space (label indicating the programmable divider board). The chirp generator components after the DDS output are mounted on the right hand side plate. In the central compartment are the transmit, receive, and IF chains. The interface points of the input power lines, control signals, and output IF signal are labelled as indicated. Beyond the lid the power lines interface into a single power cable, and the signal cables were gathered into an umbilical to interface with the control PC.

5.3.1.1 Method

The range calibration measurements were made using two precision triangular trihedral reflectors of side lengths 124 mm and 223 mm with RCS values of 26.85 dBsm and

36.85 dBsm at 207 GHz respectively, where at 201 GHz these values are 0.13 dB lower. These were individually mounted on a tripod at ∼2 m above ground height, which was placed at a selection of different ranges. The reflectors were visually boresighted such that they were within ∼1° of the response pattern maximum, which varies very little over a range of −10° to +10° [168], thus ensuring that the target RCS was as close as possible to the calculated value according to the dimensions. The use of a tripod reduces multipath reflections from the ground which can alter the reflectivity of the target. The tripod itself will be somewhat reflective, however the use of comparatively very bright targets reduces the effect of the tripod on the measurements. The measurements took place at the St Andrews Observatory, with targets placed in a large open area of grass well beyond the FFD of the antennas.

5.3.1.2 Predicted curves

The power measured by the ADC at the end of the IF chain, P_{IF}, is given by Eq. 2.17, where the gain of the receiver, G_{rec}, is given in Eq. 5.11 and is defined from the mixer RF port.

$$G_{\mathrm{rec}} = G_{\mathrm{IF}} L_{\mathrm{c}} \tag{5.11}$$

The IF gain curve G_{IF} is derived from the measured data in Fig. 5.15. The value of the receiver mixer conversion loss L_{c} was calculated from the band average receiver noise figure using the model in Fig. 5.22 and the noise factor cascade Eq. 2.26. The received power P_{r} in Eq. 2.17 is given by Eq. 2.16.

5.3.1.3 Results

Data of the atmospheric conditions during the measurements are shown in Table 5.6, as measured by a portable Vaisala Humidity & Temperature Indicator HMI31 sensor at the St Andrews Observatory and by noting the atmospheric pressure as reported by the Metoffice at the time. These values were used to calculate the atmospheric loss during the experiment using the 'gaspl' function in MATLAB®, based on the 2013 ITU model for atmospheric attenuation [42]. The relative humidity RH was converted to the water vapour density ρ_{w} using Eq. D.2 in Speirs [44, p. 279]. The atmospheric parameters measured on the 16.02.24 yielded a two-way path loss values of 0.73 dB and 0.66 dB for a target at range 100 m for a frequency of 201 GHz and 207 GHz respectively.

The radar calibration curves were then simulated using Equations 2.16, 2.17, and 5.11. These are plotted alongside the measured data in Fig. 5.32. The first three measured points up to ∼60 m were recorded as spot measurements. After this it was

Date	Time	p [Pa]	T [°C]	RH [%]	ρ_w [g m^{-3}]
16.02.24	13:00	101100	13.0	73.7	8.356

Table 5.6: Weather conditions during radar range calibration measurements. The humidity and temperature values were taken during the measurements at the St Andrews Observatory, and where the atmospheric pressure was noted from a standard Metoffice forecast for the location.

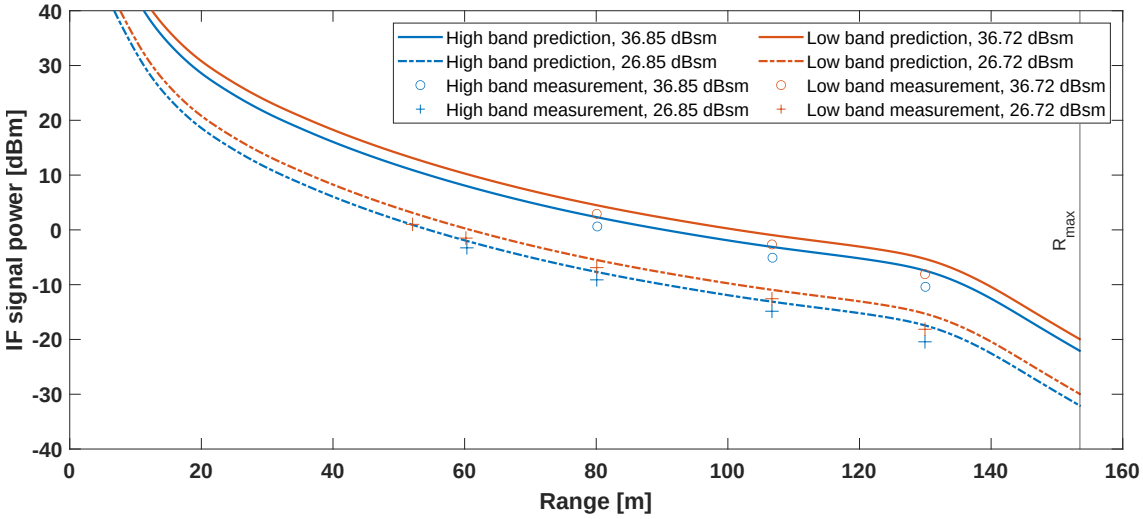

Figure 5.32: Radar range calibration results at low and high band. The data for the measured results was collected on 16.02.24 with the atmospheric conditions as shown in Table 5.6. These results were first published in Vattulainen et al. (2024) [29].

noticed that the peak value would occasionally fluctuate and spike by ∼1 dB (potentially due to a triggering issue), and so raw data was recorded for the later points to ensure that spurious readings were not taken at face value. The data was range processed as described in Section 5.2, using flattop windowing which is appropriate for RCS measurements, and then the maximum value (not including spiking) was taken and plotted.

The measured points all lie slightly lower than their corresponding curve, although the shape is a good match in all cases. This suggests there is some loss in the system which is not accounted for by the calibration curve. The discrepancy for each point is plotted in Fig. 5.33 as a function of range. From this it can be seen that the arithmetic mean of the discrepancy (i.e. the mean absolute error (MAE) calculated in linear units) is −2 dB, and is virtually the same at low and high band. This degree of error is satisfactory and represents only a minor deviation from the expected values. The same discrepancy for both low and high band suggests that the curves are a good match relative to each other, and that the difference in sensitivity is accurately represented by the modelling and is predicted to be 2.18 dB greater at low band. This primarily

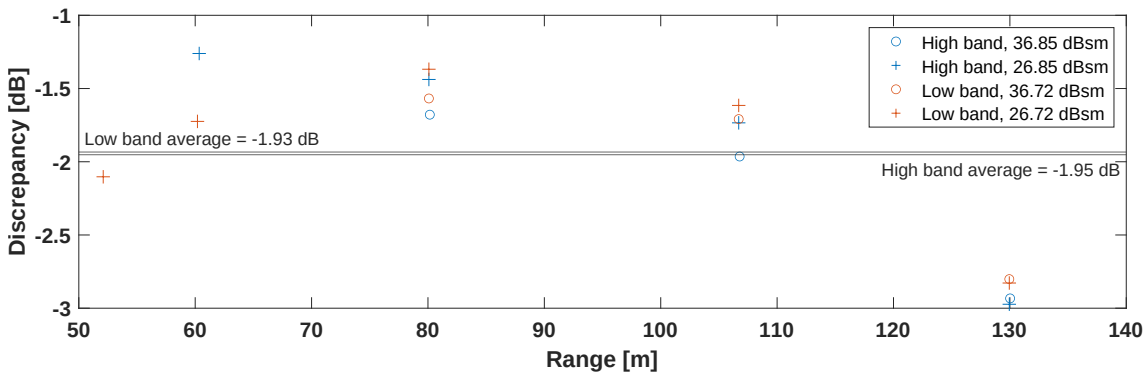

Figure 5.33: The discrepancy between the measured values for the radar calibration and each corresponding calibration curve, as a function of range.

accounts for the greater G_{rec} and lower G_{A} at low band versus high band.

The additional loss of the instrument is accounted for by taking the MAE values calculated from Fig. 5.33 and including this in the theoretical curves, which fits the level of the curve (without altering its shape) to the measured points by minimising the MAE calculated for both targets in each band. The measurements taken at ~130 m were omitted from this process as these values are in the region of the anti-aliasing filter roll-off and show some outlier behaviour in comparison to the whole. These values would compromise the fit to ranges <120 m where most measurements would be made, so it was decided to exclude these points to better optimise the fit in this region. The resulting MAE for low band was −1.66 dB and at high band −1.61 dB. Figure 5.34 shows the predicted curves for each target with the fitting adjustment and without the atmospheric loss to produce a calibration curve independent of the measurement weather conditions. To demonstrate the improved fit to the points, the atmospheric losses at each range have instead been applied to the target measurements. These final curves are used to apply the calibration to subsequent measurements of reflectivity when also accounting for the RCS of the targets used during calibration.

The possible causes for the discrepancy between the theoretical curves and measurements are effects due to ground bounce, pointing error, and antenna alignment. The ground bounce is expected to be fairly well mitigated by raising the target off the ground and conducting measurements in an open space, as the two-way spot radius does not exceed 2 m until ~150 m. The loss due to pointing error is likely to be small due to the broad response pattern of the trihedrals as discussed above. This hypothesis is reinforced by the observation that the measurements are fairly well clustered, suggesting that the loss due to pointing error is limited to ±0.3 dB.

The alignment of the twin antennas relative to each other will affect overlap of the beam footprint and thus the radar return. When the antenna optical axes are

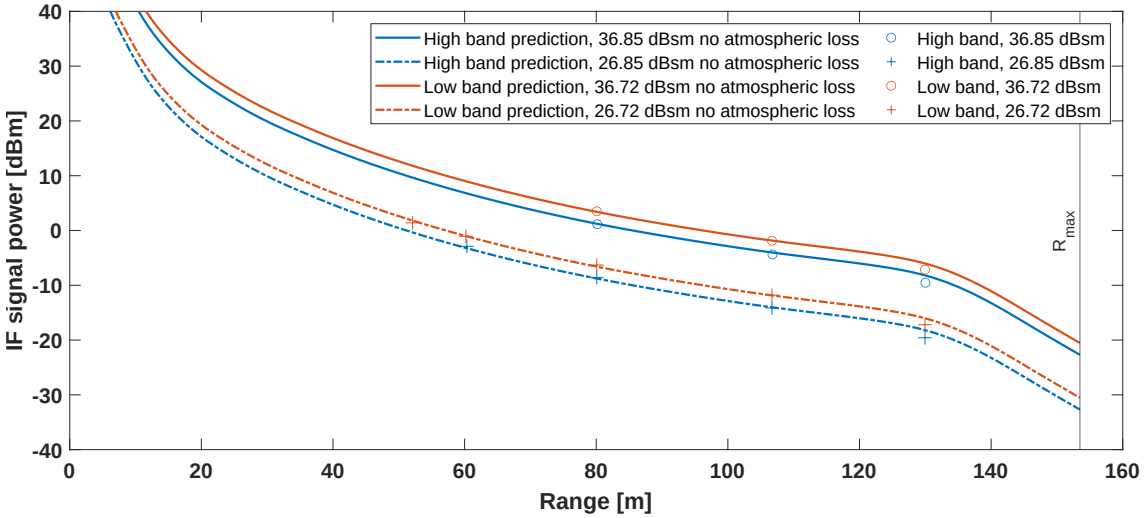

Figure 5.34: The radar range calibration curves at low and high band, where the levels of the theoretical curves have been fitted to the measured points by minimising the MAE of both targets for each band, omitting the measurements made at ~130 m. The theoretical curves shown also do not include atmospheric loss, and the atmospheric losses for the measured points have been subtracted from each value.

parallel, the overlap between footprints improves with range due to the divergence of the beams, and thus the discrepancy due to parallax decreases. For antennas which are pointing slightly outwards, the same is true. If however the antennas are pointing slightly inwards, then the overlap would be expected to decrease beyond a certain range and would then lead to a loss in received power. From Fig. 5.33, it can be seen that the magnitude of discrepancy does in fact increase with range. A brief test of antenna alignment was made by gently flexing one antenna horizontally back and forth by ~±0.5 mm within the aperture in the enclosure. Time series data of the range bin corresponding to the peak of the range profile is shown in Fig. 5.35, where it can be seen that the level varies by ~±0.4 dB. This variation corresponds to ~0.37° change in angle on the GOLA antenna patterns shown in Fig. 5.8, which is achieved for a ~0.52 mm deflection when assuming the antenna flexes at the midpoint of the waveguide at ~80 mm behind the wall of the enclosure, indicating this is plausible. The results in Fig. 5.33 and 5.35 then suggest there may indeed be an issue with the alignment of the antennas, which in future could be improved to reduce the additional loss.

5.3.2 Radar noise floor

As discussed in Chapter 4, the final sensitivity of the radar depends on the noise floor level. This was simulated using Eq. 2.23. The receiver gain was as shown above in Eq.

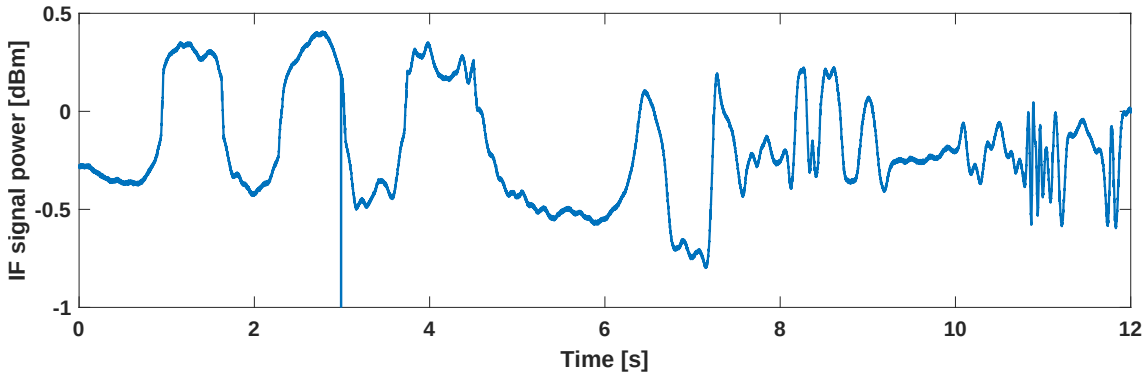

Figure 5.35: Time series data of the range bin containing the trihedral target which was recorded as one of the antennas was flexed horizontally by ∼1 mm. The alternate increase and decrease in signal level suggests that the flexing produces sequentially better or worse antenna alignment, implying that this could be optimised further.

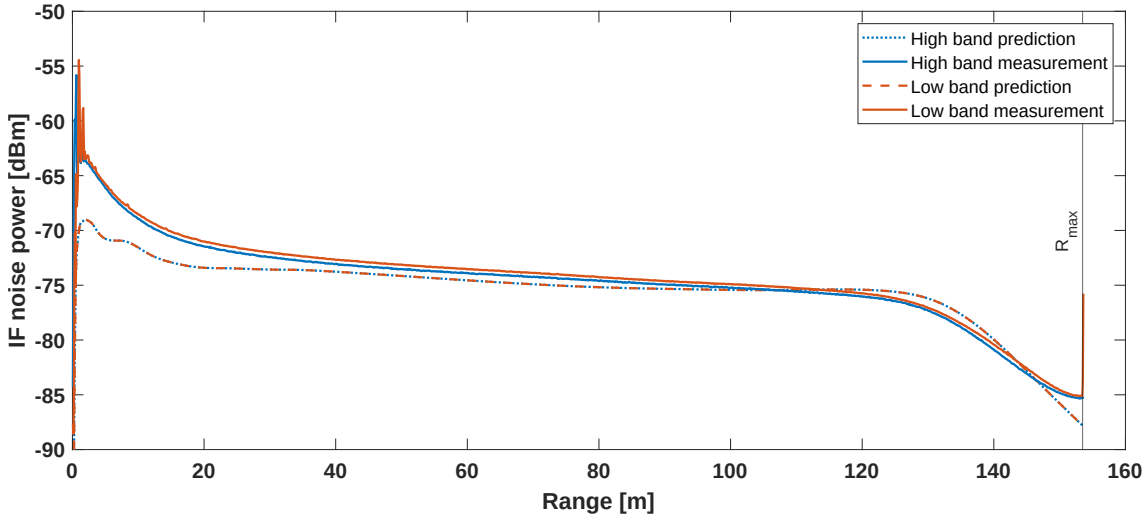

Figure 5.36: Simulated and measured radar noise floors at low and high band. The noise floor was measured by sky-pointing, where ∼5 to ∼10 s worth of data were averaged per range bin.

5.11, and the noise bandwidth was that of an IF FFT bin as shown in Eq. 2.25.

The noise floor was measured with sky-pointing measurements, where the radar is pointed upwards away from any scatterers and the sun, and data collected as normal for ∼5 to 10 s. This was then processed using a '−92 dB Four-Term Blackman-Harris' window [158, p. 105], and averaged for each range bin. The increased noise bandwidth due to the windowing function used in range processing is compensated for by Eq. 5.8. Both the simulated and measured curves at each frequency were then plotted together in Fig. 5.36.

The simulated curves for both low and high band are practically identical since they are uniquely defined by only the results of the receiver noise figure measurement shown in Fig. 5.21. In the model, the noise bandwidth is the same in both cases, and

only the receiver noise figure $\mathcal{N}_r$ and the receiver gain G_{rec} differ. The receiver gain is however defined from the receiver noise figure via the conversion loss, where the noise figure and conversion loss both change in magnitude by the same value but are defined with opposing polarity, and thus their difference remains constant.

The measured data in Fig. 5.36 is generally a good match to the simulated curves for both low band and high band. The deviation seen at close range (below ∼30 m), corresponding to f_{IF} values of $\leq$ 7.8 MHz, may be due to increasing $1/f$ noise from the SHM. The effect of this on the instrument sensitivity at these ranges will however be tempered by the much greater increase in signal power as seen in Fig. 5.32.

Beyond ∼30 m the noise floors at both low and high band gently slope downwards due to the response of the IF chain in Fig. 5.15. For high band, the decrease is 3.6 dB from −72.4 dBm at 30 m (7.8 MHz) to −76.0 dBm at 120 m (31.1 MHz). The low band noise floor tracks this almost exactly at a level 0.35 dB above, the difference between the two same ranges being 3.75 dB. The mean level of the region between 30 to 120 m is −74.01 dBm for low band and −74.37 dBm for high band, making the error between this and the simulation 0.79 dBm and 0.43 dBm respectively. This error is quite low, indicating that the value of the receiver noise figure is accurate to within what could be expected for measurement uncertainty. Given the average of the mostly flat region between 30 to 120 m of ∼−74 dBm and the maximum uncompressed ADC input level of 10 dBm, the dynamic range of the radar is determined to be ∼84 dB for both low and high band.

The very minor difference seen between low and high band measurements show that the assumption made in the noise figure cascade analysis summarised in Table 5.4, that mixer conversion loss can be uniquely defined from the receiver noise figure, is a good approximation. It does however introduce a small error, since if it were true, the conversion loss would exactly track with the receiver noise figure as a function of frequency as discussed above, and the measurements would produce the same noise floor.

Beyond ∼120 m, the noise floor begins to roll-off due to the SLP-30 anti-aliasing filter, with a nominal cut-off of 32 MHz (123.5 m). The mean level over the whole measured curve at high band is −74.67 dBm per FFT bin, and likewise for low band this value is −74.34 dBm per FFT bin. The average over the simulated curve is −75.44 dBm per FFT bin, meaning the deviation is 0.77 dB at high band and 1.10 dB at low band. This shows good overall agreement, however both measured values are slightly greater than the simulations. The difference is expected to be because of the additional $1/f$ noise which was not included in the Y-factor measurement as the power meter head had a lower limit of 10 MHz, leading to the simulated noise floor being slightly under-

estimated.

To determine the suitability of the level of receiver gain, the RF noise floor is compared with the ADC noise floor. The following calculation is explained in terms of dB units and is described in Kester [169]. The ADC noise floor is calculated from the estimated number of bits (ENOB), starting with Eq. 5.12 which gives the dynamic range of the ADC, DR_{ADC}.

$$DR_{ADC} = 6.02 \cdot ENOB + 1.76 \quad [dB] \tag{5.12}$$

For the Spectrum ADC model M2p.5940-x4, the ENOB = 12.0 and thus the ADC dynamic range is DR_{ADC} = 74 dB. The maximum signal level measurable by the ADC is +1 V and its input impedance is 50 Ω, thus the maximum power is +10 dBm. Subtracting the dynamic range from this value gives the ADC quantisation noise floor as −64 dBm. To give the ADC noise floor, the range processing FFT gain of $10\log_{10}(4096/2)$ = 33 dB is subtracted, and the noise bandwidth factor for the windowing is added, where this is 2.0045 ≈ 3 dB for a −92 dB Four-Term Blackman-Harris window [158, p. 105]. This gives the final ADC noise floor as −94 dBm. This is 18 dB below the RF receiver noise floor at 120 m. This suggests that the dynamic range of the radar could be safely increased by ∼12 dB by reducing the IF gain by adding an attenuator of the same value to the IF chain, ideally between the two amplifiers such that the harmonic performance of the second amplifier is maintained. The RF noise floor would then be at an acceptable margin of ∼6 dB above the ADC noise floor over the plateau region and the the dynamic range increased at the top end of the scale.

The noise figure of the receiver could be reduced by adding a suitable LNA to the front-end, immediately after the antenna and waveguide section, since as shown by Eq. 2.26 and discussed in Subsection 5.1.4.3, the influence of individual components on the total noise figure is much greater earlier in the chain. A suitable candidate would be an R&S G-LNA 140-220 20 6, with a gain of 30 dB and a noise figure of 5 dB [170]. Modelling the total receiver noise figure then yields a value of 6.5 dB, which would increase the 10 dB CNR distance to ∼118 m for high band and ∼124 m for low band, exceeding the desired performance values and giving additional sensitivity. This upgrade would be the most feasible improvement to increase sensitivity, where the alternative would be to increase the output power of the W-band PA on the transmit arm. This is likely to be more expensive and less convenient, as a replacement model would be a much larger component with more significant power and cooling requirements. PA technology is however constantly evolving, and so practical solutions at high W-band may become available in future as these could be driven by 6G and future communication hardware.

5.3.3 Noise floor degradation due to transmitter phase noise

As explained in Subsection 5.1.2.1, the reflected transmitter phase noise was found to be a problem with the initial radar design. Isolated targets produce a characteristic lobed pattern on a decibel amplitude scale due to the modulation shown in Eq. 2.60, where for a continuum of scatterers these patterns coherently sum to cause a general increase in the noise floor, without the modulation. Upgrades were then made to the chirp generator to reduce the phase noise as described in Subsection 4.3.3.1 and 5.1.2.1, and characterised in Subsection 5.1.2.1. The results presented in Fig. 5.37 were first published in Vattulainen et al. (2024) [29].

5.3.3.1 Method

Quantifying the impact of the transmitter phase noise involved measuring trihedral targets with the same procedure as for the calibration curve, except in this case the targets were placed deliberately close to the radar to produce a large return signal, but where necessary rotated significantly off boresight to reduce the signal level and prevent ADC clipping at 10 dBm. Targets were measured at a variety of ranges to observe different modulation patterns, which are a function of the round trip delay, in both the old and new chirp generator configurations. These measurements were made at high band only.

5.3.3.2 Results

To aid comparison, two range profiles were selected where the target was placed at approximately the same range for measurements in both configurations, where these results are shown in Fig. 5.37. The phase noise model shown in Eq. 2.64 as published by Cooper [54] was then fitted to both range profiles, and an averaged noise floor also plotted for comparison. The parameters used in the model for the two fits are shown in Table 5.7, and where the phase noise spectrum for each configuration is shown in Fig. 5.13.

Version	B_N [dB]	h_{PN} [dB]	K [dB]	$C1$ [dB]	$C2$ [dB]	$C3$ [dB]	$C4$ [dB]
Old	42.8828	33.6248	7.13	−44.0	0	−1.5	31.0
New	42.8828	27.6042	4.77	−66.2	0	−1.5	31.0

Table 5.7: Phase noise model parameters for both chirp generator versions.

The measured data in both configurations shows the characteristic lobed pattern caused by the reflected phase noise when represented on a decibel amplitude scale.

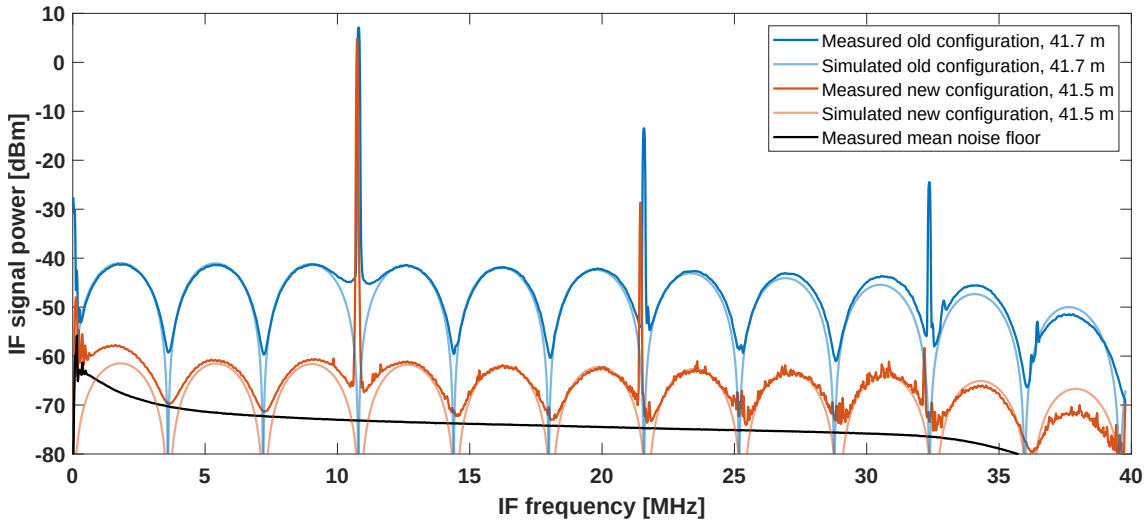

Figure 5.37: Measured and simulated range profiles for data taken of trihedrals in both old and new chirp generator configurations. The old configuration had a phase noise level which was 21.5 dB greater as shown in plot Fig. 5.13. The degree of the lobed effect shown is dependent on the phase noise level in the transmitter. A significant reduction of ~20 dB has been achieved with the new chirp generator configuration.

The signal peaks at ~11 MHz are from the target, where subsequent peaks are due to IF chain harmonics. The level of the harmonics seen in the new configuration was greatly reduced compared to the original, where this improvement is due to changing the second IF amplifier as detailed in Subsection 5.1.3.

The lobed pattern seen in the data for the old chirp generator is ~32 dB higher than the true (thermal) noise floor. This will effectively decrease the receiver sensitivity by the same amount, masking weak scattering along the same line of sight. The overall decrease in phase noise measured in Fig. 5.13 is 21.5 dB, which corroborates well with the measured trace for the new configuration shown in Fig. 5.37, which is ~20 dB lower than previously. This reduces the noise floor due to phase noise cancellation to a level which is only ~12 dB above the thermal noise floor.

In the model, the factors $C3$ and $C4$ remain the same since both of the target measurements were at approximately the same range, whilst $C2$ is unused here. This is because the original formula in [54] was developed to model a radar using a phase-locked loop (PLL) oscillator, whereas in this design both the DROs used are free-running. PLL oscillators show a characteristic suppression of phase noise near to the carrier frequency, followed by a bump before returning to a linearly decaying spectrum (on a logarithmic frequency scale) at higher offset frequencies [171]. This final section is similar to a free-running oscillator, like that of the traces shown in Fig. 5.13. The PLL oscillator behaviour described above was modelled by $C2$, but was unnecessary for this data.

By using Eq. 2.65, the difference in chirp generator phase noise at the IF frequency corresponding to the target peak in the spectrum can be calculated from the parameter for the mean level in the models, $C1$, and the signal peak level, K. The factors for IF noise bandwidth in Eq. 2.61 remain constant, and the factor for phase noise multiplication gain, h_{PN}, is included as being part of the difference between chirp generators. The models thus suggest an improvement of 19.8 dB, which agrees well with the measurements made in Fig. 5.13.

Improvements could be made to the instrument which reduce the phase noise further. Figure 5.37 suggests that the phase noise is ∼30 dB above the thermal noise floor, and with a potential LNA improvement (as described above in Subsection 5.3.2) this could then be >20 dB above the RF thermal noise. Reducing this entirely is likely not practical, but a partial improvement would be possible by selecting an oscillator with a lower intrinsic phase noise, and one which has a higher output frequency to remove another frequency doubling stage. This would then however require a greater DDS bandwidth, which may become problematic depending on the frequency spurs of the spectrum. Phase noise is a key challenge in sub-THz radars with high values of frequency multiplication, as demonstrated previously by Cooper [54].

This concludes the final radar characterisation results presented in this thesis. These began with the results for each subsystem, followed by a section describing the radar range processing used on the raw data. The final section showed the results for the radar as a whole, including the radar range calibration, noise floor measurements, and measurements and modelling of the impact of transmitter phase noise on the receiver noise floor. The following chapter begins the reporting of sea clutter measurements made at 207 GHz with a qualitative analysis of the data gathered. This is then followed by the final chapter of results, which present the quantitative analysis of the same data.

6

207 GHz Sea Clutter Data Collection and Qualitative Analysis

THIS chapter and Chapter 7 describe the field trial undertaken on the 21st of July 2023 at the FloWave wave tank facility at the University of Edinburgh and its results. The motivation for the collection of this data was to measure the amplitude statistics of sea clutter at sub-THz frequencies under controlled conditions, varying wave height, wave direction, grazing angle, and polarisation. A small number of other field trials were also conducted with this aim during the STREAM project, however this analysis focuses only on the data and results from the FloWave trial, since the high degree of control of the environment allowed for the most complete exploration of the parameter space. Measurements during the trial were conducted with radars operating at 77, 150, and 207 GHz, however only the data and results from the measurements made at 207 GHz are presented here as there was limited time to conduct the analysis and the higher carrier frequency data was of the most interest to the STREAM project goals. This chapter presents a qualitative assessment of trends seen in the data, where Chapter 7 carries out a further quantitative analysis on the same data.

6.1 Trial description

6.1.1 Motivation

Given the general reasons for the measurement of sea clutter as already defined previously in Subsection 2.3.1, the specific motivation for conducting a trial at the FloWave facility was the use of the wave tank for improved sampling of the environmental parameters of wave height and wave direction. The indoor wave tank allowed different wave heights and directions to be produced quickly and consistently, where

a key advantage of a circular wave tank over a more conventional rectangular tank is the ability to set waves to travel in any direction. This facilitated a more thorough exploration of these parameters than would otherwise have been possible without many individual field trials and a reliance on the weather to produce a diversity of sea states and wave directions. The consistency of the wave surfaces also meant that measurement parameters such as polarisation and radar depression angle could be varied with some assurance that the conditions had not changed significantly between measurements, whereas in nature the local sea can change fairly quickly and thus can make experiments more difficult to control.

6.1.2 Location

The FloWave facility [172] is a indoor circular wave tank with a diameter of 25 m, depth of 2 m and surrounded by 168 actuator paddles which control the surface of the water, and are programmed to produce different surface conditions. As well as being able to force the water to move and create a wave, they are used to absorb an incoming wave and prevent standing waves and reflections from the edge of the pool. A plan view diagram of the tank is shown in Fig. 6.1, which also shows the gantry which can be positioned over the pool. The water level itself was approximately 0.6 m below floor level, and the nominal edge of the tank was marked with a yellow safety rail, also seen in the photographs of the tank in Fig. 6.2. In addition to the safety railing, wire mesh panels extended over the edge of the pool by ~1 m at floor level, as shown in Fig. 6.1.

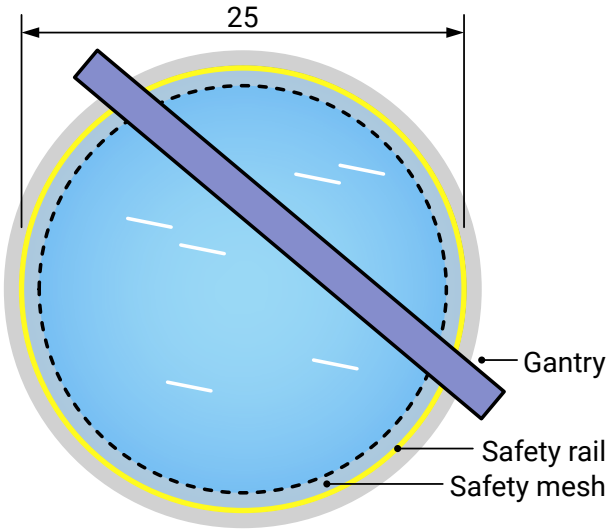

Figure 6.1: A plan view diagram of the FloWave tank, showing the 25 m diameter pool, movable gantry, yellow safety rail fixed at the pool outer diameter, and the safety mesh suspended over the edge of the pool and extending towards its centre by ~1 m.

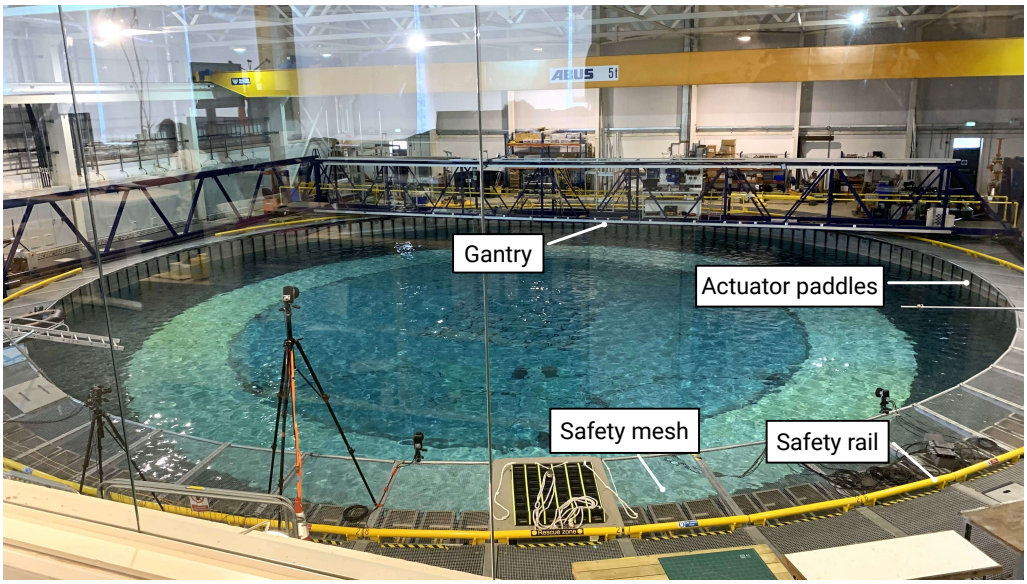

(a)

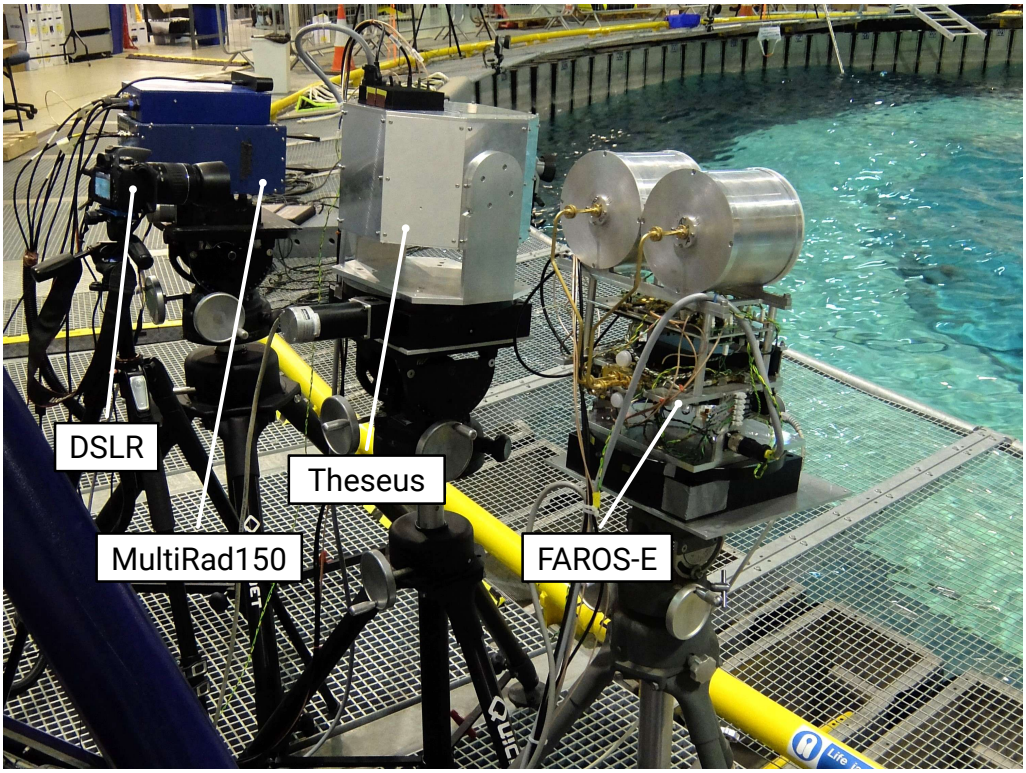

(b)

Figure 6.2: (a) A photograph of the FloWave wave tank. (b) A photograph showing the positioning of the three radars and the DSLR camera used during the trial, with the Theseus radar in the centre. As only the 207 GHz data are presented, only cursory details of the other two radars are provided: FAROS-E, $f_0 = 77$ GHz, $\phi_1 = \theta_1 = 2.0°$ (symmetric); MultiRad150, $f_0 = 150$ GHz, $\phi_1 = 1.7°$, $\theta_1 = 11.3°$ (vertical fan beam), owned by the University of Birmingham.

6.1.3 Apparatus

As explained in Chapter 1, sea clutter data at low grazing angles were of the most interest to the project. During the trial, the lowest achievable grazing angle, as given by Eq. 2.15, was limited by the maximum range at which the radars could be placed from the pool, and the lowest height at which the tripods could be set. These constraints were optimised according to the following practicalities:

- **Range:** the edge of the pool was surrounded by a wire safety mesh, as shown in Figures 6.1 and 6.2, which could not be removed and could not support the weight of the radars. Strong reflections from the mesh would reduce instrument sensitivity due to the reflected transmitter phase noise as explained in Subsection 2.1.12. For this reason, the radars were placed as close as possible to the yellow safety rail at the edge of the pool so as to minimise the obstacle presented by the mesh. This however limited the maximum practical range to approximately that of the pool diameter.
- **Height:** the gantry on which the radars were placed was 0.6 m above the water's surface. The lowest height which could be set on the tripods was 1.6 m, meaning that the total height from the instrument axis to the water's surface was 1.9 m.

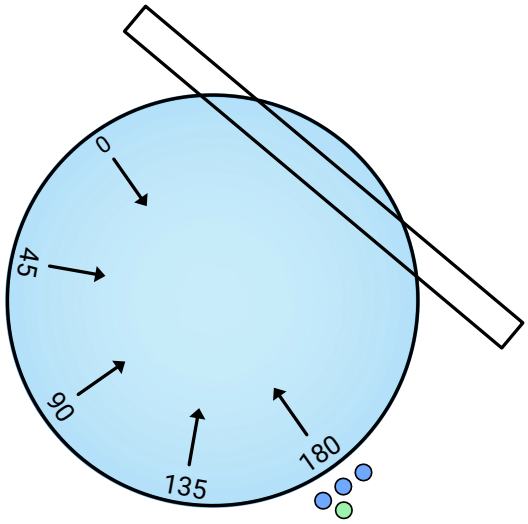

Figure 6.3: Approximate positions of radars (blue dots) and DSLR camera (green dot) during measurements, with the gantry moved to the far edge and wave directions indicated by arrows with an angle defined with 0° as the direction from which waves directly approach the radar.

A diagram of the measurement set up at the tank is shown in Fig. 6.3 indicating the position of the radars and digital single lens reflex (DSLR) camera. In addition

to the concern about reflections from the wire mesh, positioning the radars at the edge of the pool provided sufficient space behind them to set up the control PCs and to work around and position the instruments. The movable gantry which spans the pool was positioned as near to the edge as possible to provide the maximum possible unobstructed view across the water's surface. Given the maximum range of 25 m and the radar axis height of 1.9 m, the minimum grazing angle observable was ∼4.4°.

To prevent the possibility of ADC saturation occurring from static clutter in the indoor environment, the anti-aliasing filter of the Theseus radar was changed to a MC SLP-5 which limited the range to ∼25 m. In all other respects the performance of the radar was unchanged from the results presented in Chapter 5. Additional key instrumentation used during the trial included:

- A digital inclinometer[1] to accurately set the depression angle of each radar.
- A wide field of view webcam which was used to constantly record an overview of the trial, including audio recordings of comments and instructions between staff. This footage was timestamped during recording, and used as additional context to help corroborate events during the trial.
- A Canon EOS 700D DSLR video camera with 200 mm focal length lens, set up with the same line of sight as the radars to record coincident video of the pool. To help synchronise the video and radar data after the trial, the trigger switch used to initiate data collection was wired up with an indicator light which was then placed at the edge of the camera field of view. This would turn off when data collection began, allowing time synchronisation to the nearest video frame.

6.1.4 Conditions

The simulated sea surface during the trial was produced using the Pierson-Moskowitz spectrum and a cosine-squared spreading function. Measurements of the resulting surfaces were made using four wave gauges positioned across the pool as shown in Fig. 6.4, suspended from the gantry which had been moved to the middle of the pool. The spacing between gauges was 3 m, and their positioning was centred with respect to the centre of the pool such that they covered a 9 m transect as indicated in Fig. 6.4. The gauges were numbered 1 to 4, in ascending order according to the direction of the waves.

The maximum SWH that the tank can produce for realistic sea states (as opposed to simple sinusoidal waves) is approximately 0.3 m. To strike a balance between the sampling of this parameter and the total number of measurements to be made,

[1] Level Developments Pro 3600 Digital Protractor.

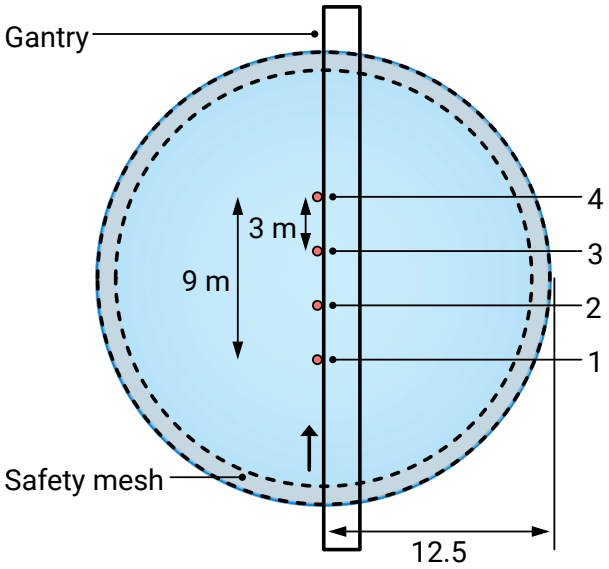

Figure 6.4: A view of the pool during the measurement of SWH with wave gauges, where the gantry edge has been moved to the centre of the tank and the gauges (red dots) suspended along its length with the indicated spacing. The gauges are numbered 1 to 4 according to the wave direction indicated, with waves travelling parallel to the line of gauges.

three SWH levels were selected of 0.1, 0.2, and 0.3 m. The choice of 0.1 m as the minimum was made by considering the likely minimum wave height which would produce detectable clutter, from experience of previous measurements. All three of these surfaces were sampled with wave gauge measurements to verify the SWH. The surfaces were set to repeat over an interval of 90 s, so measurements were conducted for a duration of 95 s.

Since the water surfaces generated by the tank could be reliably expected to be very similar, it was decided that simultaneous wave gauge and radar measurements would not provide significant further information. The measurements of the SWH were thus made during the day prior to the radar observations, where FloWave staff emphasised that the wave tank behaviour was very repeatable and thus asynchronous measurements would still be representative. Co-located *and* simultaneous measurements would have provided the ability to make a more direct comparison between instantaneous surface displacement and radar backscatter, however this would have been impractical since the wave gauges would themselves have contributed some non-negligible amount of backscatter, especially when considering the additional clutter of either the gantry or some other rig to suspend them at the right height above the water.

The results of the measurements are shown in Fig. 6.5, where a 40 s interval of the total 95 s data is shown. Each run had some degree of ramp-up and ramp-down time which was excluded, as the eventual radar measurements would only be made

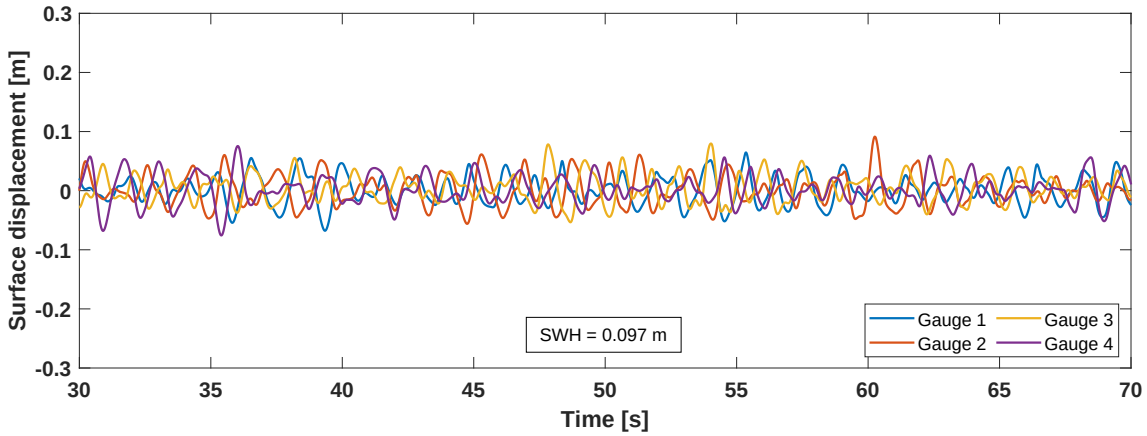

(a)

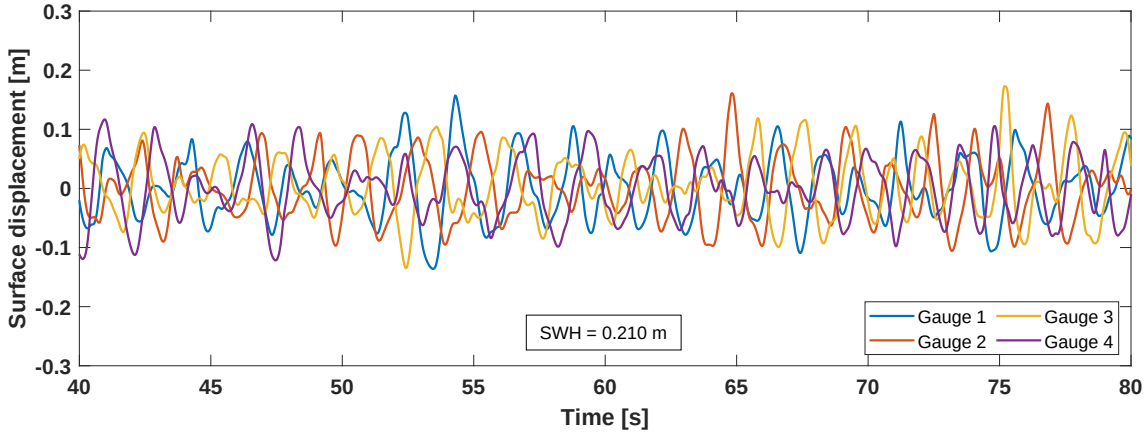

(b)

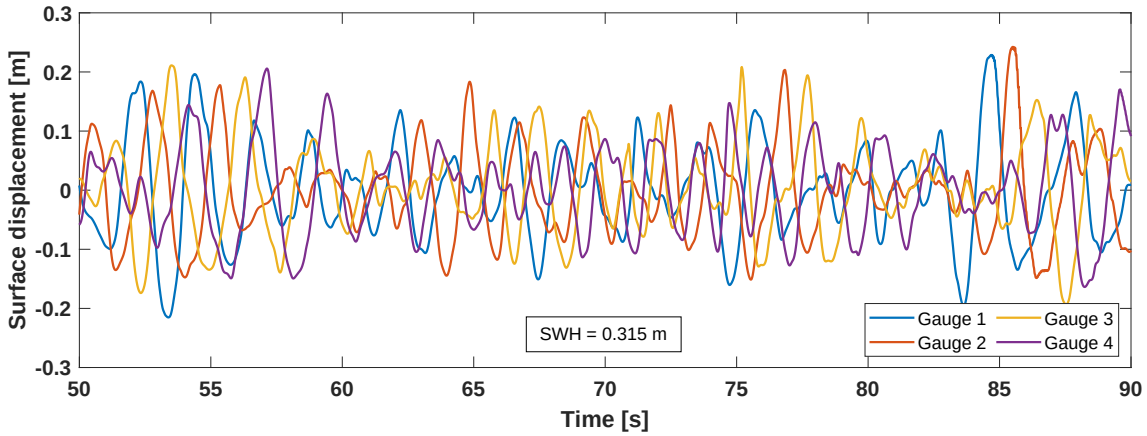

(c)

Figure 6.5: Results of wave gauge measurements made of three sea surfaces generated in the FloWave tank, with nominal SWH of (a) 0.1 m, (b) 0.2 m, and (c) 0.3 m. The four wave gauges were set up in the tank as shown in Fig. 6.4.

once the surface had settled to the programmed sea state after which the tank would be continuously running. The SWH was then calculated for each wave gauge from the 40 s intervals of the data as shown in the Figures using Eq. 2.66, reproduced here for

convenience:

$$H_{1/3} = 4\langle\zeta^2\rangle^{1/2}$$

and the mean of these four values taken to produce the final values on the plots: 0.097 m, 0.210 m, and 0.315 m each for the nominal wave heights of 0.1, 0.2, and 0.3 m, indicating a good agreement between the measurements and the expected SWH. Given the very near match between the measured SWH and the nominal values, it is hereafter assumed that the nominal values are correct.

6.1.5 Data collection methods

The data presented in this thesis were collected of water surfaces in staring mode, and recorded as a function of the four measurement parameters: wave height, wave direction, grazing angle, and polarisation. Directly oncoming waves were defined to be at 0° in keeping with the definitions in Subsection 2.3.4.4 and as shown in Fig. 6.3. The trial covered four (overlapping) experiments to explore each of the measurement parameters:

1. **Grazing angle:** the grazing angle of the observations was varied by changing the radar depression angle, where at the short ranges involved, the grazing angle on boresight is equal to the radar depression angle. Measurements were taken at depression angle values of 3°, 5°, 7°, and 10°, where the angle was set using the digital inclinometer. The wave direction was kept fixed at 0° and the measurements repeated for all wave heights. For the avoidance of doubt, the depression angle δ is the pointing angle of the radar boresight, whereas the grazing angle γ is the local angle to the water within the beam footprint. These quantities are treated separately as the beam has a finite footprint and these measurements were conducted at close range.
2. **Wave height:** measurements were taken at all three SWH values of 0.1 m, 0.2 m, and 0.3 m as defined in Subsection 6.1.4. Specifically for this objective the lowest possible γ of ~5° was of most interest[2], however the full range of grazing angles was also covered for each wave height during the first experiment. Additionally, the wave direction was set to 0°.
3. **Wave direction:** measurements taken at 0°, 45°, 90°, 135°, and 180° as indicated in Fig. 6.3. The SWH was set to 0.3 m to maximise the returns as these were

[2]The lowest possible grazing angle being limited by the range to the edge of the pool, and being greater than the lowest depression angle setting.

expected to be significantly reduced at wave directions other than 0° and possibly 180°. These measurements were conducted at depression angles of 5° and 10°, where the lower angle was of greater interest to the project goals. The higher angle was chosen as part of contingency planning as returns at steeper angles were expected to be greater in amplitude and would thus act to mitigate the reduction in backscatter, and thus increase the probability that the variation with wave direction could be recorded given the radar sensitivity.

4. **Polarisation:** all the measurements mentioned above were repeated for both VV and HH polarisations.

In general, the total number of increments taken for a given parameter was limited by the time available during the trial day. Since different combinations of these parameters (such as the sweep through different depression angle values for each SWH setting) were also of interest the number of measurements could increase rapidly for only a small change in the number of increments. The time taken for each measurement additionally needed to include the settlement time for the tank (2.5 minutes), and the time taken to change the radar set up (1.5 minutes). The number of different wave directions and depression angles were thus limited to the values above as this was expected to sample the parameter space with the optimum range and density, with similar consideration taken for the wave height values as explained in Subsection 6.1.4.

The final measurement schedule was developed by considering the order in which the set up time could be minimised, e.g. the switch over of polarisation from HH to VV was conducted only once since this was a time consuming process to perform for all the radars. Each measurement was also to be repeated twice to produce a back up for that combination of parameters in case an individual file was corrupted or lost, and also to increase the quantity of data as it was anticipated that the backscatter events may only occur sparsely in time.

To summarise the measurement procedure:

- The individual parameters for a given measurement (depression angle, wave height, wave direction, polarisation) are set and the wave tank started.
- The wave tank is allowed to settle to the programmed state, after which the programme runs continuously and data collection can begin.
- When collecting data, recording is started simultaneously with all three radars. Most observations individually last ~10 to 20 s.
- Data collection is repeated for the same set of measurement parameters.
- The measurement parameters are changed, where these were cycled through in order of most often changed to least: depression angle, wave height, wave

direction, polarisation. This order was chosen to minimise the total time spent on altering the measurement settings.

During the trial, some adaptations were made to the procedure to optimise data collection. It became apparent that in many instances that no significant backscatter was being observed at e.g. low wave height and low depression angle settings, and so either shorter data files were recorded or some repeat measurements were skipped given the time pressures on the trial day. In total, the three radars produced 258 data files during the trial. The dataset has the following breakdown: 77 and 207 GHz 70 staring mode files (each) and 26 scanning mode files (each); 150 GHz 41 staring mode files and 25 scanning mode files. The analysis of this thesis is based on the 207 GHz staring mode subset of the data.

6.2 Range-time-intensity plots of sea clutter

The following section presents an overview of the typical data collected by the Theseus radar of 207 GHz sea clutter during the FloWave trial. This is carried out by reference to RTI plots of data and their matching, time synchronised coincident video. An analysis of the commonly observed sea clutter features is shown first, followed by discussions on the potential mechanisms for the scattering as inferred from the RTI data and video. A brief summary of the signals seen in the data which are unrelated to sea clutter is made, and is followed by a detailed qualitative examination of the changes observed in the backscatter signals as a function of the measurement parameters of grazing angle, wave height, wave direction, and polarisation.

The RTI plots in this chapter are presented in terms of IF power, where a later numerical analysis in terms of NRCS is presented in the following chapter (Chapter 7) based on the same data. Using IF power is not suitable for quantitative analysis which compares signal levels as a function of grazing angle, so in general direct comparison of power values in this chapter is limited to some spot measurements, where these were taken on or near to boresight such that the beam pattern gain was controlled. The boresight position is marked on all the RTI plots by a horizontal dashed line. The effects of the calibration curve are however not controlled for in these plots, and the reader should be aware of this.

The decision to show the RTIs as IF power was made as this preserves the shape of the noise floor, and was thought to more clearly show the features of the data for qualitative analysis. Part of the quantitative analysis, the CCDF plots in Section 7.2, are also based on processing the IF power data (as explained in Subsection 7.1.6, where in

essence this is to prevent contamination of the signal distribution with noise samples), so it was thought important that the RTIs be shown in this form.

6.2.1 Processing

The data produced by the Theseus radar was catalogued and then range processed according to the steps shown in Section 5.2. A flat-top window [158, p. 193] was used to process the data as is standard practice for calibrated measurements of target and clutter backscatter, since this best preserves the amplitude information. To generate RTI plots, the range axis was formed from the frequency information using the range-frequency relationship in Eq. 5.10. The time axis is formed using Eq. 6.1:

$$t = N_{\mathrm{c}}\mathrm{CRI} \tag{6.1}$$

where t is the time value for each chirp, N_{c} is the chirp number, and CRI is the chirp repetition interval.

The method described here is of course general to the radars operating at other frequencies, however this discussion from this point forward is limited only to the 207 GHz data and results.

6.2.2 Common features of the data

Two RTI plots with features often seen in the data are shown in Fig. 6.6. This presentation was also typical of the two other lower frequency radars used during the trial, albeit with differences due to differing sensitivities (with the 77 GHz radar being the most sensitive, followed relatively closely by the 207 GHz, and the 150 GHz being the least sensitive). These data were collected in either HH or VV polarisation, at a SWH of 0.3 m, a wave direction of 0° and at a depression angle of 7°. These plots, and indeed the other RTI plots presented, are not time synchronised as indicated by the collection time-stamps shown in the figure captions, and so the reader should not attempt to directly compare them as such. The commonly observed features, labelled on the plots, include:

- **Sea spikes** which can appear as sparse, small patches of high amplitude signal or long, thin, diagonal features approaching the radar with increasing time for a wave direction of 0°. The number of spikes observed in a single run was highly variable, where out of two runs separated by around 60 s, often only one would contain spikes as shown later in Subsection 6.2.6.2.

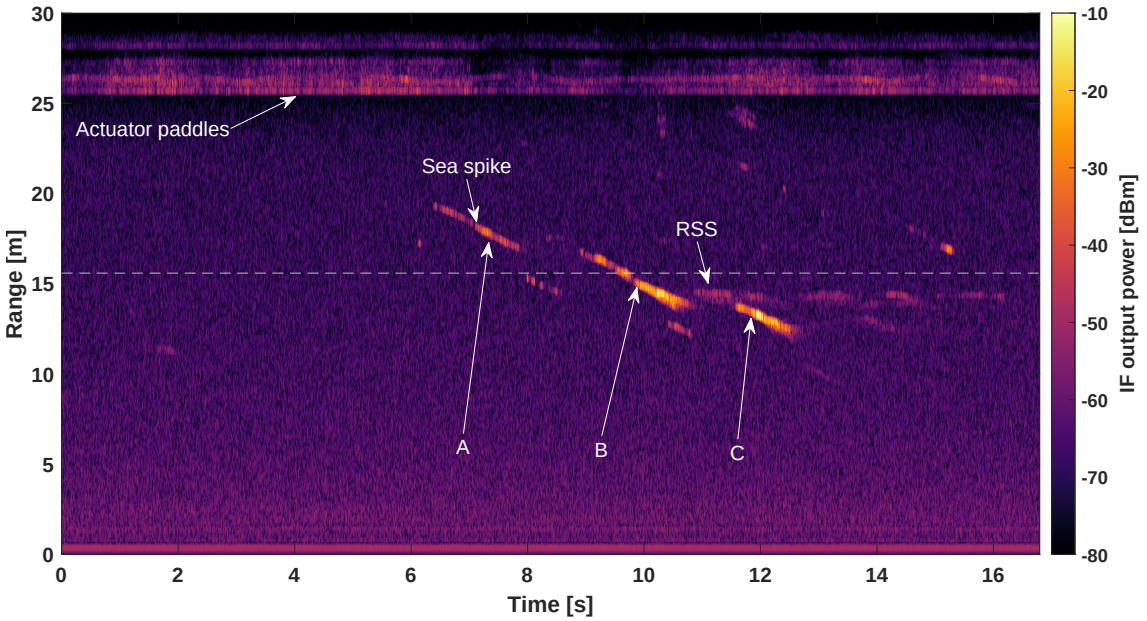

(a) HH polarisation, time-stamp 10 – 08 – 22.

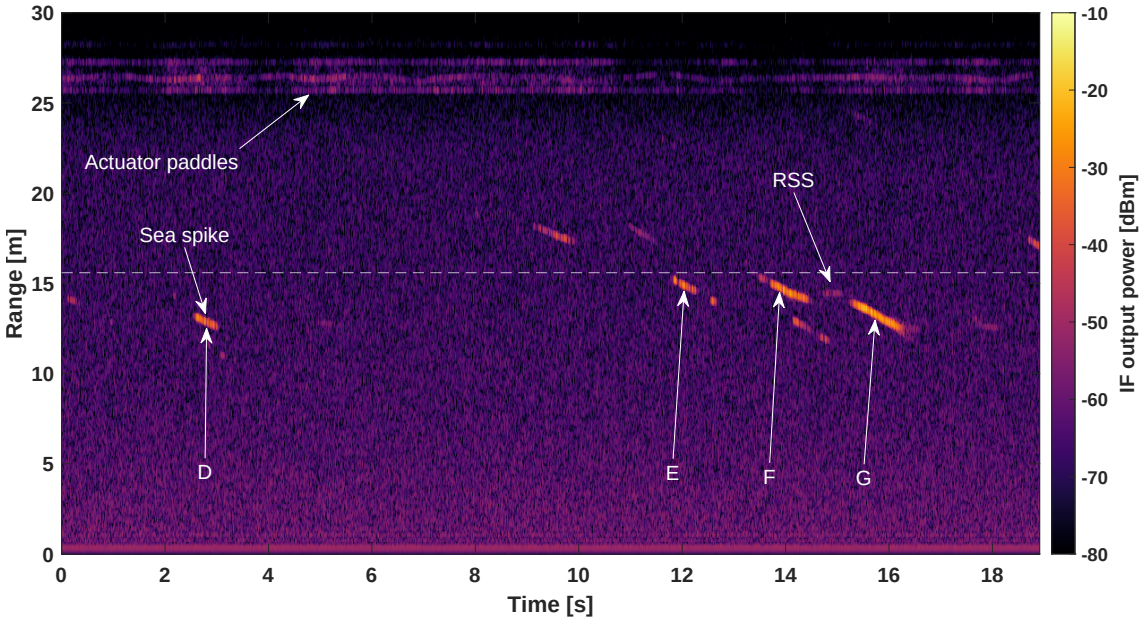

(b) VV polarisation, time-stamp 11 – 50 – 33.

Figure 6.6: RTI plots exhibiting common features of the 207 GHz FloWave dataset. These data were gathered at a SWH of 0.3 m, a wave direction of 0° and at a depression angle of 7°, with either HH or VV polarisation as indicated.

- **RSS** where these events are seen as faint patches of signal which are constant in range, sometimes fluctuating as a function of time.
- **Signals unrelated to sea clutter** such as reflections from the actuator paddles, seen as bands of signal beyond a range of 25 m. Additionally, some isolated chirps are corrupted and can manifest as spurious signals extending across range

but which cannot easily be seen at this image resolution. These are discussed later in Subsection 6.2.5.

- **The radar noise floor** which in the region of interest between 9.5 to 24.5 m, is on average −70.7 dBm at 207 GHz.

6.2.3 Burst and whitecap spikes

The spikes seen in the data are almost exclusively due to burst scattering. The relatively low SWH generated by the FloWave tank and the absence of wind meant that whitecap events were scarce and possibly of a less substantial size compared to what might be seen in nature at a given SWH. Accordingly there was little foam formation due to the very limited mixing of air and water. Additionally, whilst the water's surface was clearly a realistic imitation of a wave field, on a very fine scale it was exceptionally smooth and glassy as can be seen in Fig. 6.7. In general, the diffuse scattering of visible light from the surface was mostly absent, where in nature this could be expected to be seen at any sea state due to the effects of wind causing small surface disturbances, as can be seen in Fig. 2.11a and Fig. 2.11d, for example.

Given the nature of the water's surface, the main analysis of this thesis is restricted to that of burst scattering events. Nonetheless, the contribution of this scattering type to the spikiness of the amplitude statistics is likely to be very significant (see Subsection 2.3.5), and will be a key contributor to overall NRCS (see Subsection 2.3.4.3). A brief examination of the other scattering types observed is shown here, but is not pursued further in the quantitative analysis of Chapter 7. This is in part because these phenomena can be difficult to isolate from one another, but also because the other scattering types occurred relatively infrequently in the dataset.

To illustrate the following discussion, two sequences of synchronised coincident

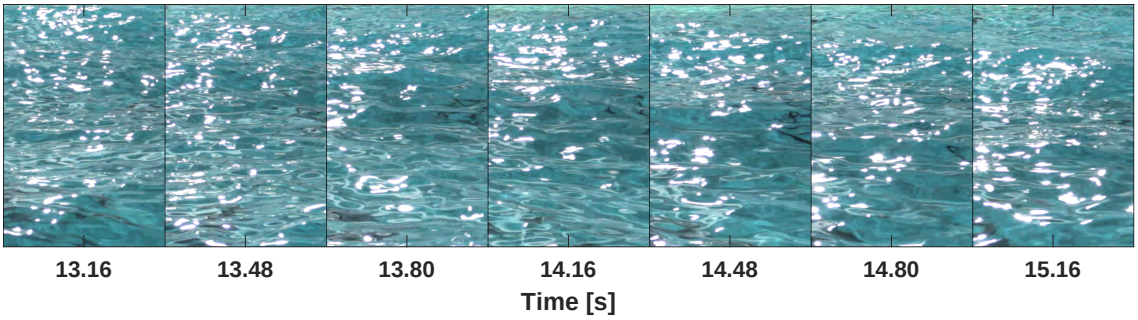

Figure 6.7: A sequence of cropped video frames showing the water's surface which was generated at FloWave for SWH 0.3 m and wave direction 0°. The surface shows a typical wave passing through the field of view, where attention is drawn to the lack of very fine scale ripples or roughening as would be caused by wind over the surface.

video frames and RTI plots with corresponding time axes are shown. These RTI plots are from the same data as presented in Fig. 6.6. The sequences of video frames and sections of RTI were chosen to show the occurrence of several scattering events, where the video files are also provided as supplementary material to this thesis. Specifically, the figures show data in:

- **HH polarisation:** Fig. 6.8, with RTI in Fig. 6.10a, starting from 9.60 s in Fig. 6.6a lasting 3.76 s. The video file matching this sequence of frames is named 'video_10-08-22.avi'.
- **VV polarisation:** Fig. 6.9, with RTI in Fig. 6.10b, starting from 11.56 s in Fig. 6.6b lasting 5 s. The video file matching this sequence of frames is named 'video_11-50-33.avi'.

From observations made during the trial and from inspecting the data and video footage (which is easier to interpret than the static frames presented in the figures, and is provided as supplementary material to this thesis), it can be seen that burst scattering events are due to steepening or cresting waves in keeping with observations at lower frequencies as discussed in Subsection 2.3.3.2. The resulting diagonal features are generally ∼8 range bins wide, and so are localised to a range swath of ∼0.6 m for both polarisations. The group velocity of the waves was approximately the same for a given SWH, thus the diagonals in a single RTI plot are all at the same angle.

6.2.3.1 Backscatter intensity

From Fig. 6.6a, spike A beginning at ∼6.4 s has signal levels varying between approximately −45 to −30 dBm, and the latter, brighter spikes (B and C) beginning at ∼9 s and ∼11.5 s being between approximately −35 to −10 dBm. In Fig. 6.6b, spike D beginning at 2.5 s, spike E beginning at 11.8 s, and spike F beginning at 13.5 s have intensities between −45 to −25 dBm, and spike G beginning at 15.2 s has intensities ranging between −40 to −20 dBm. In general, the clutter features are very similar in presentation although VV backscatter is suppressed compared to HH.

6.2.3.2 Maximum backscatter

The brightest returns in the HH data shown in Fig. 6.10a are observed as very short duration (on the order of hundredths of a second) events at 10.1, 10.2, and 10.3 s during spike B, and for an extended period of ∼0.1 s beginning at 11.9 s in spike C. The maximum signal level during clutter spike B is ∼−7 dBm, and during spike C it is ∼−3 dBm. These are clearly very high peaks in comparison with the general level, and will have significant implications for the detection of targets amongst such clutter.

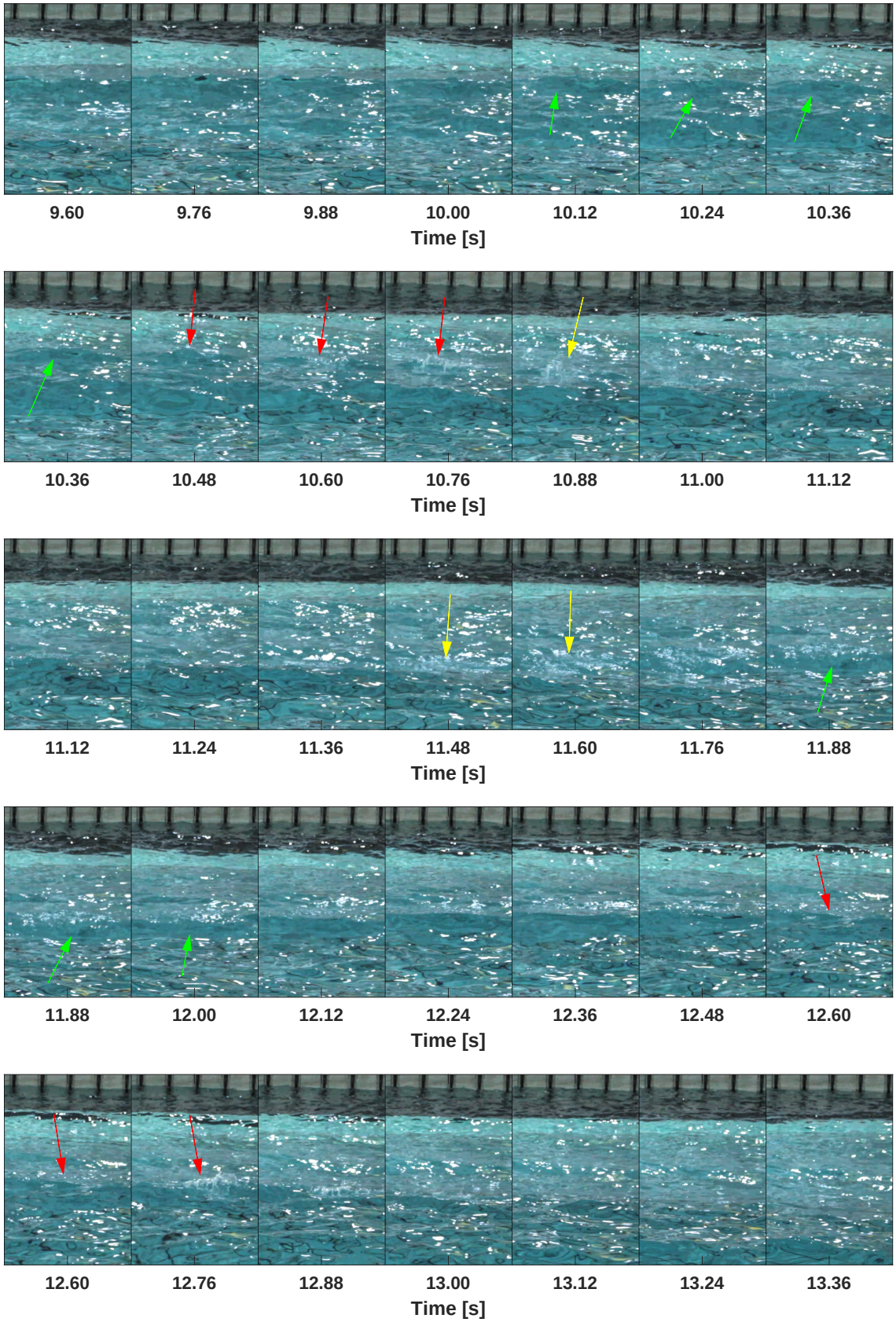

Figure 6.8: A sequence of video frames matching the HH radar data RTI plots shown in Fig. 6.6a and Fig. 6.10a. Green arrows indicate burst scattering, red for whitecap, and yellow for RSS. The file for this sequence is 'video_10-08-22.avi'.

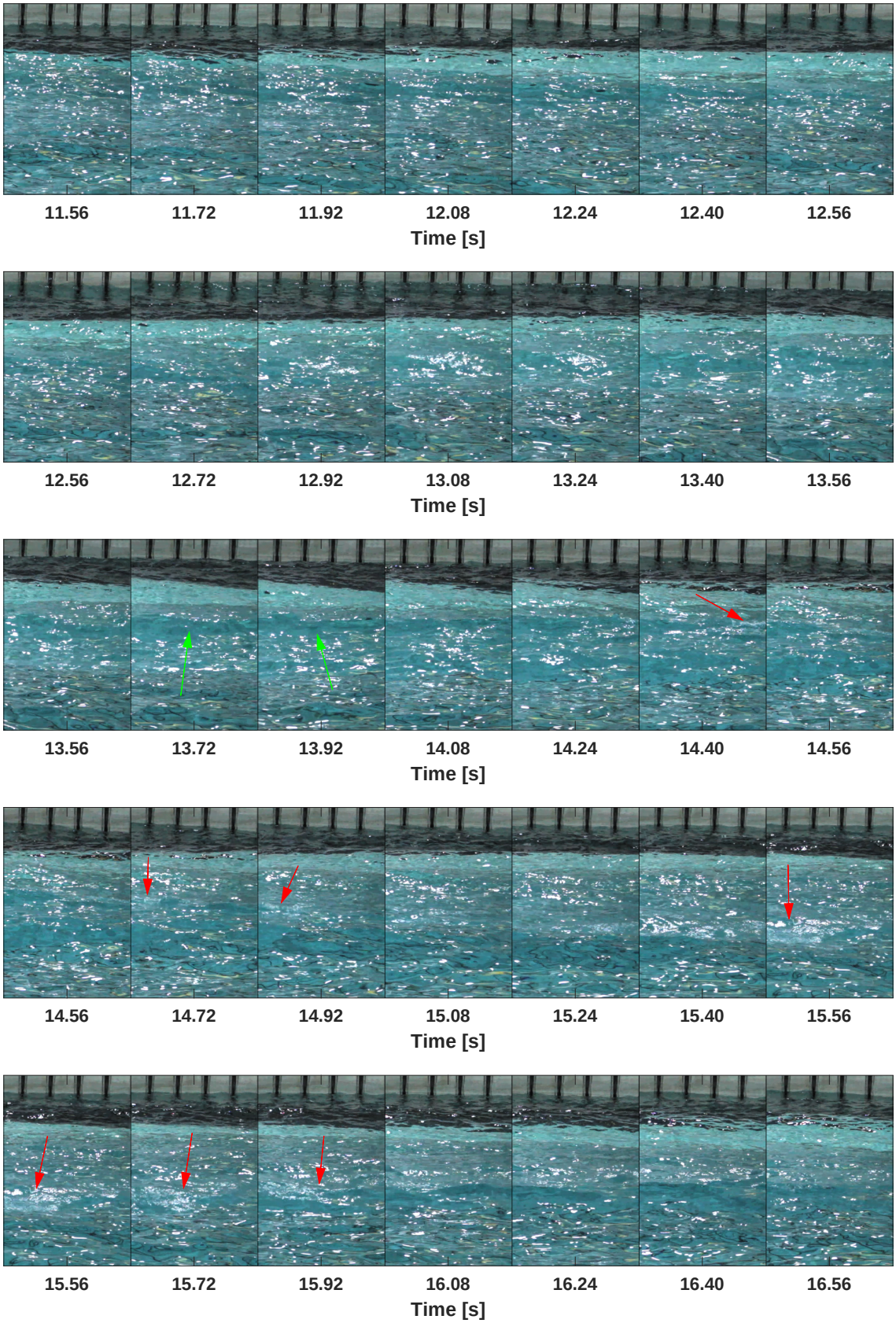

Figure 6.9: A sequence of video frames matching the VV radar data RTI plots shown in Fig. 6.6b and Fig. 6.10b. Green arrows indicate burst scattering, and red for whitecap. The video file matching this sequence of frames is named 'video_11-50-33.avi'.

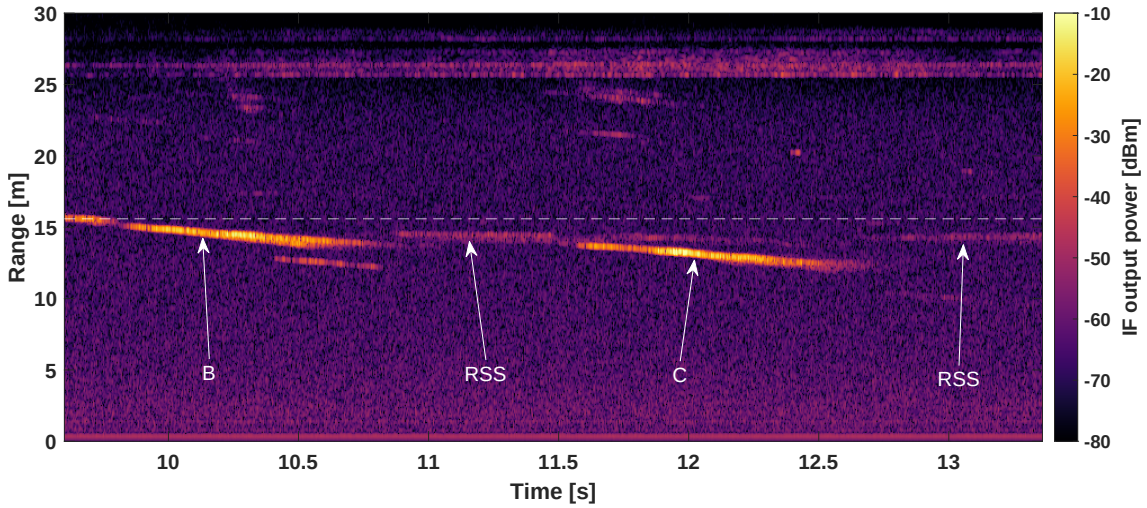

(a) HH polarisation, time-stamp 10 − 08 − 22.

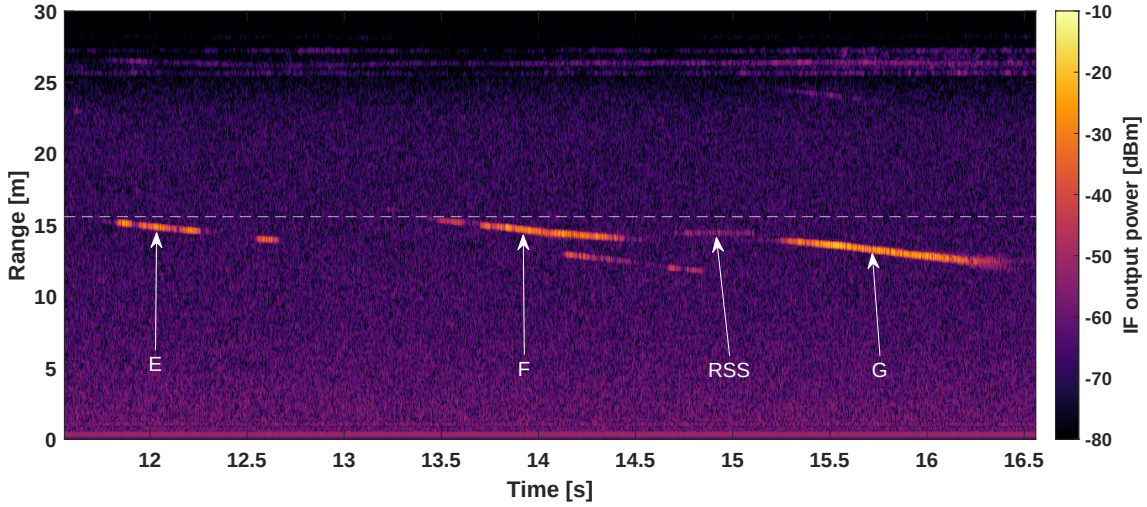

(b) VV polarisation, time-stamp 11 − 50 − 33.

Figure 6.10: RTI plots matching the same time intervals of coincident video shown in Figures 6.8 and 6.9. These were plotted from the same data as the plots in Fig. 6.6, where data were gathered at a SWH of 0.3 m, a $\psi = 0°$ and $\delta = 7°$, with either HH or VV polarisation as indicated.

In the VV data shown in Fig. 6.10b, the maximum amplitude peaks are limited to a maximum of ∼−15 dBm. A peak above −20 dBm up to ∼−17 dBm occurs during spike F at 13.8 s lasting ∼0.002 s, with two longer lived events occurring in spike G at 15.5 s and 16.0 s, lasting ∼0.05 s and reaching a maximum of −14 dBm.

6.2.3.3 Mechanism for maximum backscatter

As insight into the cause of the peak values, the video sequence shown in Fig. 6.8 shows a whitecap begin to break between frame times of 10.48 s and 10.76 s, and again

between 12.60 s and 12.76 s (red arrows). These events are too delayed from what is seen in the radar data to reasonably consider that the broken whitecap itself is the cause of the high peak, however it seems to indicate that they are related. Inspecting the frames at the times associated with the peak intensities, it can be seen that this coincides with a very steepened front surface of the wave in frames 10.12 s, 10.24 s, and 10.36 s, and possibly again in 11.88 s and 12.00 s (green arrows). The exact profile of the wave is difficult to determine given the camera angle, however it seems likely that the very intense returns are due to the steepened and possibly parabolic wave surface prior to a whitecap, as explained in Subsection 2.3.3.2 referring specifically to [83].

This evidence points towards burst scattering being the most significant cause of high amplitude backscatter spikes in HH polarisation at the SWH of 0.3 m seen here, with the greatest return from the whitecap event at ~10.5 s being roughly on par with the the moderate returns seen from burst scattering along spike B.

It would be expected, however, that whitecap returns in the wave tank environment are somewhat suppressed in comparison to what would be seen in nature given the lack of wind as mentioned previously, although for natural whitecaps of a similar size to those observed at FloWave the conclusion is likely valid. Since this analysis is drawn from a limited number of RTIs and accompanying video footage, this does not conclusively determine the hierarchy of contributions to scattering, where this would require a more in-depth analysis concentrating on this aspect in particular, and a larger dataset. As alluded to previously, the analysis in this thesis does not attempt to further distinguish between the two types of scattering due to the relative infrequency of whitecaps. As such, the returns analysed in Chapter 7 will contain some contributions from whitecap scattering however since these will be less common, it is not expected that they will significantly alter the conclusions drawn for burst scattering from this data.

As indicated by the peak levels observed, the same level of backscatter enhancement is not observed in VV data. The peak at 13.8 is associated with a steepened wave crest as shown in frames at 13.72 s and 13.92 s in Fig. 6.9 (green arrows). The other two peaks at 15.5 s and 16.0 s seem to be caused by small breaking wave events seen between the frames at 15.56 s and 15.92 s at a slightly closer range (red arrows). This suggests that the most significant amplitude signals in VV polarisation backscatter may be caused by whitecaps. The difference seen between the two polarisations affirms that HH polarised returns are due to burst scattering, which in this polarisation is enhanced by a forward scattering and multipath effect which is suppressed in VV, as explained in Subsection 2.3.3.2.

6.2.4 Rough surface scattering

An interesting feature of the data, observed in both RTI plots, is the occurrence of RSS events which produce scattering in patches that are stationary in range. In Fig. 6.6a, this is seen first beginning at 10.9 s, and in Fig. 6.6b at 14.7 s. These appear distinct from the diagonal, and thus travelling, clutter returns discussed above. They additionally occur following larger scattering events, with particularly bright returns seemingly echoing at the same range for some time afterwards. The conclusion that these events are RSS was reached when inspecting the corresponding coincident video data, where in Fig. 6.8 a breaking wave is observed to begin at 10.48 s (red arrows), resulting in a roughened patch of water at that range from frame 10.88 s onwards, observable again e.g. in frames at 11.48 s and 11.60 s (yellow arrows). This is supported by observations from Fig. 6.9 for VV polarisation, although the source of the RSS labelled feature is less easy to discern from the video footage due to the lighting and angle. From the RTI it can be seen that the RSS must originate from a range similar to the steepened crests identified with green arrows at frame times 13.72 s and 13.92 s for feature F. A small breaking wave event is identified at an approximately matching range in the video footage at frame time 14.40 s (red arrow), and is expected to be the source of the roughened surface. The small travelling wave events in the RTI which begin at very nearly the same time as the RSS feature, but at a closer range (∼12 m versus 15 m), can be identified as the breaking wave events identified with red arrows in frames at times 14.72 s and 14.92 s. This would suggest the roughened surface should be visible in these frames, but instead a dark area at the right hand side of those frames is seen at the expected position, meaning that the wave angle was such that the observer looks into the water rather than being able to see the surface in this case. The cause of the variability of the scattering in Fig. 6.6a can be seen in the sequence of frames in Fig. 6.8, where the roughened area is alternately hidden and revealed as a wave passes through it and tilts the patch either towards or away from the radar. The amplitude of both scattering events are initially ∼−55 to −45 dBm (∼20 dB above the average noise floor at this range of −70.7 dBm), where due to the nature of the scattering the similarity with respect to polarisation is to be expected.

Videos of both events are supplied in the supplementary material, with annotations to indicate the events of interest.

This is promising evidence for the sensitivity to very small scale roughness which is expected at 207 GHz, and suggests that this is a promising line of enquiry for further research. This effect could have a large impact on the design of clutter filtering schemes for two main reasons:

1. The effect could potentially occur at even very low sea states if similar surface roughening was caused by gusts of wind, however the scattering in this case would possibly be more transient and move around with the body of air.

2. For similar constant range patches which might be caused by whitecaps at higher sea states, these cannot be filtered from PPI data using a line detecting algorithm or for example the Hough or Radon transforms such as used by Stove et al. [173] since they would not necessarily appear as linear features unlike wave-fronts.

In addition, it could be expected that patches of sea foam or small coalesced floating debris such as maybe be found in littoral or harbour environments may also exhibit a similar response. The effect may be particularly noticeable in the FloWave dataset due to the otherwise very smooth surface of the water meaning that signals were more easily distinguished.

The observed RSS is considered to be a separate natural phenomenon to the sea spikes discussed above. For the further analysis presented in Chapter 7, this is therefore excluded from the data.

6.2.5 Signals unrelated to sea clutter

As stated in Subsection 6.2.2, the data also contains signals from the actuator paddles at the edge of the pool at ranges beyond 25 m. This is within the roll-off region of the anti-aliasing filter, which strongly suppresses signals beyond this point. The sea clutter data from ranges near the actuators is excluded from that data as it can be expected to be both less representative of the natural environment and will differ more significantly from the programmed SWH of the wave tank.

The effect of the corrupted chirps mentioned previously is shown in Fig. 6.11. These occur as isolated events for chirp numbers near the start of a 64 chirp burst, and the artefacts are likely due to an unresolved data acquisition code issue. The effect is confined to a single chirp, as shown in the Figure, where it can be seen that the chirp immediately preceding the corrupted chirp is unaffected. The signal peak of a corrupted chirp is unaltered, however the noise floor is raised significantly, as can be seen when comparing the IF signal levels beyond 40 m. This region is far beyond the anti-aliasing filter roll-off, where it can be seen that the level of chirp number 152385 is $\sim$−90 dBm and for chirp number 152386 this is raised by $\sim$15 dB to $\sim$−75 dBm.

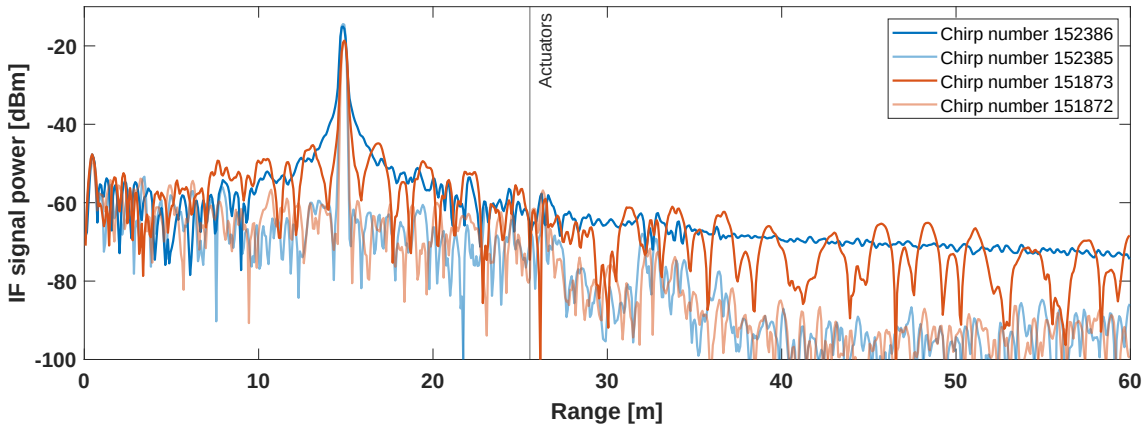

Figure 6.11: Range profiles of selected chirps from the data shown in Fig. 6.6a, demonstrating how corrupt chirps (numbers 152386 and 151873) affect the instrument noise floor in comparison with the ordinary chirp immediately preceding each of these (numbers 152385 and 151872).

6.2.6 Qualitative analysis of the effects of experiment parameters

6.2.6.1 Polarisation

As mentioned above, the data indicates that HH returns can be of a significantly higher intensity than VV, where peak values were up to 10 to 15 dB greater. It is expected that this is as a result of a multipath effect linked to the steepened and parabolic shape of the wave crest near breaking, which enhances the HH return of burst scatter. The highest intensity backscatter in VV was seen from whitecap events. This disparity was reflected in the NRCS and amplitude distributions of the data presented in Chapter 7, where HH NRCS values were greater than VV and the distribution was spikier/longer-tailed. The implication of this result is that clutter is best suppressed, and thus targets most easily detected, in VV polarisation at 207 GHz.

6.2.6.2 Grazing angle

Figures 6.12 and 6.13 show data collected by the radar with a depression angle of either 5°, 7°, or 10°, in HH or VV polarisation. A surface with SWH 0.3 m and $\psi = 0°$ was generated in each case. Each plot is additionally marked with the boundary lines of grazing angle swaths of 1°, centred on whole values on an angular scale with regular increments. The right hand plot at $\delta = 7°$ in HH polarisation seen in Fig. 6.12b is the same as shown for Fig. 6.6a, and the left hand plot in Fig. 6.13b is also the same as that shown in Fig. 6.6b, where these are reproduced in this set to aid comparison of data at different grazing angles.

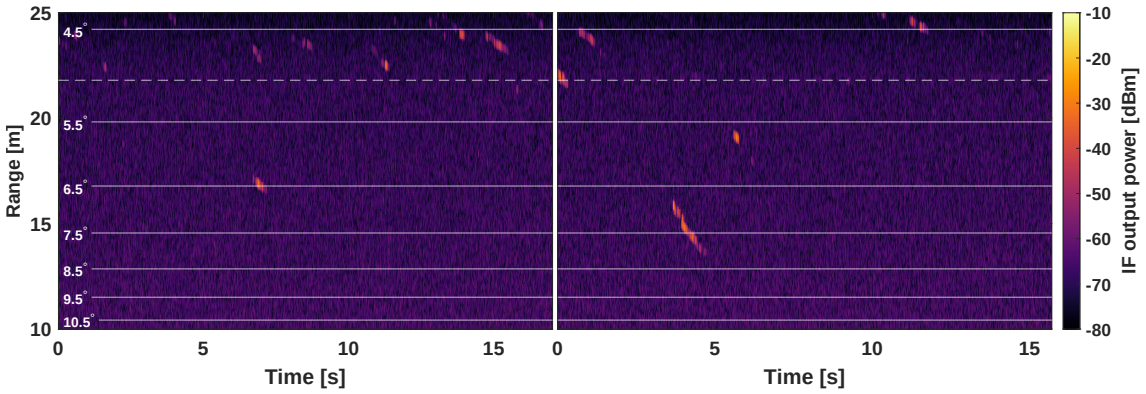

(a) Radar depression angle of 5°, time-stamps $10-04-54$ (left) and $10-05-43$ (right).

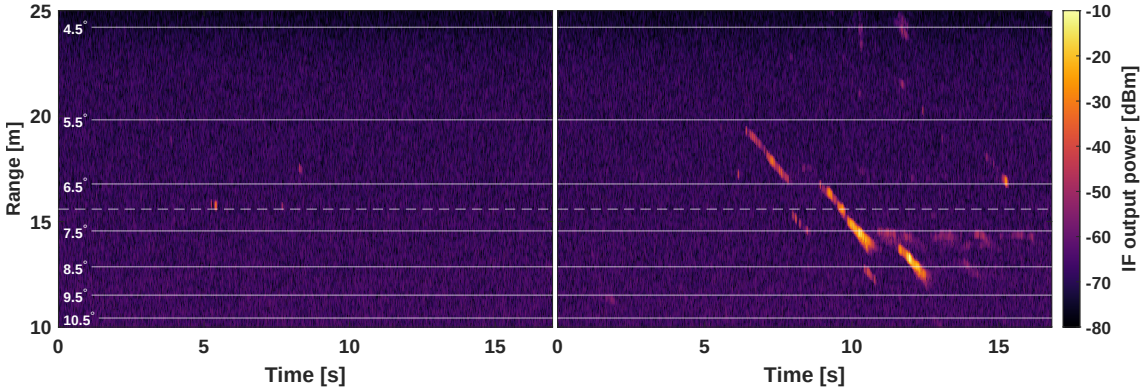

(b) Radar depression angle of 7°, time-stamps $10-07-37$ (left) and $10-08-22$ (right).

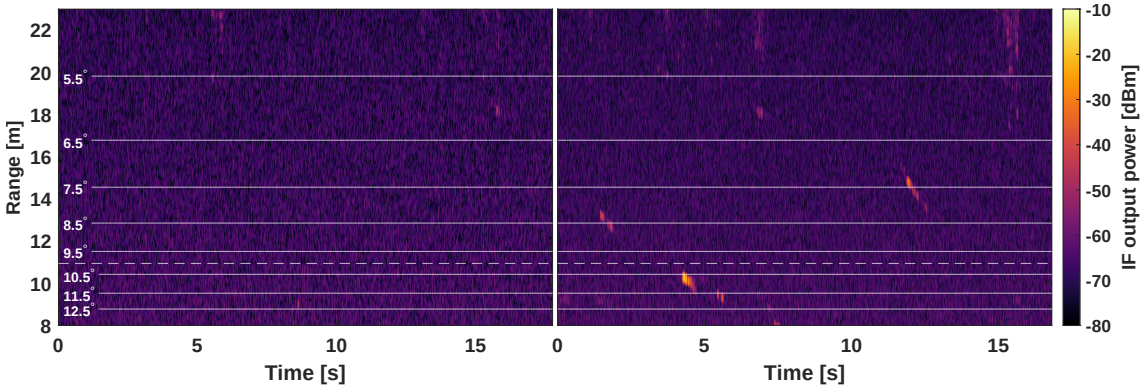

(c) Radar depression angle of 10°, time-stamps $10-10-08$ (left) and $10-11-40$ (right).

Figure 6.12: RTI plots of waves with SWH 0.3 m, $\psi = 0°$, in HH polarisation. The data shown were gathered at a depression angle of either $\delta = 5°$, 7°, or $\delta = 10°$.

The data indicates that the greatest number of returns are seen when the radar is at depression angles of 5° and 7°, where 10° shows relatively few returns. This may be due to the smaller beam footprint at 10° resulting in less coverage of sparsely occurring scattering events (the average two-way beamwidth of each antenna being 1.43°). Generally speaking, the grazing angle swath which is at the same angle as the depression angle or 1° above (closer in range) contains the highest amplitude spikes,

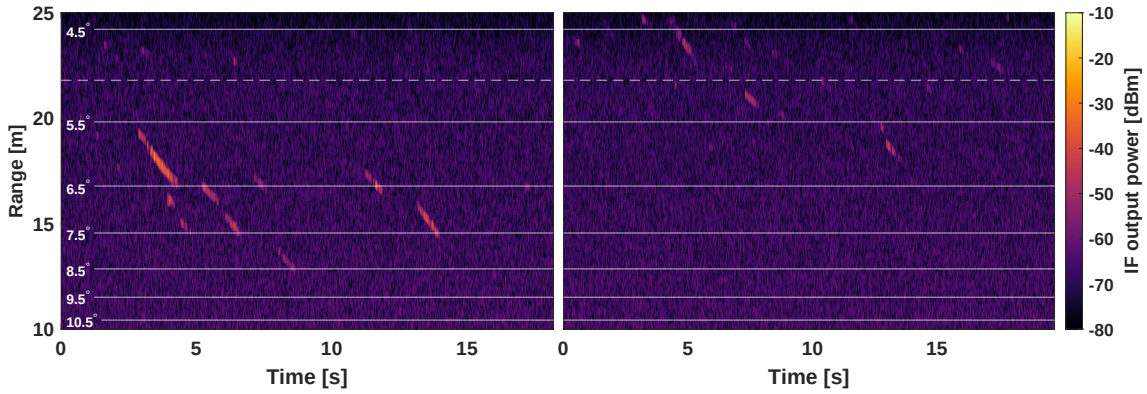

(a) Radar depression angle of 5°, time-stamps $11-47-52$ (left) and $11-48-30$ (right).

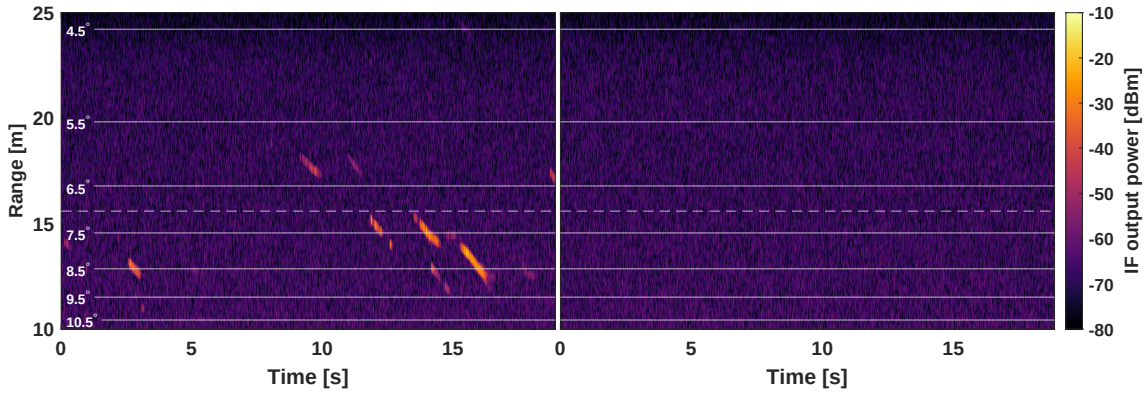

(b) Radar depression angle of 7°, time-stamps $11-50-33$ (left) and $11-51-23$ (right).

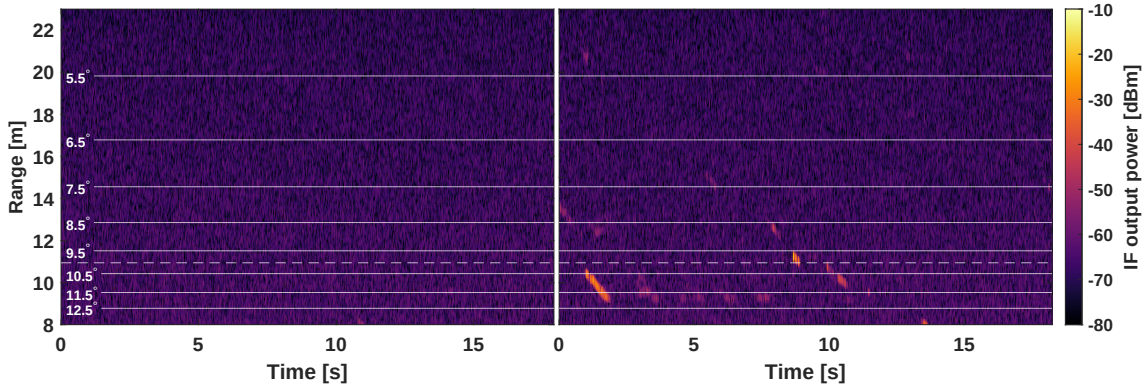

(c) Radar depression angle of 10°, time-stamps $11-53-20$ (left) and $11-54-00$ (right).

Figure 6.13: RTI plots of waves with SWH 0.3 m, $\psi = 0°$, in VV polarisation. The data shown were gathered at a depression angle of either $\delta = 5°$, $\delta = 7°$, or $\delta = 10°$.

which is to be expected given the narrow beamwidth.

Table 6.1 summarises the peak values and the estimated typical level of a spike event for the data, where these spot measurements were made near boresight range to control for the change in antenna pattern gain. For peak powers, the table shows that HH is uniformly greater, and that for both polarisations the level at 7° depression angle is the greatest, followed by 10° and 5°. This disparity appears more pronounced

δ[°]	5		7		10	
Polarisation	HH	VV	HH	VV	HH	VV
Peak IF signal power [dBm]	−17.6	−19.5	−2.8	−14.0	−13.3	−16.7
Typical IF signal power [dBm]	−35	−40	−25	−30	−40	−35
Fraction of runs with spikes	3/3	3/3	2/2	1/2	1/2	2/2

Table 6.1: Peak and estimated typical IF signal power levels from sea spikes measured at depression angles of 5° (21.8 m), 7° (15.6 m), 10° (10.9 m), in HH and VV polarisations, from sea surfaces with SWH 0.3 m and a wave direction of 0°.

in HH polarisation. Typical power levels would seem to follow these trends, with the exception that VV returns at 10° are greater than those in HH. Given the low number of spike events at 10° however this is difficult to distinguish, and in general these values are only estimates which have not been corrected for the effects of beam pattern, range, and beam footprint area.

These results seem to show that the backscatter intensity is greatest at some grazing angle close to 7°, however this conclusion may change given a larger number of measured spike events since results from lower frequencies suggest that backscatter intensity is monotonically increasing in the LGA regime, as shown in Fig. 2.25. Given the peak intensity values however, it may be reasonable to infer that the enhancement seen for burst scattering in HH polarisation is indeed optimal at grazing angles of around 7°. This may be due to the geometry of the front surface of the wave responsible for the enhancement; the approximately parabolic shape of the front surface of the wave which causes the multipath effect may only be ideal over a relatively narrow range of incidence angles, or the forward scatter in front of the wave may be directed mostly over the crest if the grazing angle is too steep (see [83, Fig. 17]). The large disparity between the values lends some legitimacy to this thought, although it is possible that this particular result was caused by a fortuitous wave and the grazing angle was not the direct cause. The quantitative analysis in Chapter 7 examines this further.

In both polarisations and at all depression angles, there is a large variability in the number of spikes observed, where generally one of two RTI plots for the same set of parameters appears mostly empty and the other contains a significant number of spikes. In all cases, these data runs were recorded consecutively ~60 s apart. This demonstrates the very variable nature of the entire dataset, where occurrences of a group of spikes could be separated by tens of seconds. This is demonstrated in Fig. 6.14 for both polarisations at 5° depression angle.

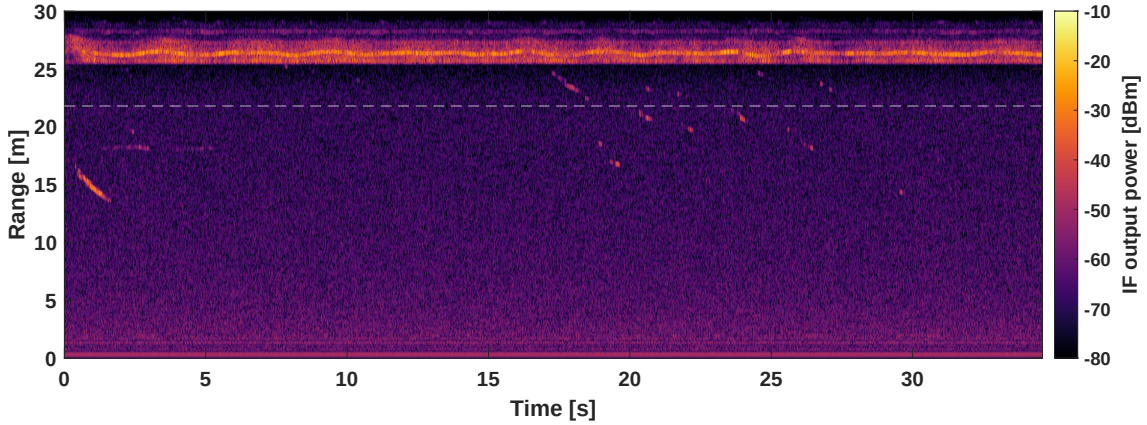

(a) HH polarisation, time-stamp 10 – 14 – 52.

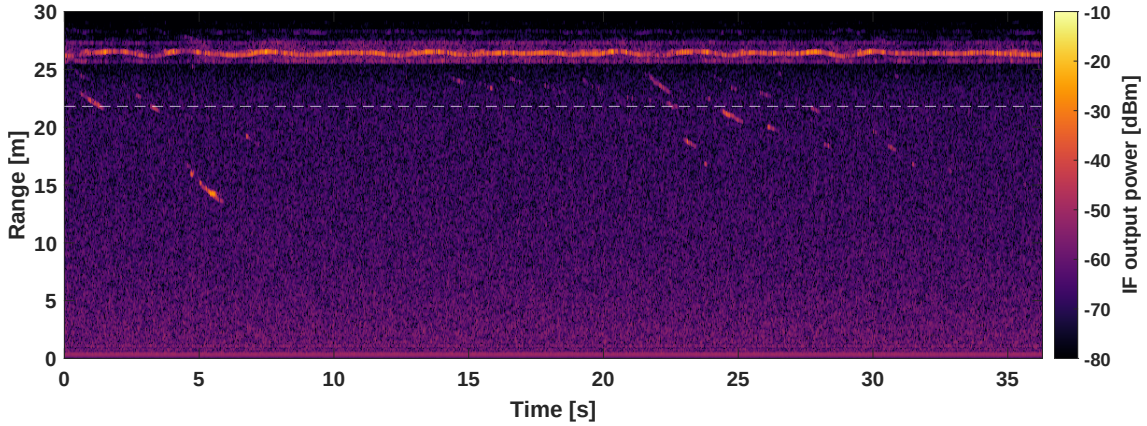

(b) VV polarisation, time-stamp 11 – 46 – 27.

Figure 6.14: Long duration RTI plots of HH and VV polarised data taken at $\delta = 5°$, $\psi = 0°$ for SWH 0.3 m. It should be noted that these runs were not collected synchronously, even though some clutter spikes may appear to be nearly simultaneous in this presentation. These data show the sparsity of spikes, and show how they often appeared as intermittent clusters and with significant stretches of little to no signal.

6.2.6.3 Wave direction

The observation of spike events was highly sensitive to wave direction. Very little backscatter was observed by the radar for wave directions other than 0°, where typically only a single, short-lived spike is seen in ~10 to 20 s of data at non-zero wave directions. As summarised in Subsection 6.1.5, the data were collected at SWH 0.3 m and at depression angles of 5° and 10°. In hindsight, data collection at 7° depression angle may have better optimised the level of returns, however 5° was chosen as lower grazing angles were more relevant to the application geometry of autonomous vessels, and a depression angle of 10° was expected to maximise returns, given the closer range and expected monotonic increase in backscatter amplitude with grazing angle, as shown in Fig. 2.25.

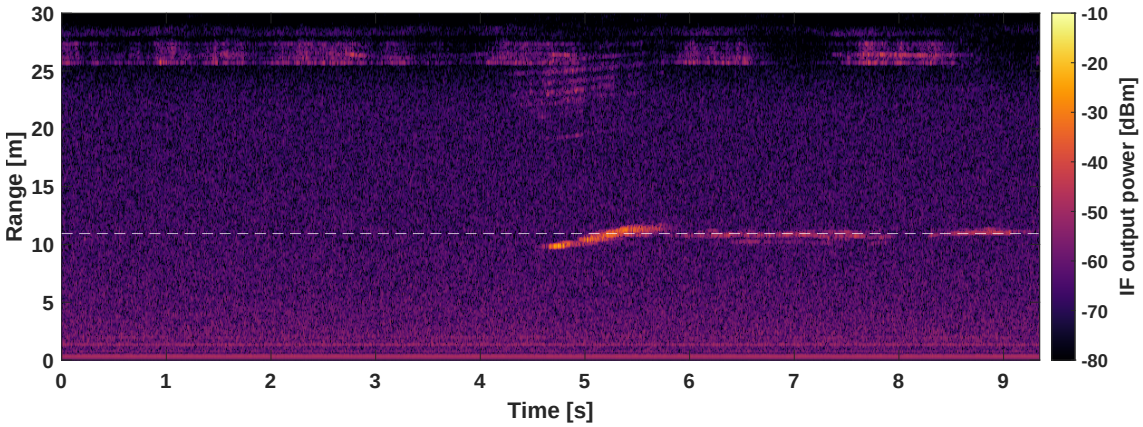

(a)

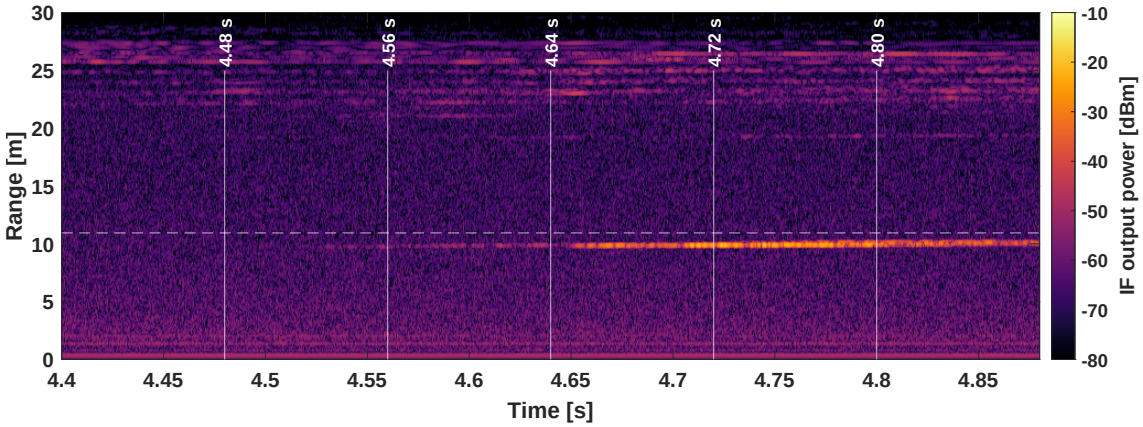

(b)

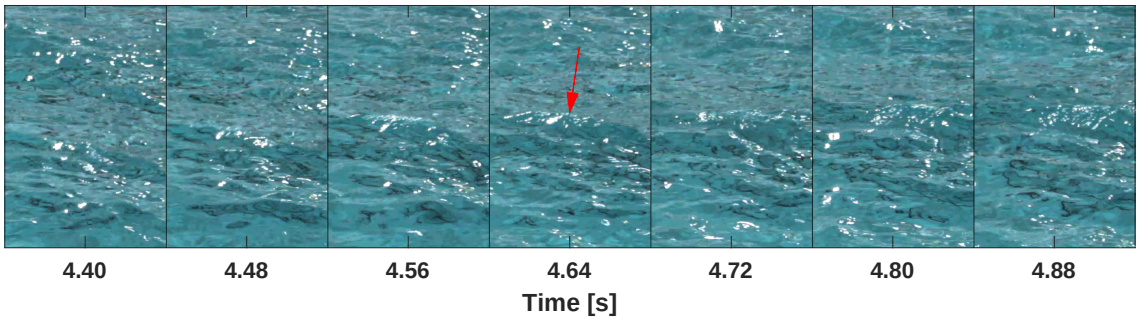

(c)

Figure 6.15: Data taken at 10° depression angle (time-stamp $10-40-12$), in HH polarisation for $\psi = 135°$ and SWH of 0.3 m. (a) The full RTI plot of the data run, (b) the beginning of the only spike event detected during the run, (c) a sequence of coincident video frames, synchronous with (b), showing a whitecap (red arrow) occurring at the time of the spike. The file for this sequence of frames is named 'video_10-40-12.avi'.

Out of 20 total measurements made for wave directions other than 0°, only 6 runs contained any backscatter from the water, 1 in HH polarisation and 5 in VV. The most significant return from HH is shown in Fig. 6.15a, and for VV in Fig. 6.16a. It is not clear whether one polarisation is favoured over another, as although spikes were

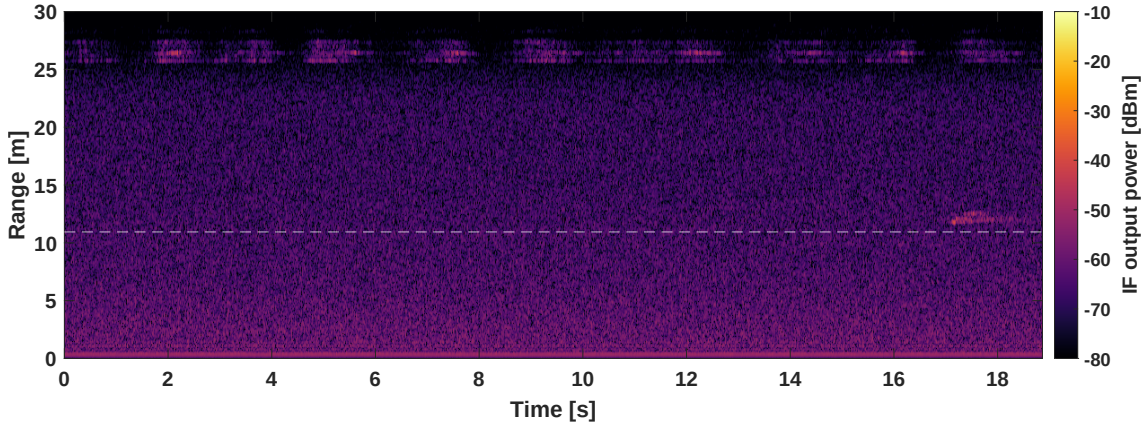

(a)

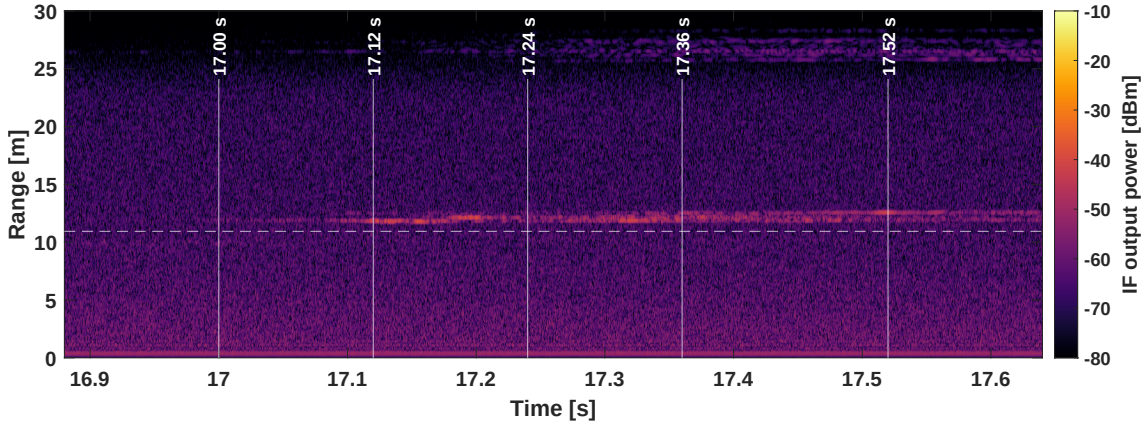

(b)

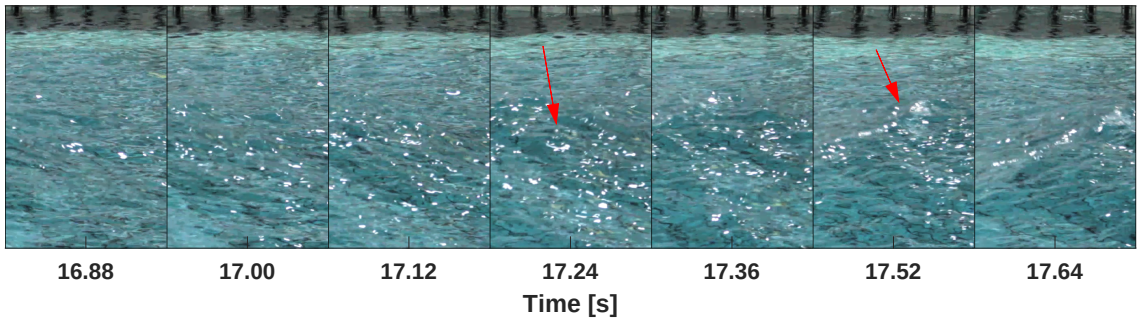

(c)

Figure 6.16: Data taken at 10° depression angle (time-stamp $12-06-27$), in VV polarisation for $\psi = 90°$ and SWH of 0.3 m. (a) The full RTI plot of the data run, (b) the beginning of the only spike event in the data, (c) a sequence of coincident video frames, synchronous with (b), showing a whitecap occurring at the time of the spike (red arrows). The video file matching this sequence of frames is named 'video_12-06-27.avi'. Given the fine range resolution of the radar, the signal can be seen to extend over two range bins, implying the feature is up to ~15 cm long.

seen in more VV data files they were all of a lesser intensity and more measurements were made at that polarisation than in HH, with a split of 12 to 8. Minor spikes were observed in VV at 45°, 90° (including Fig. 6.16c), 135°, and 180°. Figure 6.15a in HH is for a wave direction at 135°. These data do not reveal any clear pattern, and in general, given the low number of returns, it is difficult to conclude any major trend with wave direction or any combination of this and either polarisation or grazing angle.

The level of the spike in the HH polarised data is ∼−35 dBm, and around ∼−45 dBm in VV. In general the VV returns from the other data runs containing spikes were also of this level, indicating that any variation in backscatter intensity with wave direction is not particularly clear from this dataset, other than the conclusion that at all other wave directions apart from 0° the returns are highly suppressed.

Further examination of the video data for the scattering events is presented in Fig. 6.15 and Fig. 6.16, where the videos corresponding to the still frames shown are 'video_10-40-12.avi' and 'video_12-06-27.avi', respectively. The sequence of coincident video frames for the beginning of each scattering event is displayed here, and shows that the cause is a whitecap event (indicated with a red arrow) in each instance; for HH polarisation the bubbles from the whitecap can be observed in the frame from 4.64 s, and for VV a disrupted surface can be seen at 17.24 s and is fully breaking at 17.52 s. The level of the returns seen in the data is also consistent with the small whitecaps seen at this depression angle. Additionally, considerable RSS is seen after the scattering event in Fig. 6.15a, which indicates a whitecap event.

The results presented above suggest that the wave returns seen whilst not looking directly in the direction of their approach is predominantly from whitecaps. This stands to reason, since burst scattering relies on specular reflection from steepened wave crests, which is only likely to redirect the scattering back towards the radar when looking into the waves, whereas for other wave directions it will be scattered away. Conversely, whitecap scattering is more isotropic as the roughened and foamy peak of the wave appears similar from a wide range of look angles. Since in this case the foam is at the crest, it is not shadowed by the wave, even though as is the case in Fig. 6.15 the waves are travelling at 135° and thus mostly away from the radar.

6.2.6.4 Wave height

Tables 6.2 and 6.3 summarise the observed signal levels from the data at $H_{1/3} = 0.1$ m and $H_{1/3} = 0.2$ m respectively. The data at SWH 0.1 are shown in Fig. 6.17, and for SWH 0.2 m these are shown in Fig. 6.18. For SWH 0.3 m these are shown in Figures 6.12 and 6.13 with a summary made previously in Table 6.1. The list below discusses the results from each wave height in more detail.

δ[°]	5		7		10	
Polarisation	HH	VV	HH	VV	HH	VV
Peak IF signal power [dBm]	<−60	<−55	∼−35	<−55	∼−50	-
Fraction of runs with spikes	2/2	1/1	2/2	2/2	1/2	0/2

Table 6.2: Estimated peak IF signal power levels from sea spikes measured at depression angles of 5° (21.8 m), 7° (15.6 m), 10° (10.9 m), in HH and VV polarisations, from sea surfaces with SWH 0.1 m and a wave direction of 0°.

δ[°]	5		7		10	
Polarisation	HH	VV	HH	VV	HH	VV
Peak IF signal power [dBm]	−25	−40	−35	−35	-	−55
Fraction of runs with spikes	2/2	2/2	1/2	1/2	0/2	1/2

Table 6.3: Estimated peak IF signal power levels from sea spikes measured at depression angles of 5° (21.8 m), 7° (15.6 m), 10° (10.9 m), in HH and VV polarisations, from sea surfaces with SWH 0.2 m and a wave direction of 0°.

- **SWH 0.1 m**
  - Depression angle 5° (not shown): very few returns are seen in both polarisations, where signal levels are very low and not significantly different.
  - Depression angle 7° (Fig. 6.17): spikes are observed in both polarisations but have a noticeably higher amplitude in HH (∼−35 dBm) compared to VV (∼−55 dBm).
  - Depression angle 10° (not shown): a very minor spike was observed in HH polarisation, this being lower than that seen at $\delta = 7°$. No returns were seen in VV.
- **SWH 0.2 m**
  - Depression angle 5° (Fig. 6.18a and Fig. 6.18b): both polarisations observed a run of data with very few spikes and another where significant clutter is seen. HH polarised returns are more significant and at ∼−25 dBm are ∼15 dB greater than VV.
  - Depression angle 7° (Fig. 6.18c): only one repeat of two at each polarisation contained sea clutter. Both RTI plots look very similar and returns are of a similar intensity ∼−35 dBm in each polarisation.
  - Depression angle 10° (not shown): no returns were observed in either polarisation.
- **SWH 0.3 m**

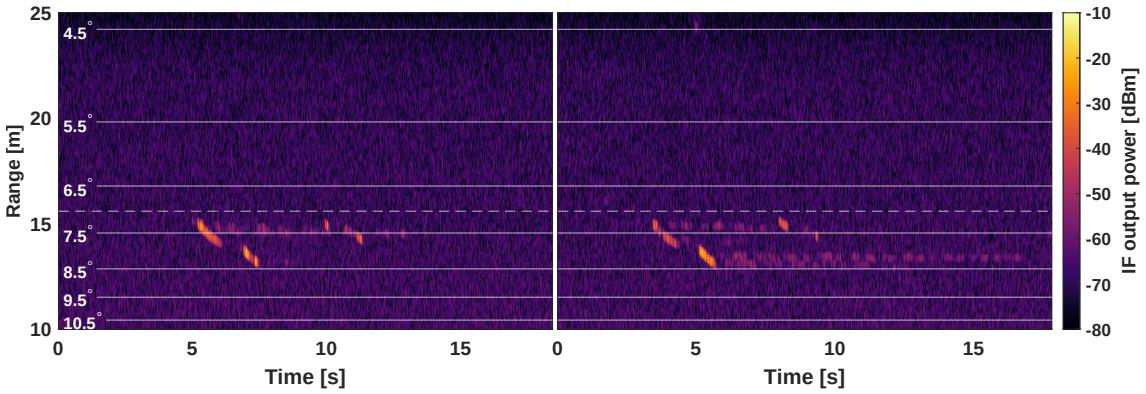

(a) HH polarisation, time-stamps $09-36-45$ (left) and $09-37-29$ (right).

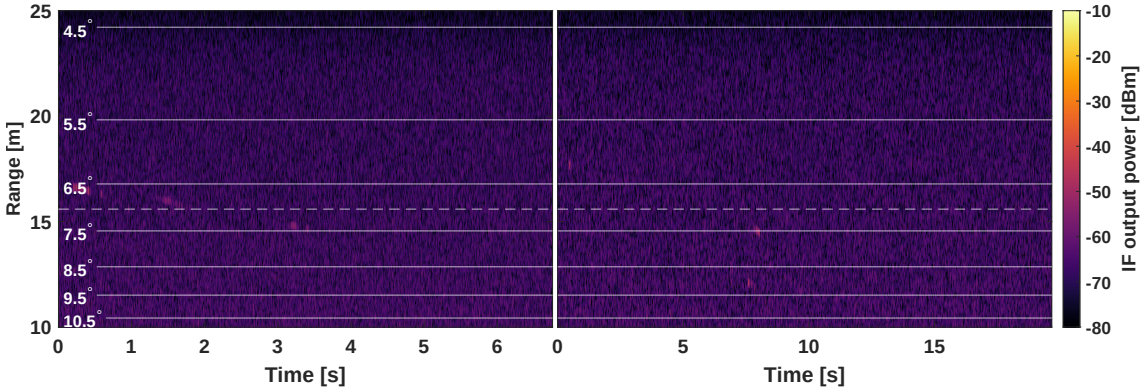

(b) VV polarisation, time-stamps $11-17-37$ (left) and $11-19-31$ (right).

Figure 6.17: RTI plots of HH and VV polarised data taken at $\delta = 7°$, $\psi = 0°$ for SWH 0.1 m. It is interesting to note that the two plots for (a) are very similar, however these were separated by less than the repeat time of the pool so this is expected to be a coincidence.

- Depression angle 5° (Fig. 6.12a, Fig. 6.13a, Fig. 7.1a, Fig. 7.1b): the number and level of returns seen for both polarisations was similar, however HH polarised intensities were slightly greater than VV.
- Depression angle 7° (Fig. 6.12b, Fig. 6.13b): the maximum backscatter intensity observed in either polarisation was recorded at this angle, where HH returns were clearly enhanced compared to VV.
- Depression angle 10° (Fig. 6.12c, Fig. 6.13c): the number and intensity of backscatter events was reduced compared to 7° depression angle, however the clutter signals were still significant.

As would be expected, the intensity of returns generally increases with the SWH for all depression angles and both polarisations. The number of returns is also generally increasing, although the fraction of runs with no returns is approximately equal for $H_{1/3} = 0.1$ m and $H_{1/3} = 0.2$ m. This perhaps follows the reasoning that the backscatter

intensity will be a function of the scatterer (i.e. wave) size. In HH polarisation, 1 of 6 measurements contained no clutter signals at SWH 0.1 m, where this fraction was 3 of 6 for 0.2 m, compared with 1 of 7 for SWH 0.3 m. In VV polarisation, 2 of 5 and 2 of 6 runs were empty for SWH 0.1 m and 0.2 m respectively, compared with only 1 of 7 for SWH 0.3 m. Backscatter was most reliably observed at a depression angle of 5° at all wave heights despite returns often being lower than at higher depression angles, this perhaps being a function of the larger beam footprint.

6.2.7 Conclusions

6.2.7.1 Polarisation

The sea clutter observed during the FloWave trial was seen to be greater in HH than in VV due to the prevalence of burst scattering. The cause of greatest backscatter in VV was conversely whitecap scattering. The trend seen with polarisation as a result of burst scattering has been predicted previously from extrapolation of NRCS models (such as the NRL model) based on results at lower frequency. VV scattering is generally seen to be dominant at lower frequencies such as X-band, as shown in Fig. 2.25, however as the intensity of burst scattering increases and Bragg scattering diminishes, HH becomes more significant as explained in Subsection 2.3.4.3.

6.2.7.2 Grazing angle

The intensity of scattering events was seen to be greatest for a depression angle of 7°, suggesting that the response peaks at grazing angles of between 6.5 to 8.5° in both polarisations, although the reduction at a depression angle of 10° may be due to the relatively smaller beam footprint coinciding with fewer wave fronts. The suggestion from the data that the burst scattering response in HH polarisation is not monotonically increasing with grazing angle is a significant departure from lower frequency results shown in Fig. 2.25.

6.2.7.3 Wave direction

The results for wave direction are interesting, although the typical cosinusoidal response of scattering intensity to wave direction, shown in Fig. 2.27, was not recovered due to a combination smooth, relatively low SWH waves, and insufficient sensitivity. This behaviour may be revealed in environments with more whitecaps. Burst scattering was not observed at wave directions other than 0°, where rare spike events are thought to be caused by whitecap scattering.

6.2.7.4 Wave height

The results for wave height follow the general expectation and trend seen from lower frequency results, where the number and intensity of scattering events generally increased with SWH (when comparing $H_{1/3} = 0.1$ m and $H_{1/3} = 0.3$ m) and thus with the size of wave front. Whilst the observed intensities at $H_{1/3} = 0.2$ m were somewhat greater than seen at $H_{1/3} = 0.1$ m, the fraction of runs with spikes was similar, and less than what was seen at $H_{1/3} = 0.3$ m.

6.2.7.5 Remarks

From the results presented above, it is evident that even a single data file, along with its coincident video, contains a wealth of information and multiple potential avenues for analysis. The main disadvantage of this trial was that it did not incorporate the effects of wind on sea clutter, which are likely to be significant in increasing all types of scattering, but particularly RSS and whitecap scattering in comparison to what was observed at FloWave. In general, the lack of wind also contributed to a reduced number of scattering events than was seen at other trials including at Coniston Water [26]. It is expected however that the trends seen here will be representative of what is seen in nature, especially for the case of burst scattering.

This chapter presented the data gathered during the FloWave trial, and the qualitative analysis based on the results. The following chapter continues with a quantitative approach to the analysis of the same data.

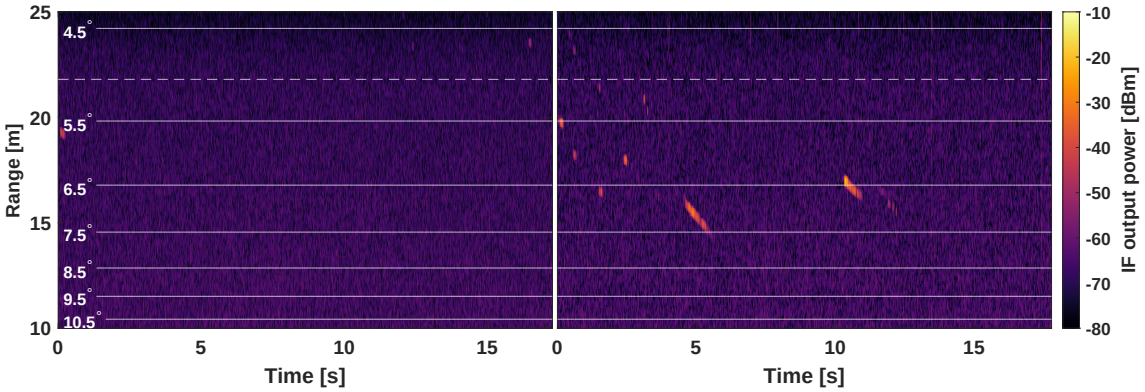

(a) HH polarisation at $\delta = 5°$, time-stamps $09-50-01$ (left) and $09-50-42$ (right).

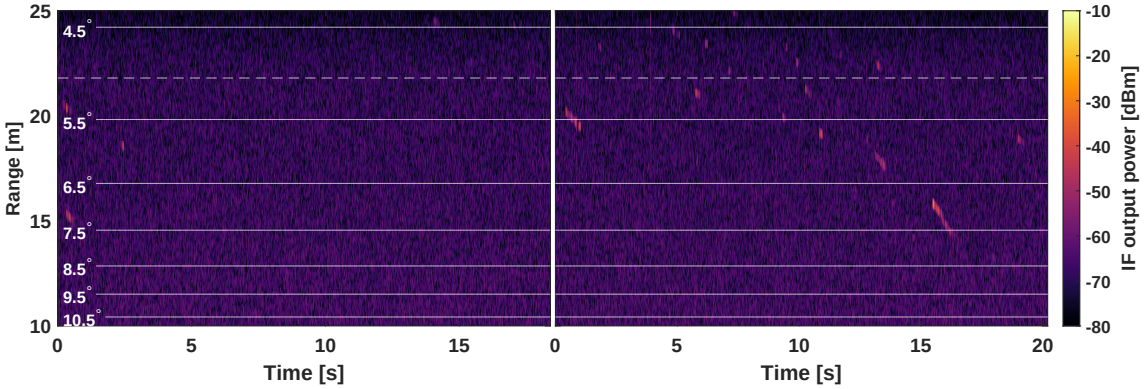

(b) VV polarisation at $\delta = 5°$, time-stamps $11-36-00$ (left) and $11-36-46$ (right).

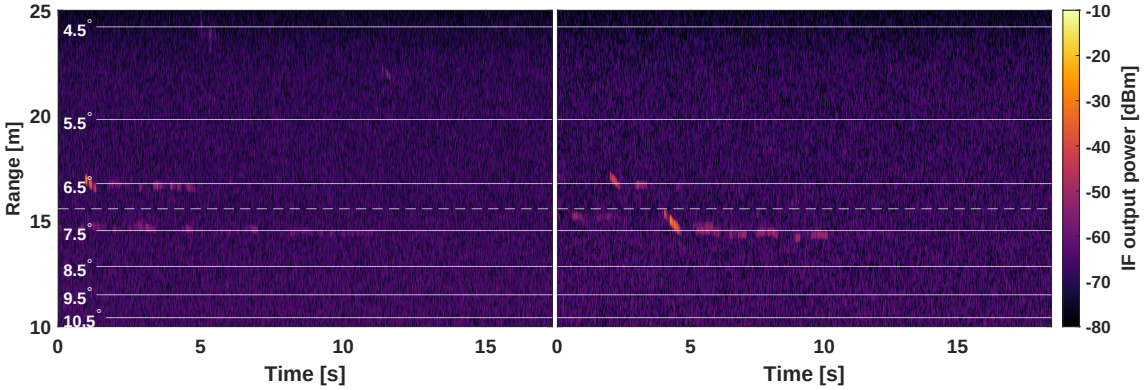

(c) Data taken at $\delta = 7°$, in HH polarisation on the left (time-stamp $09-47-50$) and VV polarisation on the right (time-stamp $11-29-41$).

Figure 6.18: RTI plots of HH and VV polarised data gathered at either 5° or 7° depression angle, $\psi = 0°$ and SWH 0.2 m.

7

207 GHz Sea Clutter Amplitude Statistics

In this chapter, the 207 GHz data from the FloWave trial are examined further following a quantitative approach. This chapter is intended to complement Chapter 6, and so the details of the motivation and process for the trial are not repeated here. The analysis follows two main strands:

1. An examination of the amplitude distribution of the data using the CCDF curves, also equivalently known as probability of false alarm ($\mathbb{P}_{fa}$) plots,
2. Calculation of the mean NRCS of the data.

The first analysis thread is intended to shed light on how spiky or long-tailed the amplitude distributions of the data are, this having implications for radar detection schemes. The results of the second thread provide information relevant to the design of radar systems by quantifying the expected backscatter level under different conditions.

7.1 Amplitude statistics processing methods

7.1.1 Selection of data

Data for further processing were selected only if clutter signals could be identified. Additionally, data collected at a depression angle of 3° were excluded from the analysis as the strong reflections from the metallic clutter at the edge of the pool induced a raised noise floor due to the transmitter phase noise. Since the minimum grazing angle observable was ~4.4°, the benefits of including the data from these runs was diminished given that the clutter spikes would be significantly off-boresight and the radar sensitivity thus reduced. The combined effect of the reduction in sensitivity and

Number	Time stamp	Duration [s]	Pol.	SWH [m]	Wave dir. [°]	δ [°]
1	09 – 33 – 36	19.10	HH	0.1	0	5
2	09 – 34 – 40	17.57	HH	0.1	0	5
3	09 – 36 – 45	18.44	HH	0.1	0	7
4	09 – 37 – 29	17.83	HH	0.1	0	7
5	09 – 40 – 02	17.51	HH	0.1	0	10
6	09 – 50 – 01	17.27	HH	0.2	0	5
7	09 – 50 – 42	17.79	HH	0.2	0	5
8	10 – 04 – 54	17.03	HH	0.3	0	5
9	10 – 05 – 43	15.71	HH	0.3	0	5
10	10 – 07 – 37	16.97	HH	0.3	0	7
11	10 – 08 – 22	16.80	HH	0.3	0	7
12	10 – 11 – 40	16.82	HH	0.3	0	10
13	10 – 14 – 52	34.60	HH	0.3	0	5
14	10 – 40 – 12	9.35	HH	0.3	135	10
15	11 – 15 – 36	17.20	VV	0.1	0	5
16	11 – 17 – 37	6.76	VV	0.1	0	7
17	11 – 19 – 31	19.67	VV	0.1	0	7
18	11 – 26 – 52	18.52	VV	0.2	0	10
19	11 – 29 – 41	18.52	VV	0.2	0	7
20	11 – 36 – 00	18.40	VV	0.2	0	5
21	11 – 36 – 46	20.20	VV	0.2	0	5
22	11 – 46 – 27	36.29	VV	0.3	0	5
23	11 – 47 – 52	18.18	VV	0.3	0	5
24	11 – 48 – 30	19.72	VV	0.3	0	5
25	11 – 50 – 33	18.92	VV	0.3	0	7
26	11 – 53 – 20	17.92	VV	0.3	0	10
27	11 – 54 – 00	18.25	VV	0.3	0	10
28	11 – 59 – 10	18.85	VV	0.3	45	5
29	11 – 59 – 50	19.70	VV	0.3	45	5
30	12 – 06 – 27	18.87	VV	0.3	90	10
31	12 – 24 – 45	18.30	VV	0.3	180	5

Table 7.1: Data files which were included in the analysis based on the criteria that they contained sea spike signals and were recorded at depression angles greater than 3°.

the raised noise floor was to reduce the confidence in these results such that they were not beneficial to include.

The files which fitted these criteria are listed in Table 7.1. A total of 31 data files were used in this analysis, where the exact selections used for each set of results are shown in Sections 7.2 and 7.3.

Nominal γ [°]	Edge, γ [°]	Edge, R [m]
5	4.5	24.22
	5.5	19.82
6	6.5	16.78
	7.5	14.56
7	8.5	12.85
	9.5	11.51
8	10.5	10.43
	11.5	9.53
9		
10		
11		

Table 7.2: Grazing angle swath values used to segment the data. Swaths of 1° were chosen resulting in the edge values shown, where the corresponding slant range values were calculated using Eq. 2.15 and a radar axis height of 1.9 m.

7.1.2 Data pre-processing

Each data file was pre-processed to remove corrupted chirps and any RSS signal. The identification of corrupted chirps used the fact that the noise floor beyond the anti-aliasing filter roll-off was significantly raised as shown in Fig. 6.11 at ranges greater than ∼30 m. A simple threshold of −90 dBm on the mean decibel level between the ranges of 30 to 60 m was used to distinguish the corrupted chirps, for which every range bin was replaced with 'NaN'. The removal of RSS regions from the data required manual identification of the range and chirp indices which were to be replaced with 'NaN', which were then stored in a table and applied to each relevant file during processing.

7.1.3 Grazing angle segmentation

To control for grazing angle, each run of data was segmented in range. Each range swath corresponded to a 1° increment in grazing angle, centred on a whole number such that the edges of the grazing angle bin at e.g. 5° were 4.5° and 5.5°. The nominal grazing angle γ and the swath edges both in terms of the grazing angle and slant range R are shown in Table 7.2 for the nominal radar axis height of 1.9 m. The slant range values were calculated using Eq. 2.15. To select the swaths for each depression angle, the range values were mapped to range bin indices, where adjacent swaths were selected such that they were contiguous but non-overlapping.

A grazing swath size of 1° was chosen as this minimised off-boresight loss in gain across the swath when the grazing angle matched the depression angle of the radar, and tried to ensure that enough signal samples were included in the swath. Since the off-boresight loss in gain would later map to an increased uncertainty in the CCDF curves, as explained in Subsection 7.1.6, it made sense to reduce this as much as

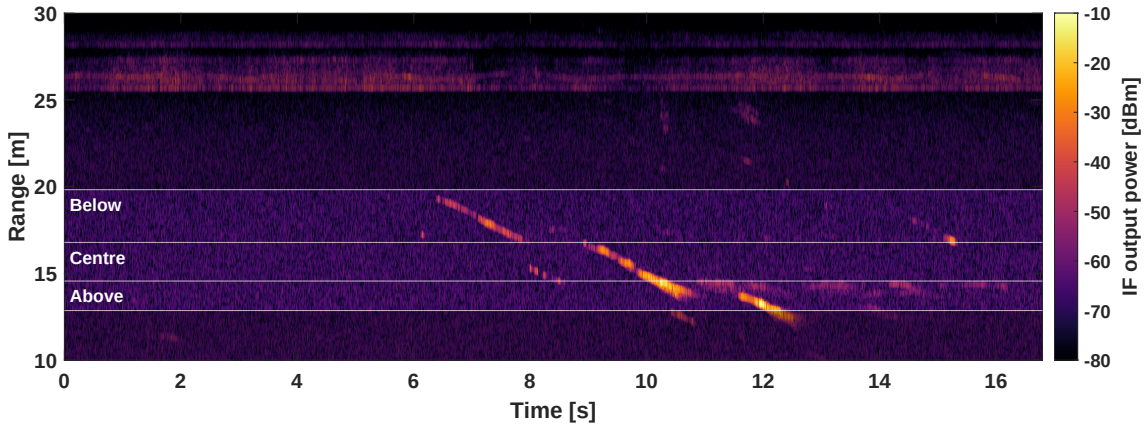

(a) $\delta = 7°$.

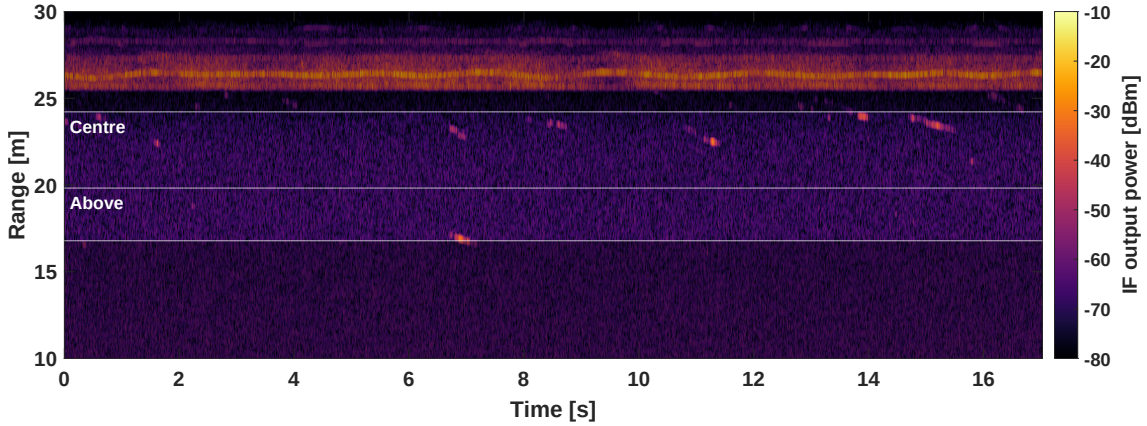

(b) $\delta = 5°$.

Figure 7.1: Example RTI plots at $\delta = 7°$ and $\delta = 5°$ showing the segmentation of the data by grazing angle in each case, where the swaths of interest 'centre', 'above', and 'below' have been labelled.

possible. These swath sizes were additionally narrow enough such that a swath on either side of the boresight swath (e.g. for data collected at a depression angle of 7°, this refers to swaths centred at 6° and 8°) could generally be included in the analysis without incurring a punitive level of uncertainty in the CCDF curves. This made use of more of the data than simply selecting the centre swath. A swath size of 1° also placed the lower edge for swath 5° at $\gamma = 4.5°$ and thus avoided exceeding the edge of the tank at ~25 m.

Each run was then segmented into a 'centre', 'above', and 'below' swath as shown in Fig. 7.1, with the exception of data from a depression angle of $\delta = 5°$ where the below swath would have exceeded the edge of the pool.

7.1.4 CCDF processing

As mentioned above, a CCDF or probability of false alarm $\mathbb{P}_{\text{fa}}$ curve is a way of representing the amplitude distribution seen in the data. The rationale for using this type of plot in this case is to better facilitate the comparison of data from different conditions:

- A histogram is a natural way to represent the same data, however multiple overlapping histograms can quickly become difficult to compare. In this case a cumulative distribution function (CDF) reduces the information to a single curve, where groups of these are easier to show on a single plot.
- By using the CCDF instead of the CDF, this is then a representation of the $\mathbb{P}_{\text{fa}}$, a commonly used detection scheme metric.

Normalising the CCDF curves with respect to total number of samples and the mean level also facilitates easier comparison of the data. Mathematically the first of these steps is expressed in Eq. 7.1, giving the histogram of intensity *probabilities* H_{p}:

$$H_{\text{p}} = \frac{1}{N_{\text{s,H}}} H(q) \tag{7.1}$$

for a histogram of intensity samples $H(q)$ and number of samples in the histogram $N_{\text{s,H}}$. The second step requires shifting the mean value to 0. This is shown in Eq. 7.2:

$$\tilde{H}(q) = H_{\text{p}}(q - \langle q \rangle) \longrightarrow \tilde{H}(\alpha) \tag{7.2}$$

for the fully normalised histogram $\tilde{H}(q)$, where the intensity variable maps to the normalised threshold α by subtracting the mean intensity $\langle q \rangle$ from each intensity value, to finally give the fully normalised histogram as a function of the normalised threshold $\tilde{H}(\alpha)$. Using the normalised threshold allows for comparison between different radar systems and different carrier frequencies.

To calculate the CCDF of this function, a sum of all the values from a threshold level of α to infinity is calculated, as in Eq. 7.3:

$$\text{CCDF} = \sum_{x=\alpha}^{\infty} \tilde{H}(x) \tag{7.3}$$

using a dummy variable x. As the CCDF takes a wide range of values and the top end values of low probability are of specific interest in this analysis, the $\log_{10}$(CCDF) is generally plotted to better represent this visually. The effects of the different stages of normalisation on the resulting CCDF curves are shown in Fig. 7.2.

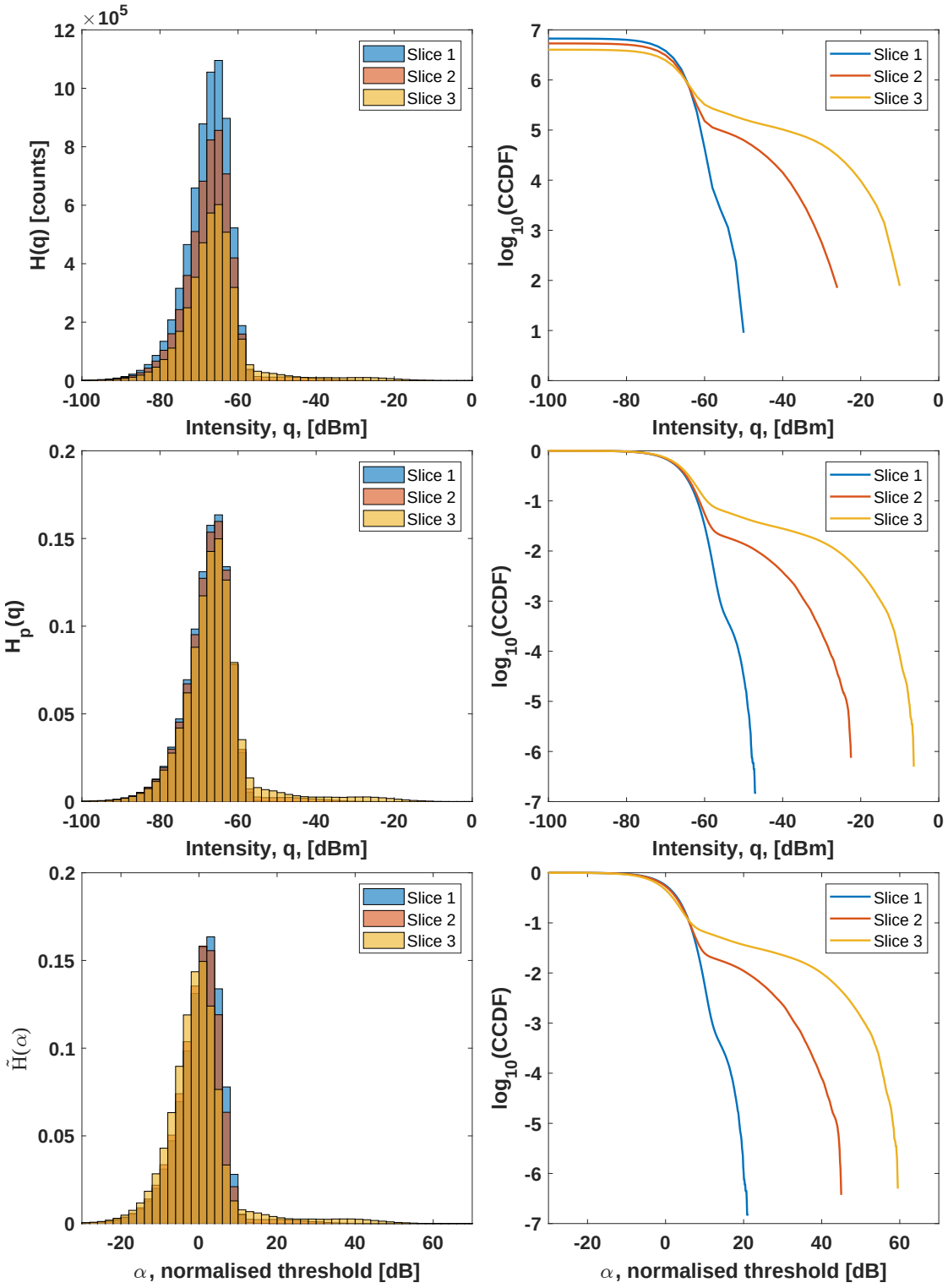

Figure 7.2: Stages of CCDF processing, showing the effects of each normalisation stage: before normalisation (top), data normalised by number of samples according to Eq. 7.1 (middle), data normalised by both the number of samples, and by mean intensity according to Eq. 7.2 (bottom). The slices of data are for demonstration only, coming from a single 'centre' range swath and containing variable numbers of samples from non-overlapping time periods where differing levels of scattering were observed.

The threshold normalisation step in Eq. 7.2 must be carried out with an **arithmetic mean with respect to the axis scale to properly align the curves in terms of threshold**. This means that since the abscissa of the plots is represented in a decibel scale (to better show the wide dynamic range of amplitudes), the normalisation is carried out with respect to the arithmetic mean of the decibel power values, i.e. the geometric mean of the linear power values. This is to specifically preserve the alignment property which means the curves all cross the ordinate at approximately the same point, whereas normalising by the arithmetic mean of the linear powers converted to decibels does not provide this functionality when the curves are plotted with a decibel scale abscissa. If the plots instead used a linear power scale, then the alignment would be achieved with the arithmetic mean of the linear powers.

The step in Eq. 7.2 is often referred to in literature as shifting the mean value to unity. Since this terminology is potentially confusing, as it does not specify the scale nor make the distinction that the normalisation should be carried out with respect to the axis scale, this is clarified here. The author believes this term expresses the process as it would be in linear powers, and this is equivalent in the decibel scale to a mean of zero as shown above.

The result of using the arithmetic mean of the decibel values is that the specific value produced is of less standard utility, however for the purposes of these plots this is not necessarily a drawback. After choosing a normalised threshold α, the absolute threshold intensity, q_t, can be recovered by the addition of the same mean value as shown in Eq. 7.4:

$$q_t = \alpha + \langle q \rangle \tag{7.4}$$

where the absolute threshold is then again in units of decibels referenced to power (in this case milliwatts).

7.1.5 NRCS processing

Calculating the NRCS for a given received power value is discussed in Subsection 2.1.9. The processing requires corrections for the effects of the radar range calibration as modelled by Eq. 2.16, the beam footprint area shown in Eq. 2.44, and the two-way antenna beam pattern of the radar, derived from the one-way measurement shown in Fig. 5.8. Since the level of each factor which is applied to each range cell has a slant range dependence, they are also dependent on the radar height and depression angle as shown in Eq. 2.15.

For measurements of sea clutter made at lower frequencies, the NRCS is generally

calculated from a section of the data without any further steps. For the results in this thesis, the data is first thresholded to remove noise, and then the NRCS is calculated. This is because in this data, the clutter signals are very sparse i.e. most of the data samples consist of noise. The signal presents itself in this way for several reasons which differ from lower frequency systems:

- The range resolution is very fine (7.5 cm).
- The noise floor is relatively high.
- The backscatter from the sea at this frequency appears to be less smoothly distributed.

As a result, treating the data in the same way as for lower frequencies is less appropriate. Thresholding preserves a greater level of detail for the results which would otherwise be diluted by a comparatively large number of noise samples, and would consequently be very similar to each other and to the noise level. This approach gives a more accurate representation of the signal intensities which were measured, with confidence above the noise threshold. To remove the noise, a threshold level which reduces the probability of detection of noise to 10^{-4} is calculated for the corresponding grazing angle swath using Eq. 7.4. This threshold was chosen such that most of the noise was excluded. The results from this processing should then be more properly considered to be a measurement of the mean NRCS of the clutter spikes.

The correction factor for each range bin was calculated at the mid-point of the bin to avoid under- or over-estimation. The applied total correction factors and their components as a function of range are shown in Fig. 7.3. These plots were produced for both polarisations and the different depression angles at which the measurements were made, and with a radar axis height of 1.9 m as measured during the trial. The depression angle alters the projection of the beam pattern on to the ground plane, and similarly changes the ground range resolution length and hence the correction due to beam patch area, although the latter effect is negligible. Since the beam pattern is different in the E and H planes, there is a small difference between the corrections for HH and VV polarisation, although in the swaths of interest (as shown) the difference is small. For the beam pattern correction, the elevation beam pattern is selected for the polarisation where HH→H and VV→E. For the beam patch area, this depends on the azimuth pattern, and thus the choices for the polarisations are HH→E and VV→H.

7.1.6 CCDF error processing

The aim of the CCDF error processing method is to generate an estimated region of uncertainty associated with each plotted CCDF curve. This is achieved by applying

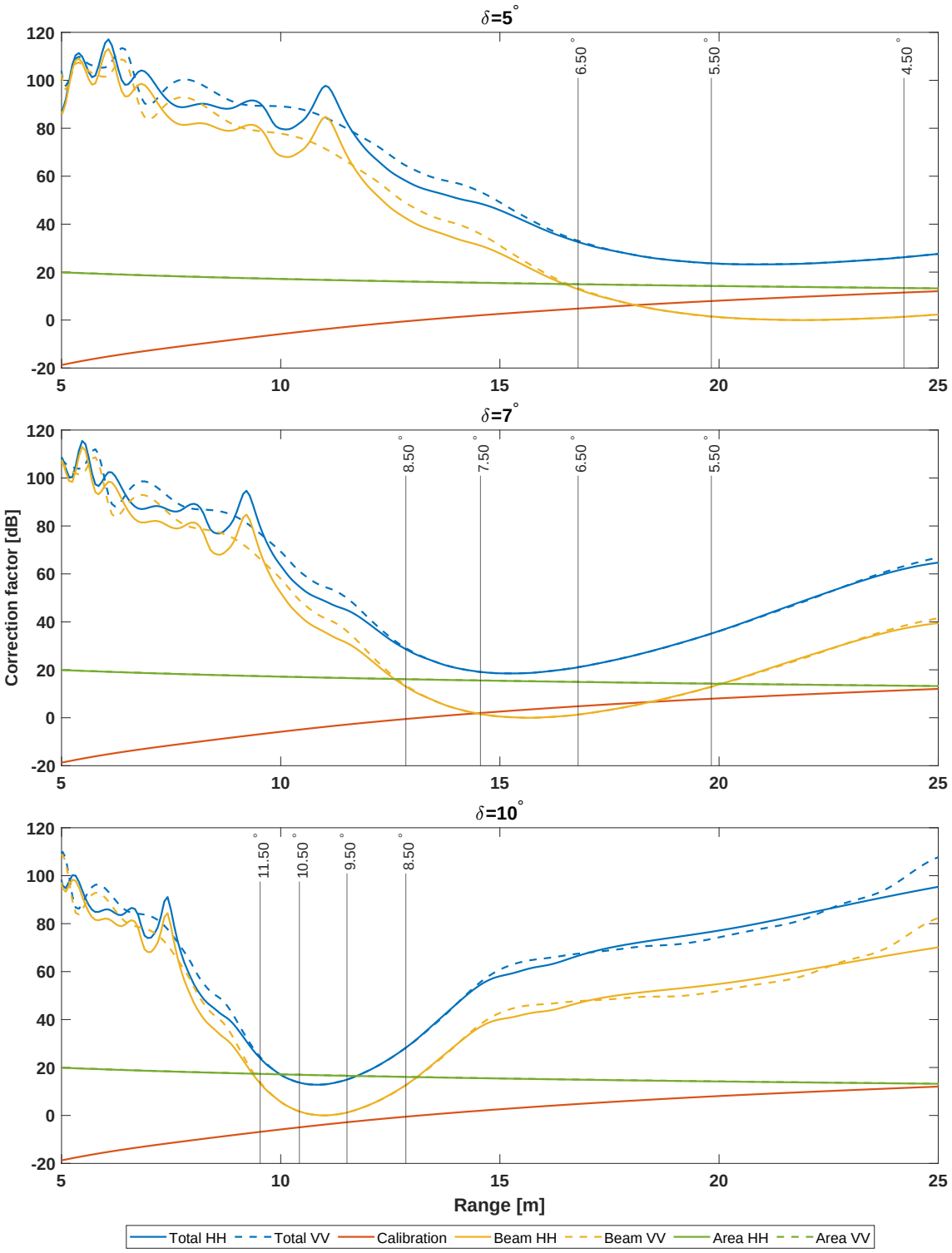

Figure 7.3: The correction factor components and combined totals used for normalising radar received power values to yield NRCS, as a function of range. The plots are generated for the different radar depression angles which alter the beam pattern and area corrections, and a consistent radar axis height of 1.9 m.

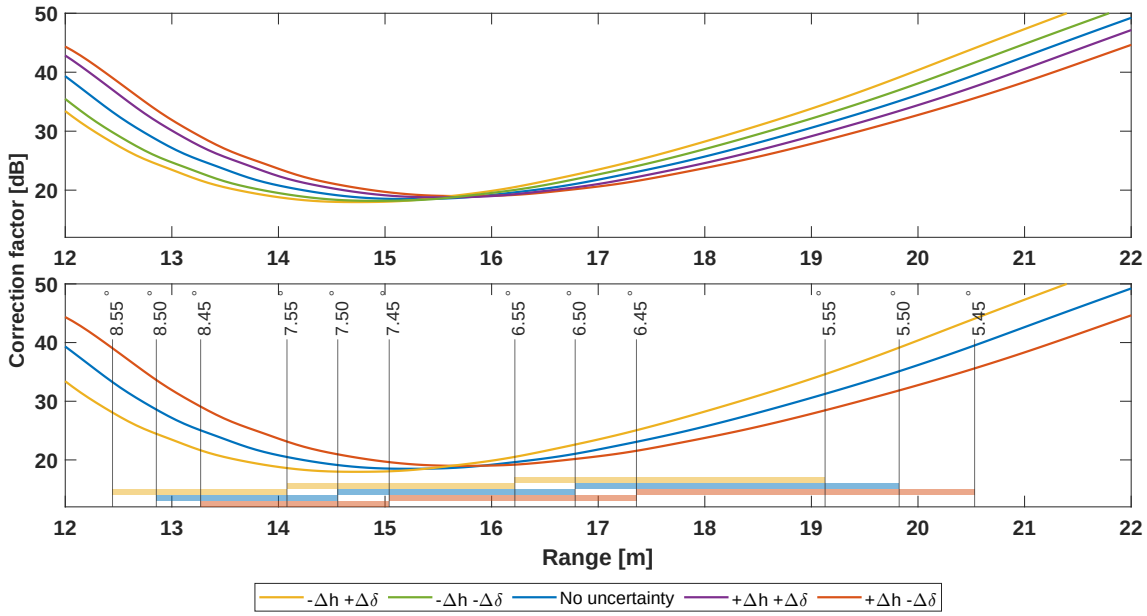

Figure 7.4: The total correction factor plotted as a function of range for different combinations of uncertainty in height, Δh, and uncertainty in depression angle $\Delta\delta$. The top graph shows all four possible combinations of the uncertainties as well as the curve without any uncertainties applied, for reference. The bottom graph shows the two cross combinations $+\Delta h - \Delta\delta$ and $-\Delta h + \Delta\delta$ which produce the most different results. On this plot the edges of the grazing angle swaths are indicated as an example, where the exact swath changes slightly when accounting for the combinations of uncertainties, and the swaths belonging to each combination are indicated by the coloured bars.

the NRCS corrections to a swath before running the CCDF processing again. The corrections which are applied also take into account the uncertainties in radar height and depression angle which change the value as explained in Subsection 7.1.5.

The nominal curve itself is not additionally processed beyond what is discussed in Subsection 7.1.4 (i.e. no NRCS corrections are applied). This is so that the shape of the noise floor distribution remains undistorted, and also preserves the physical interpretation of the CCDF curves as the probability of false alarm versus threshold level. Furthermore, since in the error processing method detailed here the corrections are applied agnostic of whether a sample is signal or noise, this would have the unwanted effect on the nominal curve of shifting some noise samples into what would have been previously interpreted only as signal, thus contaminating the signal distribution with noise samples, and vice versa.

The uncertainty regions are thus limited to the use of giving an indication of how the distribution may change after accounting for the effects of errors, range, antenna pattern and so on. They no longer correspond to the probability of false alarm curve for the individual radar used to make the measurement, unlike the nominal curve.

For the purposes of determining the uncertainty regions, it was sufficient to determine which uncertainty combinations would produce the maximum and minimum effect, or the effects which differed by the greatest degree, since this would then define the edges of the region. Figure 7.4 was used to determine these combinations, where the plot shows the total correction factor as a function of range for a nominal height of $h = 1.9$ m and depression angle $\delta = 7°$, and also with the four different combinations of the uncertainties in these values. These were estimated to be $\Delta h = 5$ cm and $\Delta\delta = 0.05°$.

Figure 7.4 shows that the greatest difference between correction factors is produced when using the cross combinations of the two uncertainties, $+\Delta h - \Delta\delta$ and $-\Delta h + \Delta\delta$, named combination 1 and 2 respectively. It is also noted that the swath ranges being analysed change somewhat according to the uncertainties in height and depression angle. For example, considering the grazing angle swath centred on 6°, where this runs from 5.5° to 6.5° (covering the range of the left-most blue bar), which in range is ∼3 m. The shift between this swath and the $-\Delta\delta$ swath running from 5.45° to 6.45° (the left-most red bar) is ∼0.7 m, thus the shift is ∼20% of the entire swath. This increases the variability of the uncertainty regions relative to the nominal curve since there is a change in some of the signal samples being processed, as well as the correction factor which is applied.

For the processing of errors, the corrections for each cross combination are applied to the data and then CCDF processed to generate the estimated uncertainty region. The uncertainty region is then plotted by finding the maximum and minimum CCDF value at each normalised threshold increment of the two uncertainty curves together with the nominal curve. These maximum and minimum values then define the edge of the uncertainty region.

7.1.7 NRCS error processing

The full data processing chain is summarised graphically in Fig. 7.5, including the final step of estimating the errors associated with the calculated NRCS values. To do this, the same uncertainty combinations which were identified as producing the maximally different results as shown in Fig. 7.4 were used. The correction curves resulting from combinations 1 and 2 were then applied separately to the data, such that each swath had a triplet of NRCS values associated with it: the NRCS calculated using the correction curve not influenced by uncertainties, and the NRCS values resulting from using the curves produced by combinations 1 and 2.

To generate the error bars from these values, the centre value was first calculated as the average of all three, with the error bars then determined as the maximum

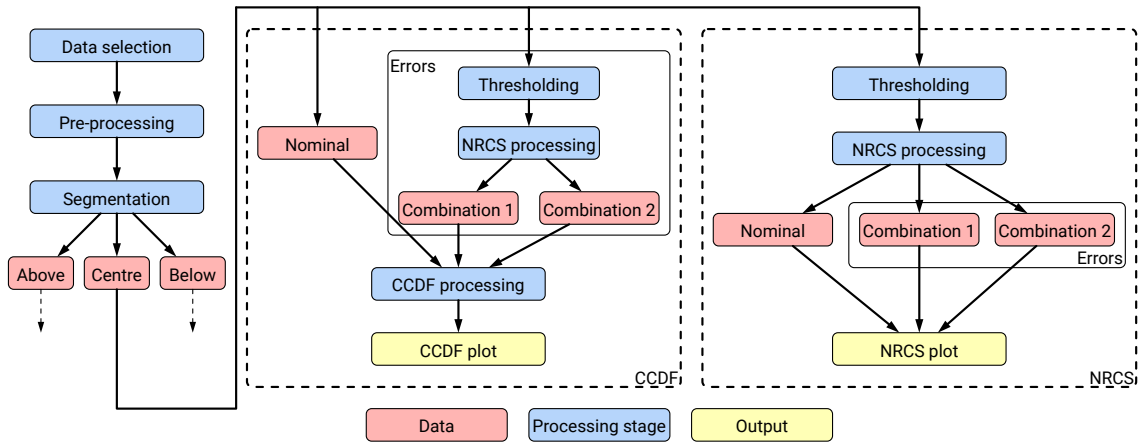

Figure 7.5: Summary diagram of the data processing chain.

and minimum values in the triplet. In the case where NRCS measurements from different runs were averaged together, the centre value was similarly calculated by averaging all the values. The error bars were determined by first averaging separately the centre values, the values from combination 1, and the values from combination 2. The maximum and minimum from these three results were then used to define the error bars. All averages during this process were calculated as arithmetic means of linear power values.

7.2 CCDF results

This section presents the results of the analysis investigating the amplitude distribution of 207 GHz sea clutter. The distributions are examined as a function of the four measurement parameters during the FloWave trial: wave direction, wave height, grazing angle, and polarisation. Each subsection presents a list of which measurements were analysed to produce the relevant plots, and a description of the results that these show. The section ends with a summary on the trends observed in the data, where these are discussed further in Section 7.4.

7.2.1 Processed noise floor data

To provide a baseline for comparison, pure noise floor data from the trial was processed in the same way as would later be done for data with scattering signals but without thresholding. Since the noise floor was not completely flat as a function of range and the processing for different grazing angle values considered different range swaths, the noise floor was processed individually for each of these conditions. Since data were collected at depression angles of 5°, 7°, and 10°, the processing of noise floor data at

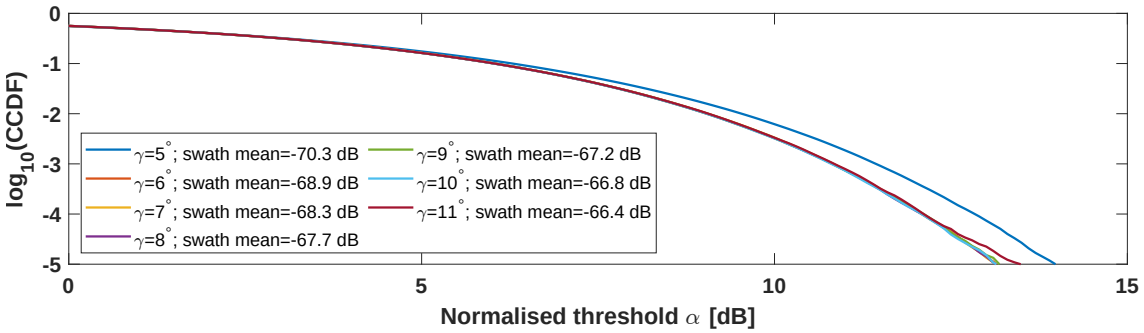

Figure 7.6: CCDF plots of the noise floor at each grazing angle swath. The curves are all very similar since the noise floor distribution is mostly unchanging as a function of range, apart from $\gamma = 5°$ where the signal distribution is skewed due to the anti-aliasing filter roll-off. The geometric mean values used for the threshold normalisation are also shown in the plot, where the variation is due to the slope of the noise floor.

the matching grazing angles was performed on-boresight, whereas at other angles this was treated as off-boresight to account for the change in antenna gain which would be observed when processing clutter signals collected under these conditions.

The CCDF curves (without uncertainty regions) for each swath of noise floor data are shown in Fig. 7.6. In keeping with the method as discussed in Subsection 7.1.4, the legend values show the **geometric mean noise level** of each swath such that normalised threshold values may be converted to absolute threshold levels. From these values the decrease in noise floor level with increasing range (decreasing grazing angle) may be observed. All the CCDF curves appear tightly clustered except for the curve for swath $\gamma = 5°$, which differs by 0.8 dB at a $\log_{10}(\text{CCDF}) = -5$. The reason for this is that the distribution of the noise in each swath is very similar, apart from at $\gamma = 5°$ since at this range the anti-aliasing filter begins to attenuate the IF signal resulting in a skewed distribution. This pushes the CCDF curve to a higher threshold value since even though the mean level is in fact reduced, the distribution becomes wider. The CCDF curves are all however very similar at a high $\log_{10}(\text{CCDF})$ as the change in distribution caused by the filter is still minor at this range. The difference between the curves is magnified here to illustrate the effect by the use of a shorter scale for the normalised threshold.

Figure 7.7 shows the CCDF curves with uncertainty regions for each swath. The uncertainty for each curve is negligible, again apart from $\gamma = 5°$ where this is seen to be 1.5 dB at $\log_{10}(\text{CCDF}) = -5$. Similarly the reason for this is that the distribution at this range is changing because of the filter roll-off. Due to the slight shift in the range bins being analysed because of the uncertainty in depression angle and radar height, the change in distribution for $\gamma = 5°$ is variable and generates the larger spread in possible $\log_{10}(\text{CCDF})$ values at a given threshold level than is observed for the other

curves.

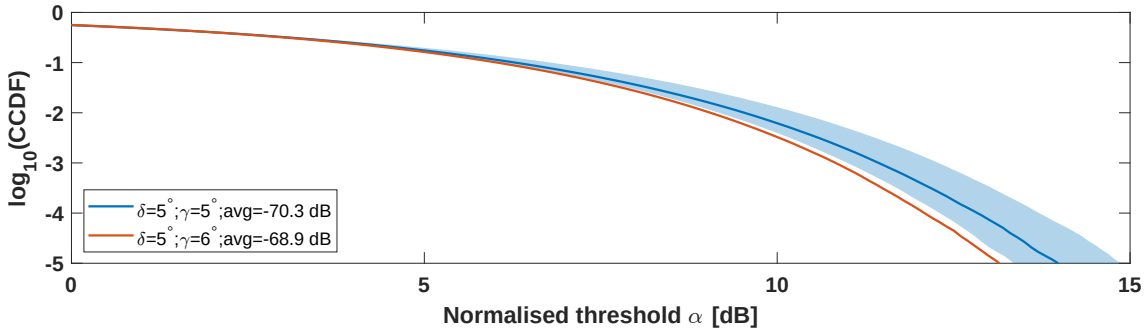

(a) $\delta = 5°$.

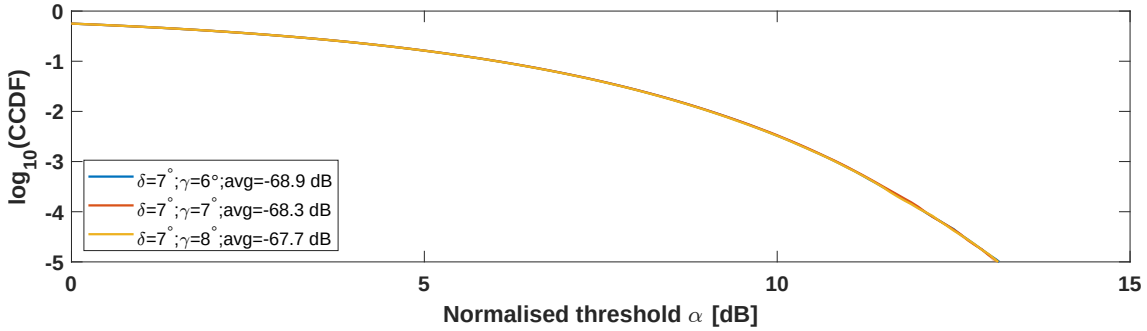

(b) $\delta = 7°$.

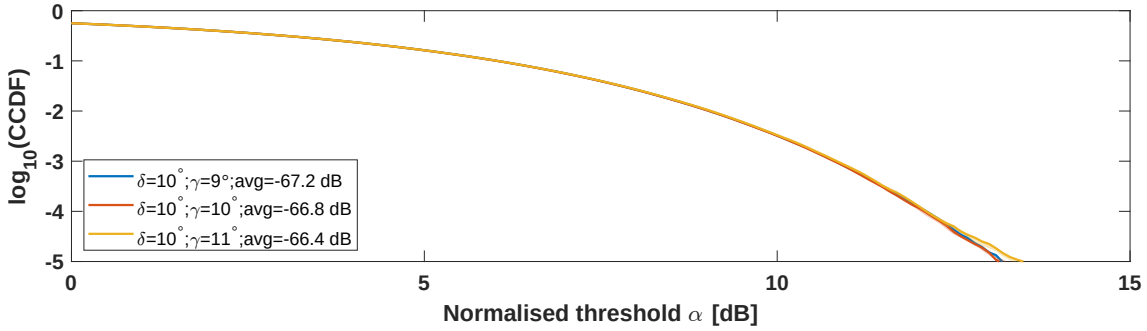

(c) $\delta = 10°$.

Figure 7.7: CCDF plots of the radar noise floor including uncertainty regions, processed for $\delta = 5°$, $\delta = 7°$, and $\delta = 10°$. In each case, the sizes of the uncertainty regions are negligible and generally similar for both the boresight swath and the neighbouring swaths, apart from at $\gamma = 5°$ where the changing slope of the anti-aliasing filter at this range causes a broadening of the uncertainty region.

7.2.2 Wave direction

Number	Time stamp	Duration [s]	Pol.	$H_{1/3}$[m]	ψ[°]	δ[°]	γ[°]
Figure 7.8a							
22	$11-46-27$	36.29	VV	0.3	0	5	6
23	$11-47-52$	18.18	VV	0.3	0	5	6
24	$11-48-30$	19.72	VV	0.3	0	5	6
25	$11-50-33$	18.92	VV	0.3	0	7	6
28	$11-59-10$	18.85	VV	0.3	45	5	6
29	$11-59-50$	19.70	VV	0.3	45	5	6
31	$12-24-45$	18.30	VV	0.3	180	5	6
Figure 7.8b							
27	$11-54-00$	18.25	VV	0.3	0	10	9
30	$12-06-27$	18.87	VV	0.3	90	10	9
Figure 7.9a							
12	$10-11-40$	16.82	HH	0.3	0	10	9
14	$10-40-12$	9.35	HH	0.3	135	10	9
Figure 7.9b							
12	$10-11-40$	16.82	HH	0.3	0	10	10
14	$10-40-12$	9.35	HH	0.3	135	10	10
Figure 7.9c							
12	$10-11-40$	16.82	HH	0.3	0	10	11
14	$10-40-12$	9.35	HH	0.3	135	10	11

Table 7.3: Data used for the wave direction analysis.

The data used for the wave direction analysis are shown in Table 7.3. CCDF curves of VV polarised data with wave directions of either $\psi = 0°$, $\psi = 45°$, and $\psi = 180°$ are shown in Fig. 7.8a at a grazing angle of 6°, and of wave directions $\psi = 0°$ and $\psi = 90°$ at a grazing angle of 9° in Fig. 7.8b, the latter matching the RTI data shown in Fig. 6.16. Figure 7.9 shows curves for wave directions of 0° and 135° in HH polarisation at grazing angles of 9°, 10°, and 11°, with the 135° wave direction data matching Fig. 6.15. The selection of data is limited due to the low number of runs exhibiting any clutter signal for wave directions other than $\psi = 0°$. Additionally, all the curves are for data with a $H_{1/3} = 0.3$ m for the same reason. As discussed in Subsection 6.2.6.3, this shows that the incidence of clutter is in general highly sensitive to wave direction and greatly suppressed for non-approaching waves.

In Fig. 7.8, both of the VV polarisation plots show that the spikiness of the distribution decreased as the wave direction angle was increased. This pairs well with the observations made in the qualitative analysis in Subsection 6.2.6.3, as the level and

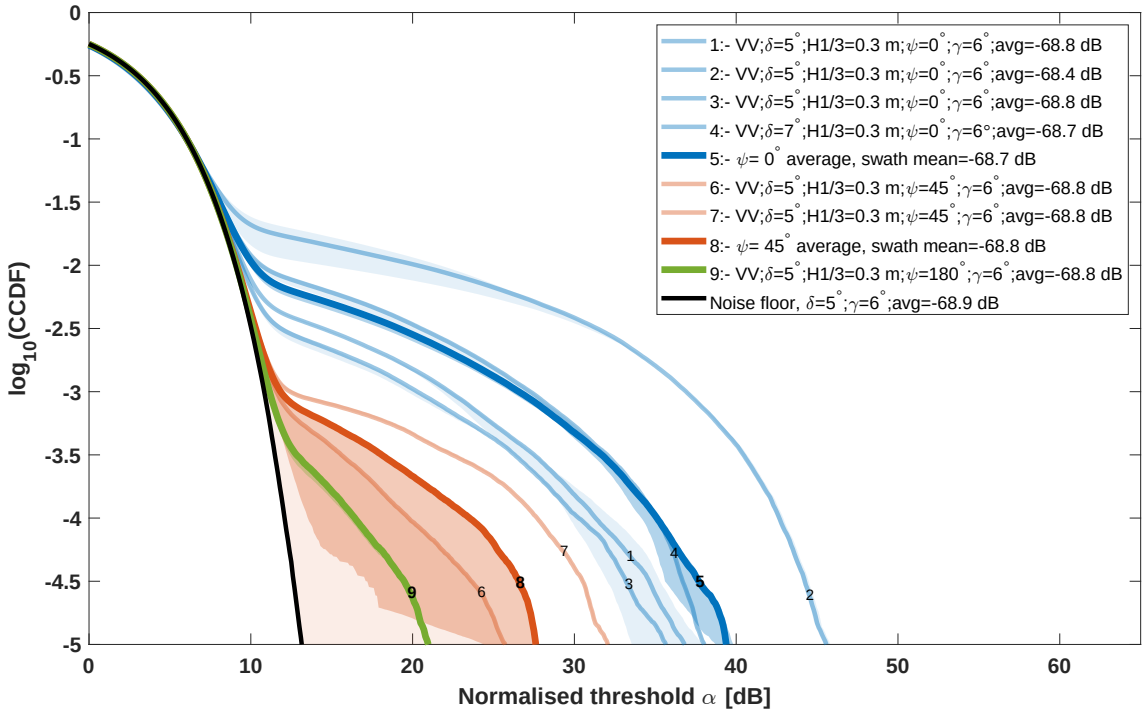

(a) $\gamma = 6°$.

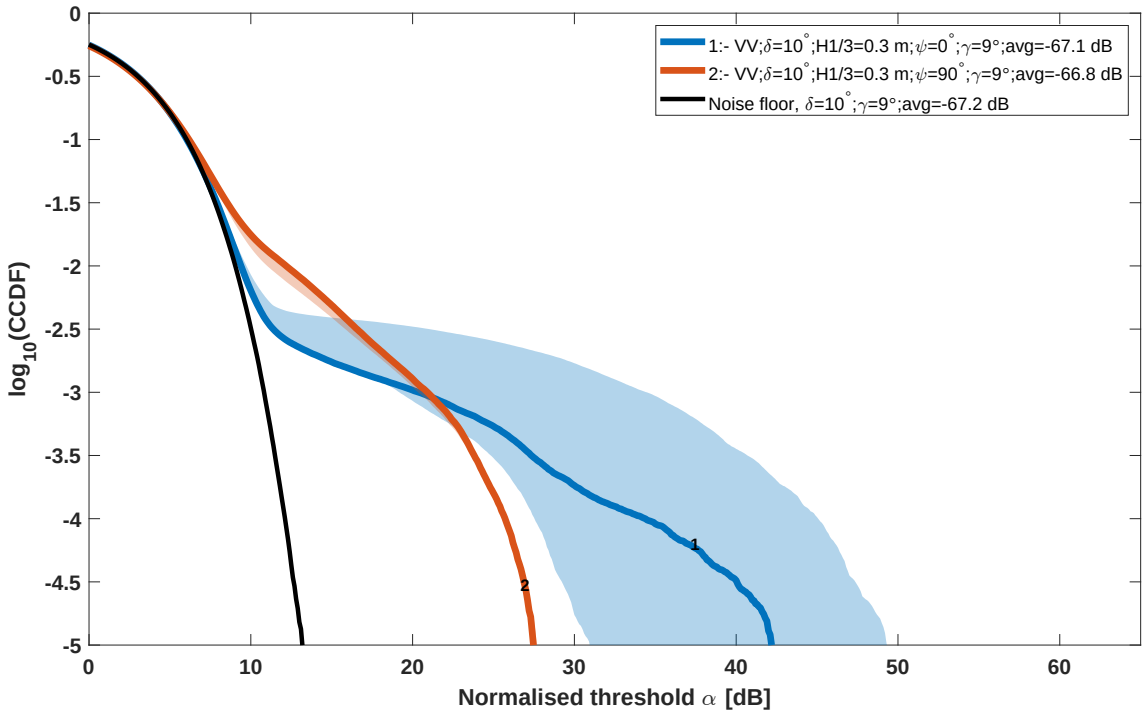

(b) $\gamma = 9°$.

Figure 7.8: Plots of CCDF curves for VV polarised data from grazing angle swaths at either a γ of 6° for wave direction angles of 0°, 45°, and 180°; or 9°, for wave direction angles of 0° and 90°. Results at both grazing angles indicate that the amplitude distribution becomes less spiky with increasing wave direction angle.

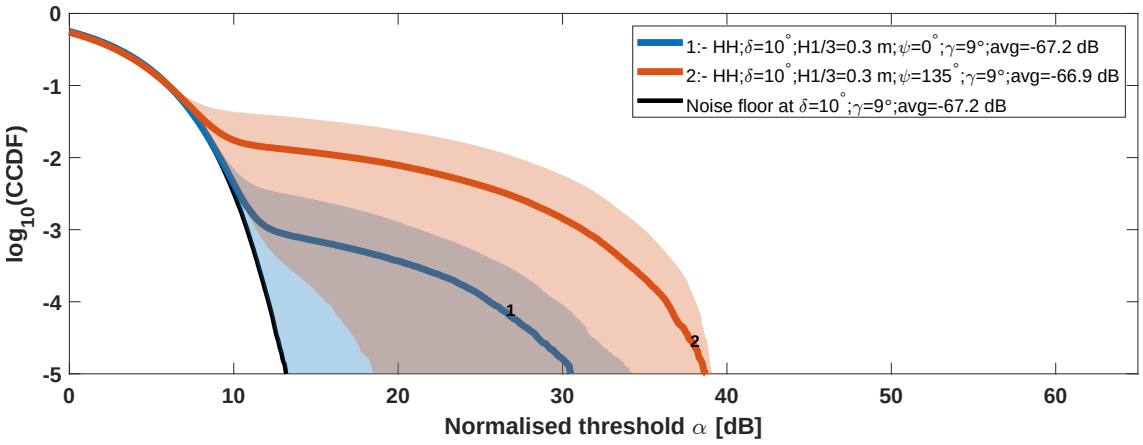

(a) $\gamma = 9°$.

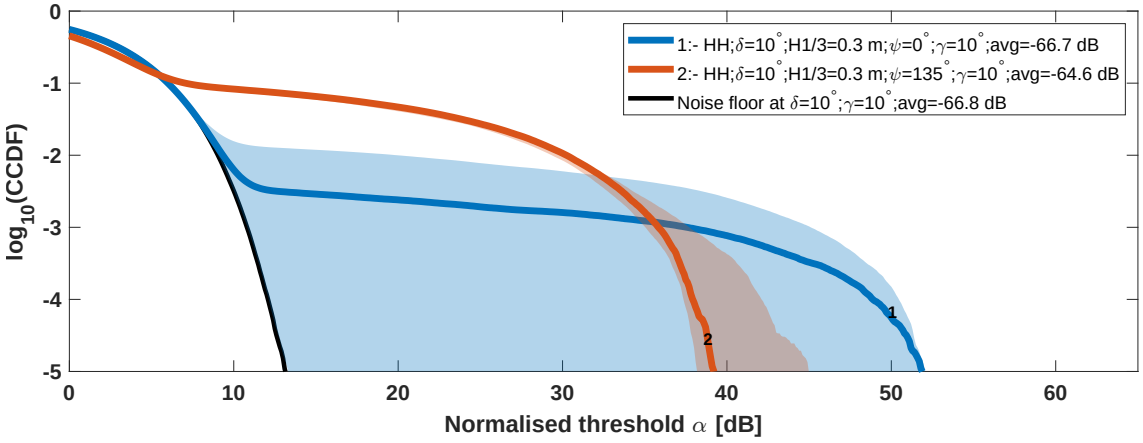

(b) $\gamma = 10°$.

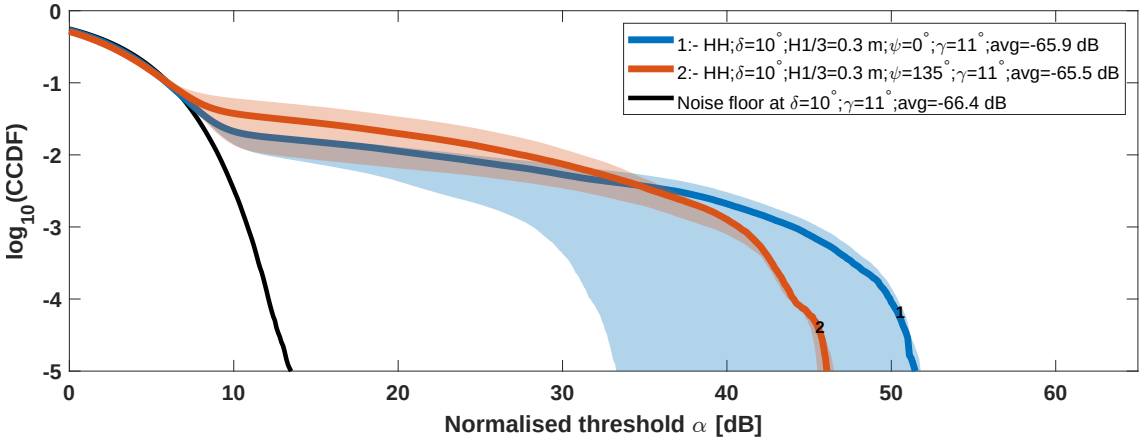

(c) $\gamma = 11°$.

Figure 7.9: Plots of CCDF curves at wave directions of 0° and 135° for HH polarised data at grazing angles of 9°, 10°, and 11°. The trend of the amplitude distribution as a function of wave direction in this data is inconclusive across the grazing angles observed.

frequency of occurrence of clutter events for wave directions other than 0° were greatly reduced, and so the CCDF curves would tend towards the noise floor baseline.

The three plots in Fig. 7.9 show somewhat inconsistent and uncertain results for HH polarisation. The expected trend of spikier data at $\psi = 0°$ is observed in Figures 7.9b and 7.9c, however the data at $\gamma = 10°$ is subject to a large uncertainty. When the uncertainty region is observed to stretch to the noise floor baseline, this indicates that the slight shift in range incurred by the uncertainties in depression angle and radar height results in a swath with no clutter and only noise. The slight deviation from the noise floor curve observed in Fig. 7.9b is due to the higher mean level of the data for that run, resulting in a larger negative shift along the threshold axis during normalisation.

Given that the HH data is seen to be generally spikier at $\psi = 0°$, the change in spikiness with wave direction in this polarisation could be expected to be more pronounced than for VV polarisation since burst scattering is likely to be fairly sensitive to the orientation of the wave fronts. This is however not conclusively observed from the limited dataset presented here and more data is required to determine the trend with certainty.

7.2.3 Wave height

The data used for the wave height analysis are listed in Table 7.4. Figures 7.10, 7.11, 7.12, and 7.13 show CCDF curves for HH polarised data at grazing angles of 5°, 6°, 7°, and 8°. VV polarised data is shown in Figures 7.14, 7.15, and 7.16 at grazing angles of 5°, 6°, and 7°. All the data shown is for a wave direction of 0°.

In general, the amplitude distributions tend to become more spiky as wave height increases, being as high as 15 dB when comparing $H_{1/3} = 0.1$ m and 0.3 m in HH polarisation, and as high as 20 dB for VV polarisation. This is the expected trend, since at the relatively low wave heights investigated during the trial the observation of scattering was noise-limited and the scattering intensity tended to increase with wave height, thus only widening the range of amplitudes observed and hence increasing the spikiness. Even in a non-noise limited case, this could reasonably be expected to be the result. The trend remains generally consistent for the range of grazing angles observed, and for both polarisations.

The large variation in the curves observed in some of the plots, such as ~25 dB in Fig. 7.11 for $H_{1/3} = 0.3$ m, reflects the highly variable nature of the data. The results from Figures 7.11 and 7.14 are inconclusive, however given the trend seen in the plots as a whole the confidence in the result that spikiness increases with wave height is high.

Number	Time stamp	Duration [s]	Pol.	$H_{1/3}$[m]	$\psi[^\circ]$	$\delta[^\circ]$	$\gamma[^\circ]$
Figure 7.10							
6	09 − 50 − 01	17.27	HH	0.2	0	5	5
7	09 − 50 − 42	17.79	HH	0.2	0	5	5
8	10 − 04 − 54	17.03	HH	0.3	0	5	5
9	10 − 05 − 43	15.71	HH	0.3	0	5	5
13	10 − 14 − 52	34.60	HH	0.3	0	5	5
Figure 7.11							
6	09 − 50 − 01	17.27	HH	0.2	0	5	6
7	09 − 50 − 42	17.79	HH	0.2	0	5	6
8	10 − 04 − 54	17.03	HH	0.3	0	5	6
9	10 − 05 − 43	15.71	HH	0.3	0	5	6
10	10 − 07 − 37	16.97	HH	0.3	0	7	6
11	10 − 08 − 22	16.80	HH	0.3	0	7	6
13	10 − 14 − 52	34.60	HH	0.3	0	5	6
Figure 7.12							
3	09 − 36 − 45	18.44	HH	0.1	0	7	7
4	09 − 37 − 29	17.83	HH	0.1	0	7	7
10	10 − 07 − 37	16.97	HH	0.3	0	7	7
11	10 − 08 − 22	16.80	HH	0.3	0	7	7
Figure 7.13							
3	09 − 36 − 45	18.44	HH	0.1	0	7	8
4	09 − 37 − 29	17.83	HH	0.1	0	7	8
11	10 − 08 − 22	16.80	HH	0.3	0	7	8
Figure 7.14							
15	11 − 15 − 36	17.20	VV	0.1	0	5	5
20	11 − 36 − 00	18.40	VV	0.2	0	5	5
21	11 − 36 − 46	20.20	VV	0.2	0	5	5
22	11 − 46 − 27	36.29	VV	0.3	0	5	5
23	11 − 47 − 52	18.18	VV	0.3	0	5	5
24	11 − 48 − 30	19.72	VV	0.3	0	5	5
Figure 7.15							
15	11 − 15 − 36	17.20	VV	0.1	0	5	6
16	11 − 17 − 37	6.76	VV	0.1	0	7	6
17	11 − 19 − 31	19.67	VV	0.1	0	7	6
19	11 − 29 − 41	18.52	VV	0.2	0	7	6
20	11 − 36 − 00	18.40	VV	0.2	0	5	6
21	11 − 36 − 46	20.20	VV	0.2	0	5	6
22	11 − 46 − 27	36.29	VV	0.3	0	5	6
23	11 − 47 − 52	18.18	VV	0.3	0	5	6
24	11 − 48 − 30	19.72	VV	0.3	0	5	6
25	11 − 50 − 33	18.92	VV	0.3	0	7	6
Figure 7.16							
16	11 − 17 − 37	6.76	VV	0.1	0	7	7
17	11 − 19 − 31	19.67	VV	0.1	0	7	7
19	11 − 29 − 41	18.52	VV	0.2	0	7	7

25	11 − 50 − 33	18.92	VV	0.3	0	7	7

Table 7.4: Data used for the wave height analysis.

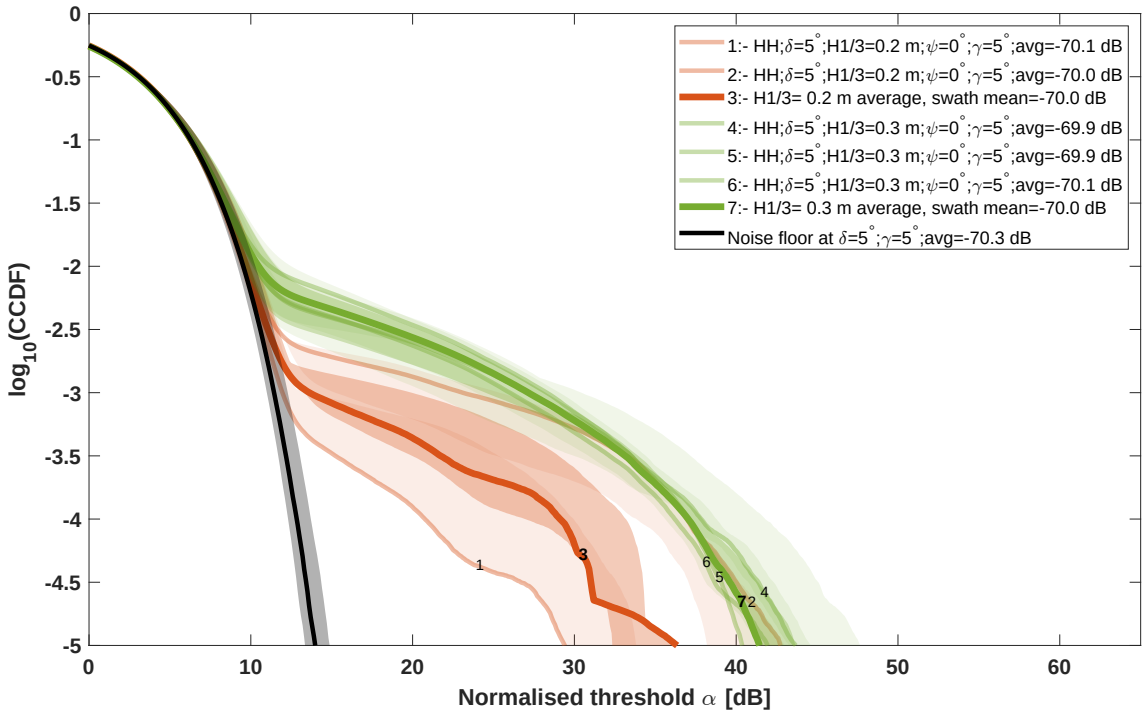

Figure 7.10: CCDF curves as a function of wave height, for $H_{1/3} = 0.2$ m and $H_{1/3} = 0.3$ m at $\gamma = 5°$ in HH polarisation.

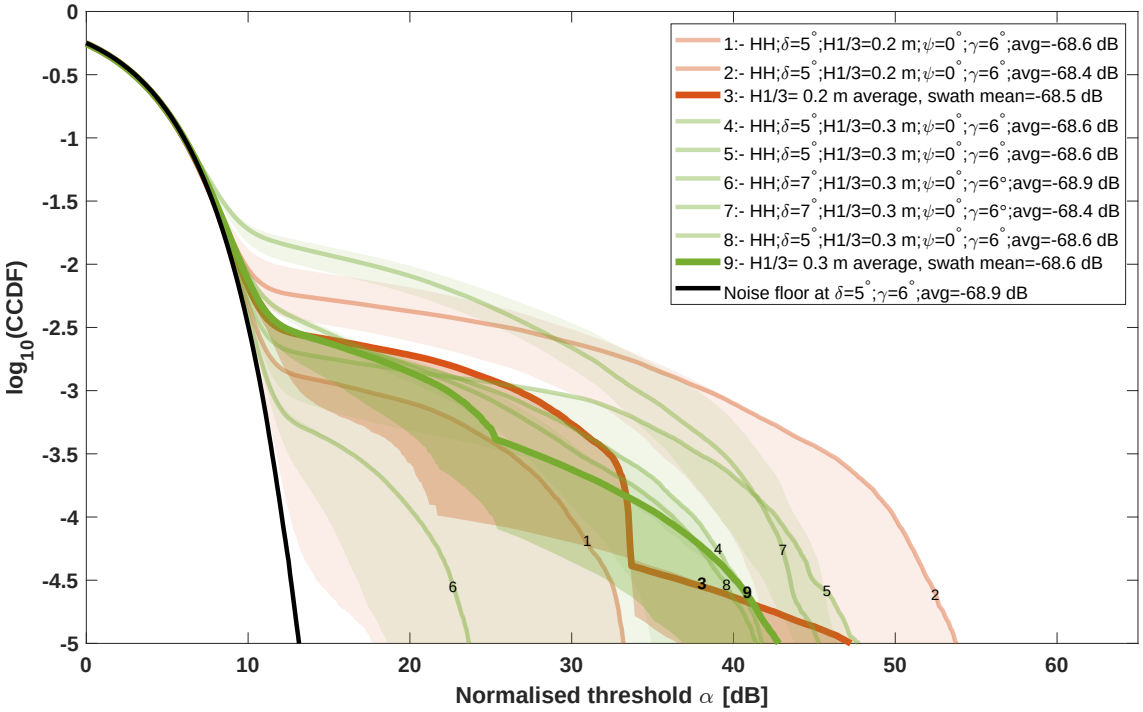

Figure 7.11: CCDF curves as a function of wave height, for $H_{1/3} = 0.2$ m and $H_{1/3} = 0.3$ m at $\gamma = 6°$ in HH polarisation.

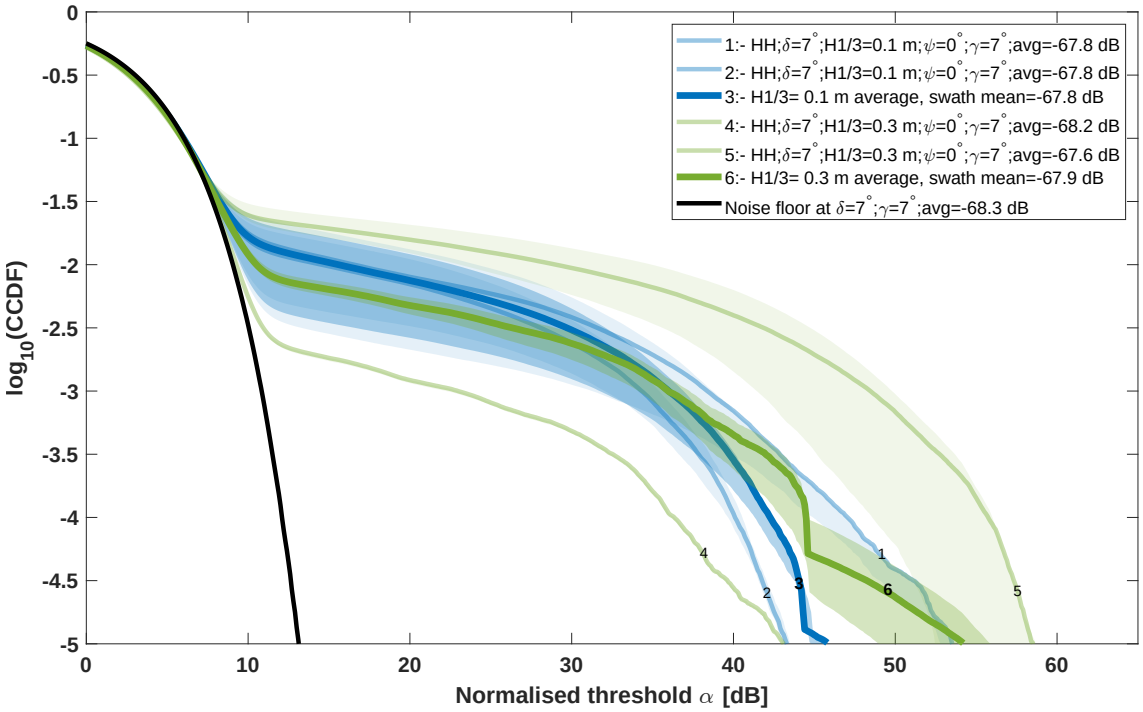

Figure 7.12: CCDF curves as a function of wave height, for $H_{1/3} = 0.1$ m and $H_{1/3} = 0.3$ m at $\gamma = 7°$ in HH polarisation.

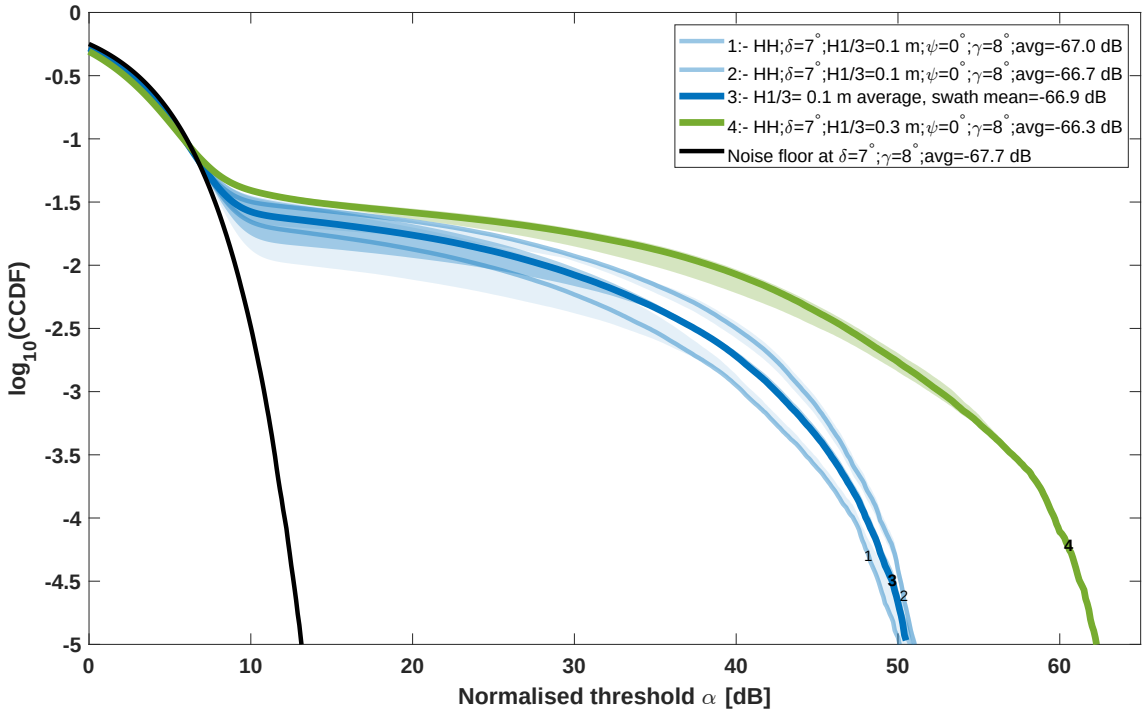

Figure 7.13: CCDF curves as a function of wave height, for $H_{1/3} = 0.1$ m and $H_{1/3} = 0.3$ m at $\gamma = 8°$ in HH polarisation.

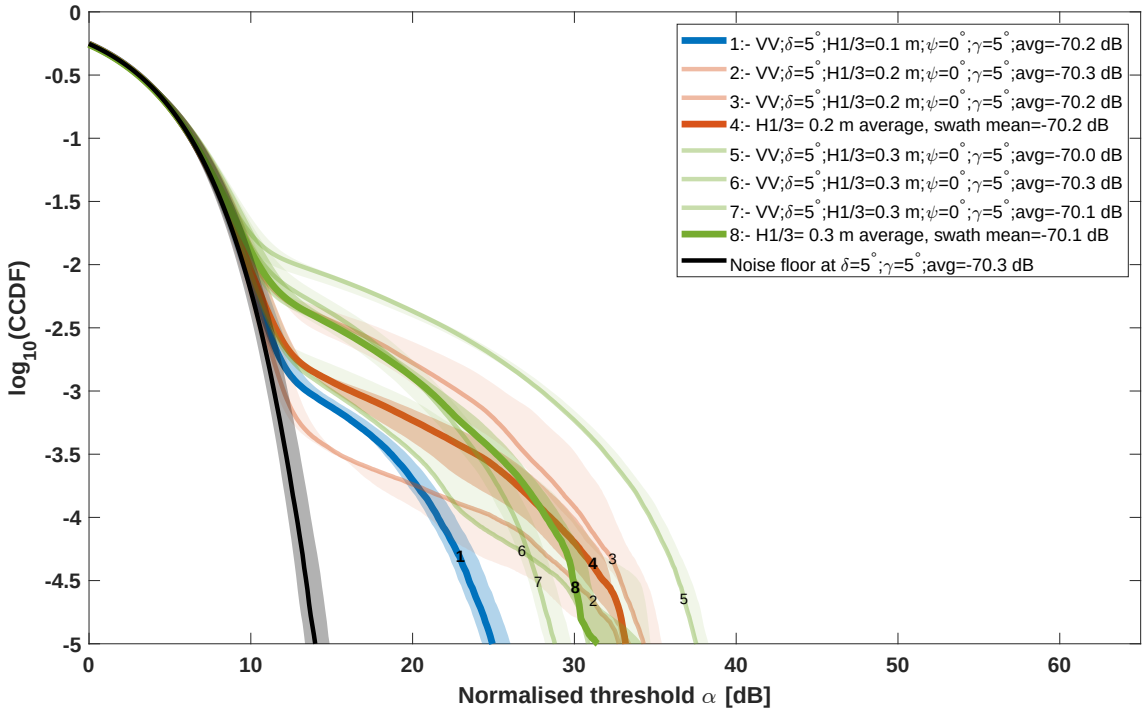

Figure 7.14: CCDF curves as a function of wave height, for $H_{1/3} = 0.1$ m, $H_{1/3} = 0.2$ m, and $H_{1/3} = 0.3$ m at $\gamma = 5°$ in VV polarisation.

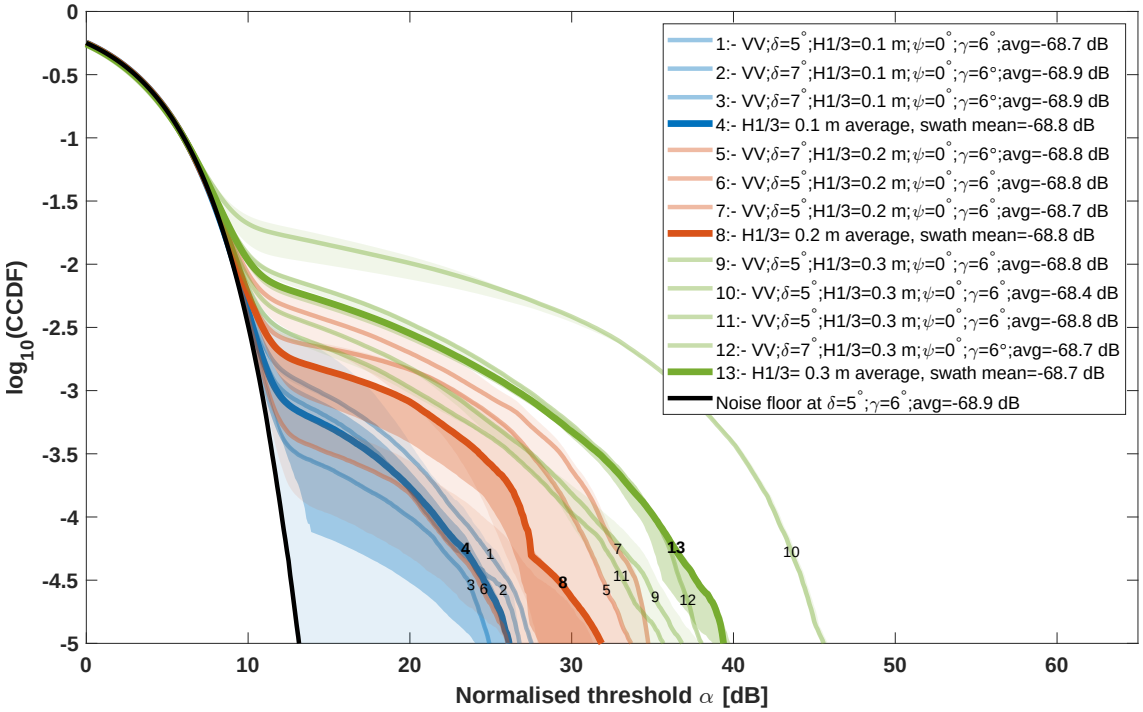

Figure 7.15: CCDF curves as a function of wave height, for $H_{1/3} = 0.1$ m, $H_{1/3} = 0.2$ m, and $H_{1/3} = 0.3$ m at $\gamma = 6°$ in VV polarisation.

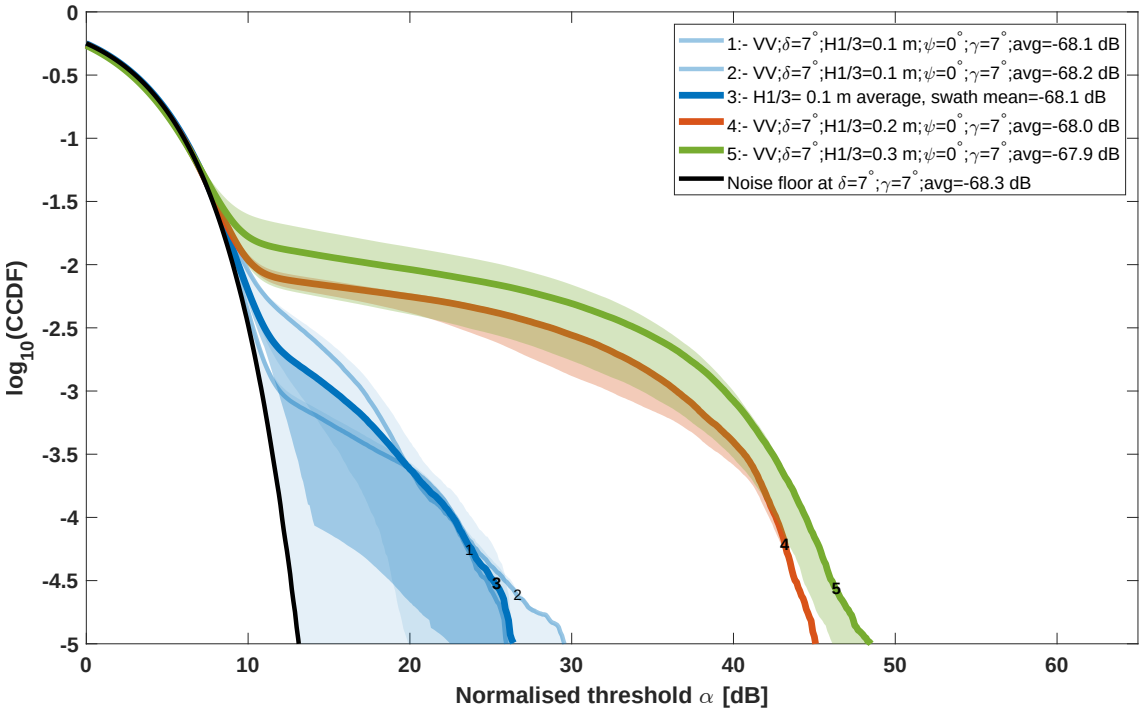

Figure 7.16: CCDF curves as a function of wave height, for $H_{1/3} = 0.1$ m, $H_{1/3} = 0.2$ m, and $H_{1/3} = 0.3$ m at $\gamma = 7°$ in VV polarisation.

7.2.4 Grazing angle

The data used in the grazing angle analysis is shown in Table 7.5. The plots shown in Figures 7.17 and 7.18 show CCDF curves as a function of grazing angle for $H_{1/3} = 0.3$ m in both HH and VV polarisation respectively. In each case, the data gathered at a depression angle of 10° is plotted separately (on identical axes) to show the results from 5° and 7° depression angles more clearly.

First considering the results from depression angles of 5° and 7°; in both polarisations, the overall trend observed is that the amplitude distribution becomes spikier with increasing grazing angle (results from $\gamma = 5°$ and $\gamma = 6°$ in Fig. 7.17 notwithstanding), and at the level where $\log_{10}(\text{CCDF}) = -5$ the threshold increases by ∼23 dB in HH and by ∼20 dB in VV between grazing angle values of 5° and 8°. The curves for $\gamma = 5°$ and $\gamma = 6°$ in HH polarisation are an outlier to the general trend and appear very close, where from this dataset no significant difference is seen. When inspecting the results from a depression angle of 10°, the results are less conclusive, however in each case these are drawn only from a single run of data in each polarisation. Given the large uncertainties for some of these curves, and the departure from trends seen from the larger body of evidence at depression angles of 5° and 7°, the confidence in these results is lower. The conservative conclusion is then that the amplitude distribution becomes spikier with increasing grazing angles in the range of 5° to 8°, where beyond this the trend is uncertain from this data.

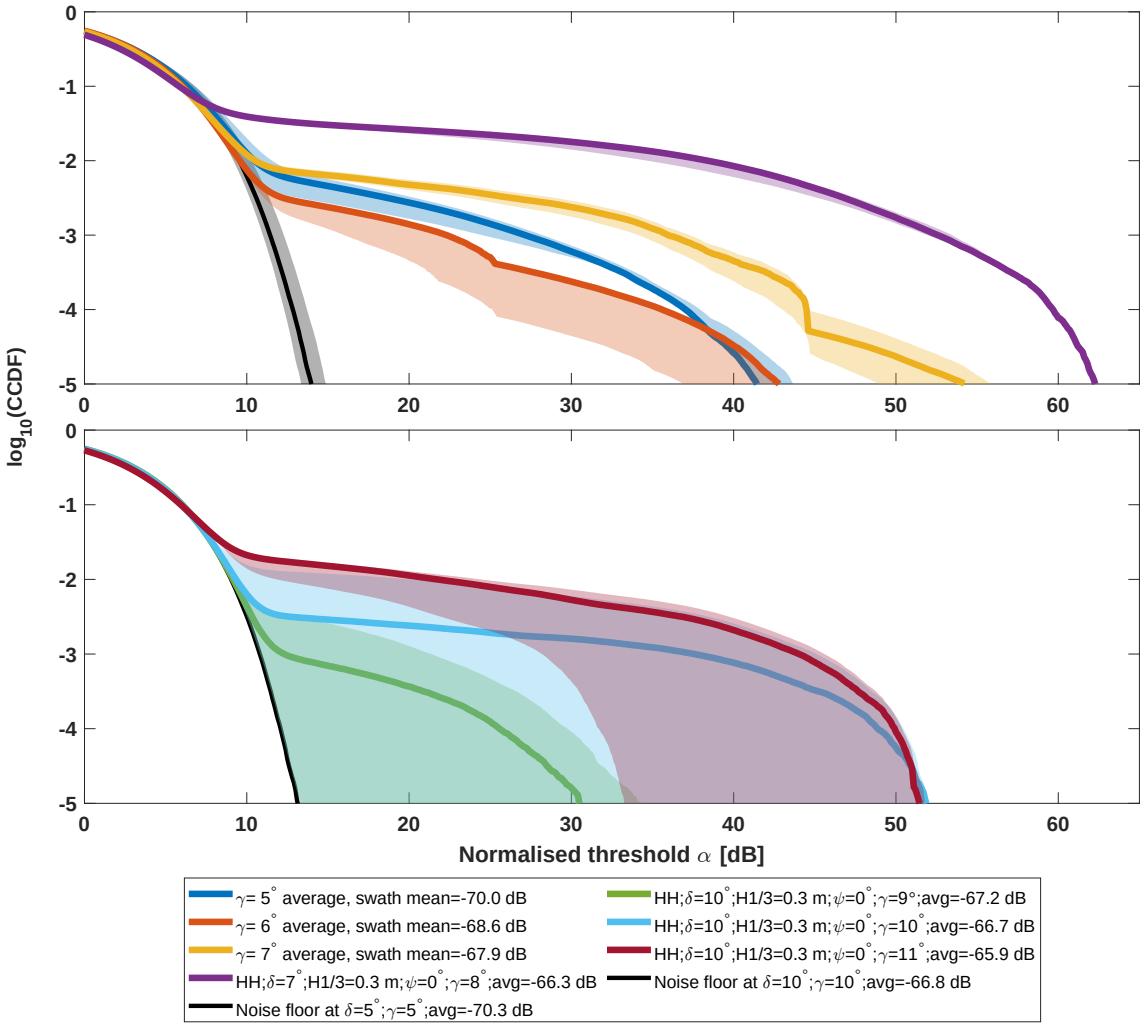

Figure 7.17: Plots of CCDF curves as a function of grazing angle for a SWH of 0.3 m in HH polarisation. The curves derived from measurements made at a depression angle of 10° are plotted separately for clarity.

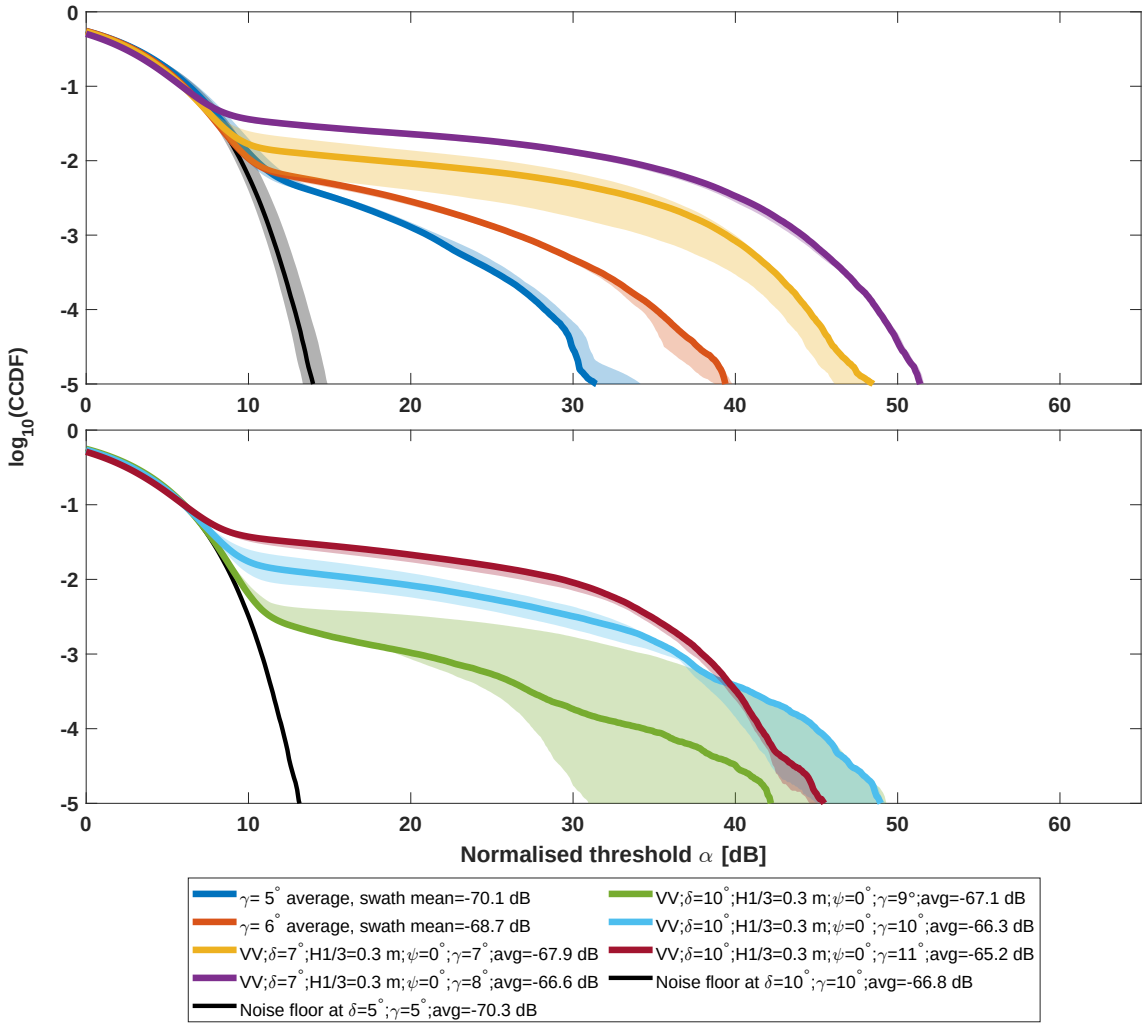

Figure 7.18: Plots of CCDF curves as a function of grazing angle for a SWH of 0.3 m in VV polarisation. The curves derived from measurements made a depression angle of 10° are plotted separately for clarity.

Number	Time stamp	Duration [s]	Pol.	$H_{1/3}$[m]	ψ[°]	δ[°]	γ[°]
Figure 7.17							
8	10 – 04 – 54	17.03	HH	0.3	0	5	5
9	10 – 05 – 43	15.71	HH	0.3	0	5	5
13	10 – 14 – 52	34.60	HH	0.3	0	5	5
8	10 – 04 – 54	17.03	HH	0.3	0	5	6
9	10 – 05 – 43	15.71	HH	0.3	0	5	6
10	10 – 07 – 37	16.97	HH	0.3	0	7	6
11	10 – 08 – 22	16.80	HH	0.3	0	7	6
13	10 – 14 – 52	34.60	HH	0.3	0	5	6
10	10 – 07 – 37	16.97	HH	0.3	0	7	7
11	10 – 08 – 22	16.80	HH	0.3	0	7	7
11	10 – 08 – 22	16.80	HH	0.3	0	7	8
12	10 – 11 – 40	16.82	HH	0.3	0	10	9
12	10 – 11 – 40	16.82	HH	0.3	0	10	10
12	10 – 11 – 40	16.82	HH	0.3	0	10	11
Figure 7.18							
22	11 – 46 – 27	36.29	VV	0.3	0	5	5
23	11 – 47 – 52	18.18	VV	0.3	0	5	5
24	11 – 48 – 30	19.72	VV	0.3	0	5	5
22	11 – 46 – 27	36.29	VV	0.3	0	5	6
23	11 – 47 – 52	18.18	VV	0.3	0	5	6
24	11 – 48 – 30	19.72	VV	0.3	0	5	6
25	11 – 50 – 33	18.92	VV	0.3	0	7	6
25	11 – 50 – 33	18.92	VV	0.3	0	7	7
25	11 – 50 – 33	18.92	VV	0.3	0	7	8
27	11 – 54 – 00	18.25	VV	0.3	0	10	9
27	11 – 54 – 00	18.25	VV	0.3	0	10	10
27	11 – 54 – 00	18.25	VV	0.3	0	10	11

Table 7.5: Data used for the grazing angle analysis.

7.2.5 Polarisation

The data used for the polarisation analysis are listed in Table 7.6. The plots shown in Figures 7.19, 7.20, 7.21, and 7.22 compare the distributions seen in HH and VV. These results are presented for grazing angles between 5 to 8° and at different wave heights according the availability of suitable data.

In all cases it was observed that the amplitude distribution is spikier in HH polarisation than in VV, as suggested by the results seen in the prior qualitative analysis in Section 6.2.3. The difference at a level of $\log_{10}(\text{CCDF}) = -5$ varies from a minimum of ∼3 dB to a maximum of ∼22 dB in threshold level. This is another indicator of the variable nature of the dataset, where some of the individual runs of VV data are observed to be spikier than HH runs. The confidence in the overall conclusion is however high. This result mirrors that seen at lower frequencies as described in Subsection 2.3.5, and is expected since burst scattering is almost exclusively occurs in HH polarisation and greatly increases spikiness.

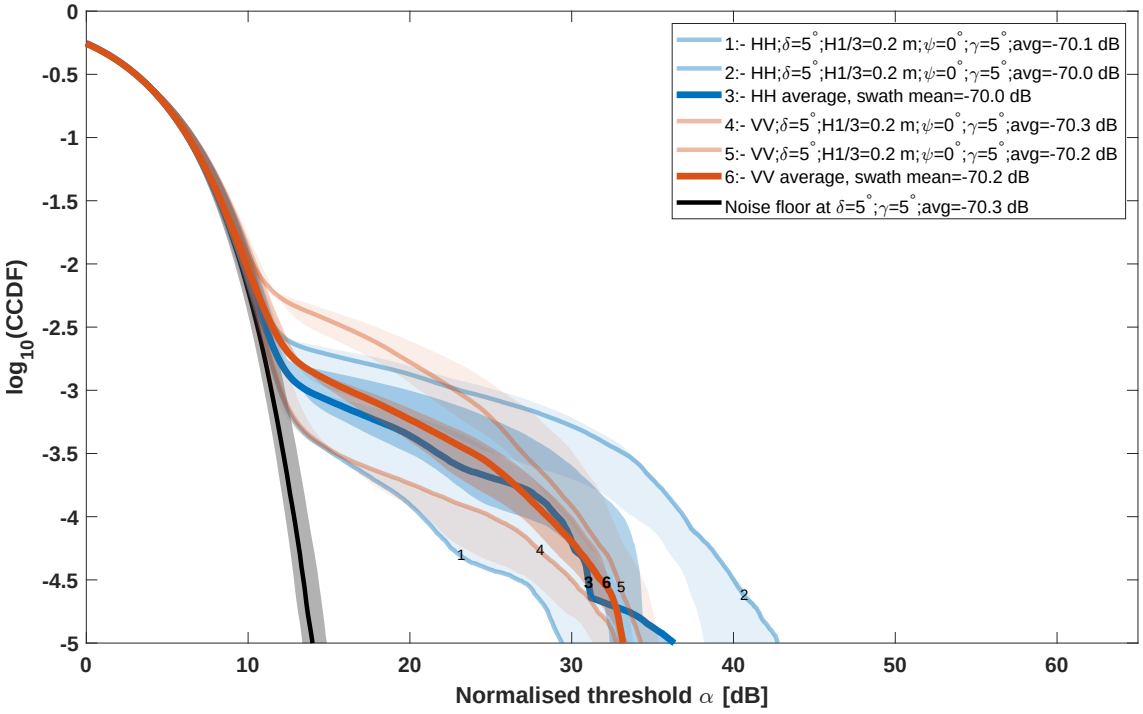

(a) $H_{1/3} = 0.2$ m.

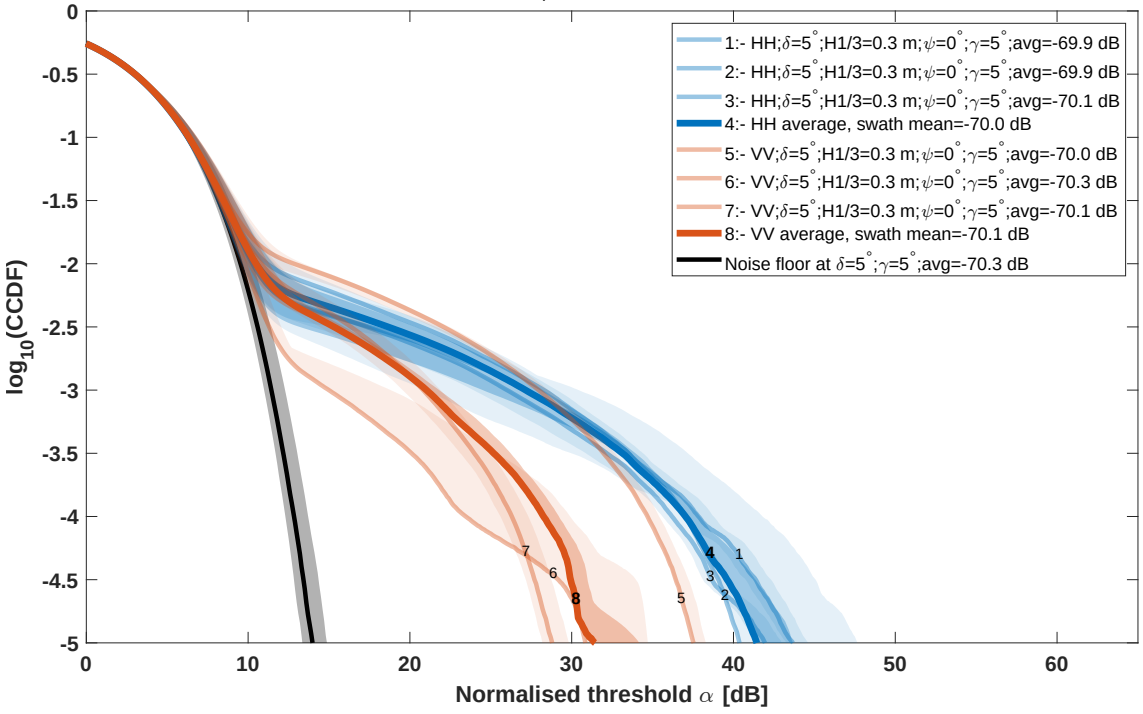

(b) $H_{1/3} = 0.3$ m.

Figure 7.19: CCDF curves in both HH and VV polarisations, for $\gamma = 5°$.

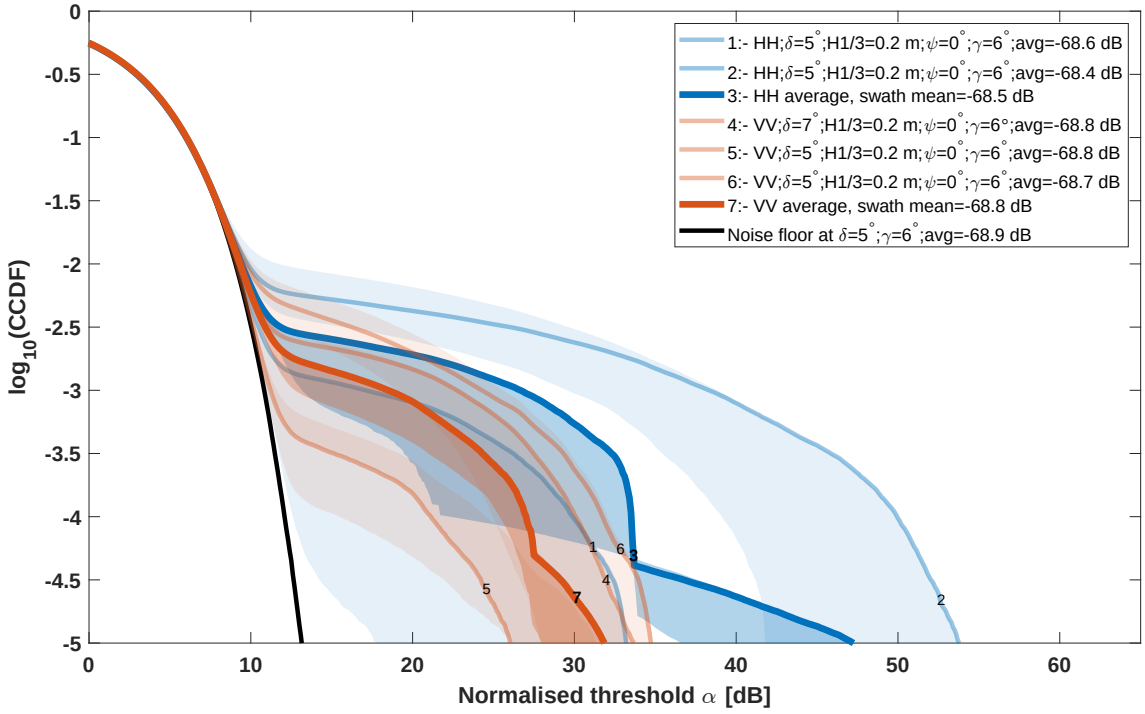

(a) $H_{1/3} = 0.2$ m.

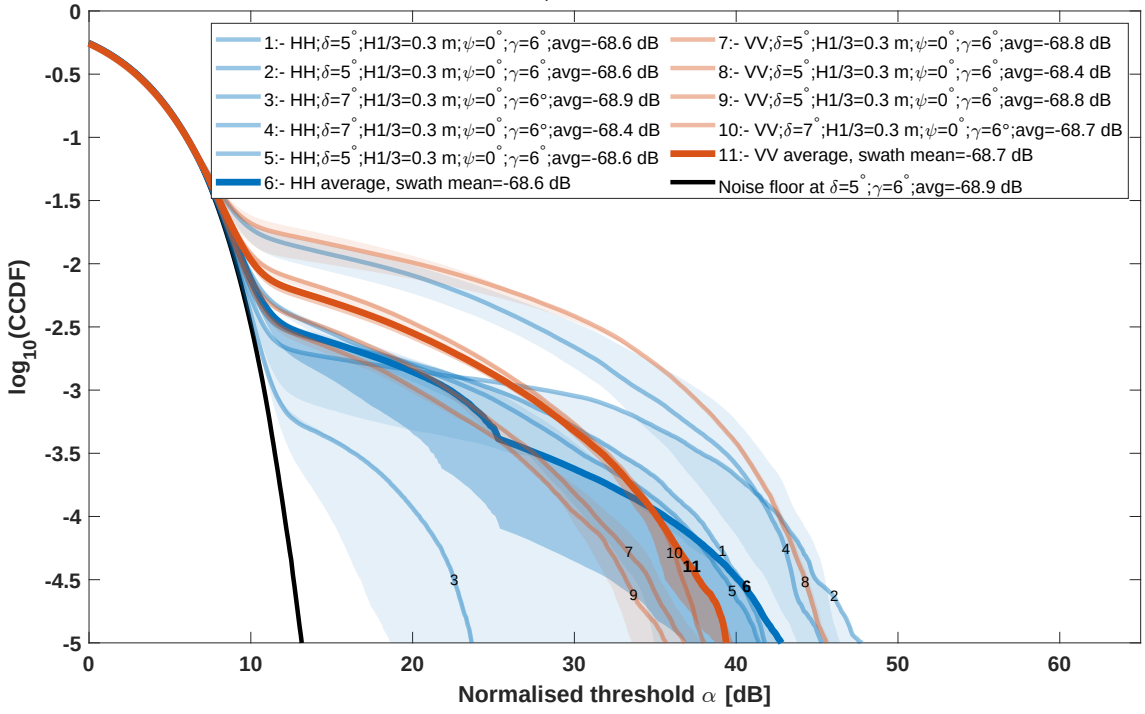

(b) $H_{1/3} = 0.3$ m.

Figure 7.20: CCDF curves in both HH and VV polarisations, for $\gamma = 6°$.

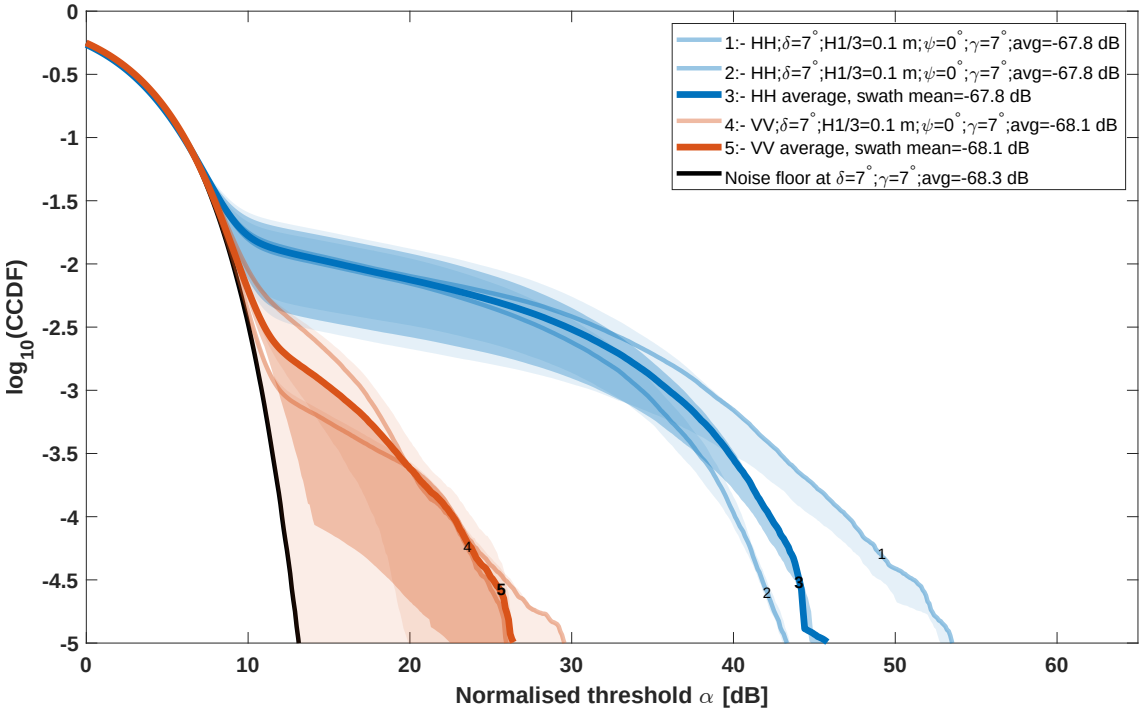

(a) $H_{1/3} = 0.1$ m.

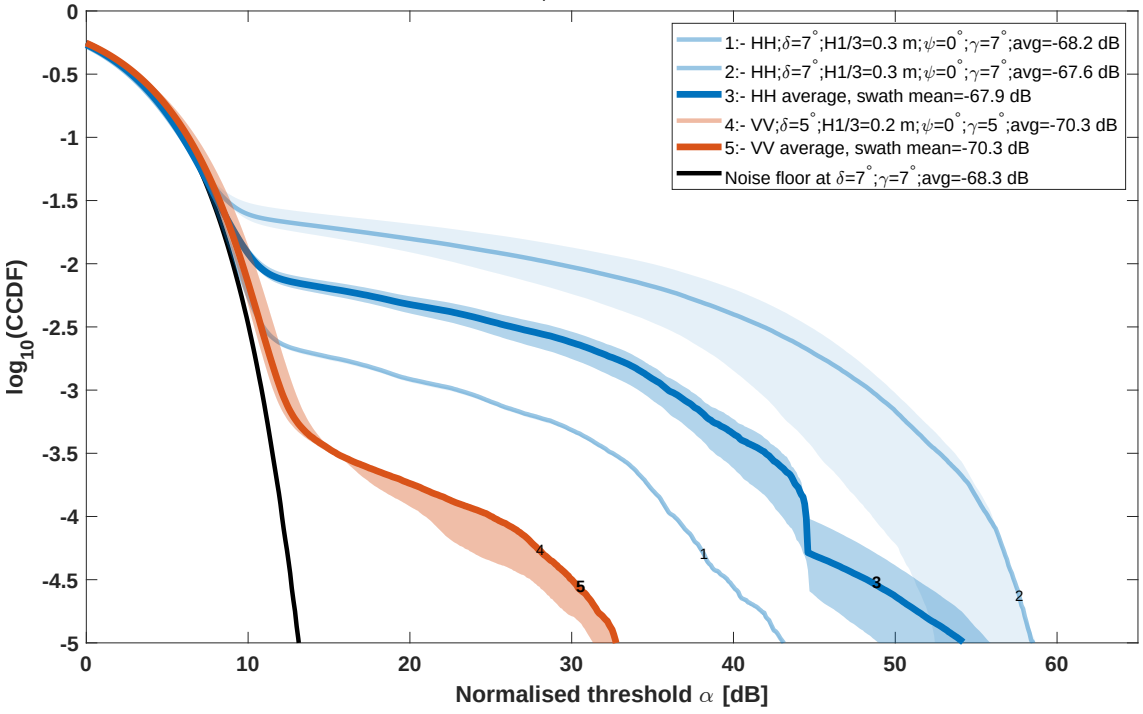

(b) $H_{1/3} = 0.3$ m.

Figure 7.21: CCDF curves in both HH and VV polarisations, for $\gamma = 7°$.

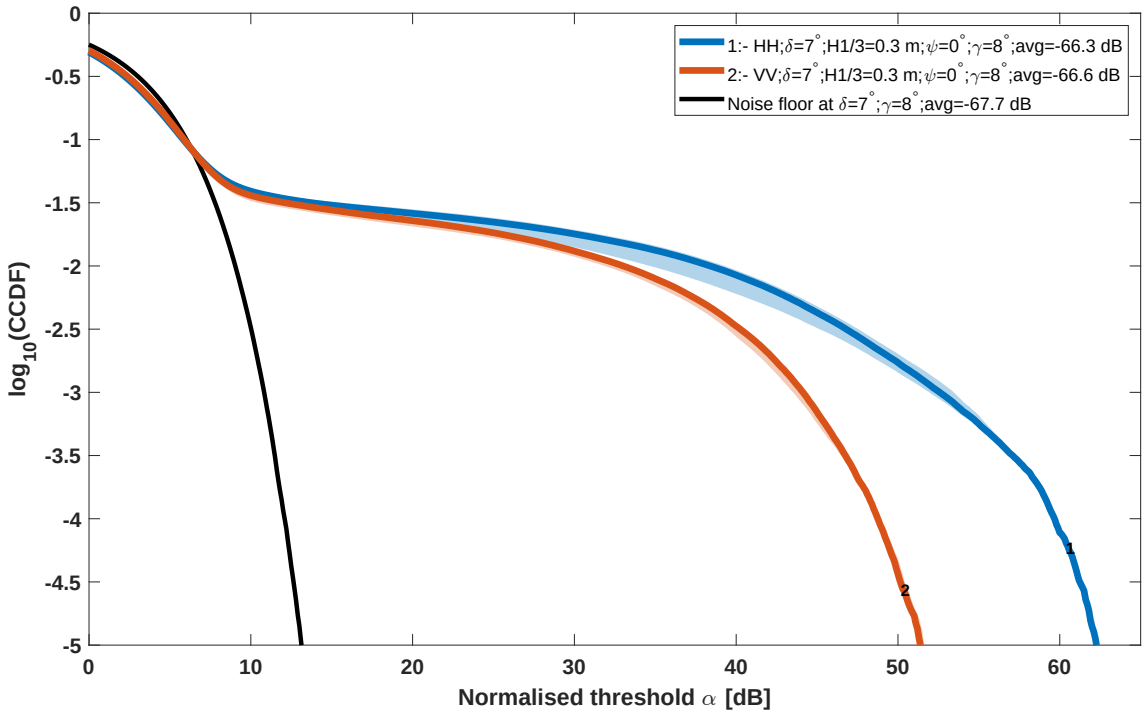

Figure 7.22: CCDF curves in both HH and VV polarisations, for $\gamma = 8°$ and $H_{1/3} = 0.3$ m.

Number	Time stamp	Duration [s]	Pol.	$H_{1/3}$[m]	Wave dir. [°]	δ[°]	γ[°]
Figure 7.19a							
6	09 − 50 − 01	17.27	HH	0.2	0	5	5
7	09 − 50 − 42	17.79	HH	0.2	0	5	5
20	11 − 36 − 00	18.40	VV	0.2	0	5	5
21	11 − 36 − 46	20.20	VV	0.2	0	5	5
Figure 7.19b							
8	10 − 04 − 54	17.03	HH	0.3	0	5	5
9	10 − 05 − 43	15.71	HH	0.3	0	5	5
13	10 − 14 − 52	34.60	HH	0.3	0	5	5
22	11 − 46 − 27	36.29	VV	0.3	0	5	5
23	11 − 47 − 52	18.18	VV	0.3	0	5	5
24	11 − 48 − 30	19.72	VV	0.3	0	5	5
Figure 7.20a							
6	09 − 50 − 01	17.27	HH	0.2	0	5	6
7	09 − 50 − 42	17.79	HH	0.2	0	5	6
19	11 − 29 − 41	18.52	VV	0.2	0	7	6
20	11 − 36 − 00	18.40	VV	0.2	0	5	6
21	11 − 36 − 46	20.20	VV	0.2	0	5	6
Figure 7.20b							
8	10 − 04 − 54	17.03	HH	0.2	0	5	6
9	10 − 05 − 43	15.71	HH	0.2	0	5	6
10	10 − 07 − 37	16.97	HH	0.2	0	7	6
11	10 − 08 − 22	16.80	HH	0.2	0	7	6
13	10 − 14 − 52	34.60	HH	0.2	0	5	6
22	11 − 46 − 27	36.29	VV	0.2	0	5	6
23	11 − 47 − 52	18.18	VV	0.2	0	5	6
24	11 − 48 − 30	19.72	VV	0.2	0	5	6
25	11 − 50 − 33	18.92	VV	0.2	0	7	6
Figure 7.21a							
3	09 − 36 − 45	18.44	HH	0.2	0	7	7
4	09 − 37 − 29	17.83	HH	0.2	0	7	7
16	11 − 17 − 37	6.76	VV	0.2	0	7	7
17	11 − 19 − 31	19.67	VV	0.2	0	7	7
Figure 7.21b							
10	10 − 07 − 37	16.97	HH	0.2	0	7	7
11	10 − 08 − 22	16.80	HH	0.2	0	7	7
20	11 − 36 − 00	18.40	VV	0.2	0	7	7
Figure 7.22							
11	10 − 08 − 22	16.80	HH	0.2	0	7	8
25	11 − 50 − 33	19.82	VV	0.2	0	7	8

Table 7.6: Data used for the polarisation analysis.

7.2.6 Summary

7.2.6.1 Wave direction

The VV polarised data demonstrate a trend of reduced spikiness for wave directions away from direct approach at $\psi = 0°$. The results from HH data are less conclusive due to the limited dataset available. The expected result is that spikiness is reduced away from 0° as the clutter returns become suppressed, as seen in the VV results, and it would likely also be seen to occur in HH polarisation with more data. In general, more data would be beneficial to better sample each wave direction, and future measurements at finer increments would help to determine at what wave direction angle the clutter returns begin to be significantly suppressed and spikiness therefore reduced.

7.2.6.2 Wave height

The amplitude distribution is seen to become spikier with increasing wave height in both polarisation and at most of the grazing angles shown. These are the expected results, as larger waves generate higher amplitude scattering, and thus lengthen the tail of the distribution. This result is seen at lower frequencies as described in Subsection 2.3.5. A maximal increase in threshold at a level of $\log_{10}(\text{CCDF}) = -5$ of up to 15 dB and 20 dB is seen in HH and VV polarisations respectively comparing results from conditions with $H_{1/3} = 0.1$ m and $H_{1/3} = 0.3$ m. This is a significant increase in spikiness from only a moderate increase in wave height, indicating that a slight change in environmental conditions could produce an large impact in detection scheme effectiveness. Although a small proportion of the plots shown did not display the same trend clearly, is is expected that this is due to the highly variable nature of the data and that further measurements would improve consistency.

7.2.6.3 Grazing angle

The plots shown in each polarisation encompassing grazing angles of $\gamma = 5°$, $\gamma = 6°$, $\gamma = 7°$, and $\gamma = 8°$ show that the amplitude distribution spikiness increases with grazing angle in this range, by ~23 dB and ~20 dB in HH and VV respectively at a level where $\log_{10}(\text{CCDF}) = -5$. Referring to Subsection 2.3.5, this is not the expected trend, where in general it is observed that lower grazing angles produce spikier data for microwave radars. This may however be a result of the clutter level being noise-limited in this sensor, where since lower grazing angle data has a lower mean level a larger portion of the bottom end of its distribution is being truncated to the noise level,

resulting in a narrower overall distribution. For both polarisations, the results shown for grazing angles of $\gamma = 9°$, $\gamma = 10°$, and $\gamma = 11°$ do not show a clear trend. Since these are derived from only one run of data each and given the sparsity of scattering events, the uncertainty is due to a low quantity of data.

7.2.6.4 Polarisation

The plots shown confirm that HH polarised data is spikier than VV at this frequency. This is also the result seen at lower frequencies, where the suppression of burst scattering in VV shortens the tail of the amplitude distribution. The plots show the trend for the full range of sampled wave heights and at grazing angles between 5° and 8°. The difference in threshold between the two polarisations at $\log_{10}(\text{CCDF}) = -5$ was variable and did not display a consistent trend as a function of wave height, where the smallest difference of ∼3 dB was observed in data for $H_{1/3} = 0.2$ m in Fig. 7.20a whereas Fig. 7.21a showed a difference of ∼18 dB. For grazing angle, the difference was generally increasing, with values of ∼10 dB, ∼4 dB, ∼22 dB, and ∼12 dB for grazing angles of 5°, 6°, 7°, and 8°, although very variable.

7.3 NRCS results

This section presents the results of the analysis of mean NRCS of 207 GHz sea clutter, specifically from the FloWave trial as detailed in Chapter 6. The results are presented as scatter plots with error bars. The processing used to produce the figures is described in Subsections 7.1.5 and 7.1.7. The points on the scatter plot are an arithmetic mean of the triplet of mean NRCS results from processing the data without the effect of uncertainties, and the two combinations of uncertainty which produce the largest change. Where multiple runs of data are averaged for a single point, the mean is calculated from all the combined triplets. The error bar limits are determined as the minimum and maximum values from each triplet. When multiple runs are averaged, the error bars are derived by taking the individual means of each of the uncertainty combinations and the nominal NRCS, where the minimum and maximum from the resulting three mean values are used as the error bars.

Each point on the scatter plots then represents the centre value of the set of all NRCS values, incorporating the effects of uncertainties, and the error bars represent the maximum and minimum values (or the average maximum and minimum values in the case where multiple runs are combined).

These results are for thresholded data, and thus represent the mean NRCS of the clutter spikes which lie above the threshold. Due to the sensitivity limitations of the

radar and the generally low reflectivity of the water's surface, only the top of the full amplitude distribution could be measured, the rest being obscured by the noise floor. The NRCS values presented are thus correct for the defined threshold levels, whereas a more sensitive radar would have a lower noise threshold, and thus see more of the total clutter distribution, resulting in a lower overall mean value for NRCS. The threshold level is set using noise floor data such that the noise is at a level of $\log_{10}(\text{CCDF}) = -4$, meaning a false alarm rate due to noise of 10^{-4}. This varies for each swath, the values being shown in Table 7.7.

7.3.1 Grazing angle

The data from both polarisations listed in Table 7.5 are used to plot Fig. 7.23. The results in Fig. 7.23 show the trend of the mean NRCS as a function of grazing angle for both polarisations. These results show that the mean NRCS for HH polarisation is almost universally greater than VV polarisation as a function of grazing angle, with a difference of 1 to 8 dB.

The plot also shows the NESZ, calculated by applying the NRCS processing to noise floor data. These values show the sensitivity limits of the radar, and are the minimum detectable NRCS values for each grazing angle. The NESZ fluctuates due to the antenna beam pattern correction, which increases (thus pushing up the NESZ) for off-boresight grazing angles. Where the depression angle of the radar matches the grazing angle, the NESZ is reduced as sensitivity is increased. All the mean NRCS values lie well above the NESZ points, and thus the signal is well separated from the noise. This is similarly observed in the following subsections on the effects of wave direction (Subsection 7.3.2) and wave height (Subsection 7.3.3).

Assessing the trend with grazing angle, a breakpoint is observed between $\gamma = 8°$ and $\gamma = 9°$. This feature seems unlikely to be representative of the true behaviour given other general observations on sea clutter at lower frequencies, however it is not possible to determine this conclusively without further investigation. This feature was also observed in the CCDF results in Figures 7.17 and 7.18, where the data from $\gamma = 9°$ to $\gamma = 11°$ are both from the same runs with only one acquisition at $\delta = 10°$ for each polarisation. The corresponding RTI plots of the data are shown in Fig. 6.12c (right hand plot) for HH polarisation and in Fig. 6.13c (right hand plot) for VV polarisation, where in both of these the clutter returns appear dimmer than at lower depression angles. Given that clutter spikes were generally sparse, this possibly implies that for those runs there may have incidentally been less scattering, or that the smaller beam footprint meant that fewer spikes were seen by the radar. On the other hand, given that only one run from each polarisation for a $H_{1/3} = 0.3$ m and $\delta = 10°$ (out of

two) showed any clutter, and that the clutter level is much lower (when it would be expected to be greater due to the shorter range), it may also be possible that this is a real phenomenon. In either case, the results from the different regimes are considered separately.

For grazing angle values between 5° and 8°, there is an upward trend in mean NRCS which rises >15 dB for both polarisations, from minima of −17.3 dB (HH) and −23.7 dB (VV) at $\gamma = 5°$ to maxima of 2.1 dB (HH) and −6.4 dB (VV) at $\gamma = 8°$. In general the spread of possible values produced by the measurement uncertainties is fairly modest in comparison, being less than 5 dB.

The results for grazing angles between 9° and 11° also indicate a somewhat rising trend but with a decrease of 15 to 20 dB between 8° and 9°. The central values run from −20.9 dB (HH) and −19.0 dB (VV) at $\gamma = 9°$ to −13.1 dB (HH) and −15.6 dB (VV) at $\gamma = 11°$. The fluctuation in mean NRCS due to the estimated errors in radar height and depression angle are also much greater, being between 13 to 28 dB. It is expected that the calculated NRCS at higher grazing angle values will be more sensitive to the estimated errors for two reasons; firstly, since the sparse clutter signals fall into progressively narrower range swaths, and factoring in the small drift in the swath edges caused by the errors, the signal captured in the nominal swath may vary; and secondly, due to narrowing of the range swaths with increasing grazing angle as shown in Table 7.2, swaths contain progressively fewer samples, meaning each sample has a greater impact on the final result and increases measurement noise. Overall, the mean NRCS indicates that these may be outlier results, however as stated previously this is difficult to say conclusively from these results due to the limitations of the dataset.

Results at microwave frequencies show that the mean NRCS increases with grazing angle, as shown in Figures 2.24 and 2.25. As discussed in Section 3.3, the same trend is seen for millimetre-wave clutter at 94 GHz. Additionally the VV to HH ratio is seen to decrease with increasing grazing angle, however that is not discernible from the 207 GHz results presented in Fig. 7.23. In the LGA regime, microwave results as seen in Fig. 2.25 show that VV polarised returns exceed HH, however the opposite trend is observed in the data presented here and in the qualitative results in Section 6.2. The different millimetre-wave results summarised in Section 3.3 were somewhat conflicted as to which polarisation resulted in the greater NRCS. Together, these three observations are consistent with suggesting a crossing point between the mean NRCS trends for HH and VV in the region of W-band, whereby with increasing frequency the mean NRCS for HH polarisation overtakes VV.

γ [°]	α [dB]	Swath geometric mean [dB]	Absolute threshold [dB]
5	12.1	−68.8	−56.7
6	12.1	−68.3	−56.2
7	12.1	−67.9	−55.8
8	12.0	−67.4	−55.4
9	12.1	−67.0	−54.9
10	12.0	−66.5	−54.5
11	12.2	−66.1	−53.9

Table 7.7: Threshold levels for each grazing angle, producing a noise false alarm rate of 10^{-4}.

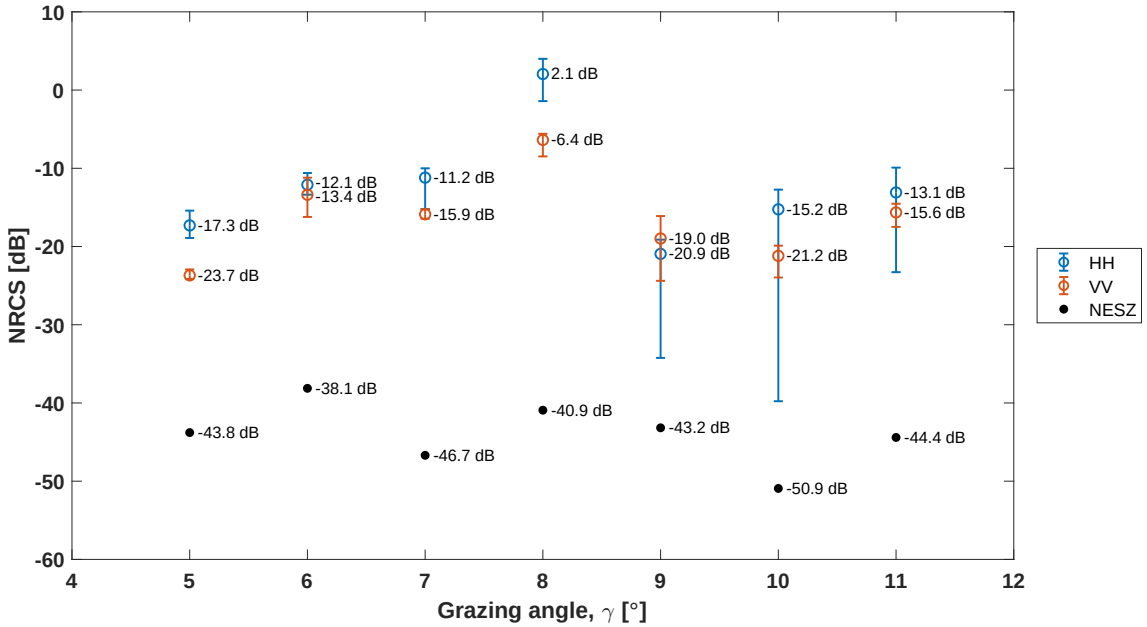

Figure 7.23: Mean NRCS as a function of grazing angle for HH and VV polarised data for $H_{1/3} = 0.3$ m and $\psi = 0°$. The data shows a trend of increasing NRCS with grazing angle, with a break point at 9° which may be the result of a low number of samples. Also shown is the NESZ at each grazing angle, where this fluctuates due to the antenna beam pattern correction increasing off-boresight.

7.3.2 Wave direction

The data used for the plots in Fig. 7.24 are shown in Table 7.3, where the runs for a single polarisation were combined into their own respective plots. These plots show the trend of mean NRCS as a function of wave direction, at several different grazing angles. As previously stated in Subsection 6.2.6.3, the proportion of runs which contained backscatter returns was low, resulting in a sparse sampling of wave directions. This indicated that backscatter was highly suppressed for wave directions other than 0°, as suggested by the CCDF results for VV polarisation shown in Fig. 7.8. It is also noted that the error bars shown for HH results in Fig. 7.24 are very large, particularly for $\psi = 0°$. This is likely to do with the shift in the range swath being processed coupled with the sparse returns, meaning that for one uncertainty combination the signal was very low, resulting in a significantly lower measured NRCS. This observation was similarly discussed in Section 7.3.1.

The mean NRCS for VV polarised returns shown in Fig. 7.24a is seen to decrease away from $\psi = 0°$. This would be expected from the amplitude distribution results, however the decrease is less dramatic than might have been suggested; at $\gamma = 6°$ the maximum decrease was 8.3 dB for $\psi = 180°$, and at $\gamma = 9°$ this was 9.4 dB for $\psi = 90°$. Figure 7.24b for the HH polarised results also shows similar values for the decline in mean NRCS away from $\psi = 0°$, the maximum reductions being 5 dB, 9.4 dB, and 2.6 dB for the grazing angles of 9°, 10°, and 11° respectively, and all at $\psi = 135°$. The lowest result in VV polarisation being at $\psi = 90°$ is what would be expected when considering results from lower frequencies, although as the measurements at $\psi = 45°$ and $\psi = 180°$ for this polarisation were gathered at a different grazing angle it is difficult to make a fair comparison. It could be argued however that in general the NRCS would increase going from $\gamma = 6°$ to $\gamma = 9°$, and so this may give confidence that the result at $\psi = 90°$ for $\gamma = 6°$ would be lower still than that measured for $\gamma = 9°$ as shown.

Whilst these are notable changes, they suggest that the scattering events which are seen at angles away from $\psi = 0°$ are still in fact of a similar level, but given the prior observations it is clear that the number of backscatter samples after thresholding for noise will decline precipitously as scattering events become less common. The relative invariance of mean NRCS with wave direction seen here is consistent with the observation in Subsection 6.2.6.3 that the scattering away from $\psi = 0°$ is from whitecap events.

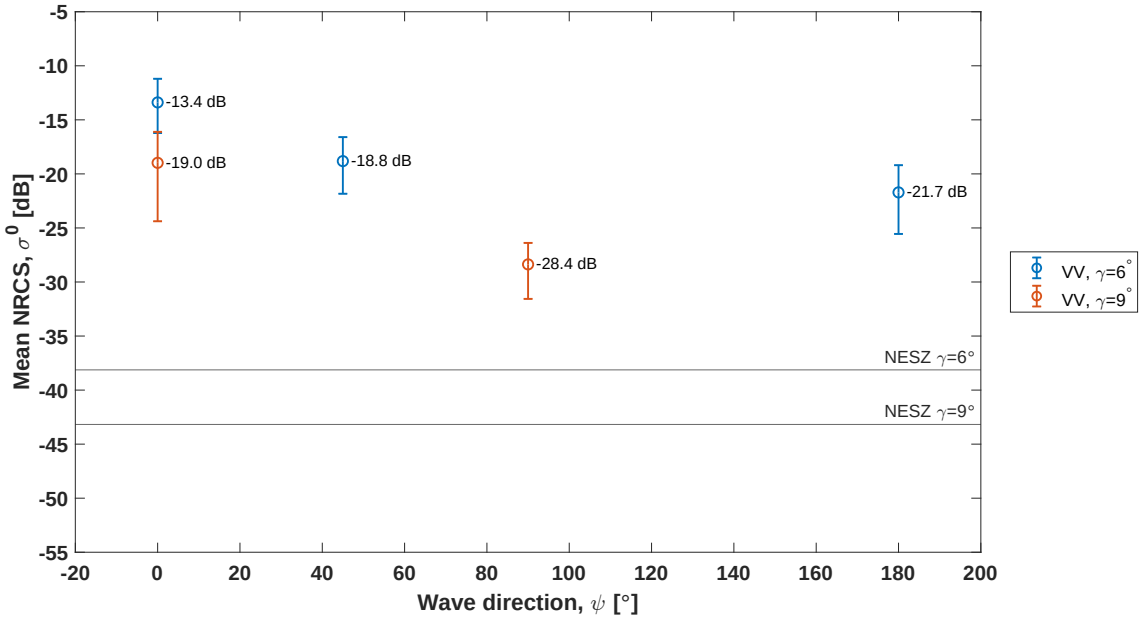

(a) VV polarisation.

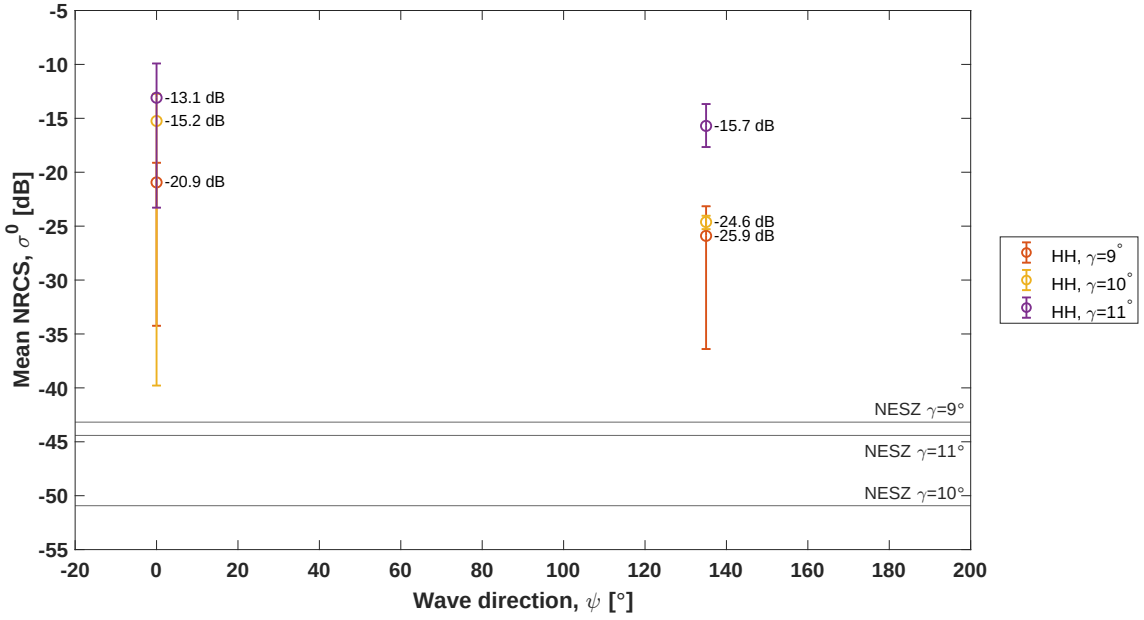

(b) HH polarisation.

Figure 7.24: Plots of mean NRCS as a function of wave direction for VV polarisation at $\gamma = 6°$ and $\gamma = 9°$, and in HH polarisation at grazing angles 9°, 10°, and 11°. The plots show a decline in mean NRCS for wave directions away from $\psi = 0°$ for all grazing angles.

7.3.3 Wave height

The data used for the plots in Fig. 7.25 are listed in Table 7.4, where data for both polarisations at a given grazing angle were combined into a single plot i.e. for Fig. 7.25a, the data correspond to those listed for Figures 7.10 and 7.14, for Fig. 7.25b these data are from the runs listed for Figures 7.11 and 7.15, and for Fig. 7.25c from those listed for Figures 7.12 and 7.16.

The plots in Fig. 7.25 show the trend for mean NRCS as a function of SWH, for grazing angles of 5°, 6° and 7° in both polarisations.

In VV, it can be seen that the mean NRCS always increases over the interval of $H_{1/3} = 0.1$ m to $H_{1/3} = 0.3$ m, the differences being 4.4 dB, 10.8 dB, and 15.6 dB for grazing angles of 5°, 6°, and 7° respectively. This shows that mean NRCS is generally increasing, although at $\gamma = 5°$ and $\gamma = 7°$ the difference between $H_{1/3} = 0.2$ m and $H_{1/3} = 0.3$ m was negligible. The plots also shows that the trend of increasing NRCS as a function of grazing angle likely holds for each wave height.

An increasing trend is less discernible in HH polarised data, however there are fewer data points. An increase with SWH is probable from these results, however the data point at $\gamma = 6°$, $H_{1/3} = 0.2$ m would be a clear outlier to this. In all cases where clutter was observed, HH polarised returns were seen to be greater than VV. In the instances where HH polarised returns were not observed, this is expected to be due to the sparse nature of the events rather than a lower reflectivity, but could also be due to the distribution of HH returns being spikier than VV, and thus HH clutter may be observed somewhat less reliably above the noise floor than for VV.

As explained in Subsection 2.3.4.4, mean backscatter is observed to increase with SWH at microwave frequencies for both HH and VV polarisations. The conclusions in Section 3.3 also indicate this trend for millimetre-wave clutter at 35 GHz and W-band, and so it can be reasonably concluded from the results above that this trend is continuous up to 207 GHz. Given the expected increase in burst scattering with wave height, it would be expected that HH polarised backscatter would see increasing enhancement over VV with increased wave heights, however this is not observed from this dataset, perhaps due to the limited range of wave heights sampled.

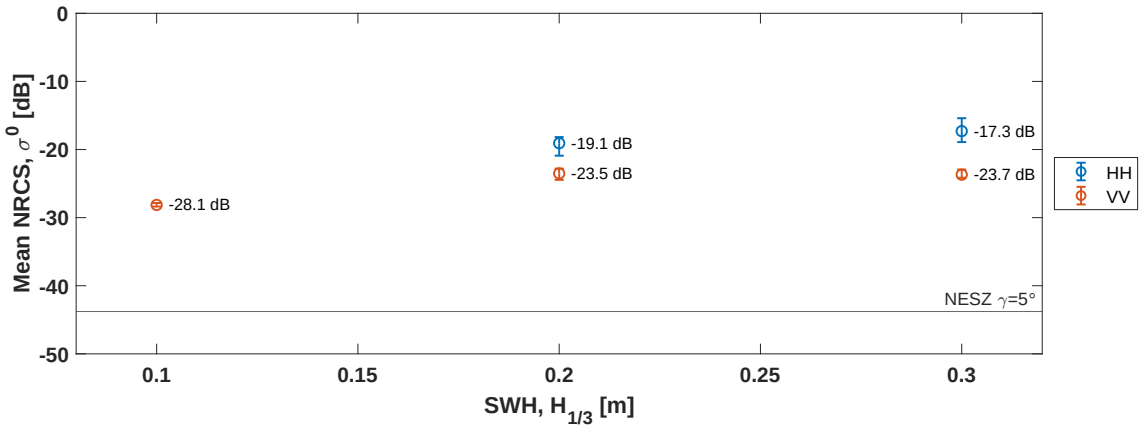

(a) $\gamma = 5°$.

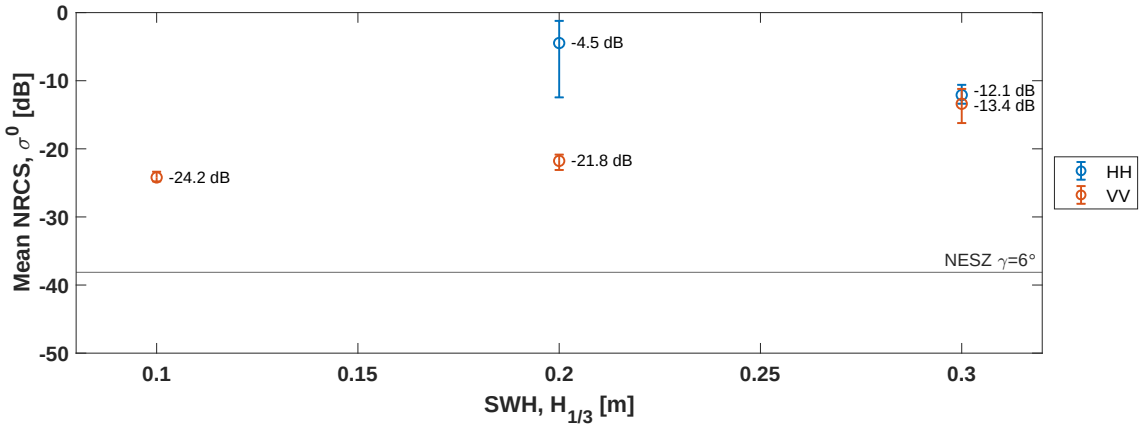

(b) $\gamma = 6°$.

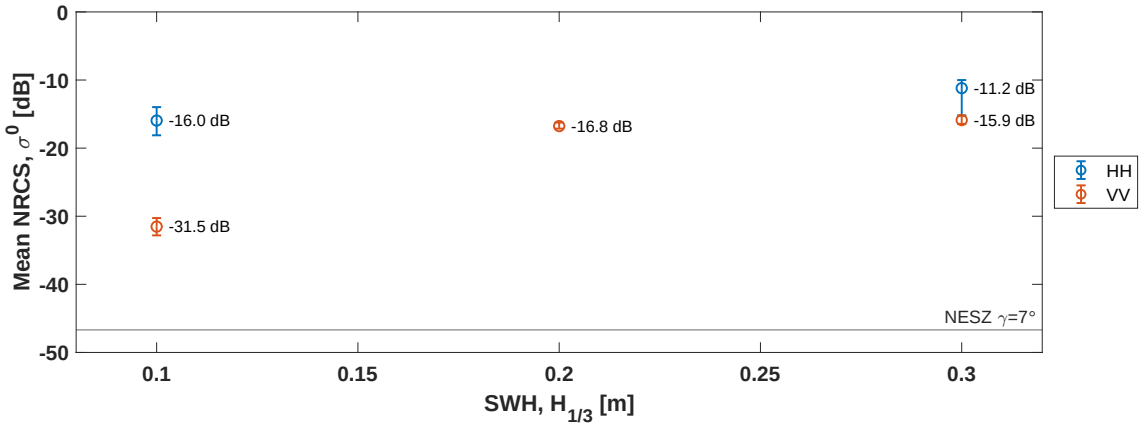

(c) $\gamma = 7°$.

Figure 7.25: Plots of mean NRCS as a function of SWH in both HH and VV polarisation, at grazing angles of 5°, 6°, and 7°. The plots show a clear increase in mean NRCS between $H_{1/3} = 0.1$ m and $H_{1/3} = 0.3$ m for VV polarisation, although with negligible differences seen between the values at $H_{1/3} = 0.2$ m and $H_{1/3} = 0.3$ m at $\gamma = 5°$ and $\gamma = 7°$. An increasing trend is somewhat less clear for HH data, however there are fewer available data points. These observations are consistent for all the grazing angle values shown.

7.4 Discussion

This chapter has outlined the processing methodology and the results for the amplitude distribution and mean NRCS of 207 GHz sea clutter derived from data gathered during the FloWave trial. The main conclusions from these results are summarised here with comparison to the behaviour seen at microwave and lower millimetre-wave frequencies.

In addition, similarity with prior results of 207 GHz sea clutter published in [26] are also discussed. These results were derived from a different trial conducted at Coniston Water in the Lake District, UK. The results of that publication are summarised here, and a correction is made to the stated values for mean NRCS. Due to an arithmetic error (usage of degrees rather than radians, which had reduced the NRCS correction factor by 17.6 dB) and changes to the calculation of the radar calibration curve (where an increase of 0.7 dB now reduces the correction factor by the same value), those results were underestimated by a constant value of 16.9 dB.

The data used for the analysis performed in that work were collected for water surfaces with maximum wave heights of ∼0.1 m, corresponding to a Douglas sea state of 1. The wave directions were between −10 to +10° from direct approach, caused by wind with sustained speeds of 10 to 19 km h^{-1} and gusts up to 22 km h^{-1}, varying in directions between −30 to +30° relative to direct approach. Prevailing weather conditions were fair, being generally sunny with light cloud, and with air temperatures of ∼18°C. Data were analysed for two grazing angle swaths, these being $\gamma = 2°$ and $\gamma = 4°$. The results from the trial are summarised:

- **RTI plots:** similar to the plots shown in Section 6.2, the observed clutter was sparse. There were however a significant number of shorter-lived clutter events in the Coniston data, which corresponded to periods of increased local wind. The wind caused small whitecaps and roughened wave crests where otherwise due to the low sea state the wave crests would have remained rounded and smooth.
- **CCDF results:** these showed that HH data were spikier than VV at both grazing angles. At $\gamma = 2°$, the HH thresholds varied between 28 to 31 dB, and VV between 22 to 28 dB. At $\gamma = 4°$, the thresholds varied between 33 to 42 dB in HH, and 24 to 36 dB in VV.
- **Mean NRCS:** the following values are given after applying the correction stated above. At $\gamma = 2°$, the mean NRCS for wave crests (after applying a threshold) was −16.3 dB in HH and −18.2 dB in VV. At $\gamma = 4°$, the mean NRCS was −21.3 dB in HH and −24.6 dB in VV. Thus the values for the lower grazing angle are greater,

which is against the expected trend, which was noted in the work. A possible effect which might explain this is ducting, which becomes increasingly apparent for lower grazing angles and lower sea states [13, p. 17], however no independent evidence was gathered of that phenomenon occurring.

7.4.1 Wave direction

7.4.1.1 Amplitude distribution

As seen in Subsection 7.2.2, the amplitude distributions for both HH and VV polarised data were highly sensitive to wave direction, where the intensity and thus spikiness was greatly suppressed for non-directly approaching waves (ψ>0°). For both polarisations, the sensitivity to wave direction primarily manifested in runs of data with no observable return, which are not shown in Fig. 7.8. This observation was also made previously when inspecting the RTI plots of the data in Subsection 6.2.6.3. Other trends for HH polarised data were inconclusive, primarily due to the limitations of the dataset since very few runs away from $\psi = 0°$ contained any backscatter. It was not possible to perform further comparisons except between data collected at $\psi = 0°$ and $\psi = 135°$ for $\delta = 10°$, where the data at 0° is suspected to be somewhat of an outlier e.g. when compared with other grazing angles in Fig. 7.17. The decrease in normalised threshold level at a $\log_{10}(\text{CCDF}) = -5$ observed in VV results as wave direction angle was increased was due to a general decrease in the level of backscatter, thus the curve tended towards the baseline of the noise floor curve.

The trends at microwave frequencies, showing the increase in mean level for directly approaching waves shown in Fig. 2.27 (where wind direction is taken as a proxy for wave direction) would suggest that spikiness also increases in this direction. As discussed in Subsection 2.3.5 however, it has been noted in Ward et al. [49, p. 31] that there is no significant trend as a function of wind direction. This may be because the sensitivity of lower frequency systems is in general greater, where in systems which are significantly less noise limited the full width of the amplitude distribution may be seen separate from the noise, and thus a broadening or contraction independent of the mean level may be observed. The behaviour of the amplitude distribution as a function of wave direction has not been reported for millimetre-wave results.

7.4.1.2 Mean NRCS

The greatest mean NRCS was observed at $\psi = 0°$ in keeping with prior observations. The change in level was however less variable than the CCDF results may have otherwise suggested, showing a decrease of 9.3 dB between $\psi = 0°$ and $\psi = 90°$ (cross-

wind[1]), in VV polarisation. This does not however account for the low proportion of runs with observable backscatter which was reported in Subsection 6.2.6.3, this being 6 out of 20 total in both polarisations. It is expected that the decrease in clutter is due to forward scattering from the surface of the water and away from the radar, due to the angle of the wave. Had the surface of the water been roughened by wind, the effect would likely be less pronounced as some backscatter may still be seen from a plane which is angled away from the radar.

For the measurable signals represented in Fig. 7.24, the low level of change of the mean NRCS values other than at $\psi = 0°$ is consistent with the observation made in Subsection 6.2.6.3 that these are from small whitecaps, where the roughened crest causes scattering which is isotropic in nature.

No significant difference was observed between HH and VV results from the limited dataset. The HH data in particular are potentially not as representative as would be hoped, where the expected behaviour would be to see a larger enhancement at $\psi = 0°$ due to burst scattering, observed at microwave frequencies as discussed in Subsection 2.3.4.4. This may again be due to the limitations of the recorded data; burst scattering was observed clearly in HH data at $\gamma = 7°$ and $\gamma = 8°$, but there were no runs with backscatter at these grazing angles for wave directions other than 0°; as seen from Fig. 2.25 it would seem that the returns seen in the data collected at $\delta = 10°$ are a low outlier but these were the only available choice for comparison with another wave direction.

It is not possible to infer any other major trends from these data, such as whether or not the mean NRCS follows a cosinusoidal pattern as a function of wave direction as seen at microwave (as shown in Fig. 2.27) and for 35 GHz and W-band frequencies (as discussed in Subsection 3.3.6). The maximum observed variations (between $\psi = 0°$ up-wind and $\psi = 90°$ cross-wind) in mean NRCS are 5 dB and 10 to 15 dB for microwave and 35 GHz/W-band frequencies results, where the results for 207 GHz are 9.3 dB for VV and 9.4 dB for HH (where this is instead between $\psi = 0°$ and $\psi = 135°$). This suggests that results at 207 GHz are similar to those at lower millimetre-wave frequencies.

[1] $\psi = 90°$ is known as cross-wind by convention, although perhaps more appropriately would be 'along wave' for the measurements from FloWave, since there was no wind.

Source	f_0[GHz]	γ [°]	$H_{1/3}$[m]	Pol.	α [dB]
Coniston	207	4	~0.1	HH	33 to 41
FloWave	207	5	0.2	HH	29 to 36
Stove et al. [115]	94	2	0.5 to 1.25	HH	17 to ~30
Coniston	207	4	~0.1	VV	24 to 36
FloWave	207	5	0.1	VV	24 to 26
Stove et al. [115]	94	2	0.5 to 1.25	VV	14 to 21

Table 7.8: Comparison of normalised threshold levels between results from the Coniston and FloWave trials, and those conducted by Stove et al. [115] at 94 GHz, at a $\log_{10}(\text{CCDF}) = -5$.

7.4.2 Wave height

7.4.2.1 Amplitude distribution

The statistics of 207 GHz clutter were found to become spikier with increasing wave height. Increases were as high as 15 dB in HH and 20 dB in VV going from a $H_{1/3} = 0.1$ m to $H_{1/3} = 0.3$ m. This was the expected trend, since larger waves produce more backscatter, and thus widen the distribution which remains noise limited at the lower end. This is also the expected behaviour for microwave frequencies as whitecap scattering becomes more prevalent.

In the results presented from the Coniston trial in [26], the trend with wave height was not specifically investigated, however an approximate comparison can be made between the results at $\gamma = 4°$ and the FloWave trial at $\gamma = 5°$. These values are presented in Table 7.8. This comparison shows that the Coniston results are spikier for both polarisations, even in the case of a lower wave height for HH, and this is expected to be due to the effects of wind on the surface of the water creating roughened and steepened wave crests.

In comparison with millimetre-wave results from Stove et al. [115] also shown in Table 7.8, it can be seen that the distributions at 207 GHz for both trials are much longer-tailed. In those results the range bins are approximately doubled in size, however they are for a Douglas sea state of 3 rather than of 2 as in the measurements from FloWave. Accepting those caveats, it can still be inferred that the increase in carrier frequency has increased the degree of spikiness dramatically.

7.4.2.2 Mean NRCS

Inspecting Fig. 7.25, a clear increase in mean NRCS in VV polarisation is seen, with a similar but less certain trend in HH due to fewer data points. The increase is more

Source	f_0[GHz]	γ [°]	$H_{1/3}$[m]	Pol.	σ^0 [dB]
FloWave	207	5	0.3	HH	−17.3
FloWave	207	6	0.3	HH	−12.1
FloWave	207	7	0.3	HH	−11.2
FloWave	207	5	0.3	VV	−23.7
FloWave	207	6	0.3	VV	−13.4
FloWave	207	7	0.3	VV	−15.9
Coniston	207	4	∼0.1	HH	−21.3
Coniston	207	4	∼0.1	VV	−24.6
Rosenberg and Watts [13, p. 18]	10	∼5	∼0.3	VV	−42 to −36
Stove et al. [115]	94	2	0.5 to 1.25	HH	∼−12
Stove et al. [115]	94	2	0.5 to 1.25	VV	∼−12
Weidong Hu et al. [119]	91.5	1.2	0.1 to 0.5	HH	−24.5

Table 7.9: Comparison of mean NRCS between results from the Coniston and FloWave trials, and literature millimetre-wave and microwave results.

pronounced at higher grazing angles. Given that the trend at microwave frequencies, 35 GHz, and W-band (discussed in Subsection 2.3.4.4 and 3.3.4) is of increasing NRCS with wave height, it can be determined that these results show a continuation of this trend up to 207 GHz.

The incidence of burst scattering is expected to increase with wave height, and thus an increasing enhancement of the HH to VV backscatter ratio would be expected. This was not conclusively observed in these results, although certainly the distributions of HH were longer-tailed and thus had the highest intensity of backscatter. It seems that this scattering did not have a particularly strong effect on the mean NRCS due to the sparsity of these events.

The mean NRCS levels for measurements made at 207 GHz, microwave frequencies and at lower millimetre-wave frequencies are presented in Table 7.9. The values for 10 GHz were estimated by using Table 2.2 to approximate the equivalent sea state for $H_{1/3} = 0.3$ m to be 2.5, and then using Eq. 2.82 to calculate the corresponding wind speed to be ∼6.6 m s^{-1}. The resulting NRCS was then estimated using Fig. 2.26. The results from Stove et al. [115] and Weidong Hu et al. [119] were selected in this instance as they represent values from the wave crests. The microwave results are valid over a full wave, where this will reduce their level in comparison. The results collected in Table 7.9 show that 207 GHz exhibits the brightest backscatter, or at least similar to the greatest values seen at 94 GHz for a higher sea state.

7.4.3 Grazing angle

7.4.3.1 Amplitude distribution

In the results from FloWave, the distribution tail lengthens with increasing grazing angle between $\gamma = 5°$ and $\gamma = 8°$ in both polarisations. Between $\gamma = 8°$ and $\gamma = 9°$ there is a sharp decrease in both cases, however as discussed previously these results each come from one run of data in both polarisations and are probably outliers. A large increase in threshold is seen between $\gamma = 5°$ and $\gamma = 8°$ for both polarisations, this being 20 dB in VV and 23 dB in HH at $\log_{10}(\text{CCDF}) = -5$, the greater increase in HH being due to burst scattering. As noted above, the results from Coniston also showed an increase in spikiness in both polarisations, the increase being 2 to 8 dB in VV and 5 to 11 dB in HH, comparing results from $\gamma = 2°$ and $\gamma = 4°$. This contrasts with what is observed for microwave frequencies, where lower grazing angles are seen to produce spikier data, particularly in HH polarisation.

7.4.3.2 Mean NRCS

For the results presented here, the mean NRCS was seen to increase with grazing angle between $\gamma = 5°$ and $\gamma = 8°$. Figure 2.25 shows a breakpoint thereafter, however as discussed this seems unlikely given the expected behaviour from lower frequencies. Considering the results from $\gamma = 5°$ to $\gamma = 8°$, the NRCS rises >15 dB in both polarisations, up to a maximum of 2.1 dB in HH and −6.4 dB in VV at $\gamma = 8°$.

In terms of experimental design, a vertical fan beam antenna may have been beneficial instead of a pencil beam since the footprint would have varied less as a function of grazing angle. This would potentially have resulted in better data, as sensitivity would not have varied as considerably with range due to the beam pattern, and more scattering events would have been observed. This could have contributed to further results at higher grazing angle values. Ultimately however, the pencil beam design was chosen since this was both easier to switch between polarisations and to achieve the required gain, where manufacturing antennas with high gain and a highly asymmetric pattern is difficult.

The results from the Coniston trial for $\gamma = 4°$ showed NRCS levels of −21.3 in HH and −24.6 in VV, which are reasonably similar to the values from the FloWave trial at $\gamma = 5°$ of −17.3 dB in HH and −23.7 dB in VV. Considering that the waves during the Coniston trial were smaller than those presented here but also rougher and more wind-blown, it is concluded that these results are consistent with each other.

Results from microwave frequencies also show that NRCS increases with grazing angle (Figures 2.25 and 2.24). HH returns are lower than VV until approximately

$\gamma = 45°$ at which point they become equal. For grazing angles similar to the those investigated in the trial, values in the region of −40 to −30 dB are expected, indicating that results from 207 GHz are greater (although these are for the thresholded values only). Results from 35 GHz and W-band show increasing NRCS with grazing angle as shown by results collected in Table 3.4. Furthermore, the VV to HH ratio is seen to decrease with increasing grazing angle, which is plausible for results at 207 GHz.

7.4.4 Polarisation

7.4.4.1 Amplitude distribution

At 207 GHz, HH polarised backscatter is generally spikier than VV. This was expected from the qualitative results in Subsection 6.2.3 such as in Fig. 6.10, where some very high returns were observed in HH polarisation. This behaviour was seen in the CCDF plots for grazing angles of 5°, 6°, 7°, and 8°. The difference in maximum threshold levels between HH and VV ranged from ∼3 dB to ∼22 dB for $\log_{10}(\text{CCDF}) = -5$, and this difference was seen to be generally increasing with grazing angle. The greatest observed threshold level was seen in HH at $\gamma = 8°$ and $H_{1/3} = 0.3$ m, where the threshold was up to 62 dB above the mean for $\log_{10}(\text{CCDF}) = -5$. The results from Coniston corroborate this, where for both grazing angles the HH returns were spikier than VV. This result is also seen at microwave frequencies as discussed in Subsection 2.3.5, and was also found to be the case at W-band in Stove et al. [115] and Weidong Hu et al. [119].

7.4.4.2 Mean NRCS

From the measurements made at FloWave, the NRCS of HH polarised data was observed to be almost universally greater than VV. This was seen at almost all the grazing angles measured in Fig. 2.25, with HH up to 8.5 dB greater, the arithmetic mean of the difference being 5.0 dB. For the wave height results in Fig. 7.25, the maximal difference was 17.3 dB, and the arithmetic mean of all the differences between HH and VV points was 12.2 dB. The markedly higher level of HH returns suggests that HH returns are enhanced by burst scattering whereas the VV returns have possibly been reduced by the lack of Bragg scattering. The results from Coniston also showed HH returns being of a higher level than VV.

This is in contrast to what is seen at microwave frequencies, where as shown in Fig. 2.25, VV is greater than HH up to $\gamma = 45°$. This is due to the Bragg scattering at these frequencies, which favours VV polarisation. It has occasionally been observed that HH exceeds VV returns in conditions which would increase burst scattering. The

trend with polarisation at W-band is unclear, however the results from 207 GHz would confirm that the HH and VV trends cross at some frequency in the region of W-band, and thus the equivocal results at W-band are a possible indication that HH and VV polarised returns are nearer equal in this frequency region.

7.4.5 Frequency

In general then, it is seen that 207 GHz results are much spikier than at either microwave or at the lower millimetre-wave frequencies which have been reported, where in part this could be due to the finer range resolution of this radar, where the smaller clutter patches at 207 GHz reduce the degree of spatial averaging. The mean NRCS levels observed at 207 GHz are also higher than seen at lower frequencies, although the thresholding process contributes to this difference. This trend is consistent with results from the microwave regime, where NRCS is seen to increase with frequency as shown in Fig. 2.24. Some results at W-band have indicated that the major contributions to scattering at this frequency come from rough surfaces. For the results presented here, the water surfaces were generated without the effect of wind, and so it could be reasoned that the NRCS for the FloWave results is suppressed in comparison. The results from the Coniston trial corroborate this, where as shown in Table 7.9 the NRCS values were −21.3 dB (HH) and −24.6 dB (VV), are similar or greater than those from FloWave in the most comparable conditions shown in Fig. 7.25a, with values of −19.1 dB for HH at $H_{1/3} = 0.2$ m and −28.1 dB in VV at $\gamma = 5°$. As discussed in Subsection 6.2.4, RSS is picked up in 207 GHz data when it occurs in the pool, thus this is likely to be a phenomenon which significantly contributes to the mean NRCS in the presence of wind.

This brings the final reporting of results for this thesis to a close. The following chapter presents the conclusions of this work as a whole.

8

Conclusion

THIS Ph.D. was motivated by the emerging need for situational awareness for ASVs, specifically agile or fast moving craft of small to medium size. Radar as a sensor type offers several advantages in this domain in terms of day/night operation and more robust performance in poor weather conditions than other alternatives. The high manoeuvrability and the platform sizes under consideration require a sensor type which can gather more detail of the immediate surroundings than traditional marine radars, and is of a more compact size. For these reasons, sub-THz sensing – operating above ~100 GHz – was of interest. This is because a higher frequency improves Doppler resolution, a greater available bandwidth is possible and allows for a finer range resolution, and the antenna size required for a well confined beam – producing a fine angular resolution – is small.

For the eventual development of future marine sub-THz radar sensors, fundamental research into the phenomenology of radar sea clutter at this frequency needed to be conducted. Most of the measurements which had previously been carried out were at Ka-band or below, and no results had been reported for LGA sea clutter at sub-THz. This then led to the central research question of this thesis:

What are the amplitude statistics of sub-THz radar sea clutter?

The research objectives formulated to answer this question were:

1. The development and testing of a radar at 207 GHz for data collection.
2. The collection of sea clutter data at 207 GHz.
3. The analysis of the collected data to determine the amplitude statistics of sea clutter for different environmental and observation conditions.

The development of a new instrument was necessary to fulfil the need to gather new data. As discussed in Subsection 4.3.3, the specific operational frequency of 207 GHz

was determined by the goal to operate as close as possible to the 220 GHz atmospheric transmission window whilst maintaining acceptable sensitivity and being limited by the available signal generation technology and project budget.

The main aspects of the work covered over the course of this Ph.D. then addressed the objectives above. This involved the development, building, and testing of the new radar, which constituted approximately half of the time of the Ph.D. Several field trials were undertaken during the course of the project as part of a data collection campaign, where latterly these involved the new instrument along with other radars. The focus of this work is on the 207 GHz data from the FloWave trial, as this was collected for the greatest range of parameters at a sub-THz frequency. The final stages of this thesis then consisted of developing and executing an analysis of the amplitude statistics of the collected data.

The key contributions of this thesis are summarised:

1. A review of all published results on sea clutter above Ka-band, to the author's knowledge.
2. A review of all published G-band radar systems to date, to the author's knowledge.
3. The development and testing of a new 207 GHz FMCW Doppler radar, designed to be field portable and with changeable polarisation, where the combination of these features is a significant novelty.
4. The analysis of 207 GHz sea clutter data collected using the radar, to determine the variation of the mean reflectivity and amplitude distribution of clutter spikes as a function of measurement variables, where this analysis is for the highest recorded radar frequencies used to measure sea clutter to date.

8.1 Primary conclusions

8.1.1 Radar development

As detailed in Chapter 4, a forward model for the 207 GHz (G-band) 'Theseus' radar was developed and used to determine the design and the required performance of the constituent components. Operation at sub-THz frequencies and the intended application of environmental measurements at field trials both favoured a solid state, FMCW implementation, and so this was developed in the project. The sensitivity requirements were based on the expected NRCS of sea clutter, where this was conservatively estimated to be $\sim$−30 dB at 207 GHz, and would likely be less than the reflectivity of targets of interest.

The maximum unambiguous Doppler velocity necessary for the design was estimated to be 5 $\mathrm{m\,s^{-1}}$ from X-band Doppler spectra of waves, which determined the minimum estimated CRF to be ∼13.81 kHz. This, along with a nominal maximum range of 150 m, the range resolution of 0.075 m, and a plausible ADC sampling rate of 80 MHz produced an estimated chirp time of t_c∼50 µs. The estimated maximum required IF FFT resolution was then calculated from this to be ∼20 kHz. These were used as inputs to the forward model, which determined that the minimum desired value for the figure of merit of $P_t/(F-1)$ (transmit power versus noise factor) was ∼−18.5 dB for a CNR of 10 dB at 100 m and at a centre frequency of 207 GHz.

In addition to these desired performance values, the radar needed the following features:

- Configurable linear polarisation, as needed for target and clutter phenomenology measurements.
- Low power consumption to be compatible with operation at field trials.
- A full enclosure, which was also compact, for practicality on field trials and to fit inside the mount of a positioning gimbal.
- Switchable internal and external triggering for staring and scanning mode acquisitions.

The ability to slightly tune the centre frequency was also desired so that future measurements could be made to determine the changes in reflectivity with frequency in G-band. A secondary centre frequency of 201 GHz was determined to be feasible (termed low band, with the 207 GHz centre coined as high band). These considerations then all fed into the final design presented in Fig. 4.2 and the frequency multiplication scheme shown in Table 4.2.

The waveform design estimated above was then subsequently refined to determine the ADC sampling frequency f_s, and the final t_c and CRF. A DRO with a clock frequency of 3.5 GHz was chosen for use with the DDS board, where the allowable ADC sampling frequencies would in part be determined as being an integer fraction of the DRG update rate (Eq. 4.13, the first coherency constraint), itself derived by dividing the clock frequency by 24. The number of range bins per measurement was defined as 4096, this being a power of two to maximise the efficiency of the range processing FFT. This gave the number of real samples, N_{FFT}, as 2048. Multiplying this by the range resolution from above defined the maximum instrumented range as ∼153.5 m. The number of real samples then also placed a lower bound on f_s – which along with the minimum desired CRF of ∼13.81 kHz, the second coherency constraint (Eq. 4.17) which requires f_s to be an integer fraction of the CRF, and a upper bound imposed by

budget – defined the final sampling frequency to be 79.5494 MHz. This determined the chirp time to be 51.49 μs, and given the required dead time between chirps and the second coherency constraint the final CRF was determined to be 14.796 kHz.

The rest of the chapter details each radar subsystem and the design of the twin GOLAs, which were specified to have a gain of ∼39 dBi with a 2° one-way beamwidth. This was mandated by the sensitivity requirements, but also balanced by the need for a wide enough beam for easy manual pointing. The chapter ends with the mechanical designs for the enclosure and antennas, which were developed as a balance between the considerations explained above and also the total weight, ease of manufacture, and need for access to the internal space.

8.1.2 Radar characterisation

Chapter 5 first detailed the characterisation results of each of the radar subsystems, and then the full radar itself. The key results from the subsystem measurements were:

- **Antennas:** the beam pattern showed an excellent match to simulation down to −15 dB, and a good match down to −45 dB for both low and high band measurements. The mean error in beamwidth was low, this being 6.3% (E plane) and 3.1% (H plane) at low band, and 5.7% (E plane) and 2.8% (H plane) at high band. The measured gain of each GOLA was almost identical, being 37.4 dBi at low band and 37.9 dBi at high band. This was good performance albeit slightly below the desired gain, having ∼0.8 dB more loss than expected from simulation.
- **Chirp generator**: this was determined to be functioning as required, with band limits (at the resultant transmit frequency after multiplication) of ∼200 to ∼211 GHz encompassing the desired frequency range. After initial full system testing, the chirp generator was upgraded with a replacement DRO for better phase noise performance, the total improvement being 21.5 dB at 10^2 to 10^5 Hz from the carrier.
- **IF chain**: the small signal gain was measured to be 54.4 dB, with a maximum undistorted output power of 16.6 dBm. The frequency response imposes minimal distortion, being only gently sloping by 2 dB between 5 to 32 MHz.
- **Receiver chain**: the LO drive level to the SHM was optimised to minimise the conversion loss by measuring the integrated noise power (as proxy) as a function of LO frequency. The receiver noise figure was then measured using the Y-factor method as a function of RF frequency at low and high band, yielding values of 12.1 dB and 14.1 dB respectively. The implied mixer conversion loss was then 9.2 dB and 11.3 dB at low and high band respectively, which is slightly

worse than the values measured by the manufacturer of ∼8 dB, which were measured with an optimised bias at each frequency step, this being impractical in the radar given the swept frequency operation. Despite the slight drop in performance, the design remained wholly viable. The total gain of the receiver was then determined to be 45.3 dB and 43.2 dB at low and high band respectively.

- **Transmit chain**: the average output power of the W-band PA was measured to be 20.4 dBm and 19.9 dBm at low and high band respectively. The final transmit power at G-band was measured to be 15.3 dBm (with the doubler achieving 34.5% efficiency) and 14.4 dBm (with 31.9% doubler efficiency) in low and high band respectively. This showed good performance, where the doubler efficiency was excellent. In this design, the achievable transmit power was limited by the PA output, where this was the best commercially available solution at this frequency, package size, heat-sinking requirements, and at reasonable cost.

The system performance modelling performed in Chapter 4 was then recalculated using the parameter values measured for the radar. The system constant was calculated to be 94.3 dB at high band and 97.3 dB at low band, where these values are 6.3 dB and 3.3 dB lower than the desired 100.6 dB, respectively. This means that the desired CNR of 10 dB at 100 m for clutter with $\sigma^0 = -30$ dB is lowered by the respective shortfall at each band. The discrepancy is primarily due to a combination of insufficient transmitter power and high noise figure. For a $\beta_C = 100.6$ dB and using the realised parameters for the radar, the desired figure of merit $P_t/(F-1)$ is recalculated to be −23.3 dB at high band and −23.2 dB at low band. This is less than the estimate in Chapter 4 of ∼−18.5 dB due to the combined effect of the other measured values, meaning that the specification for transmitter power and noise figure was slightly more relaxed. When evaluating $P_t/(F-1)$ with the transmitter power values and noise factors, this gives −29.5 dB at high band and −26.5 dB at low band. The discrepancy is ∼6.2 dB and ∼3.3 dB respectively, values which are approximately equal to the shortfalls. Additionally, the antenna directivity is slightly lower and the antenna loss slightly greater than in the design calculations, both of which contribute to the somewhat degraded performance. This ultimately limits the range at which clutter measurements can be made at, meaning that a CNR of 10 dB for the specified NRCS would be seen at a range of ∼63 m for high band and ∼78 m for low band instead of at 100 m. This performance for clutter was still acceptable however, and given this sensitivity, the measurement of targets would still be very good due to the generally higher RCS. It was then suggested that the most practical path to improve the system sensitivity would be the addition of a G-band LNA as the front-end of the receiver, where further details are provided in Subsection 8.2.1 below.

Results for the fully integrated system were then presented. The measurement of the calibration curve found that this matched the model based on subsystem measurements well, albeit the measured curve lying on average 1.66 dB or 1.61 dB lower for low and high band respectively for ranges <120 m. These values were then used to calibrate the radar. The source of the calibration discrepancy was investigated, and it was determined that this in part could plausibly be due to a slight misalignment of the antennas.

The noise floor of the system was also modelled using the subsystem results, and compared with measured data. This showed a very good match, differing mainly at close range <∼30 m for $f_{\mathrm{IF}} \leq 7.8$ MHz, thought to be due to increasing $1/f$ noise from the SHM which was not measured for this subsystem due to the limitations of the test equipment, and subsequently not included in the model. Between 30 to 120 m, the noise level decreases by 3.75 dB with a mean of −74.01 dBm and −74.37 dBm for low and high band respectively. From these results and given the ADC limit of $< +10$ dBm, the dynamic range of the radar is determined to be ∼84 dB at low and high band. A subsequent analysis comparing the ADC and RF noise floors determined that the dynamic range of the receiver could be improved with the addition of a ∼12 dB attenuator between the two IF amplifiers.

The end of the chapter then showed the effect of the improved radar phase noise performance on the radar noise floor. Measured results showed that the upgraded chirp generator reduced the raised noise floor level due to reflected transmitter phase noise by ∼20 dB compared to the original design, and to a level which is only 12 dB above the thermal noise floor.

8.1.3 Data collection and qualitative observations

Chapter 6 described the FloWave trial, where the Theseus radar was one of three deployed for measurements of sea clutter and targets. Context for the radar measurements was provided by coincident video recordings of each measured water surface using a DSLR camera, and by an overview of the trial recorded with a tripod mounted webcam.

The choice to run a trial at the circular wave tank was motivated by the potential for a highly controllable environment where different wave directions and wave heights could be simulated, providing the opportunity to conduct target and clutter measurements over a wide parameters space. For clutter measurements, the radar depression angle and polarisation were also varied to investigate their effect. During the trial, data were also collected at 77 and 150 GHz, however only the 207 GHz results are presented in this thesis since they were at the highest frequency and thus of greatest interest to

the project, and time to analyse results was limited.

The 207 GHz results were presented in this chapter as RTI plots which were then qualitatively analysed along with coincident video of the generated waves. The RTIs revealed two types of sea clutter phenomena; diagonal sea spike signals originating from travelling wave crests, and RSS events which appeared as stationary in range.

In the RTIs, RSS events were often seen to follow particularly bright sea spikes. It was then observed in the video footage that these spikes were first caused by a steepened and curved wave front which then broke into a small whitecap, leaving a roughened patch of water which stayed at a constant range whilst the progenitor wave travelled away. This showed the sensitivity of this frequency to very small scale roughness, and suggests that this could be a significant phenomenon in sea clutter which should be investigated further in future.

The remainder of the analysis focused only on observations on the behaviour of sea spikes. It was observed that these were primarily due to burst scattering because of the smooth surface of the water in the absence of any wind, and also due to the maximum SWH being only equivalent to Douglas sea state of 2, and thus whitecaps were very limited both in occurrence and size.

The effect of the environmental and observation parameters was then examined, and is summarised:

- **Polarisation**: HH returns were observed to be significantly greater than VV, where this was associated with the steepened and parabolic wave crests seen, often prior to breaking. The highest returns in VV were seen for rare whitecap events.
- **Grazing angle**: the results showed that the greatest number of spikes were observed for when the radar was set to $\delta = 5°$ or $\delta = 7°$, where the resulting grazing angles were also similar due to observations being made near boresight. The intensity of returns was seen to be greatest at $\delta = 7°$. For both polarisations and all depression angles, the number of spikes and backscatter intensities were highly variable.
- **Wave direction**: the occurrence of sea spikes was highly sensitive to wave direction, where the number of spikes fell dramatically for wave directions greater than 0°. Due to the sparse nature of the spikes, it was difficult to determine any other trend in the spike intensity by inspecting the RTIs. Inspection of the video footage showed that the few spikes which were observed in the data were due to small whitecaps, where the roughened and foamy surfaces at the crest of the wave were not shadowed.

- **Wave height**: the number and intensity of spikes was seen to increase between $H_{1/3} = 0.1$ m and $H_{1/3} = 0.3$ m as would be expected from results at lower frequencies, although the number of runs with spikes was generally the same for $H_{1/3} = 0.1$ m and $H_{1/3} = 0.2$ m.

Whilst the FloWave trial generated a large quantity of novel data – the staring mode 207 GHz subset consisting of 70 files – the main limitations of the trial were that the wave heights were only up to $H_{1/3} = 0.3$ m (equivalent to Douglas sea state of 2), and that the waves were generated in the absence of wind, without which the surface roughening of the water was much reduced. The expected result of this was that the intensity of backscatter and the number of spikes was reduced, and is thus less representative of the real world. Despite these limitations, the trial did reveal a number of phenomena for sea clutter at sub-THz which were apparent from the qualitative analysis, where these results were complemented by further details from the quantitative analysis in the chapter which followed.

8.1.4 Statistical analysis of 207 GHz radar amplitude sea clutter

Finally, Chapter 7 presented the method and results for the quantitative analysis of the FloWave data. This was split into two analysis threads, the first considering the amplitude distribution represented as CCDF plots, and the second considering the calculation of thresholded NRCS values from the data.

These results are summarised with respect to the measurement parameters:

- **Wave direction**
  - **Amplitude distribution**: in VV polarisation, the spikiness of the distribution was plausibly observed to decrease with increasing wave direction angle away from zero, which would follow from the decrease in general number of spikes and backscatter intensity which was observed in the qualitative analysis. The reduction in spikes implies that the amplitude distribution is highly sensitive to wave direction (in contrast to microwave results). Further conclusions could not be drawn from the HH results as the number of runs with signal became very limited and sufficient data were not available.
  - **Mean NRCS**: results showed that the greatest mean level was observed into the direction of approaching waves ($\psi = 0°$) as expected from results at lower frequencies and from the observations made in the qualitative analysis. Due to the limitations of the dataset, no significant difference was

observed between HH and VV, and consequently the cosinusoidal variation in mean NRCS as a function of wave direction was not seen. In VV between wave directions $\psi = 0°$ and $\psi = 90°$ a difference in level of 9.3 dB was observed, with a similar difference of 9.4 dB seen in HH between wave directions of $\psi = 0°$ and $\psi = 135°$. It is possible that the HH data which were analysed were not as representative of the full distribution as would be hoped due to the sparse sampling, so it is plausible that the difference may in fact be greater for HH.

- **Wave height**
  - **Amplitude distribution**: spikiness increased with wave height, with differences of up to 15 dB in HH and 20 dB in VV between $H_{1/3} = 0.1$ m and $H_{1/3} = 0.3$ m. Comparing the FloWave results from those of an earlier, outdoor, trial at Coniston water, the implication is that wind blowing across the surface of the water increases the spikiness of the observed distributions as would be expected.
  - **Mean NRCS**: results suggest that backscatter intensity rises with wave height for VV polarisation, although the difference between $H_{1/3} = 0.2$ m and $H_{1/3} = 0.3$ m is small. This is compatible with trends seen at lower frequencies. In HH is is difficult to see a similar trend due to fewer available data points at $H_{1/3} = 0.1$ m. The NRCS values are in general similar to those reported at 94 GHz, and greater than those seen at lower frequencies.
- **Grazing angle**
  - **Amplitude distribution**: the spikiness of the statistics is seen to increase with grazing angle up to $\gamma = 8°$ by threshold levels of 20 dB in VV and 23 dB for $\log_{10}(\text{CCDF}) = -5$. This is in contrast to results from microwave frequencies, where lower grazing angles produce spikier data.
  - **Mean NRCS**: backscatter intensity is also seen to rise between grazing angles $\gamma = 5°$ and $\gamma = 8°$, by >15 dB in both polarisations, up to a maximum level of 2.1 dBm in HH and −6.4 dBm in VV at $\gamma = 8°$. This is in keeping with trends at lower frequencies. For both the amplitude distribution and mean NRCS analyses, the results from $\gamma = 9°$ to $\gamma = 11°$ do not fit with the trend from lower grazing angles but it is likely that these data are outliers.
- **Polarisation**
  - **Amplitude distribution**: HH polarised data is seen to be generally spikier than VV. For grazing angles between 5° and 8°, the difference in maximum

thresholds ranges from ∼3 dB to ∼22 dB for $\log_{10}(\text{CCDF}) = -5$, with the difference generally increasing with grazing angle. The greatest observed threshold level was seen in HH polarisation for $\gamma = 8°$ and $H_{1/3} = 0.3$ m, at 62 dB above the mean for $\log_{10}(\text{CCDF}) = -5$. HH is also seen to be spikier than VV at lower frequencies, where the results from FloWave indicate that this trend is continuous up to this frequency.

  - **Mean NRCS**: HH backscatter is almost universally greater than VV, with HH being ∼10 dB greater. It is expected that this is due to the enhancement from burst scattering in HH polarisation. This result is in contrast to microwave frequencies, where VV is greater than HH up to $\gamma = 45°$. The trend for W-band is not clear from published results, however in context with the observations from microwave frequencies and 207 GHz this is consistent with a cross-over in the curves for mean NRCS as a function of frequency in HH and VV somewhere in the region of W-band.

- **Frequency**

  - **Amplitude distribution**: in comparison to published 94 GHz results, the 207 GHz results have dramatically greater spikiness, although some of this effect is likely due to the fine range resolution of the 207 GHz radar.
  - **Mean NRCS**: values for the grazing angles in question are −40 to −30 dB for X-band, and −20 to 0 dB for 207 GHz results. The thresholding process may contribute to the increase between G-band and X-band results. The results from FloWave at 207 GHz are similar to published results at W-band. As discussed previously, the NRCS values at FloWave are likely suppressed due to the absence of wind, where this is corroborated by results from the Coniston trial. Considering this, the difference between 207 GHz and microwave or W-band results will increase for waves measured in similar conditions.

Chapter 7 was the final chapter of results of this thesis. The sea clutter measurements made at 207 GHz were the highest frequency results presented to date, and will inform the future design of radar sensors for marine autonomy.

8.2 Future work

This section covers some suggestions for future work which could be carried out next to build on the results of this thesis.

8.2.1 Improvements to hardware

- The alignment of the antennas could be further investigated and possibly tuned to improve the sensitivity of the instrument.

- An attenuator could be inserted into the IF chain between the first and second IF amplifiers to improve dynamic range.

- The high noise figure of the receiver could be improved by the addition of an LNA prior to the SHM. A suitable candidate would be an R&S G-LNA 140-220 20 6, with a gain of 30 dB and a noise figure of 5 dB [170]. This results in a receiver noise figure of 6.5 dB, and would increase the 10 dB CNR distance to ~118 m for high band and 124 m for low band. This modification would be the most feasible improvement to the sensitivity, where the alternative would be to increase the output power of the W-band PA on the transmit arm. This is likely to be more expensive and less convenient, as a replacement model would be a much larger component with more significant power and cooling requirements. PA technology is however constantly evolving, and so practical solutions at high W-band may become available in future as these could be driven by 6G and future communication hardware.

- The pencil-beam antennas could be exchanged for vertical fan-beam patterns to reduce the decrease in sensitivity as a function of grazing angle, which would make measurements of sea clutter more convenient. This would probably incur an additional penalty to sensitivity, and so would need to be balanced with this consideration, and that the procedure for changing polarisation becomes slightly more complex as the fan beam must be vertically orientated for both HH and VV measurements.

- The phase noise of the instrument could be further reduced by selecting an oscillator with a yet lower phase noise than the Nexyn DRO. Figure 5.37 suggests that the phase noise is ~30 dB above the thermal noise floor, and with a potential LNA improvement this could then be >20 dB above the RF thermal noise. Reducing this entirely is likely not practical, but a partial improvement would be possible by selecting an oscillator with a lower intrinsic phase noise, and one which has a higher output frequency to remove another frequency doubling stage. Phase noise is a key challenge in sub-THz radars with high values of frequency multiplication, as demonstrated previously by Cooper [54].

8.2.2 Future data collection

Although a substantial quantity of data were collected, due to the breadth of the parameter space and the sparse nature of the sea spikes which were observed, additional data would strengthen and clarify some of the conclusions to the analysis made in this work. Data from outdoor conditions made with concurrent measurements of local wind would also be desirable to quantify its effect on sea clutter. The data which have been collected thus far are however of high quality, where the Theseus radar has a proven track record in field trials as a capable and reliable data collection instrument.

8.2.3 Additional analysis

To improve the comparison between different frequencies, the FloWave data could be processed to reduce the range resolution to match that at lower frequencies, and to investigate the effect this has on the amplitude distribution. Some modelling work could also be performed to investigate the suitability of the K-distribution to representing the data and determine the shape parameter values. As well as work on the 207 GHz data, processing and analysis of the data collected with the other radars during the trials is of interest and relevance to the motivation, and is yet to be undertaken. The Doppler data which were collected with all radars during the trial is also highly relevant, where the Theseus radar was specifically developed as a coherent instrument to make these measurements. This would be another fruitful avenue for future research.

In all, this work has contributed new knowledge that is relevant to the design of future sub-THz sensors for marine autonomy, where this application is likely to have broad and significant impact on the world in terms of the economic, safety, and environmental benefits. The work presented here will provide a suitable foundation for continuing research into G-band sea clutter, and the instrument which was developed as part of this work will be useful for this use and research into other applications at sub-THz, where the promise of this frequency range continues to grow.

Bibliography

[1] S. S. Swords, *Technical History of the Beginnings of Radar*. Institution Of Engineering and Technology, 1986 (cit. on p. 1).

[2] J. N. Briggs, *Target detection by marine radar*. IET, 2004 (cit. on p. 1).

[3] OECD, *The Ocean Economy in 2030*. Paris: OECD Publishing, Apr. 2016. DOI: 10.1787/9789264251724-en (cit. on p. 1).

[4] "Global Marine Radar Market Share, Size, Analysis, Forecast: By Product Type: X Band, S Band; By Component: Transmitter, Receiver, Antennae, Others; By Application: Fishing Vessel, Recreational Boat, Merchant Marine, Others; Regional Analysis; Market Dynam," Expert Market Research, Tech. Rep., 2023 (cit. on p. 1).

[5] IRENA. "Offshore wind energy capacity worldwide from 2009 to 2022 (in megawatts) [Graph]." (2023), [Online]. Available: https://www.statista.com/statistics/476327/global-capacity-of-offshore-wind-energy/ (cit. on p. 1).

[6] T. Philbeck and N. Davis, "The Fourth Industrial Revolution: Shaping a New Era," *J. Int. Aff.*, vol. 72, no. 1, pp. 17–22, 2019 (cit. on p. 2).

[7] O. Levander, "Autonomous ships on the high seas," *IEEE Spectr.*, vol. 54, no. 2, pp. 26–31, Feb. 2017. DOI: 10.1109/MSPEC.2017.7833502 (cit. on p. 2).

[8] R. R. Negenborn, F. Goerlandt, T. A. Johansen, *et al.*, "Autonomous ships are on the horizon: here's what we need to know," *Nature*, vol. 615, no. 7950, pp. 30–33, Mar. 2023. DOI: 10.1038/d41586-023-00557-5 (cit. on p. 2).

[9] Autonaut Ltd. "Home | Autonaut." (2023), [Online]. Available: https://www.autonautusv.com/ (visited on 10/10/2023) (cit. on p. 2).

[10] Saildrone Inc. "Saildrone: Real-time Ocean Data Solutions." (2023), [Online]. Available: https://www.saildrone.com/ (visited on 10/10/2023) (cit. on p. 2).

[11] Offshore Sensing AS. "Offshore Sensing - Sailbuoy - Technology." (2023), [Online]. Available: http://sailbuoy.no/technology (visited on 10/10/2023) (cit. on p. 2).

[12] L3Harris Technologies Inc. "C-Worker 5 ASV | L3Harris Fast. Forward." (2023), [Online]. Available: https://www.l3harris.com/all-capabilities/c-worker-5-asv (visited on 10/10/2023) (cit. on p. 2).

[13] L. Rosenberg and S. Watts, *Radar Sea Clutter: Modelling and target detection*. Institution of Engineering and Technology, Dec. 2021. DOI: 10.1049/SBRA530E (cit. on pp. 2, 33, 41, 46, 47, 53, 54, 60–71, 101, 255, 258).

[14] "RADAR SENSOR DRS X-Class Series(DRS6A X-Class, DRS12A X-Class, DRS25A X-Class) | FURUNO." (2024), [Online]. Available: https://www.furuno.com/special/en/radar/drs6ax-class/%7B%5C#%7DSpecifications (visited on 06/27/2024) (cit. on p. 3).

[15] C. Waldschmidt, J. Hasch, and W. Menzel, "Automotive Radar From First Efforts to Future Systems," *IEEE J. Microwaves*, vol. 1, no. 1, pp. 135–148, 2021. DOI: 10.1109/jmw.2020.3033616 (cit. on p. 3).

[16] A. V. Muppala, A. Alburadi, A. Y. Nashashibi, H. N. Shaman, and K. Sarabandi, "A 223-GHz FMCW Imaging Radar With 360° FoV and 0.3° Azimuthal Resolution Enabled by a Rotationally Stable Fan-Beam Reflector," *IEEE Trans. Geosci. Remote Sens.*, vol. 61, 1000709, 2023. DOI: 10.1109/TGRS.2023.3284715 (cit. on pp. 3, 99, 100, 112).

[17] S. M. Sabery, A. Bystrov, M. Navarro-Cía, P. Gardner, and M. Gashinova, "Study of low terahertz radar signal backscattering for surface identification," *Sensors*, vol. 21, no. 9, 2021. DOI: 10.3390/s21092954 (cit. on p. 4).

[18] P. Lang, X. Fu, M. Martorella, *et al.*, "A Comprehensive Survey of Machine Learning Applied to Radar Signal Processing," pp. 1–49, Sep. 2020. arXiv: 2009.13702 (cit. on p. 4).

[19] Z. Geng, H. Yan, J. Zhang, and D. Zhu, "Deep-Learning for Radar: A Survey," *IEEE Access*, vol. 9, pp. 141 800–141 818, 2021. DOI: 10.1109/ACCESS.2021.3119561 (cit. on p. 4).

[20] T. Maiwald, T. Li, G.-R. Hotopan, *et al.*, "A Review of Integrated Systems and Components for 6G Wireless Communication in the D -Band," *Proc. IEEE*, vol. 111, no. 3, pp. 220–256, Mar. 2023. DOI: 10.1109/JPROC.2023.3240127 (cit. on p. 4).

[21] F. E. Nathanson, J. P. Reilly, and M. N. Cohen, *Radar design principles: Signal Processing and the Environment*, Second. SciTech Publishing, Incorporated, 1999 (cit. on pp. 5, 16, 27, 31, 32, 46, 61, 62, 64, 67, 74, 91, 92, 94, 100).

[22] S. Rahman, A. Vattulainen, and D. A. Robertson, "Amplitude Characteristics of Littoral Sea Clutter Data at K-band and W-band," in *2022 IEEE Radar Conf.*, New York City, NY, USA: IEEE, Mar. 2022, pp. 1–6. DOI: 10.1109/RadarConf2248738.2022.9764262 (cit. on pp. 7, 89–92).

[23] A. B. Vattulainen, S. Rahman, and D. A. Robertson, "G-band FMCW Doppler radar for sea clutter and target characterization," in *Radar Sens. Technol. XXVI*, A. M. Raynal and K. I. Ranney, Eds., vol. 12108, Orlando, Florida, USA: SPIE, May 2022. DOI: 10.1117/12.2618497 (cit. on pp. 7, 96, 108–111, 113, 114, 120, 122, 128, 153, 159).

[24] S. Rahman, A. B. Vattulainen, D. A. Robertson, and R. Milne, "Millimetre wave radar signatures of sea lions," in *Int. Conf. Radar Syst. (RADAR 2022)*, Edinburgh: Institution of Engineering and Technology, 2022, pp. 14–19. DOI: 10.1049/icp.2022.2284 (cit. on pp. 7, 8).

[25] S. Rahman, A. B. Vattulainen, and D. A. Robertson, "Doppler Characteristics of Sea Clutter at K-band and W-band: Results from the St Andrews and Coniston Water Trials," in *2023 IEEE Int. Radar Conf.*, Sydney, Australia: IEEE, Nov. 2023, pp. 1–6. DOI: 10.1109/RADAR54928.2023.10371023 (cit. on pp. 7, 8, 91).

[26] A. B. Vattulainen, S. Rahman, A. G. Stove, and D. A. Robertson, "Amplitude Distribution of Low Grazing Angle G-band Littoral Sea Clutter," in *2023 IEEE Int. Radar Conf.*, Sydney, Australia: IEEE, Nov. 2023, pp. 1–6. DOI: 10.1109/RADAR54928.2023.10371097 (cit. on pp. 7, 8, 73, 87, 89, 90, 210, 254, 257).

[27] S. Rahman, A. B. Vattulainen, and D. A. Robertson, "Machine learning-based approach for maritime target classification and anomaly detection using millimetre wave radar Doppler signatures," *IET Radar, Sonar Navig.*, vol. 18, no. 2, pp. 344–360, Dec. 2023. DOI: 10.1049/rsn2.12518 (cit. on pp. 7, 8).

[28] S. Rahman, A. B. Vattulainen, D. A. Robertson, and R. Milne, "Radar signatures of sea lions at K-band and W-band," *IET Radar, Sonar Navig.*, vol. 18, no. 1, pp. 147–157, Jan. 2024. DOI: 10.1049/rsn2.12498 (cit. on pp. 7, 8).

[29] A. B. Vattulainen, S. Rahman, and D. A. Robertson, "G-Band FMCW Doppler Radar for Close-Range Environmental Sensing," *IEEE Trans. Radar Syst.*, vol. 2, pp. 355–371, 2024. DOI: 10.1109/TRS.2024.3378123 (cit. on pp. 7, 8, 96, 108–112, 114, 135, 140, 145, 146, 153, 156, 162, 165, 170, 176).

[30] A. Stove, A. Vattulainen, D. Kumar, *et al.*, "Radar Cross Sections of Flotsam at Sub-THz Frequencies," in *2024 21st Eur. Radar Conf.*, IEEE, Sep. 2024, pp. 91–94. DOI: 10.23919/EuRAD61604.2024.10734965 (cit. on pp. 7, 8).

[31] W. L. Melvin and J. A. Scheer, *Principles of Modern Radar: Radar Applications*, W. L. Melvin and J. A. Scheer, Eds. Institution of Engineering and Technology, Dec. 2013. DOI: 10.1049/SBRA503E (cit. on p. 11).

[32] G. Brooker, *Sensors for Ranging and Imaging*, 2nd. Institution of Engineering and Technology, Nov. 2021. DOI: 10.1049/SBEW553E (cit. on p. 11).

[33] A. Meta, P. Hoogeboom, and L. P. Ligthart, "Signal Processing for FMCW SAR," *IEEE Trans. Geosci. Remote Sens.*, vol. 45, no. 11, pp. 3519–3532, Nov. 2007. DOI: 10.1109/TGRS.2007.906140 (cit. on p. 15).

[34] M. Richards, J. Scheer, and W. Holm, *Principles of Modern Radar: Basic principles*, M. A. Richards, J. A. Scheer, and W. A. Holm, Eds. Institution of Engineering and Technology, Jan. 2010. DOI: 10.1049/SBRA021E. arXiv: arXiv:1011.1669v3 (cit. on pp. 16, 20, 27, 28, 32, 34, 35, 37, 164).

[35] N. C. Currie and C. E. Brown, *Principles and Applications of Millimeter-Wave Radar*, N. C. Currie and C. E. Brown, Eds. Artech House, Inc., 1987 (cit. on pp. 16, 28, 32, 74, 91, 93–95, 98).

[36] M. I. Skolnik, *Radar Handbook*, 3rd. McGraw-Hill, 2008 (cit. on pp. 16, 33, 61, 63, 73, 74, 92, 94).

[37] C. Lin, G. Y. Li, and L. Wang, "Subarray-Based Coordinated Beamforming Training for mmWave and Sub-THz Communications," *IEEE J. Sel. Areas Commun.*, vol. 35, no. 9, pp. 2115–2126, Sep. 2017. DOI: 10.1109/JSAC.2017.2720038 (cit. on p. 20).

[38] H. Vettikalladi, W. T. Sethi, A. F. B. Abas, W. Ko, M. A. Alkanhal, and M. Himdi, "Sub-THz Antenna for High-Speed Wireless Communication Systems," *Int. J. Antennas Propag.*, vol. 2019, Mar. 2019. DOI: 10.1155/2019/9573647 (cit. on p. 20).

[39] Y. Xing, T. S. Rappaport, and A. Ghosh, "Millimeter Wave and Sub-THz Indoor Radio Propagation Channel Measurements, Models, and Comparisons in an Office Environment," *IEEE Commun. Lett.*, vol. 25, no. 10, pp. 3151–3155, Oct. 2021. DOI: 10.1109/LCOMM.2021.3088264. arXiv: 2103.00385 (cit. on p. 20).

[40] P. Kyösti, M. F. De Guzman, K. Haneda, N. Tervo, and A. Pärssinen, "How Many Beams Does Sub-THz Channel Support?" *IEEE Antennas Wirel. Propag. Lett.*, vol. 21, no. 1, pp. 74–78, Jan. 2022. DOI: 10.1109/LAWP.2021.3118464 (cit. on p. 20).

[41] "Sub-terahertz communication in 6G - Ericsson." (2024), [Online]. Available: https://www.ericsson.com/en/6g/spectrum/sub-thz (visited on 06/29/2024) (cit. on p. 20).

[42] Radiocommunication Sector of International Telecommunication Union, "Recommendation ITU-R P.676-10: Attenuation by atmospheric gases," 2013 (cit. on pp. 20, 169).

[43] Radiocommunication Sector of International Telecommunication Union, "Recommendation ITU-R P.835-2, Reference Standard Atmopheres," Tech. Rep., 1997, pp. 1–5 (cit. on p. 21).

[44] P. J. Speirs, "Millimetre-wave radar measurement of rain and volcanic ash," Ph.D. dissertation, University of St Andrews, 2013 (cit. on pp. 21, 103, 169).

[45] J. D. Kraus, M. Tiuri, A. V. Räisänen, *et al.*, *Radio Astronomy*, 2nd. Cygnus-Quasar Books, 1986 (cit. on pp. 21–23, 153, 155).

[46] J. D. Kraus, *Antennas*, 2nd ed., A. E. Elken, Ed. McGraw-Hill, Inc., 1988 (cit. on pp. 24–26, 117).

[47] M. I. Skolnik, *Introduction to Radar Systems*, Third. McGraw-Hill, 1981 (cit. on pp. 28, 29, 33, 54).

[48] N. C. Currie, R. D. Hayes, and R. N. Trebits, *Millimeter-wave radar clutter*. Artech House, Inc., 1992 (cit. on pp. 28, 32, 74).

[49] K. D. Ward, R. J. Tough, and S. Watts, *Sea clutter: Scattering, the K distribution and radar performance*, Second. The Institution of Engineering and Technology, 2006, pp. 1–452. DOI: 10.1049/PBRA020E (cit. on pp. 32, 46, 53, 55–60, 62, 64, 66, 67, 70, 71, 255).

[50] J. Rutman and F. Walls, "Characterization of frequency stability in precision frequency sources," *Proc. IEEE*, vol. 79, no. 7, pp. 952–960, Jul. 1991. DOI: 10.1109/5.84972 (cit. on p. 38).

[51] K. Cooper, S. Durden, R. Roy, *et al.*, "Improving FM Radar Dynamic Range Using Target Phase Noise Cancellation," *IEEE J. Microwaves*, vol. 1, no. 2, pp. 586–592, 2021. DOI: 10.1109/jmw.2021.3061887 (cit. on pp. 38, 40).

[52] A. Stove, "Linear FMCW radar techniques," *IEE Proc. F Radar Signal Process.*, vol. 139, no. 5, pp. 343–350, 1992. DOI: 10.1049/ip-f-2.1992.0048 (cit. on p. 38).

[53] P. D. Beasley, "The influence of transmitter phase noise on FMCW radar performance," *Proc. 36th Eur. Microw. Conf. EuMC 2006*, pp. 1810–1813, 2006. DOI: 10.1109/EUMC.2006.281023 (cit. on p. 38).

[54] K. B. Cooper, "Modeling broadband phase noise from extended targets in a 170 GHz cloud-imaging radar," in *Passiv. Act. Millimeter-Wave Imaging XXV*, D. A. Robertson and D. A. Wikner, Eds., vol. 12111, SPIE, Jun. 2022. DOI: 10.1117/12.2621073 (cit. on pp. 38, 40, 176–178, 272).

[55] P. D. L. Beasley, "Advances in millimetre wave FMCW radar," in *2008 Microwaves, Radar Remote Sens. Symp.*, IEEE, Sep. 2008, pp. 246–249. DOI: 10.1109/MRRS.2008.4669588 (cit. on p. 38).

[56] P. Stoica and R. L. Moses, *Spectral Analysis of Signals*. Prentice Hall, 2005 (cit. on p. 39).

[57] M. Ryabkova, V. Karaev, J. Guo, and Y. Titchenko, "A Review of Wave Spectrum Models as Applied to the Problem of Radar Probing of the Sea Surface," *J. Geophys. Res. Ocean.*, vol. 124, no. 10, pp. 7104–7134, 2019. DOI: 10.1029/2018JC014804 (cit. on p. 41).

[58] B. Jähne and K. S. Riemer, "Two–dimensional wave number spectra of small-scale water surface waves," *J. Geophys. Res. Ocean.*, vol. 95, no. C7, pp. 11 531–11 546, Jul. 1990. DOI: 10.1029/JC095iC07p11531 (cit. on pp. 41, 55, 78, 90).

[59] R. H. Stewart, *Introduction to Physical Oceanography*. Robert H. Stewart, 2008 (cit. on pp. 41, 44, 45, 47, 50).

[60] N. Pizzo, L. Deike, and A. Ayet, "How does the wind generate waves?" *Phys. Today*, vol. 74, no. 11, pp. 38–43, Nov. 2021. DOI: 10.1063/PT.3.4880 (cit. on pp. 42, 44).

[61] O. M. Phillips, "On the generation of waves by turbulent wind," *J. Fluid Mech.*, vol. 2, no. 05, pp. 417–445, Jul. 1957. DOI: 10.1017/S0022112057000233 (cit. on p. 42).

[62] J. E. Hunt and S. E. Belcher, "Turbulent shear flow over fast-moving waves," *J. Fluid Mech.*, vol. 386, pp. 345–371, May 1999. DOI: 10.1017/S0022112099004383 (cit. on p. 42).

[63] J. W. Miles, "On the generation of surface waves by shear flows," *J. Fluid Mech.*, vol. 6, no. 4, pp. 568–582, Nov. 1959. DOI: 10.1017/S0022112059000830 (cit. on p. 42).

[64] H. Jeffreys, "On the formation of water waves by wind," *Proc. R. Soc. London. Ser. A, Contain. Pap. a Math. Phys. Character*, vol. 107, no. 742, pp. 189–206, Feb. 1925. DOI: 10.1098/rspa.1925.0015 (cit. on p. 42).

[65] K. Hasselmann, T. P. Barnett, E. Bouws, *et al.*, "Measurements of wind-wave growth and swell decay during the joint North Sea wave project (JONSWAP).," 1973 (cit. on pp. 44, 49, 50).

[66] R. G. Dean and R. A. Dalrymple, *Coastal Processes with Engineering Applications*. Cambridge University Press, Nov. 2001. DOI: 10.1017/CBO9780511754500 (cit. on p. 44).

[67] I. R. Young, *Wind Generated Ocean Waves* (Elsevier Ocean Engineering Series). Elsevier, 1999, vol. 2. DOI: 10.1016/S1571-9952(99)X8001-9 (cit. on p. 44).

[68] E. H. Owens, "Sea conditions," in *Encycl. Beaches Coast. Environ.* M. L. Schwartz, Ed., 1982. DOI: 10.1007/0-387-30843-1_397 (cit. on pp. 46, 67).

[69] NOAA. "Marine Publications." (2024), [Online]. Available: https://www.weather.gov/marine/pub (visited on 08/21/2024) (cit. on p. 48).

[70] W. J. Pierson and L. Moskowitz, "A proposed spectral form for fully developed wind seas based on the similarity theory of S. A. Kitaigorodskii," *J. Geophys. Res.*, vol. 69, no. 24, pp. 5181–5190, Dec. 1964. DOI: 10.1029/JZ069i024p05181 (cit. on p. 47).

[71] W. H. Michel, "Sea Spectra Simplified," *Mar. Technol. SNAME News*, vol. 5, no. 01, pp. 17–30, 1968. DOI: 10.5957/mt1.1968.5.1.17 (cit. on p. 51).

[72] S. Lavery, "Simulation and Modelling of Sub-THz Radar Sea Clutter," University of St Andrews, Tech. Rep., 2020 (cit. on pp. 51, 52).

[73] O. C. Rodríguez, A. J. Silva, J. P. Gomes, and S. M. Jesus, "Modeling arrival scattering due to surface roughness," in *Eur. Conf. Underw. Acoust.*, 2010, pp. 1–8 (cit. on p. 51).

[74] H. Mitsuyasu and T. Uji, "A comparison of observed and calculated directional wave spectra in the East China Sea," *J. Oceanogr. Soc. Japan*, vol. 45, no. 5, pp. 338–349, 1989. DOI: 10.1007/BF02123487 (cit. on p. 51).

[75] D. E. Hasselmann, M. Dunckel, and J. A. Ewing, "Directional Wave Spectra Observed during JONSWAP 1973," *J. Phys. Oceanogr.*, vol. 10, pp. 1264–1280, 1980 (cit. on p. 51).

[76] WAFO Group, *WAFO: a Matlab Toolbox for Analysis of Random Waves and Loads*. Lund University, 2017 (cit. on p. 52).

[77] G. Lindgren and M. Prevosto, "WafoL: a Wafo module for Analysis of Random Lagrange Waves Tutorial for WafoL version 1.2," Tech. Rep., 2015 (cit. on p. 52).

[78] N. W. Guinard, J. T. Ransone, and J. C. Daley, "Variation of the NRCS of the sea with increasing roughness," *J. Geophys. Res.*, vol. 76, no. 6, pp. 1525–1538, Feb. 1971. DOI: 10.1029/JC076i006p01525 (cit. on p. 55).

[79] F. T. Ulaby, R. K. Moore, and A. K. Fung, *Microwave remote sensing: Active and passive, Volume II: Radar remote sensing and surface scattering and emission theory*. Boston, MA: Addison-Wesley, 1982 (cit. on p. 55).

[80] ThorLabs. "Diffraction Gratings Tutorial." (2023), [Online]. Available: https://www.thorlabs.com/newgrouppage9.cfm?objectgroup%7B%5C_%7Did=9026 (visited on 12/19/2023) (cit. on p. 55).

[81] D. Walker, "Doppler modelling of radar sea clutter," *IEE Proc. - Radar, Sonar Navig.*, vol. 148, no. 2, pp. 73–80, 2001. DOI: 10.1049/ip-rsn:20010182 (cit. on pp. 56, 58, 59).

[82] L. Rosenberg, "Sea-spike detection in high grazing angle X-band sea-clutter," *IEEE Trans. Geosci. Remote Sens.*, vol. 51, no. 8, pp. 4556–4562, 2013. DOI: 10.1109/TGRS.2013.2239112 (cit. on p. 56).

[83] J. Fuchs, D. Regas, T. Waseda, S. Welch, and M. P. Tulin, "Correlation of hydrodynamic features with LGA radar backscatter from breaking waves," *IEEE Trans. Geosci. Remote Sens.*, vol. 37, no. 5 II, pp. 2442–2460, 1999. DOI: 10.1109/36.789641 (cit. on pp. 58, 196, 202).

[84] V. Gregers-Hansen and R. Mital, "An Improved Empirical Model for Radar Sea Clutter Reflectivity," *IEEE Trans. Aerosp. Electron. Syst.*, vol. 48, no. 4, pp. 3512–3524, Oct. 2012. DOI: 10.1109/TAES.2012.6324732 (cit. on pp. 61, 69, 86, 87, 92, 93, 95).

[85] D. K. Barton, *Modern Radar System Analysis*. Norwood, MA: Artech House, 1988 (cit. on p. 62).

[86] L. Rosenberg, S. Watts, and M. S. Greco, "Modeling the Statistics of Microwave Radar Sea Clutter," *IEEE Aerosp. Electron. Syst. Mag.*, vol. 34, no. 10, pp. 44–75, 2019. DOI: 10.1109/MAES.2019.2901562 (cit. on p. 63).

[87] S. Watts and L. Rosenberg, "A review of high grazing angle sea-clutter," *2013 Int. Conf. Radar - Beyond Orthodox. New Paradig. Radar, RADAR 2013*, pp. 240–245, 2013. DOI: 10.1109/RADAR.2013.6651992 (cit. on pp. 62, 66).

[88] M. W. Long, "On a Two-Scatterer Theory of Sea Echo," *IEEE Trans. Antennas Propag.*, vol. 22, no. 5, pp. 667–672, 1974. DOI: 10.1109/TAP.1974.1140870 (cit. on p. 63).

[89] P. H. Lee, J. D. Barter, K. L. Beach, *et al.*, "X band microwave backscattering from ocean waves," *J. Geophys. Res.*, vol. 100, no. C2, pp. 2591–2611, Feb. 1995. DOI: 10.1029/94JC02741 (cit. on p. 63).

[90] D. B. Trizna, J. P. Hansen, P. Hwang, and Jin Wu, "Laboratory studies of radar sea spikes at low grazing angles," *J. Geophys. Res.*, vol. 96, no. C7, pp. 529–541, Jul. 1991. DOI: 10.1029/91jc00705 (cit. on pp. 63, 64).

[91] M. M. Horst, F. B. Dyer, and M. T. Tuley, "Radar sea clutter model," in *Int. Conf. Antennas Propag.*, London, England: IEEE, 1978, pp. 6–10 (cit. on p. 67).

[92] G. Ewell, M. Horst, and M. Tuley, "Predicting the Performance of Low-Angle Microwave Search Radars– Targets, Sea Clutter, and the Detection Process," in *Ocean. '79*, IEEE, 1979, pp. 373–378. DOI: 10.1109/OCEANS.1979.1151333 (cit. on pp. 68, 69, 73).

[93] K. D. Ward, C. J. Baker, and S. Watts, "Maritime surveillance radar. Part 1. Radar scattering from the ocean surface," *IEE proceedings. Part F. Commun. radar signal Process.*, vol. 137, no. 2, pp. 51–62, 1990. DOI: 10.1049/ip-f-2.1990.0009 (cit. on p. 71).

[94] J. C. Wiltse, S. P. Schlesinger, and C. M. Johnson, "Back-Scattering Characteristics of the Sea in the Region from 10 to 50 KMC," *Proc. IRE*, vol. 45, no. 2, pp. 220–228, 1957. DOI: 10.1109/JRPROC.1957.278393 (cit. on p. 73).

[95] W. K. Rivers, "Low-angle radar sea return at 3 mm wavelength," Georgia Institute of Technology, Atlanta, Tech. Rep., Nov. 1970 (cit. on pp. 73, 74).

[96] F. B. Dyer, N. C. Currie, and M. S. Applegate, "Radar backscatter from land, sea, rain, and snow at millimeter wavelengths," in *Radar-77*, Jan. 1977, pp. 539–563 (cit. on p. 74).

[97] M. W. Long, *Radar reflectivity of land and sea*, 3rd. Artech House, 2001 (cit. on p. 74).

[98] R. N. Trebits, N. C. Currie, and F. B. Dyer, "Multifrequency Radar Sea Return," in *URSI Comm. F Symp.*, Quebec, 1980 (cit. on p. 74).

[99] G. P. Kulemin, *Millimeter-wave radar targets and clutter*. Artech House, 2003 (cit. on pp. 74, 91–93, 95).

[100] R. Makaruschka and H. Essen, "Remote Sensing of the Sea Surface at 94 GHz," in *20th Eur. Microw. Conf. 1990*, vol. 2, IEEE, Oct. 1990, pp. 1408–1412. DOI: 10.1109/EUMA.1990.336264 (cit. on pp. 75, 77, 92, 93, 95).

[101] H. H. Fuchs, "Measurements of radar backscatter from the ocean surface at 94 GHz as a function of wind speed, direction and the modulation by the ocean waves during the SAXON-FPN experiment.," in *AGARD Conf.*, Rotterdam, 1993, p. 43 (cit. on pp. 76, 93).

[102] S. Boehmsdorff, H. Essen, and R. Makaruschka, "Polarimetric multifrequency SAR measurements over sea at millimeter-wave frequencies," *Wideband Interferom. Sens. Imaging Polarim.*, vol. 3120, no. December 1997, pp. 336–345, 1997. DOI: 10.1117/12.283847 (cit. on pp. 76, 78, 95).

[103] S. Boehmsdorff and H. Essen, "Sea surface and ship observation with MEMPHIS," in *Int. Geosci. Remote Sens. Symp.*, vol. 2, IEEE, 1998, pp. 807–809. DOI: 10.1109/igarss.1998.699590 (cit. on pp. 78, 79, 82, 92, 94, 95).

[104] G. Connan, H. Griffiths, and R. Garello, "Millimetre-wave radar measurements from laboratory surface waves," *Int. Geosci. Remote Sens. Symp.*, vol. 1, pp. 176–178, 1999. DOI: 10.1109/igarss.1999.773438 (cit. on pp. 78, 92).

[105] T. Lamont-Smith, "Doppler spectra of laboratory wind waves at low grazing angle," *Waves Random Media*, vol. 10, no. 1, pp. 33–41, 2000. DOI: 10.1088/0959-7174/10/1/303 (cit. on pp. 79, 80, 85, 92).

[106] D. Walker, "Experimentally motivated model for low grazing angle radar Doppler spectra of the sea surface," *IEE Proc. - Radar, Sonar Navig.*, vol. 147–120, no. 3, p. 114, 2000. DOI: 10.1049/ip-rsn:20000386 (cit. on pp. 80, 81).

[107] T. Schlick, M. Gade, H. H. Essen, K. W. Gurgel, and P. A. Lange, "W-band radar backscattering at low grazing angles measured in a wave tank at various wind speeds," in *Int. Geosci. Remote Sens. Symp.*, vol. 3, 2002, pp. 1825–1827. DOI: 10.1109/igarss.2002.1026267 (cit. on pp. 80, 81, 92–94).

[108] T. Lamont-Smith, "Investigation of the variability of Doppler spectra with radar frequency and grazing angle," *IEE Proc. - Radar, Sonar Navig.*, vol. 151, no. 5, pp. 291–298, 2004. DOI: 10.1049/ip-rsn:20040859 (cit. on p. 81).

[109] L. Li, G. M. Heymsfield, L. Tian, and P. E. Racette, "Measurements of ocean surface backscattering using an airborne 94-GHz cloud radar - Implication for calibration of airborne and spaceborne W-band radars," *J. Atmos. Ocean. Technol.*, vol. 22, no. 7, pp. 1033–1045, 2005. DOI: 10.1175/JTECH1722.1 (cit. on p. 81).

[110] P. Bell, J. Williams, S. Clark, B. Morris, and A. Vila-Concejo, "Nested Radar Systems for Remote Coastal Observations," *J. Coast. Res.*, vol. SI39, pp. 483–487, 2006 (cit. on pp. 82, 83, 86, 89, 91).

[111] H. Essen, H.-H. Fuchs, and A. Pagels, "Remote sensing of the sea surface by millimeterwave SAR," in *Remote Sens. Ocean. Sea Ice, Large Water Reg. 2006*, C. R. Bostater, Jr., X. Neyt, S. P. Mertikas, and M. Vélez-Reyes, Eds., vol. 6360, Sep. 2006. DOI: 10.1117/12.688423 (cit. on pp. 82, 84, 85, 91–93, 95).

[112] H. Essen, H.-H. Fuchs, and A. Pagels, "High resolution millimeterwave SAR for the remote sensing of wave patterns," in *2007 IEEE Int. Geosci. Remote Sens. Symp.*, IEEE, 2007, pp. 963–966. DOI: 10.1109/IGARSS.2007.4422959 (cit. on p. 85).

[113] T. Lamont-Smith, T. Waseda, and C.-K. Rheem, "Measurements of the Doppler spectra of breaking waves," *IET Radar, Sonar Navig.*, vol. 1, no. 2, pp. 149–157, 2007. DOI: 10.1049/iet-rsn:20060109 (cit. on pp. 85, 91).

[114] T. Leonard, T. Lamont-Smith, R. Hodges, and P. Beasley, "94-GHz Tarsier radar measurements of wind waves and small targets," *Eur. Microw. Week 2011 "Wave to Futur. EuMW 2011, Conf. Proc. - 8th Eur. Radar Conf. EuRAD 2011*, no. October, pp. 73–76, 2011 (cit. on p. 85).

[115] A. G. Stove, D. A. Robertson, and D. G. Macfarlane, "Littoral sea clutter returns at 94GHz," in *2014 Int. Radar Conf. Radar 2014*, Institute of Electrical and Electronics Engineers Inc., Mar. 2014, pp. 1–6. DOI: 10.1109/RADAR.2014.7060308 (cit. on pp. 86–89, 92–95, 100, 257, 258, 260).

[116] A. Battaglia, M. Wolde, L. P. D'Adderio, *et al.*, "Characterization of Surface Radar Cross Sections at W-Band at Moderate Incidence Angles," *IEEE Trans. Geosci. Remote Sens.*, vol. 55, no. 7, pp. 3846–3859, Jul. 2017. DOI: 10.1109/TGRS.2017.2682423 (cit. on p. 87).

[117] V. Fabbro, G. Biegel, J. Forster, *et al.*, "Measurements of Sea Clutter at Low Grazing Angle in Mediterranean Coastal Environment," *IEEE Trans. Geosci. Remote Sens.*, vol. 55, no. 11, pp. 6379–6389, Nov. 2017. DOI: 10.1109/TGRS.2017.2727057 (cit. on p. 88).

[118] A. Danklmayer, J. Forster, V. Fabbro, *et al.*, "Radar Propagation Experiment in the North Sea: The Sylt Campaign," *IEEE Trans. Geosci. Remote Sens.*, vol. 56, no. 2, pp. 835–846, Feb. 2018. DOI: 10.1109/TGRS.2017.2755506 (cit. on p. 88).

[119] B. X. Weidong Hu, Z. Li, Y. Liu, and Y. Zhao, "W-band Littoral Low Grazing Angle Sea Clutter Measurement," *2019 IEEE Int. Conf. Comput. Electromagn. ICCEM 2019 - Proc.*, pp. 13–15, 2019. DOI: 10.1109/COMPEM.2019.8779195 (cit. on pp. 88, 92, 95, 258, 260).

[120] R. J. Roy, K. B. Cooper, M. Lebsock, *et al.*, "First Airborne Measurements With a G-Band Differential Absorption Radar," *IEEE Trans. Geosci. Remote Sens.*, vol. 60, 2022. DOI: 10.1109/TGRS.2021.3134670 (cit. on pp. 89, 100).

[121] M. Greco, F. Gini, and M. Rangaswamy, "Statistical analysis of measured polarimetric clutter data at different range resolutions," *IEE Proc. - Radar, Sonar Navig.*, vol. 153, no. 6, pp. 473–481, 2006. DOI: 10.1049/ip-rsn:20060045 (cit. on p. 90).

[122] J. Nemarich, R. J. Wellman, D. Rocha, and G. B. Wetzel, "A system for measuring near-millimeter wave target signature and propagation characteristics," *EASCON'81; Electron. Aerosp. Syst. Conv.*, pp. 226–233, 1981 (cit. on p. 98).

[123] J. Nemarich, R. J. Wellman, and J. Lacombe, "Backscatter and Attenuation by Falling Snow and Rain at 96, 140, and 225 GHz," *IEEE Trans. Geosci. Remote Sens.*, vol. 26, no. 3, pp. 319–329, 1988. DOI: 10.1109/36.3034 (cit. on p. 98).

[124] R. E. McIntosh, R. M. Narayanan, J. B. Mead, and D. H. Schaubert, "Design and Performance of a 215 GHz Pulsed Radar System," *IEEE Trans. Microw. Theory Tech.*, vol. 36, no. 6, pp. 994–1001, 1988. DOI: 10.1109/22.3624 (cit. on p. 98).

[125] R. M. Narayanan, C. C. Borel, and R. E. McIntosh, "Radar Backscatter Characteristics of Trees at 215 GHz," *IEEE Trans. Geosci. Remote Sens.*, vol. 26, no. 3, pp. 217–228, 1988. DOI: 10.1109/36.3025 (cit. on p. 98).

[126] J. B. Mead, R. E. McIntosh, D. Vandemark, and C. T. Swift, "Remote Sensing of Clouds and Fog with a 1.4-mm Radar," *J. Atmos. Ocean. Technol.*, vol. 6, no. 6, pp. 1090–1097, Dec. 1989. DOI: 10.1175/1520-0426(1989)006<1090:RSOCAF>2.0.CO;2 (cit. on p. 98).

[127] J. B. Mead and R. E. McIntosh, "A 225 GHz polarimetric radar," *IEEE Trans. Microw. Theory Tech.*, vol. 38, no. 9, pp. 1252–1258, Sep. 1990. DOI: 10.1109/22.58651 (cit. on p. 98).

[128] J. B. Mead and R. E. McIntosh, "Polarimetric Backscatter Measurements of Deciduous And Coniferous Trees at 225 GHz," *IEEE Trans. Geosci. Remote Sens.*, vol. 29, no. 1, pp. 21–28, 1991. DOI: 10.1109/36.103289 (cit. on p. 98).

[129] J. B. Mead, P. M. Langlois, P. S. Chang, and R. E. McIntosh, "Polarimetric Scattering from Natural Surfaces at 225 GHz," *IEEE Trans. Antennas Propag.*, vol. 39, no. 9, pp. 1405–1411, 1991. DOI: 10.1109/8.99051 (cit. on p. 98).

[130] R. W. McMillan, C. W. Trussell, R. A. Bohlander, J. C. Butterworth, and R. E. Forsythe, "An Experimental 225 GHz Pulsed Coherent Radar," *IEEE Trans. Microw. Theory Tech.*, vol. 39, no. 3, pp. 555–562, 1991. DOI: 10.1109/22.75300 (cit. on p. 98).

[131] H. Essen, A. Wahlen, R. Sommer, *et al.*, "High-bandwidth 220 GHz experimental radar," *Electron. Lett.*, vol. 43, no. 20, pp. 1114–1116, 2007. DOI: 10.1049/el:20071865 (cit. on p. 99).

[132] H. Essen, A. Wahlen, R. Sommer, W. Johannes, M. Schlechtweg, and A. Tessmann, "Development of a 220-GHz experimental radar," *Ger. Microw. Conf. GEMIC 2008*, pp. 404–407, 2008 (cit. on p. 99).

[133] H. Essen, S. Stanko, R. Sommer, *et al.*, "A high performance 220-GHz broadband experimental radar," *33rd Int. Conf. Infrared Millim. Waves 16th Int. Conf. Terahertz Electron. 2008, IRMMW-THz 2008*, pp. 6–7, 2008. DOI: 10.1109/ICIMW.2008.4665687 (cit. on p. 99).

[134] H. B. Wallace, "Development of a video SAR for FMV through clouds," *Open Archit. Bus. Model Net-Centric Syst. Def. Transform. 2015*, vol. 9479, no. May 2015, 2015. DOI: 10.1117/12.2181420 (cit. on pp. 99, 100).

[135] S. H. Kim, R. Fan, and F. Dominski, "ViSAR: A 235 GHz radar for airborne applications," *2018 IEEE Radar Conf. RadarConf 2018*, pp. 1549–1554, Jun. 2018. DOI: 10.1109/RADAR.2018.8378797 (cit. on pp. 99, 100).

[136] D. T. Petkie, E. Bryan, C. Benton, *et al.*, "Remote respiration and heart rate monitoring with millimeter-wave/terahertz radars," *Millimetre Wave Terahertz Sensors Technol.*, vol. 7117, no. October 2008, 2008. DOI: 10.1117/12.800356 (cit. on p. 99).

[137] D. T. Petkie, C. Benton, and E. Bryan, "Millimeter wave radar for remote measurement of vital signs," *IEEE Natl. Radar Conf. - Proc.*, no. 2, pp. 9–11, 2009. DOI: 10.1109/RADAR.2009.4977021 (cit. on p. 99).

[138] G. P. Timms, "Design and testing of an active 190-GHz millimeter-wave imager," *J. Electron. Imaging*, vol. 19, no. 4, 2010. DOI: 10.1117/1.3514744 (cit. on p. 99).

[139] B. Zeng, M. Liang, C. Zhang, and Y. Zhao, "An experimental 0.2 THz stepped frequency radar system for the target detection," *Infrared, Millimeter-Wave, Terahertz Technol. II*, vol. 8562, no. December 2012, 2012. DOI: 10.1117/12.999866 (cit. on p. 99).

[140] S. Gu, C. Li, X. Gao, Z. Sun, and G. Fang, "Terahertz aperture synthesized imaging with fan-beam scanning for personnel screening," *IEEE Trans. Microw. Theory Tech.*, vol. 60, no. 12, pp. 3877–3885, 2012. DOI: 10.1109/TMTT.2012.2221738 (cit. on p. 99).

[141] T. Jaeschke, C. Bredendiek, and N. Pohl, "A 240 GHz ultra-wideband FMCW radar system with on-chip antennas for high resolution radar imaging," *IEEE MTT-S Int. Microw. Symp. Dig.*, pp. 1–4, 2013. DOI: 10.1109/MWSYM.2013.6697495 (cit. on p. 99).

[142] B. Cheng, G. Jiang, C. Wang, *et al.*, "Real-time imaging with a 140 GHz inverse synthetic aperture radar," *IEEE Trans. Terahertz Sci. Technol.*, vol. 3, no. 5, pp. 594–605, 2013. DOI: 10.1109/TTHZ.2013.2268317 (cit. on pp. 99, 100).

[143] J. Fritz, L. Scally, A. J. Gasiewski, and K. Zhang, "A sub-terahertz real aperture imaging radar," *IEEE Natl. Radar Conf. - Proc.*, pp. 1165–1169, 2014. DOI: 10.1109/RADAR.2014.6875772 (cit. on pp. 99, 100).

[144] Z. Sun, C. Li, S. Gu, and G. Fang, "Fast three-dimensional image reconstruction of targets under the illumination of terahertz gaussian beams with enhanced phase-shift migration to improve computation efficiency," *IEEE Trans. Terahertz Sci. Technol.*, vol. 4, no. 4, pp. 479–489, 2014. DOI: 10.1109/TTHZ.2014.2326004 (cit. on p. 99).

[145] M. Y. Liang, C. L. Zhang, R. Zhao, and Y. J. Zhao, "Experimental 0.22 THz stepped frequency radar system for ISAR imaging," *J. Infrared, Millimeter, Terahertz Waves*, vol. 35, no. 9, pp. 780–789, Jun. 2014. DOI: 10.1007/S10762-014-0079-7/FIGURES/7 (cit. on pp. 99, 100).

[146] M. Moallem and K. Sarabandi, "Polarimetric study of MMW imaging radars for indoor navigation and mapping," *IEEE Trans. Antennas Propag.*, vol. 62, no. 1, pp. 500–504, 2014. DOI: 10.1109/TAP.2013.2289354 (cit. on pp. 99, 100).

[147] D. A. Robertson, D. G. Macfarlane, and T. Bryllert, "220GHz wideband 3D imaging radar for concealed object detection technology development and phenomenology studies," *Passiv. Act. Millimeter-Wave Imaging XIX*, vol. 9830, no. May 2016, 2016. DOI: 10.1117/12.2222780 (cit. on pp. 99, 108).

[148] J. Grzyb, K. Statnikov, N. Sarmah, B. Heinemann, and U. R. Pfeiffer, "A 210-270-GHz Circularly Polarized FMCW Radar with a Single-Lens-Coupled SiGe HBT Chip," *IEEE Trans. Terahertz Sci. Technol.*, vol. 6, no. 6, pp. 771–783, Nov. 2016. DOI: 10.1109/TTHZ.2016.2602539 (cit. on p. 99).

[149] A. Y. Nashashibi, A. A. Ibrahim, S. Cook, and K. Sarabandi, "Experimental Characterization of Polarimetric Radar Backscatter Response of Distributed Targets at High Millimeter-Wave Frequencies," *IEEE Trans. Geosci. Remote Sens.*, vol. 54, no. 2, pp. 1013–1024, Feb. 2016. DOI: 10.1109/TGRS.2015.2472340 (cit. on pp. 99, 100).

[150] Q. Yang, Y. Qin, K. Zhang, B. Deng, X. Wang, and H. Wang, "Experimental research on vehicle-borne SAR imaging with THz radar," *Microw. Opt. Technol. Lett.*, vol. 59, no. 8, pp. 2048–2052, 2017. DOI: 10.1002/mop.30668 (cit. on p. 99).

[151] M. Bian, S. Wang, and W. Hu, "Design and experiment of spaceborne Terahertz cloud profiling radar," *Int. Conf. Infrared, Millimeter, Terahertz Waves, IRMMW-THz*, pp. 1–4, 2017. DOI: 10.1109/IRMMW-THz.2017.8066883 (cit. on p. 99).

[152] A. Y. Nashashibi, B. Alazem, and K. Sarabandi, "Fully polarimetric FMCW instrumentation radar at 228 GHz," in *2017 Usn. Radio Sci. Meet. (Joint with AP-S Symp.*, IEEE, Jul. 2017, pp. 35–36. DOI: 10.1109/USNC-URSI.2017.8074884 (cit. on pp. 99, 100).

[153] K. B. Cooper, R. R. Monje, L. Millán, *et al.*, "Atmospheric Humidity Sounding Using Differential Absorption Radar Near 183 GHz," *IEEE Geosci. Remote Sens. Lett.*, vol. 15, no. 2, pp. 163–167, Feb. 2018. DOI: 10.1109/LGRS.2017.2776078 (cit. on pp. 99, 100).

[154] Y. Zhang, Q. Yang, B. Deng, Y. Qin, and H. Wang, "Experimental research on interferometric inverse synthetic aperture radar imaging with multi- channel terahertz radar system," *Sensors (Switzerland)*, vol. 19, no. 10, 2019. DOI: 10.3390/s19102330 (cit. on pp. 99, 100).

[155] B. M. Courtier, A. Battaglia, P. G. Huggard, *et al.*, "First Observations of G-Band Radar Doppler Spectra," *Geophys. Res. Lett.*, vol. 49, no. 4, Feb. 2022. DOI: 10.1029/2021GL096475 (cit. on pp. 99, 100).

[156] R. J. Roy, M. Lebsock, L. Millán, and K. B. Cooper, "Validation of a G-band differential absorption cloud radar for humidity remote sensing," *J. Atmos. Ocean. Technol.*, vol. 37, no. 6, pp. 1085–1102, 2020. DOI: 10.1175/JTECH-D-19-0122.1 (cit. on p. 100).

[157] K. B. Cooper, R. M. Beauchamp, R. J. Roy, L. Millan, M. D. Lebsock, and R. R. Monje, "Cloud Dynamics Revealed by a G-band Humidity-Sounding Differential Absorption Radar," *IEEE Natl. Radar Conf. - Proc.*, vol. 2020-Septe, pp. 0–4, 2020. DOI: 10.1109/RadarConf2043947.2020.9266525 (cit. on p. 100).

[158] A. Doerry, "Catalog of Window Taper Functions for Sidelobe Control," Sandia National Laboratories (SNL), Albuquerque, NM, and Livermore, CA (United States), Tech. Rep. April, Apr. 2017. DOI: 10.2172/1365510 (cit. on pp. 103, 164, 173, 175, 189).

[159] K. B. Cooper, R. J. Roy, R. Dengler, *et al.*, "G-Band Radar for Humidity and Cloud Remote Sensing," *IEEE Trans. Geosci. Remote Sens.*, vol. 59, no. 2, pp. 1106–1117, Feb. 2021. DOI: 10.1109/TGRS.2020.2995325 (cit. on p. 112).

[160] D. A. Robertson, G. M. Brooker, and P. D. L. Beasley, "Very low-phase noise, coherent 94GHz radar for micro-Doppler and vibrometry studies," in *Radar Sens. Technol. XVIII*, K. I. Ranney and A. Doerry, Eds., vol. 9077, 2014. DOI: 10.1117/12.2053015 (cit. on p. 113).

[161] C. Granet, R. Bolton, and G. Moorey, "A smooth-walled spline-profile horn as an alternative to the corrugated horn for wide band millimeter-wave applications," *IEEE Trans. Antennas Propag.*, vol. 52, no. 3, pp. 848–854, Mar. 2004. DOI: 10.1109/TAP.2004.825156 (cit. on p. 115).

[162] P. F. Goldsmith, *Quasioptical systems: Gaussian beam quasioptical propagation and applications*. Wiley-IEEE Press, 1998. DOI: 10.1109/9780470546291 (cit. on pp. 116, 117).

[163] C. Pruss, E. Garbusi, and W. Osten, "Testing Aspheres," *Opt. Photonics News*, vol. 19, no. 4, pp. 24–29, Apr. 2008. DOI: 10.1364/OPN.19.4.000024 (cit. on p. 118).

[164] D. G. Macfarlane, D. A. Robertson, and S. L. Cassidy, "Second generation of AVTIS FMCW millimeter wave radars for mapping volcanic terrain," in *Radar Syst. Technol. NN, Proc. SPIE 9829*, K. I. Ranney and A. Doerry, Eds., vol. 9829, International Society for Optics and Photonics, May 2016. DOI: 10.1117/12.2223039 (cit. on p. 121).

[165] Analog Devices, "AD9914 Datasheet (Rev. G)," Tech. Rep., 2012 (cit. on p. 140).

[166] "Unique Rohde & Schwarz 170 GHz power sensors ease use and traceability in the D-band | Rohde & Schwarz." (2023), [Online]. Available: https://www.rohde-schwarz.com/uk/about/news-press/all-news/unique-rohde-schwarz-170-ghz-power-sensors-ease-use-and-traceability-in-the-d-band-press-release-detailpage%7B%5C_%7D229356-1435521.html (visited on 02/13/2024) (cit. on p. 161).

[167] "Virginia Diodes, Inc - Power Meters - Erickson." (2024), [Online]. Available: https://www.vadiodes.com/en/products/power-meters-erickson (visited on 08/12/2024) (cit. on p. 161).

[168] S. D. Robertson, "Targets for Microwave Radar Navigation," *Bell Syst. Tech. J.*, vol. 26, no. 4, pp. 852–869, Oct. 1947. DOI: 10.1002/j.1538-7305.1947.tb01325.x (cit. on p. 169).

[169] W. Kester, "Understand SINAD, ENOB, SNR, THD, THD+N, and SFDR so You Don't Get Lost in the Noise Floor," *Analog Devices Tutorial, MT-003, Rev. A*, pp. 2–9, 2009 (cit. on p. 175).

[170] Radiometer Physics, "RPG LNA - Low Noise Amplifier - Specifications," Tech. Rep., 2020 (cit. on pp. 175, 272).

[171] A. Mehrotra, "Noise analysis of phase-locked loops," *IEEE Trans. Circuits Syst. I Fundam. Theory Appl.*, vol. 49, no. 9, pp. 1309–1316, Sep. 2002. DOI: 10.1109/TCSI.2002.802347 (cit. on p. 177).

[172] "Welcome to the FloWave Ocean Energy Research Facility | FloWave Ocean Energy Research Facility." (2024), [Online]. Available: https://www.flowavett.co.uk/ (visited on 03/11/2024) (cit. on p. 180).

[173] A. Stove, L. Daniel, M. Gashinova, E. Hoare, and D. Kumar, "Finding Anomalies in Radar Sea Clutter Using Radon Transforms," in *2021 18th Eur. Radar Conf.*, IEEE, Apr. 2022, pp. 421–424. DOI: 10.23919/EuRAD50154.2022.9784544 (cit. on p. 198).